X-RAY EMISSION FROM HEAVY ATOMIC COLLISIONS: COUPLINGS OF INNER SHELLS IN SUPERHEAVY QUASIMOLECULES

Inauguraldissertation
zur
Erlangung des Doktorgrades der Naturwissenschaftlichen Fakultät
der Justus-Liebig-Universität Gießen

Fachbereich
Mathematik und Informatik, Physik, Geographie

Vorgelegt von
Punita Verma
aus (MEERUT, INDIEN)

Gießen 2010

Dedicated to

The Almighty

This work was performed at the accelerator facility at GSI-Helmholzzentrum für Schwerionenforschung Darmstadt, Germany, within the sandwich model of the Indo-German exchange program of DAAD-UGC under the joint supervision of Prof. Dr. P.H. Mokler and Prof. M.A. Wahab.

Prof. Dr. P. H. Mokler
GSI, Darmstadt, Germany
and University of Gießen,
Gießen, Germany.

Prof. M. A. Wahab
Dept. of Physics,
Jamia Millia Islamia,
New Delhi, India.

Vorgelegt am: 4.11.2010
Tag der Disputation: 21.12.2010

INDEX

CHAPTER I

SUPERHEAVY QUASIMOLECULES AND PRESENT INVESTIGATION

CHAPTER II

HEAVY ION – HEAVY ATOM COLLISION PROCESSES

CHAPTER III

EXPERIMENTAL DETAILS AND DATA ANALYSIS PROCEDURE

CHAPTER IV

A SLIGHTLY ASYMMETRIC SUPERHEAVY COLLISION SYSTEM: U^{q+}-Au

CHAPTER V

A NEAR SYMMETRIC SUPERHEAVY COLLISION SYSTEM: Bi^{q+}-Au

CHAPTER VI

COUPLING DISTANCES IN SUPERHEAVY COLLISION SYSTEMS

CHAPTER VII

CONCLUSIONS AND OUTLOOK

BIBLIOGRAPHY

CHAPTER I

SUPERHEAVY QUASIMOLECULES AND PRESENT INVESTIGATION

1.1 INTRODUCTION

The central aim of the present study is to investigate the inner shell dynamics of superheavy quasimolecules. Quasimolecules are formed transiently in close collisions of two atomic partners at moderate velocities. This is especially true for inner shells of heavy collision partners where the electron orbital velocity (v_e) is larger than the collision velocity (v_{ion}) of the projectile ($v_e > v_{ion}$). During collision, the inner shell electrons adjust continuously and adiabatically to the combined, time varying, two center potential of both the partners. For very heavy partners with $Z_1+Z_2 >100$ (Z_1 and Z_2 are the atomic numbers of the projectile and target respectively), one penetrates into the atomic world of superheavy systems with a united atomic number $Z_{UA} = Z_1+Z_2$. The quasi-stationary states of the innermost bound electrons are called “quasimolecular” states and when the internuclear distance R(t) becomes smaller than the K-shell radius of the united atom (UA) with charge Z_{UA} then these quasimolecular states may even become “quasiatomic” states. These superheavy quasimolecules arouse interest due to their strong, partially overcritical electromagnetic fields with a coupling strength of $Z_{UA} \geq 1/\alpha$ (=137, with α being the fine structure constant).

The most strongly bound electrons in these quasimolecules experience these overcritical fields transiently. As a result, the fully relativistic, many electron problem has to be solved in order to calculate the energy eigen values for the different internuclear distances (R) involved [1]. For high Z_{UA}, the solution reveals an extremely strong increase of the binding energy at very small R, thus the electrons in these orbitals may be bound with energies even beyond their rest mass. As the binding energies increase the wave functions shrink considerably e.g. in the case of Pb the K-shell radius (r_K) shrinks roughly from 700 fm at Z = 82 to 100 fm for an atom with Z_{UA} = 164 [2]. Moreover, these calculations show an extraordinary large spin orbit splitting which partially changes the well known, usual order of the levels. Both qualitative and quantitative properties of the electrons bound to such extraordinarily high nuclear charges are widely different from the known tendencies. Hence, an investigation into this widely unexplored region of extraordinary behaviour and properties of the atomic system constitutes an area of intellectual challenge.

By investigating heavy-ion heavy-atom collisions at moderate relativistic velocities, a unique possibility exists for exploring these highly relativistic, bound atomic systems in otherwise inaccessible overcritical fields. The inner shell electrons which are close to the nuclei are capable of

probing the potential most sensitively. The mean electric field probed by a 1s electron in the U-atom is for instance ~ $2x10^{16}$ V/cm which is roughly 10^6 times the field probed by a 1s electron in a H-atom. This value is close to the so called "Schwinger limit", a field where energies equivalent to the rest mass of the electron are involved by moving it over its own Compton wavelength. At the overcritical fields beyond the Schwinger limit, one is obviously in the region where pair creation has to be taken into account. For a quasiatom with $Z_{UA} \approx 171$, realized transiently (10^{-19}-10^{-20} s) in very close but adiabatic collisions of e.g. U-ions with Au atoms, the 1s binding energy is almost twice the electron rest mass and, hence, just touches the negative continuum, "the Dirac Sea". The general theoretical aspects of these systems are reviewed for instance in [4, 5].

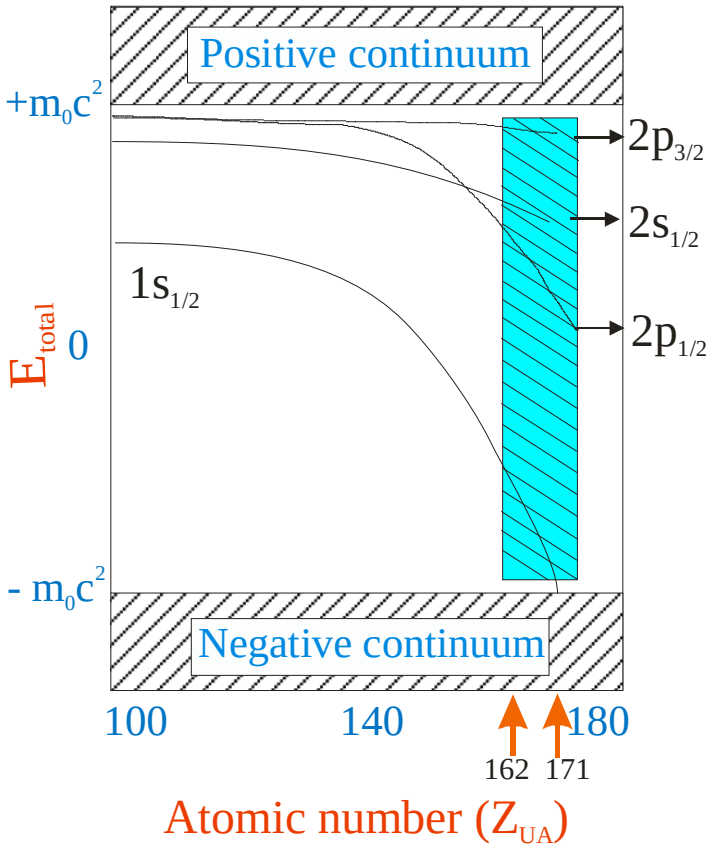

Fig. 1.1 *Dirac representation of total energy of the bound electrons (E_{total}) in superheavy atoms taken from [3]. The vertical rectangle shows the region of interest for the present investigation with Z_{UA}=162, 171.*

Fig. 1.1 gives the total energy for the bound electrons in superheavy atoms in Dirac representation as a function of the atomic number Z_{UA} (from Ref. [3]). The region of interest of the present investigation is indicated in the figure as a vertical shaded rectangle. For Z_{UA} >137, the ordinary level order of $p_{1/2}$ and $s_{1/2}$ states is swapped because of the spin orbit splitting (mentioned

earlier) for the p states. At about Z_{UA} = 173, the splitting of the L-shell is approximately equal to m_0c^2.

These superheavy systems can be investigated experimentally only during collisions where nature permits a glance at the extremely short lived superheavy "quasimolecules/quasiatoms". An investigation of the atomic processes in such electromagnetic fields became feasible in the seventies with the advent of heavy-ion accelerators, e.g. the HILAC at Berkeley, the Cyclotron at Dubna and the UNILAC at GSI, Helmholtz-Zentrum für Schwerionenforschung, GmbH, (Helmholtz Centre for heavy-ion research) Darmstadt. Numerous experimental and theoretical investigations dealing with superheavy collision systems were performed at relatively low velocities. Details regarding these investigations are given in several review articles [see e.g. 6, 7].

During the collisions, energy and momentum can be transferred to strongly bound electrons due to the time dependence of the two centre Coulomb field. These electrons can be excited into the higher lying bound states or into the continuum thereby creating a vacancy in the innermost orbitals. For these deepest vacancy states, several channels for decay are possible either in the quasimolecule itself by molecular orbital radiation or most probably by a transfer to one of the collision partners followed finally by characteristic x-ray radiation. Since the lifetimes of the inner shell vacancies are at least 1 to 2 orders of magnitude larger than the collision time, characteristic x-ray emission dominates the decay channels. An investigation of this emission for the collision partners and for the atomic shells in which the vacancies are finally transferred to, enable conclusions to be drawn regarding the excitation mechanisms of the corresponding states in the superheavy quasimolecule or even in the quasi-atom.

Heavy-ion heavy-atom collisions with highly charged projectiles at moderate collision velocities ($v_{ion}<v_e$) give, in particular, an access to the coupling of the inner-most shells in these superheavy quasimolecules [6, 7]. Using heavy-ions with a vacancy in a well defined inner shell prior to the collision and following the path of this vacancy can bring these couplings to light. A quasimolecule can only be produced at moderate collision velocities whereas normally, inner shell vacancies in a heavy projectile-ion can only be produced by stripping at a high ion velocity. These are contradicting conditions. Hence first an acceleration of the projectile-ions to high energies, followed by a stripping of the inner shell electrons and finally a deceleration of these stripped projectile-ions to desired energies is the appropriate technique to produce high intensity, highly charged, heavy-ions moving at moderate collision velocities. The acceleration-stripping-deceleration technique, (see e.g. [8]) was used successfully at the UNILAC and at other accelerator facilities to investigate inner shell processes for adiabatic collisions in the energy range 1-4 MeV/u ($Z_{UA} \leq 100$). For very heavy collision systems ($Z_{UA} \geq 100$), the study of quasimolecules was hampered partially

by the low, incoming charge state ‘q’ of the projectile, because no intensive ion beam with incoming, inner shell (K-shell) vacancies could be provided prior to the collision. To some extent the projectiles could be provided with inner shell vacancies only in the L-shell, excluding the possibility to investigate the very high fields. However, the strongest bound levels in the heaviest quasimolecules were of particular interest due to their extraordinary properties. In order to investigate the couplings of the superheavy quasimolecules in this binding energy region in more detail (Fig. 1.1, vertical shaded rectangle), prior to collision K-shell vacancies were required.

1.2 MOTIVATION

The present investigation seeks to delve deeper into the structure and dynamics of innermost levels of superheavy collision systems by using “prior to collision” inner shell projectile (K) vacancies. Such an investigation has now become possible on account of technological advances at the GSI accelerator facility i.e. at the SIS (heavy ion synchrotron) /ESR (Experimental Storage Ring), specially concerning the enhancement in beam intensities. The heavy ion accelerator facility at GSI, can now provide sufficiently intensive beams of very heavy ions with the highest charge states (H-like, He-like etc.). These ions are available for experiments moving at reasonably moderate collision velocities ($v_{ion} < v_K$) even for the heaviest elements ($Z\alpha \rightarrow 1$). Hence, inner shell vacancies can now be provided (even in the K-shell) for the incoming channel of the superheavy quasimolecule formation. This implies, quasimolecules can now be investigated overcoming the limitation of the previous investigations [6,7] with closed, incoming, inner shell vacancy channels.

Although in principle an ideal preservation of the high incoming projectile charge state can only be guaranteed for a collision with a gas target, these studies were limited in the past by the extremely low luminosities. The solid targets ensure higher luminosities and can be used for this investigation if single collision conditions for inner shell processes can be satisfied for these targets. In order to perform experiments with a H-like ion with the requirement of preservation of its charge state while penetrating a solid target, it is crucial to know the survival probability of the K-vacancy during its passage through the same.

During distant collisions, electrons are captured from different shells of the target atoms into different shells of the projectile. For highly charged projectile-ions, these electrons are captured into the outer shells mainly to excited levels and are finally observable through the characteristic x-ray emission during radiative stabilization of the projectile. For the target atom, electrons captured or lost from the medium shells may also yield to characteristic x-ray emission in the end. The capture of

electrons into different shells and angular momentum states can be distinguished partially due to the large shell and subshell splitting in heavy projectiles. For instance the very first experiments with Sm^{q+}-Xe [9] showed that electrons from the outer target shells got mainly captured into the excited levels for projectiles having energies between 3-5 MeV/u.

Table 1.1 *Summary of few review articles over the field of investigation.*

Summary of review articles
1. P.H. Mokler, S. Hagmann, P. Armbruster, G. Kraft, H.-J. Stein, K. Rashid and B. Fricke: in "Atomic Physics 4", ed. G. zu Putlitz, E.W. Weber and A. Winnacker, (Plenum Publishing Corporation, 1975), p. 301. [11]
2. P.H. Mokler and F. Folkmann: in "Topics in Current Physics", Vol. 5 Structure and Collisions of Ions and Atoms, ed. I.A. Sellin, (Springer Verlag, 1978), p. 201. [6]
3. B. Fricke: in "Progress in Spectroscopy", Part A, (Plenum Press, 1978), p. 183. [5]
4. J.S. Greenberg: in "Electronic and Atomic Collisions", ed. N. Oda and K. Takayanagi, (North Holland Publishing Company, 1980), p. 351. [12]
5. W. Greiner and W. Scheid: in "Heavy ion collisions" Vol. 3, ed. R. Bock (North Holland Publishing Company, 1982), p. 301. [13]
6. D. Liesen: in "Comments At. Mol. Phys." Vol. 2, No. 1, (Science Publishers, Inc., 1982), p. 39. [14]
7. P.H. Mokler and D. Liesen: in "Progress in Atomic Spectroscopy", Part C, ed. H.J. Beyer and Hans Kleinpoppen, (Plenum Publishing Corporation, 1984), p. 321. [7]
8. H. Backe and C. Kozhuharov: in "Progress in Atomic Spectroscopy", Part C, ed. H.J. Beyer and Hans Kleinpoppen, (Plenum Publishing Corporation, 1984), p. 459. [15]
9. P.H. Mokler: "Quasimolecular heavy ion-atom collisions", GSI-84-37 (GSI report), Invited lecture to XIX Winter School on Physics, Zakopane, Poland (3-15 April, 1984). [16]
10. J. Reinhardt and W. Greiner: in "Treatise on Heavy-Ion Science", High Energy Atomic Physics, Vol. 5, ed. D. Allan Bromley (Plenum Press, 1985), p. 3. [1]
11. J.S. Greenberg and P. Vincent: in "Treatise on Heavy-Ion Science", High Energy Atomic Physics, Vol. 5, ed. D. Allan Bromley (Plenum Press, 1985), p. 3. [17]
12. P.H. Mokler: GSI-86-25 (GSI report), "Spectroscopy of heavy few electron ions": Invited talk at 18 EGAS, Marburg, 8-11 July 1986. [18]

For intermediate and outer shells ($v_{ion} \approx$ and $> v_e$, respectively) other atomic processes are active. These processes influence the electronic configuration of the collision partners. For a detailed understanding of the inner shell processes investigated here, a knowledge of the processes in higher shells would also be helpful.

Earlier attempts [10] to understand the structure and dynamics of innermost levels in the superheavy collision systems had met with surprising successes even though quite simple physical pictures were used for the excitation processes. The literature survey showed that over about two decades a large variety of measurements for different projectile-atom systems have been made in the past and the list is almost exhaustive. Hence Table 1.1 gives a summary of some of the review articles on the subject which cite the references for the experimental and theoretical work done in this field. A need was felt for further and more selective investigation into the field using a quite novel approach.

1.3 OBJECTIVE

The central objective is to investigate the vacancy transfer between the innermost, quasimolecular levels of superheavy collision systems. K- or L-shell vacancies in the incoming channel of a close collision can be transferred to the K- or L-shell of the quasiatom during the part of the collision where the two partners approach each other. During the receding part of the collision, vacancies can be transferred to the K- or L-shell of either of the separated collision partners. Subsequently, the characteristic x-ray emission of the collision partners would indicate the final abode of these vacancies. This K-K and L-K vacancy transfer was well established for the non-relativistic region and has been confirmed even for the relativistic region (see e.g. [19]) indicating that inner shell coupling in quasimolecules can be an important process of vacancy production.

While penetrating solids, the projectile inner shell vacancies may be filled up. For a sufficiently long survival of the projectile inner shell vacancy, superheavy quasimolecules could be probed with very thin solid targets. Hence, the basis of the present investigation has been the determination of survival probability of the projectile inner shell vacancies (K and L) while its passage through a solid and therefore to find out the extent to which thin solid targets can be utilized for studying superheavy quasimolecules with well-defined, incoming inner shell vacancy channels. A target thickness dependent study of the characteristic x-ray production of the collision partners would provide information on the survival probabilities of the projectile K-vacancy as it penetrates the solid target as well as an insight into the evolution of the projectile's charge state, its distribution

and its excitation in the bulk matter. Extrapolating the x-ray emission cross sections ("absolute yields") to zero target thickness, "true" cross sections under single collision conditions could be extracted. From the true x-ray emission cross sections for different incoming vacancy conditions and using simple geometrical considerations one should be able to deduce the coupling distance for K-K and L-K vacancy transfer. The same holds true for extracting interaction distances for electron capture.

The projectile charge state dependence of the characteristic x-ray emission would unveil the various inner shell processes in play during collision and provide information on the inner shell couplings. The course of an adiabatic collision [defined by the adiabaticity parameter $\eta<1$ with $\eta = (v_{ion}/v_e)^2$] is usually described by a diabatic level diagram. For incoming projectile vacancies, the vacancy transfer can be considered within the quasimolecular picture using diabatic level diagrams. A better representation are ab initio calculated level diagrams giving the binding energies as a function of the internuclear distance (R) where mainly transitions between the levels may occur at the crossings. A comparison between extracted interaction distances and corresponding level crossing regions should reveal the inner shell vacancy transfer process in the quasimolecule.

Non-adiabatic processes in higher shells determine in particular evolution of the projectile's charge state, its distribution and its excitation while penetrating the solid. The target thickness dependence of the x-ray emission from these shells would deliver detailed information on this topic. An additional measurement of the projectile charge state distribution after the target foil (by a magnet spectrometer) would correlate the charge state evolution inside and outside the solid.

1.4 EXPERIMENTAL TECHNIQUE

In order to fulfill the above objectives, experiments have been planned with very heavy collision partners such that $Z_{UA} = Z_1+Z_2 >160$, with both a near symmetric ($Z_1 \sim Z_2$) as well as a slightly asymmetric ($Z_1 \neq Z_2$) system. The energy of the projectile ions has been so chosen that the adiabaticity parameter $\eta<1$ could be fulfilled for the electrons in the shells of concern (here the K-shell for both collision partners). The heavy-ion accelerator facility of GSI with the SIS has been used to produce relativistic very heavy ions ($v_{ion} \sim 0.4c$) followed by electron stripping to produce highly charged ions (H-like, He-like, .., up to the equilibrium 'q_{eq}'). Hence, projectiles with well defined, inner shell vacancies (K or L) in the "incoming channel" of the collision were produced. These ions then bombarded on thin foils of heavy target elements. In order to fulfill the basic as well as the central objective, it has been planned to observe the characteristic x-ray emission from both

the collision partners as a function of the target thickness ‘t’ and incident charge state ‘q’ of the projectile-ion. Moreover, the charge state evolution of the projectile ions penetrating the foil could be observed.

The study has been performed with highly charged, very heavy ions such as U (Z_1 = 92) and Bi-ions (Z_1 = 83) as projectiles incident at ~ 69 MeV/u on thin Au (Z_2 = 79) target foils. Table 1.2 gives a list of the experiments performed along with the details of projectile ion, its charge state, energy, the targets investigated and the adiabaticity parameter for the K- and L-electrons of the collision partners.

Table 1.2 *Investigated superheavy collision systems*

Parameters		**Collision type**	
Name	**Symbol**	**Near symmetric**	**Slightly asymmetric**
Quasiatom	Z_{UA}	163	171
Asymmetry	Z_1/Z_2	~1.05	~1.16
Projectile	Z_1	$_{83}Bi^{q+}$	$_{92}U^{q+}$
Charge state	q	82, 81, 77	91, 90, 88, 86, 73
Energy	E (MeV/u)	69.2	69.1
Target	Z_2	$_{79}Au$	$_{79}Au$
Target thickness	t ($\mu g/cm^2$)	21*, 42**, 79, 150, 225	18*, 50, 70
C backing	C ($\mu g/cm^2$)	*with 11$\mu g/cm^2$ C backing **with 12$\mu g/cm^2$ C backing	*with 15$\mu g/cm^2$ C backing
Adiabaticity parameter	$\eta_{K\text{-}Z1}$	0.44	0.33
	$\eta_{K\text{-}Z2}$	0.45	0.45
	$\eta_{L\text{-}Z1}$	1.8	1.4
	$\eta_{L\text{-}Z2}$	2.0	2.0

From the value of the adiabaticity parameters it is clear that the quasimolecular model for the collision processes has to be applied for the K-shells however it is not applicable for the electrons of the higher shells (L and higher). Fast collision processes e.g. loss and capture processes are effective for these higher shells. In both cases the collision partners will land up in excited states and their x-ray decay would give information on the collision processes. For observing the K and L x-ray

emission of the collision partners solid state detectors have been used. A position-sensitive diamond particle detector has been employed for observing the charge state distribution of the projectiles as well as for normalization of the x-ray emission.

The target thickness (t) dependence of the projectile K x-ray emission would reveal the extent to which projectile inner shell vacancies (here K-shell) would survive while penetrating solid targets and hence, whether solid targets can be used for collision spectroscopy of inner shells. Moreover, the K x-ray emission could be extrapolated to “zero” target thickness and hence used to approximate “single collision conditions” in the solid targets.

The charge state (q) dependence of the K x-ray emission from both the partners, on the other hand, would provide a tool to scrutinize the inner shell dynamics of the superheavy quasimolecules formed transiently during the collision. The couplings between the inner shells could be consequently elucidated. The investigation of charge state evolution of the projectiles would provide an idea about the change in initial collision conditions for a highly charged projectile while penetrating solids.

During heavy-ion heavy-atom collisions, multiple vacancies are generally created, especially in the higher lying atomic shells [cf. 20-22]. Multiple vacancies are still present during the radiative filling of the vacancies in the inner shells (K or L) and hence they act as spectators during the K or L x-ray emission. Due to the decrease in the screening of the nuclear charge, the binding energy as well as the transition energies of all the levels increase compared to the ‘single hole’ standard values [23]. This leads to energy shifts giving information on the population distributions of electrons in the higher shells during inner shell x-ray emission. Similar to the energy shifts, partially complementary information on the population distribution of the electrons in the various shells can be extracted from intensity ratios for the various x-ray lines.

Although the present investigation has not been designed for precision energy shift measurement, nevertheless even rough values for K and L x-ray emission reveal interesting trends shedding light on the collision processes acting for higher shells as well as on the charge state and evolution of the projectile’s excitation inside the target. The same is true for the intensity ratios. The determination of x-ray intensity ratios can be done with a higher precision than that for the absolute x-ray energy shifts because the main source of error arises from the counting statistics only.

Further a charge state distribution of the ejectiles behind the thin foils would confirm the survival probability of the projectile charge state ‘q’ during interaction with solid target foils. Additionally, the distributions behind the foils can be compared with the x-ray results yielding information on the charge state evolution inside the foil.

1.5 OUTLINE OF THE THESIS

The present investigation deals with x-ray emission from heavy atomic collisions, in particular with couplings of inner shells in superheavy quasimolecules. The details have been covered from Chapters 2 to 7. Chapter 2 gives an overview of the fundamental interaction processes involved in heavy-ion heavy-atom collisions. The basics of the theories for ion-atom collisions and their ranges of validity have been discussed here. Apart from Coulomb ionization processes and molecular orbital theories, the charge exchange processes have also been discussed there. Chapter 3 introduces the experimental details of the present investigation. These include the heavy-ion experimental facility at GSI, Darmstadt, Germany, the set up at the experimental area, specifications of the x-ray and particle detectors along with their efficiencies, online data acquisition system and of the data analysis procedure followed.

In chapters 4 and 5, the investigation of the slightly asymmetric, U-Au collision system and the near symmetric, Bi-Au collision systems have been discussed respectively. For both these systems, the K and L x-ray emission have been considered in detail in the chapters together with a brief interpretation of the outcome. The charge state and target thickness dependence of x-ray emission cross sections of both the projectile and target have been described. The survival probability of the projectile inner shell vacancies as the ion penetrates a solid target has been pondered upon for both the systems. The x-ray energy shifts and x-ray intensity ratios have also been considered for these systems which give information on the charge state and excitation evolution of the projectile inside the target. A refined discussion over the charge state evolution in the bulk of the target and the experimental charge exchange cross sections in comparison to theoretical values has been covered.

Chapter 6 is devoted to the interpretation and discussion of results of the present investigation where special emphasis is laid on the inner shell processes. Explanations of the strong x-ray cross section dependences on incoming projectile charge states and other interesting trends observed have been given. A discussion of the experimental findings in the light of the level diagrams used to interpret the data has been done. Interaction distances for close as well as for distant collision processes have been extracted. At the end, the conclusions drawn from the study and an outlook for future experiments are the subject of Chapter 7.

CHAPTER II

HEAVY-ION HEAVY-ATOM COLLISION PROCESSES

2.1 INTRODUCTION

This chapter introduces the relevant collision processes for the present investigation viz. "X-ray emission from heavy atomic collisions: couplings of inner shells in superheavy quasimolecules". The formation of a superheavy quasimolecule during heavy atomic collisions has been discussed already in Chapter 1. Inner shell ionization is the most important process responsible for x-ray emission in a collision (Section 2.2). The different ionization regions are elucidated in this section and the corresponding ionization processes are explained. A selective study of inner shells in superheavy quasimolecules is possible only with a survival of inner shell projectile vacancies hence the various charge changing processes in a collision such as electron loss and capture are briefly described in Section 2.3. Based on this, the charge state evolution of a projectile penetrating through matter is treated in Section 2.4. For clarity, the information that could possibly be extracted from the x-ray spectra is finally summarized in Section 2.5.

2.2 INNER SHELL IONIZATION PROCESSES

The theory of inner shell ionization by various approximate methods is a long and continuously developing field till today. Several basic approaches have been made to understand the process of inner shell vacancy production with different probes. Madison and Merzbacher [24] have reviewed the development of the various theoretical models. The inner shell ionization in various elements by light and heavy ions is caused mainly by direct Coulomb ionization, electron capture from the target to projectile and electron promotion due to quasi-molecular formation. Two parameters, the asymmetry parameter (Z_1/Z_2) and the adiabaticity parameter [$\eta = (v_{ion}/v_e)^2$] are essential for the classification of dynamic ion-atom systems. Such a rough classification known as a Madison-Merzbacher map [24] is shown schematically in Fig. 2.1. The colliding systems are divided into two regions; Region-1 with $Z_1/Z_2 << 1$ (asymmetric systems) and/or $\eta >> 1$ corresponds to the situation where the perturbing influence of the projectile nuclear motion on electrons is relatively weak due to a small strength of the projectile target interaction or due to a short interaction time. In this region single electron transitions are described by the direct ionization (DI) process caused by

direct Coulomb interaction. Region-2 with Z_1/Z_2~1 (symmetric systems) and η<1 corresponds to a strong interaction between electrons and the colliding nuclei which is responsible for the formation of a transient diatomic complex (quasimolecule).

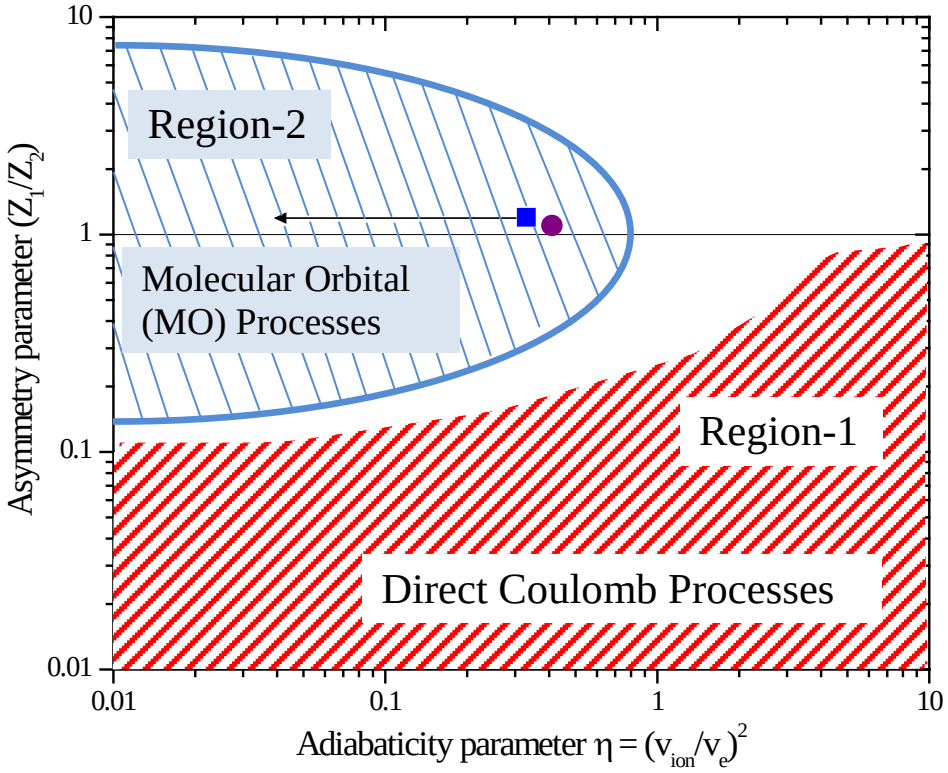

Fig. 2.1 *Diagram showing the domain of direct Coulomb ionization processes (Region-1) and Molecular Orbital processes (Region-2). The filled circle denotes the representative point for Bi-Au collision system and that of the filled square for U-Au collision system corresponding to their values of asymmetry parameter (Z_1/Z_2) and the adiabaticity parameter (η). The arrow shows the adiabaticity to which a collison system such as U-Au approaches in a superheavy collision.*

For slow and mainly symmetric (Z_1/Z_2~1) or less asymmetric collision systems Molecular Orbital [25] (MO) promotion processes are significant for vacancy production in the atomic shells. When $Z_1 \sim Z_2$ and $v_{ion} < v_e$, the target electron adjusts adiabatically in presence of two nuclear centers. As the two nuclei come closer, transient molecular orbitals (MO) are formed leading to a united atom (UA) of the target and the projectile with $Z_{UA} = Z_1+Z_2$. The electron in an inner shell of the united atom (UA) approach can be promoted to an outer shell or the continuum within the interaction time. An electron promotion could also occur by a direct curve crossing through the radial or rotational coupling [26] of the MO levels during the interaction time. Additionally, electron capture (EC) [27] can contribute to vacancy production in atomic shells, especially at moderate velocities and the probability of such a transfer becomes maximum when $v_{ion} \sim v_e$. For non relativistic collisions, the adiabaticity parameter is the appropriate criteria for classifying the collision systems.

For the near relativistic collisions of the present investigation η may not be completely suitable however it provides a reasonable picture for understanding the tendencies. Mokler and Folkmann [6] have given a complete review on "X-ray Production in Heavy Ion-Atom Collisions" including details on direct ionisation, quasimolecular excitation and electron capture.

2.2.1 Direct Coulomb ionization

The process of vacancy production by a heavy charged particle is due to the momentum transfer by the projectile to a target electron during a collision and causing the promotion of the electron to continuum level. This occurs as a result of direct Coulomb interaction of the incident projectile charge with the electron. The direct ionization (DI) theories (valid mainly for $Z_1 << Z_2$) include the 1st order theories such as Semi Classical Approximation (SCA) [28], Binary Encounter Approximation (BEA) [29] and the Plane Wave Born Approximation (PWBA) [30] and a modification of the same called ECPSSR (perturbed stationary state theory with energy loss, Coulomb deflection and relativistic effects included) [31]. Richard [32] has given a detailed review of the experimental measurements in ion-atom collisions involving direct ionization and including K and L x-ray cross sections both in solid and gas targets. Phenomena like electron capture, excitation and charge exchange in collisions of few electron projectiles with gas targets have also been discussed in the same section and the united atom phenomena has been pondered upon.

2.2.2 Molecular orbital formation

The viability of the quasimolecular description for heavy-ion collisions at higher energies rests centrally on the condition that the ratio of velocity of the moving projectile (v_{ion}) to that of the inner shell electrons (v_e) satisfies the condition $(v_{ion}/v_e)^2 << 1$. Such conditions are favourable for the atomic electrons to adjust their orbits to the combined projectile-target charge, leading to the formation of quasimolecular orbitals (MO). The variation of the molecular binding energies with changes in the interatomic distance (R) is conveniently displayed in the MO diagrams. In the evolution from the separated atom limit (R=infinity) to the united atom limit (R=0), most orbitals increase in binding energy whereas some orbitals decrease. The topography of the R-dependent molecular orbital levels and their proximity to unoccupied neighbouring states (of the collision partners or of the transient quasimolecule formed) and to the continuum provide important information on the probability of electronic transitions during the course of the collision.

In heavy ion-atom collisions two competing excitation processes occur for the inner quasimolecular levels a) MO coupling excitation and b) direct MO excitation or electron promotion. In the MO coupling excitation process interaction between approaching MO's leads to vacancy transfer down to inner shells during the collision. In direct MO excitation electrons from an inner MO level are directly transferred to the continuum (or near continuum states) during collision. When it became apparent that for $Z_1 \sim Z_2$ and $v_{ion} << v_e$, the observed cross sections for inner shell ionization (at least for small Z) were many orders of magnitude larger than predicted by any approximation discussed so far, Fano and Lichten [25] and Lichten [33] proposed that the reason for this discrepancy was the electron promotion via crossing molecular orbitals (MO). In this molecular orbital model, promoted electrons can be ejected to the continuum or couple to empty higher lying states, where the created vacancies are finally transferred to the inner shells in the separated atoms. This process was discussed in terms of diabatic level diagrams [34, 35]. The observed enhanced cross sections lent support to the MO model of inner shell ionization.

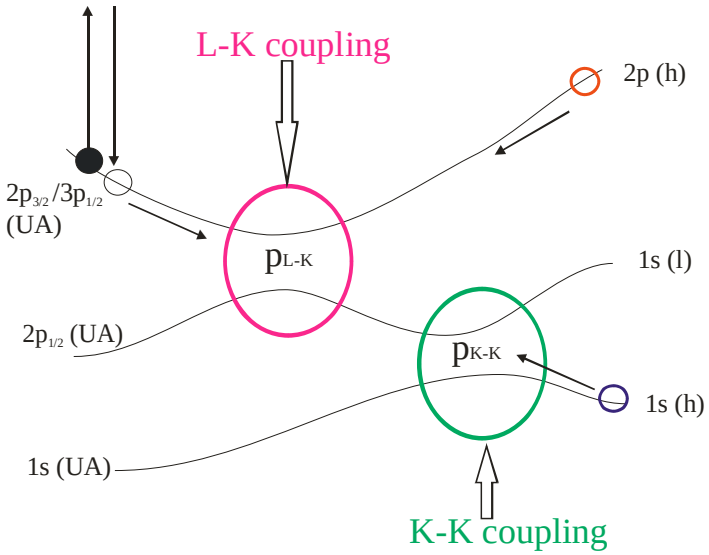

Fig. 2.2 *A schematic diagram representing L-K coupling and K-K coupling for the case of a superheavy collision system. Electron is indicated by a full circle and vacancy by an empty one. The 'h' and 'l' represent heavy and light collision partner respectively and 'UA' represents united atom. The single pass probabilities for L-K coupling (p_{L-K}) and for K-K transfer (p_{K-K}) are indicated.*

Fig. 2.2 shows a schematic diagram representing coupling between L shell of the projectile and K-shell of the target (L-K coupling), p_{L-K} is the single pass probability of vacancy transfer from L to K. The coupling between K-shells of the projectile and target (K-K coupling) is also depicted where p_{K-K} is the single pass probability of vacancy transfer. The direct MO excitation or electron promotion is shown from the united atom levels. In the earlier investigations starting from the seventies (for review see Mokler and Folkmann [6]), vacancies were produced due to electron

promotion and these vacancies then were transferred to the separated atoms in the outgoing part of the collision. However in the collision systems of the present investigation, vacancies are brought into the collision in the incoming channel itself either in the L or K-shell of the projectile. These vacancies are then transferred to the K-shell of the target either due to L-K coupling followed by K-K coupling or due to K-K transfer. Level diagrams for the collision systems of this investigation have been drawn using ab initio Self Consistent Field relativistic many electron Dirac Fock Slater (SCF DFS) calculations [36]. More details are discussed in Chapter 6.

2.3 CHARGE CHANGING PROCESSES

A collision of a highly charged projectile-ion with an atom leads to several charge changing processes. All these processes can be broadly classified as i) ionization ii) capture iii) recombination (with quasifree electrons) processes. During the collision, a highly charge projectile-ion can either lose charge by ionisation (stripping) of its own electrons or gain charge by capturing an electron from the target atom. The three basic processes can be expressed as:

i) $Z_1^{a+} + Z_2 \rightarrow Z_1^{(a+b)+} + ...$ where b ≥ 1 (projectile ionisation)

ii) $Z_1^{a+} + Z_2 \rightarrow Z_1^{(a-c)+} + ...$ where c ≥ 1 (electron capture from target)

iii) $Z_1^{a+} + e(Z_2) \rightarrow Z_1^{(a-1)+} + ...$ (recombination)

where Z_1^{a+} is the positive ion with charge a+, Z_2 is the neutral target atom and e(Z_2) is a quasifree electron attached to Z_2. The total charge changing cross-section for the projectile charge (σ_{Tot}^{X}) is a sum of the cross sections for "single and multi-electron projectile ionisation" and "electron capture"

$$\sigma_{Tot}^{Z1} = \sum_{b\geq 1} \sigma_{ion}^{b} + \sum_{c\geq 1} \sigma_{ec}^{c}$$

It is known that for high projectile-ion velocities (v_{ion}), usually the one electron processes i.e. one electron capture and one electron ionisation (b = c =1) give the main contributions to the σ_{Tot}^{Z1}, recombination with quasifree target electrons is usually unimportant for heavy collision systems, see below. The above mentioned processes are discussed in detail in the following sections.

2.3.1 Ionisation and loss processes

Ionisation is caused by the time varying perturbation due to the collision partner (projectile for the target and vice versa) observed by the electron being ionized in the shell of concern.

Projectile ionisation is an important charge changing process in collisions between few electron projectiles and neutral target atoms. During and after the acceleration process, heavy projectiles are generally highly ionised due to stripping before they hit the target atom. Due to Bohr-Lamb [37] criterion for the average charge state, the projectile electrons with orbital velocity smaller than the collision velocity (i.e. $v_e < v_{ion}$) are mostly ionised during penetration through a stripper foil. In other words accelerator produced heavy-ion projectiles can roughly be ionised up to $\eta = 1$ on the average.

2.3.2 Electron capture processes

Electron capture, the transfer of an electron from a target atom into a fast moving projectile is one of the fundamental processes in atomic-collision physics. So the ionization of a target atom by a moving ion proceeds not only through direct ionization to the continuum but also through the electron capture by the projectile. The collision of highly charged ions with bound electrons lead to three different capture processes namely Non-Radiative electron Capture (NRC), Radiative Electron Capture (REC) and Resonant Transfer and Excitation (RTE). Electron capture may take place to excited/outer states of the projectile and these states may then decay through x-ray emission to the ground state.

Capture via NRC and via REC (emission of radiation accompanying capture) are both caused by the time varying (screened) Coulomb field of the projectile on the target electrons. For NRC to occur the precondition is that the electron must be bound originally to the target so that the conservation of energy and momentum can be satisfied during the collision. REC [38] can occur even with a quasi-free (or free) target electron because here the conservation laws of energy and momentum can be fulfilled by the photon that is emitted. Since REC dominates for heavy projectiles on light target atoms ($Z_1 >> Z_2$) and for very high collision velocities, details regarding REC are not covered here. Resonant capture of a target electron accompanied by excitation (RTE) [39] and ionisation of another projectile electron are also important capture processes however they are not important for the cases considered here and hence further details are not given. For the collision velocities investigated here NRC is the dominant process for highly charged heavy ions colliding with target atoms or electrons and is briefly discussed below.

Non Radiative electron Capture (NRC)

The non-radiative or Coulomb electron capture (NRC) is the dominant electron transfer process especially for heavy collision partners. NRC occurs due to interaction of the projectile

nucleus with a target electron. The electron is transferred non-radiatively from a bound target state into a bound state of the projectile. The energy and momentum gained in the capture process are shared between the projectile and the target atom. A theoretical description of NRC is in general difficult because it is inherently a three body problem where the Coulomb field of the projectile leads to distortions of the target atomic wave functions even at large distances. The first work on the process of electron capture was taken up by Oppenheimer [40] Brinkman and Kramer [41] (OBK formalism) who found an analytical expression for the capture cross-section. Later electron capture cross-sections by inclusion of an internuclear Coulomb interaction to the OBK formalism [42] were carried out by several workers [43-49]. A rough cross-section scaling dependence is given by the first-order OBK [42] approximation for the non-relativistic case:

$$\sigma_{NRC} \propto \frac{Z_1^5 Z_2^5}{E_1^6}$$

The above dependence indicates that for medium projectile energies, in collisions of high-Z projectiles with medium or high-Z target atoms such as U^{q+} or Bi^{q+} on Au target, NRC is a dominant capture process due to its strong dependence on Z_2. The one electron capture cross section has the structure of a non-relativistic Brinkman and Kramers [41] approximation. For relativistic collision conditions, the above energy dependence has to be modified. For such a case an asymptotic energy dependence of E_1^{-1} form is approached.

Schlachter *et al*. [50] derived a semi empirical formula from the experimental data for fast, positive ions on He, N_2, Ne, Ar, Kr and Xe-gases. This analytical expression is used for calculating the one electron capture cross section generally and it agrees with about 70% of the experimental data of the above mentioned collision systems within a factor of two. Such a treatment of electron capture neglects atomic shell effects and is justified for highly charged projectiles in the intermediate velocity regime (Knudsen *et al*. [51]).

A more refined theoretical treatment of the NRC process can be obtained within the Eikonal approximation [52] in the nonrelativistic formulation. Here hydrogenic wave functions are employed and the resulting cross-section is divided by two for capture into the partially filled 1s-shell for H-like projectiles (U^{91+}, Bi^{82+}). Because Eikonal approximation is basically a high velocity approach therefore the application of this approximation to the relatively slow collision has to be considered with caution. The Eikonal approximation [52, 53] gives the calculations for NRC cross section which scales as follows:

$$\sigma_{NRC} \propto \frac{Z_1^5 Z_2^5}{E_1^6 n_f^3}$$

where n_f is the principal quantum number of the bound state into which the electron is captured. Both the Schlachter's empirical formula as well as Eikonal approximation have been used for calculation of electron capture cross sections corresponding to different incident projectile-ion (U^{q+} or Bi^{q+}) charge states (q). The same have been compared with values deduced from x-ray emission and projectile-ion's charge state distribution/evolution on passage through the thickness of solid target (Au) in Chapter 4 and 5 in Section 4.5 and Section 5.5.3 respectively.

2.4 CHARGE STATES OF SWIFT IONS IN MATTER

The charge state (q) of an energetic ion passing through a medium varies due to electron loss and capture as a function of penetration depth. An equilibrium distribution occurs when electron capture and loss into any charge state component are balanced. This equilibrium value is independent of the initial distribution of charge states in the beam incident on the target. Depending on the collision system, the length of the penetration depth at which the charge equilibrium occurs depends on the magnitude of the relevant charge exchange cross sections. Some trends of charge equilibrium thickness of foils with respect to Z_1 and E_1 have been established by Betz [54], Baron [55] and Zaikov et al. [56]. Therefore the charge state distribution of an emergent ion reflects the effect of collisions experienced by the projectile inside the solid. Ab initio calculations of charge state distributions are usually performed through the use of rate equations which require the knowledge of cross sections of above mentioned processes which are huge in number for ion-solid collisions.

Charge state distribution for a swift highly charged ion beam behind a target foil is characterized by the mean charge, the width and the shape of the distribution. The charge state distribution is varied when the target atomic number (Z_2), target thickness (t), the incident energy (E_1) or the nature of the projectile ion varies. The charge state fraction *F(q)* is defined as

$$F(q)=\frac{N(q)}{\sum_{q} N(q)}$$

Where *N(q)* is the measured number of ions of charge state q. In most cases, the incident charge state prevails for thin targets. For increasing target thickness the weight of the incident charge state decreases at the expense of neighbouring fractions. Most probable charge state is the charge associated with the most intense charge state fraction. Charge state fractions *F(q)* vary with penetrated target thickness until they reach ultimately an equilibrium value. For a given equilibrium charge state distribution, the average/mean charge state is defined as $\bar{q} = \sum_{q} q \times F(q)$.

The charge state fraction *F(q)* increases for $q < \bar{q}$ and decreases for $q > \bar{q}$. Variation of *F(q)* and $\bar{q}$ in the charge equilibration regime of foil thickness is also connected or related to the variation of the emergent ion energy due to the energy loss it experiences in traversing the foil. Nikolaev and Dmitriev's [57] relation explains well the variation of $\bar{q}$ with equilibrium foil thickness. Semi empirical formula for calculation of the mean charge state at equilibrium for heavy-ion beams emerging from a target foil with atomic number Z_2 have been reported by Betz [54], Baron [55], Nikolaev and Dmitriev [57], Shima *et al.* [58] and references therein.

Scheidenberger *et al.* [59] have reported on the development of the programs GLOBAL and CHARGE for calculating atomic charge-changing cross sections, charge state evolutions and equilibrium charge state distributions for relativistic heavy–ions. GLOBAL calculates the same for ions carrying up to 28 electrons and CHARGE for bare, H- and He-like relativistic heavy-ions penetrating through matter. These programs are based on Runge Kutta integration of the charge exchange equations; more details are covered in the mentioned section. These programs have been used in the present work to calculate the charge state evolution of the Bi^{q+}-ions on their penetration through Au target foils of varying thickness. Further details regarding this are covered in Chapter-5 where the Bi-Au collision system has been dealt in detail.

2.5 INFORMATION FROM X-RAY EMISSION

Inner shell vacancy production cross sections (ionization, excitation, capture) are normally determined by x-ray yields during their decay. The target x-rays are a result of vacancies created either due to target ionisation or capture of a target electron by a projectile. For high Z projectiles in the relativistic energy domain, the K-shell ionisation holds a particular importance and the x-ray decay of an inner shell vacancy is used as an indicator of the vacancy production. Apart from ionisation, capture to empty projectile states may also lead to x-ray emission. Hence in highly charged projectiles, x-ray emission takes place due to a) the radiative decay of the vacancies produced in the projectile either by ionization or by transitions of electrons which have been excited out of their initial inner shells to the outer shells and/or b) by transitions of electrons captured from the target into the projectile outer shells from the outer shells to the available vacancies in the inner shells.

The K and L x-ray spectra for projectile and target emission have been measured. However a detailed analytical treatment has not been given. Fig. 2.3 shows the K, L and M x-ray transitions for singly ionised heavy atoms for clarity.

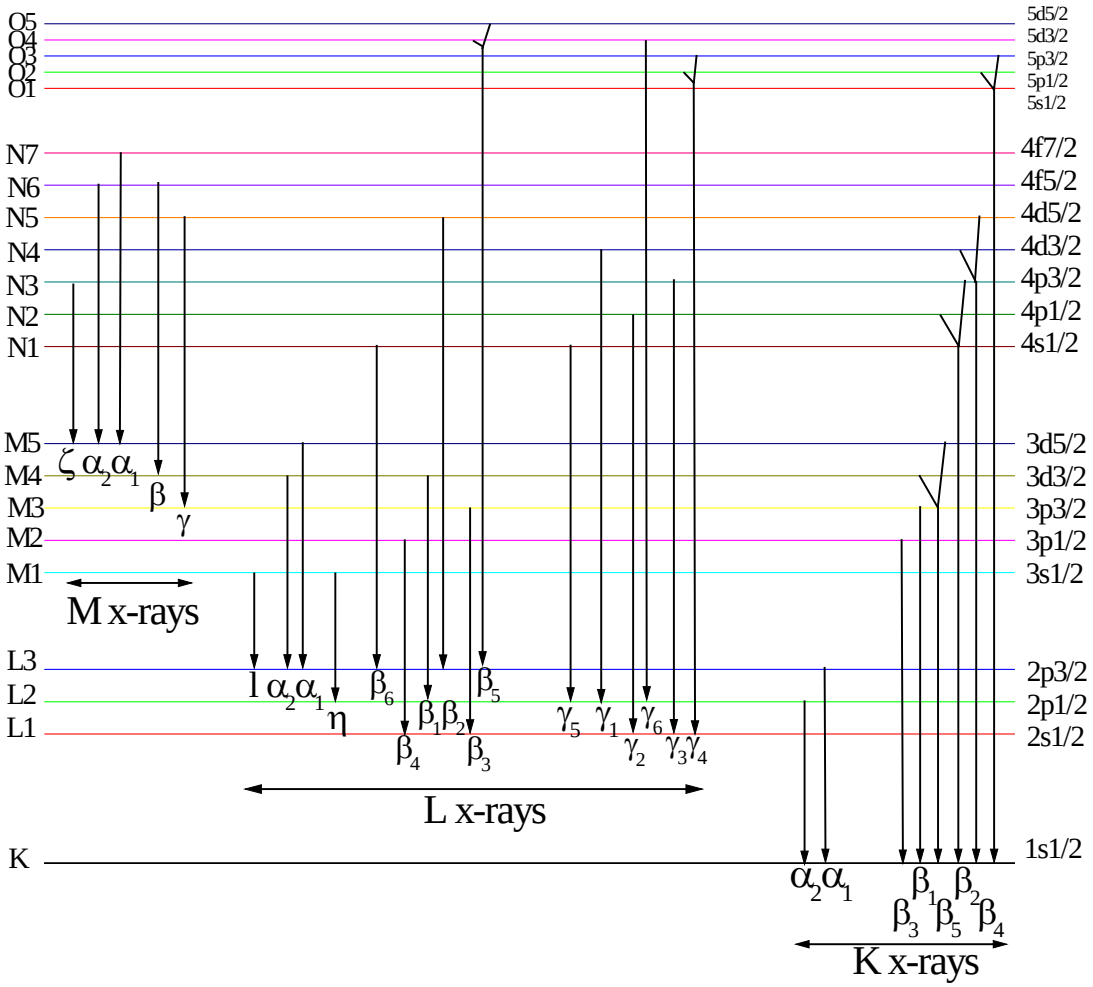

Fig. 2.3 *A schematic energy level diagram showing the transitions leading to K-, L- and M-series of x-rays. The one electron quantum numbers are listed on the right. Labels of the energy levels are given on the left.*

Multiple ionization i.e. outer-shell ionization simultaneous to inner shell ionization has been studied extensively in the past decades [60-63]. Multiple ionization can be observed by the energy shifts and the change in the intensity ratios as compared to the corresponding single hole values ([23] for energies and [64] for ratios). The multiple vacancies in the higher shells might not be filled prior to the radiative filling of the vacancy in the concerned inner shells. These vacancies then act as spectators to the radiative transitions of the electrons to the vacancy of the shell under consideration. The binding energy of all the levels thus increases due to less screening of the nuclear charge.

The relative intensities of x-ray transitions filling a vacancy in the same subshell are also influenced by the presence of these additional vacancies in the levels from where the lines originate and thus the intensity ratios of various x-ray lines filling a vacancy in the same subshell also get changed with respect to the corresponding single-hole branching ratios [64]. The ionization cross sections, fluorescence yield values and Coster-Kronig transition probabilities are not required for the

theoretical calculation of these ratios if they involve the same atomic levels. The theoretical results for these ratios are the x-ray emission rates for the relevant x-ray transitions as given by Scofield [64]. An overestimation of the Scofield values by the experimental ones would give an idea of the degree of multiple ionization of the shells.

Table 2.1 *X-ray (K and L) energies (in keV) in singly ionized atoms for the collision partners of the investigated systems (Bi^{q+}-Au and U^{q+}-Au). (Ref. Tables of Bearden [23])*

X-ray lines	Transition	Gold (Au) Z=79	Bismuth (Bi) Z=83	Uranium (U) Z=92
K x-rays				
$K\alpha_2$	K - L_2	66.9895	74.8148	94.665
$K\alpha_1$	K - L_3	68.8037	77.1079	98.439
$K\beta_1$	K - M_3	77.984	87.343	111.300
$K\beta_2$	K - N_3	80.185	89.864	114.60
L x-rays				
L_l	L_3 - M_1	8.4939	9.420	11.6183
$L\alpha_2$	L_3 - M_4	9.6280	10.731	13.4388
$L\alpha_1$	L_3 - M_5	9.7133	10.839	13.6147
L_η	L_2 - M_1	10.3083	11.712	15.3997
$L\beta_6$	L_3 - N_1	11.1602	12.482	15.7260
$L\beta_{15}$	L_3 - N_4	11.5667	12.955	16.3857
$L\beta_2$	L_3 - N_5	11.5847	12.980	16.4283
$L\beta_4$	L_1-M_1	11.2047	12.691	16.5753
$L\beta_7$	L_3 - O_1	11.8106	13.259	16.8450
$L\beta_5$	L_3 - O_{45}	11.9163	13.395	17.0701
$L\beta_1$	L_2 - M_4	11.4423	13.024	17.2200
$L\beta_3$	L_1- M_3	11.6103	13.210	17.4550
$L\beta_{10}$	L_1 – M_4	12.0617	13.700	18.0310
$L\beta_9$	L_1 – M_5	12.1474	13.808	18.2054
$L\gamma_5$	L_2 - N_1	12.9743	14.773	19.5072
$L\gamma_1$	L_2 - N_4	13.3817	15.248	20.1671
$L\gamma_2$	L_1- N_2	13.7095	15.582	20.4847
$L\gamma_8$	L_2 - O_1	13.6260	15.551	20.6210
$L\gamma_3$	L_1 - N_3	13.8090	15.710	20.7127
$L\gamma_6$	L_2 - O_4	13.7304	15.685	20.8426
	L_1 - N_4	13.999	15.904	20.9790
$L\gamma_{11}$	L_1 - N_5	14.02	15.951	21.0190
$L\gamma_{4'}$	L_1 - O_2	14.2809	16.271	21.4984
$L\gamma_4$	L_1 - O_3	14.2996	16.295	21.5620
$L\gamma_{13}$	L_1 - $P_{2,3}$	-----	16.380	21.7290
M x-rays	range	1.648 –2.883	1.883 – 3.315	2.4548 – 5.5

The emitted x-ray spectra from the collision system would contain essentially three different messages:

- The vacancy production for the inner levels can be deduced from the total emission cross sections of the collision partners for selected transitions. This is the basic information required for probing the inner quasimolecular levels and their couplings.
- Population ratio of the feeding levels can be obtained from the intensity ratios of different x-ray transitions filling the same levels; whereas the intensity ratio from the same feeding level would give the ratio of the probability of vacancies in the final levels [64].
- Presence of vacancies in the collision partners (inner and outer shells) can be extracted from shifts in the values of x-ray transition energies towards higher values. Table 2.1 shows the theoretical transition energies of K and L x-rays for the collision partners of the present investigation as given by Bearden [23] for single hole atoms.

For the K-emission of our heavy systems fluorescence yields of unity are approached however for the L-shell they are smaller and complex. During heavy ion-atom collisions multiple ionization of the inner as well as outer-shells alter the fluorescence yield values for the excited atoms [65, 66]. It is also known that for the same reason, Auger processes may be suppressed. Hence for initial investigation a fluorescence yield of unity for both K and L-shells of the collision partners is assumed for simplicity.

CHAPTER III

EXPERIMENTAL DETAILS AND DATA ANALYSIS PROCEDURE

3.1 INTRODUCTION

The present chapter gives a description of the various experimental details and the procedure for data analysis. Section 3.2 deals with accelerator facility, ion-beam preparation, experimental area and set up. Section 3.2.1 describes details of the accelerator facility existing at GSI, whereas details of the experimental set up such as the chamber, types of targets, target and detector positions, particle detector set up and magnet spectrometer are described in Section 3.2.2. Section 3.2.3 gives specifications of various types of x-ray and particle detectors used in the experiments with special emphasis to the efficiency of the particle detector used. The data acquisition and analysis procedure in Section 3.3 lays out the basics of data acquisition systems used, electronics set up for the experiments and various experimental quantities that are calculated from the data along with their formulae. The different acquisition systems used for data handling and the electronics set up for the experiments are explained in Section 3.3.1. Section 3.3.2 gives details of the energy and efficiency calibration of x-ray detectors and Section 3.3.3 explains the phenomenon of Doppler shift and Doppler correction. The x-ray peak fitting and analysis procedure is unfolded in Section 3.3.4. Section 3.3.5 presents details for calculation of experimental results such as x-ray energy shifts, intensity ratios, normalization and dead time correction as well as x-ray emission cross sections.

3.2 EXPERIMENTAL DETAILS

3.2.1 Heavy-ion accelerator facility at GSI

Fig. 3.1 gives a schematic view of the GSI accelerator facility (for details see [67]). The main components of the facility are the Ion Sources, Linear Accelerator, the UNILAC and its associated experimental area, the heavy-ion synchrotron SIS (SchwerIonen Synchrotron), the FRragment Separator (FRS), the Experimental Storage Ring (ESR) and the high-energy experimental areas also called as Cave's. Elements from hydrogen to uranium are accelerated in this facility. The atomic physics experiments at GSI are performed in the experimental area of UNILAC, Cave-A and the ESR. The experiments for the present investigation were performed at the Cave-A marked in the Fig. 3.1.

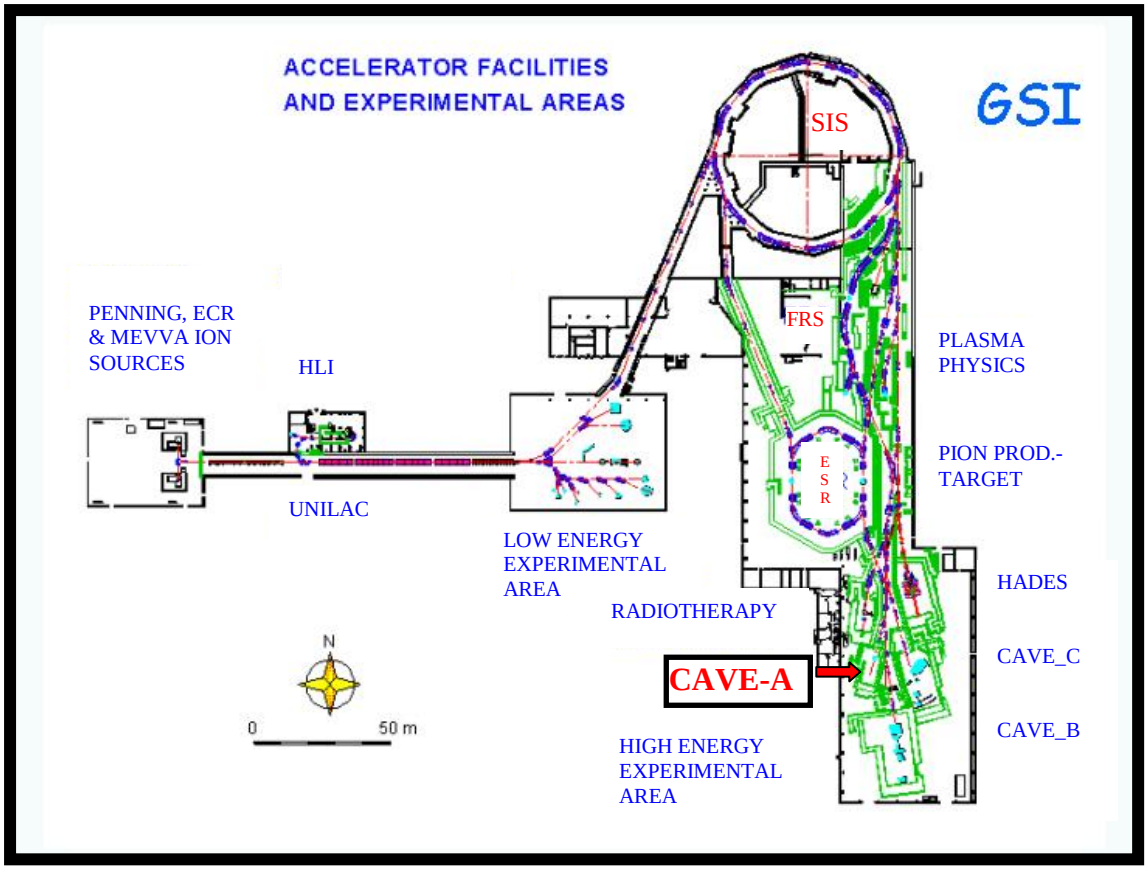

Fig. 3.1 *A schematic view of the GSI accelerator facility.*

The projectile-ions of desire are produced at the ion source {Penning Ion Gauge (PIG), MEtal Vapour Vacuum Arc ion source (MEVVA) or Electron Cyclotron Resonance ion source (ECR)}, e.g. the U- and Bi-ion beams have been produced for these investigations from PIG. The ion beam produced by the ion source is injected into the UNILAC. The UNILAC delivers beams with energies ranging from 3 to 15 MeV/u. The ions on transportation to the first part of the UNILAC (called the pre-stripper linac, operating at a frequency of 36 MHz and consisting of a RFQ and an IH structure) get accelerated to an energy of 1.4 MeV/u. They are then ionized in the following gas stripper whereby the ion-beam acquires higher charge states. For U-ion the most probable charge state is there 28+ (see Fig. 3.2). The ion beam with its most probable charge state is then transported to the second section of the UNILAC (the post-stripper linac, with its first part as an Alvarez structure at a frequency of 108 MHz) where it is accelerated to an energy of 11.4 MeV/u, the standard injection energy into the heavy ion synchrotron (SIS).

However, heavy ions can be accelerated to higher energies by the use of 15 single cavities (Einzel Resonators) which constitute the second part of the post-stripper. The linac accelerated ion-beams can be ionized further by passing them through a stripper foil of appropriate material and

thickness before injection into the SIS. For example a U-ion beam of 11.4 MeV/u acquires a most abundant charge state of 73+ through this stripping.

The SIS18 (circumference 216 m) can be operated at a maximum magnetic bending power of 18 Tm with a ramp rate of 4 T/s. On injection in the SIS, the ion beams are accelerated to high (relativistic) energies. The energy range for the lighter ions extends typically from 20 to 2000 MeV/u, while for U^{73+} it extends only up to 1 GeV/u. After acceleration in the SIS, the ion beams are extracted and transported towards a specific experimental area. The pulsed beam from the SIS can have a cycle length of 1-16 s and extraction can either be a slow one (10-8000 ms) or a fast one (~1 μs). The projectile ions can be further stripped to highest charge states (bare, H-like etc.) by bombarding them once again on stripper foils before the experimental target area. Model calculations/simulations can be performed to make an appropriate choice of the stripper, the details of which are discussed below.

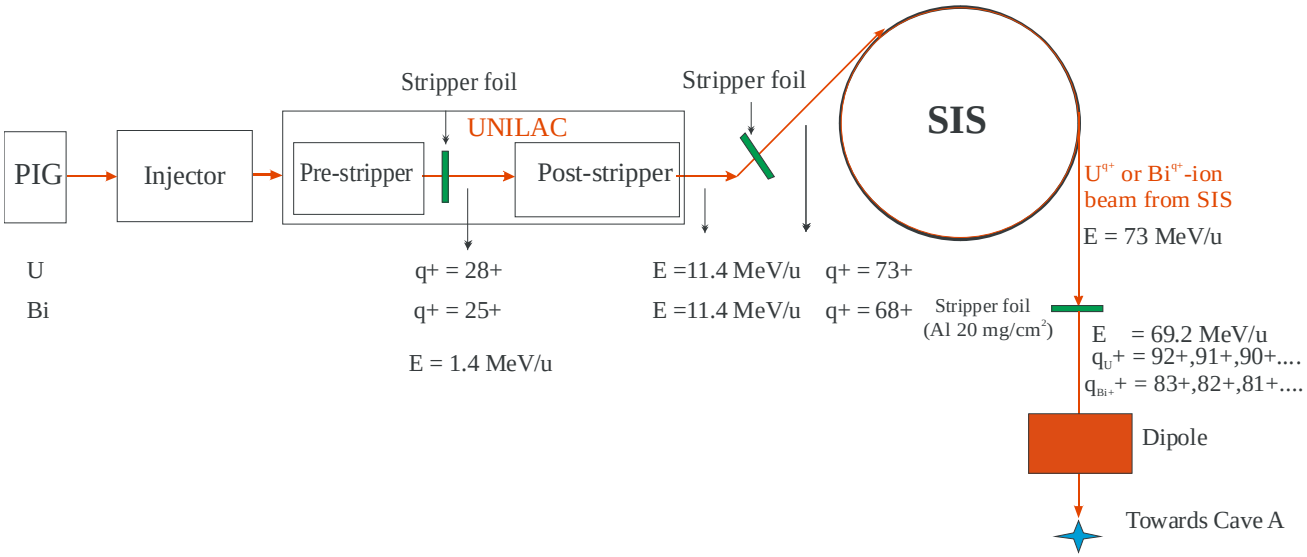

Fig. 3.2 *A schematic diagram of beam transport from the ion source towards the Cave-A experimental area.*

An analyzer magnet then separates the ion-beam of required charge state (H-like, He-like etc.) from other charge state fractions and is transported further towards the experimental area. Thus, a heavy ion (even the heaviest U-ion), highly charged (bare, H-like, He-like etc.), selected for a particular charge state and moving at high or even at moderate collision velocities bombards the target in Cave-A experimental area. Fig. 3.2 gives a schematic diagram of the beam transport from the ion source till the Cave-A experimental area.

Appropriate choice of the stripper

The general removal of electrons from an ion penetrating dense matter is called stripping. It takes place mainly by multiple soft collisions of the projectile with the target material. According to

the Bohr's criterion, roughly, all the electrons having an orbital velocity smaller than the collision velocity are stripped during the collisions. The final charge state distribution is a balance between the capture and loss processes. The choice of the material of the stripper for a projectile ion beam is dependent upon the charge state evolution of the ion through the material of the stripper. The maximum probability of obtaining a particular charge state fraction for a given incoming energy depends both on the material and its thickness. Based on models, the charge state evolution of the ions can be calculated for different possible stripper materials and for different thicknesses of each material [59].

The program GLOBAL [68] was used to estimate the charge state evolution of the ion-beams. The charge state evolution of Bi^{68+}-ions of 73 MeV/u was calculated for C, Al, Cu and Sn targets of different thicknesses ranging from 0-30 mg/cm^2. The calculations enabled a proper choice of a stripper providing a considerable yield for He-like, Li-like and C-like and in particular for the most important but less abundant H-like component. Fig. 3.3 shows this charge state evolution. Finally an Al target of 20 mg/cm^2 was chosen as it proved to be appropriate for both the experiments with U- and Bi-ions providing different charge states of the beam with reasonable intensity. Details regarding GLOBAL [68] and CHARGE [68] simulation programs along with a comparison of their values with experimental data are given in [59].

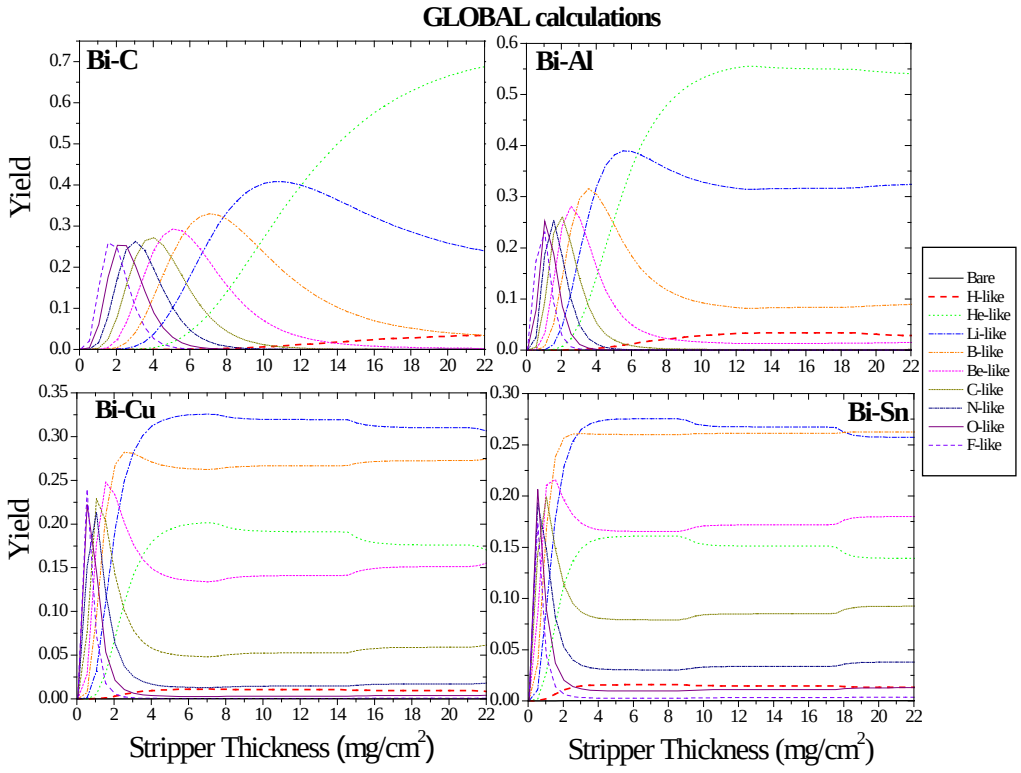

Fig. 3.3 *Charge state evolution of 73 MeV/u Bi^{68+}-ions incident on C, Al, Cu and Sn stripper targets of different thicknesses calculated by GLOBAL [68].*

The energy straggling of an ion through a solid target depends on its nuclear charge, being higher for heavier targets. Hence a low Z material (Aluminium) was preferred. The energy loss of the ion beam through the material of the stripper is additionally required to calculate the final energy of the ions interacting with the target. The choice of the stripper thickness is made keeping a minimum energy loss of the projectile and a small energy straggling under the conditions of an abundant production of the required charge state. The ATIMA [69] and CHARGE [68] programs have been used to calculate the stopping power in MeV/mg/cm^2, the total energy loss of the projectile in MeV/u and the energy straggling in MeV for the stripper; where needed ranges were calculated as well.

3.2.2 Experimental set up at Cave-A (general)

The experiments for the present investigation have been performed at the atomic physics experimental area Cave-A as mentioned above. Cave-A mainly consists of a target chamber area followed downstream by a magnet spectrometer for charge state separation of the ejectiles. For the proper transport of the beam, apart from ion optical elements like quadrupoles and dipoles, collimators and beam diagnosis detectors (screens, wire chambers) are also available in the beam line.

Fig. 3.4 shows a schematic diagram of this area starting at beam delivery point marked by the Gate Valve (GV) with all its components such as the valves (APx, x=1-3), collimators (C1 and C2), fluorescent screens (Sx, x=1-4), target chamber area (T), two different geometries of the x-ray detectors for the two experiments (at backwards angles: G1 or at forward angles: G2 with respect to the beam), magnet spectrometer (MS) with quadrupoles Q1 and Q2 and the dipole magnet and the alternative positions of the diamond particle detector (P1 and P2) for the experiments with U- and Bi-ions respectively. The valves are remotely controlled and are opened for beam transport after the appropriate vacuum has been achieved in the beam line. The fluorescent screens, Sx are ceramic ones (aluminium oxide) and are connected to individual step-motors for moving in or out of the beam path remotely. The beam position on the graduated screens is monitored by cameras installed on the glass ports opposite to the port containing the screen. The Cave-A beam line is equipped with a variable collimator C1 installed after the screen S1, it is also driven by a step motor. This collimator consists of two pairs of variable collimators (in X and Y direction) which can be moved so as to form a square opening of a definite aperture. It was used with an opening of 4 x 4 mm^2. Another fixed collimator C2 was installed only for the experiment with Bi-ions. It was a cylindrical collimator with a diameter of 8 mm and a length of 40 mm. The length was machined as a screw to reduce multiple scattering.

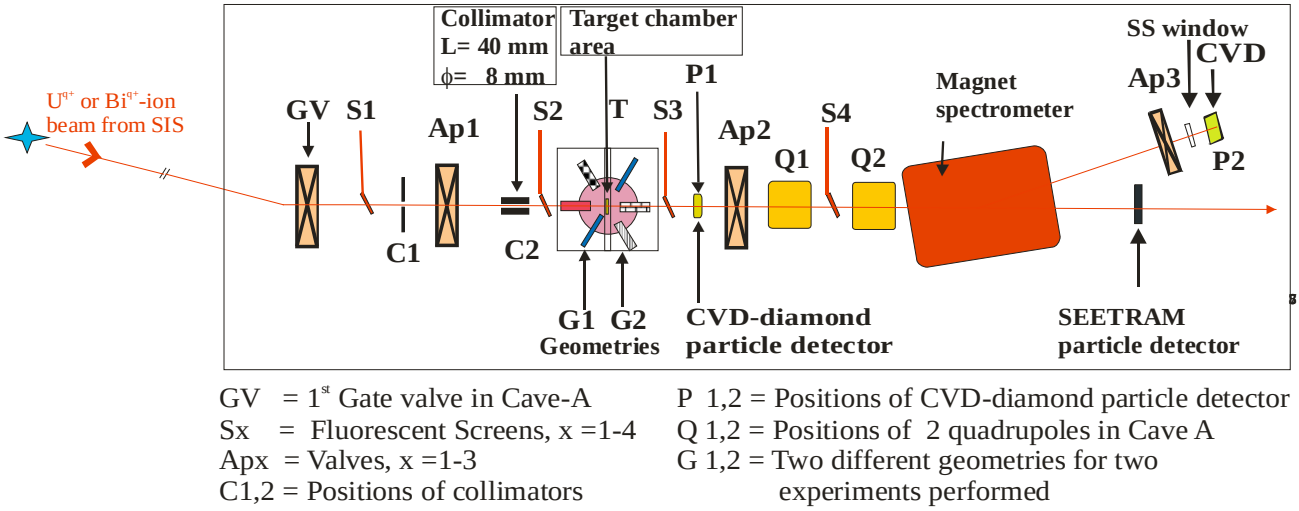

GV = 1st Gate valve in Cave-A
Sx = Fluorescent Screens, x =1-4
Apx = Valves, x =1-3
C1,2 = Positions of collimators
P 1,2 = Positions of CVD-diamond particle detector
Q 1,2 = Positions of 2 quadrupoles in Cave A
G 1,2 = Two different geometries for two experiments performed

Fig. 3.4 *The details of the beam line components in Cave A and the beam transport through them till the particle detectors.*

i) The target chamber and detector positions

The target chamber area (T) was installed with a chamber having a special geometry. As mentioned earlier, two different geometries of the target chamber were used for the two different experiments performed for the present investigation. These are indicated by two rectangles in Fig. 3.4 as G1 and G2 (for a further schematic representation see Fig. 3.6). The choice for the change in the x-ray observation angle depended upon the choice of the collision partners (projectile and target) i.e. on the expected energies of the projectile x-rays in the laboratory frame with respect to the target x-ray lines. The projectile x-rays are observed as Doppler shifted in the laboratory frame due to the relativistic velocities of the projectile. The geometry was chosen so as to facilitate an energy wise separation of the target and projectile x-ray transitions in the laboratory frame. A detailed discussion on this is given in Section 3.3.3.

Fig. 3.5 gives a photograph of the target chamber [70] in G2 geometry (for Bi-ion experiment) and a schematic drawing of the same with a top view indicating angles of the in-plane x-ray detector ports. A port for installing the target ladder has been indicated in the photograph. Assigning Z-direction to the beam transport in Cave-A downstream, the target chamber can be said to consist of two coplanar ports in the X-Z plane (used for Ge(i) detectors) both of which are at an angle of 60^{o} placed symmetrically on both sides with respect to the beam direction. It has another detector port (used for Si(Li) detector) at an angle of 45^{o} (in the Y-Z plane, shown in the photograph only) with respect to the beam axis, off plane with respect to the other two coplanar ports in the X-Z

plane mentioned above. Fig. 3.6 shows a schematic diagram of the experimental set up where geometries of both the experiments are represented by the rectangles G1 (for U-ions) and G2 (for Bi-ions). The detector ports were covered by x-ray transparent Be-windows inserted in specially designed pockets so that the detectors could be placed very close to the targets.

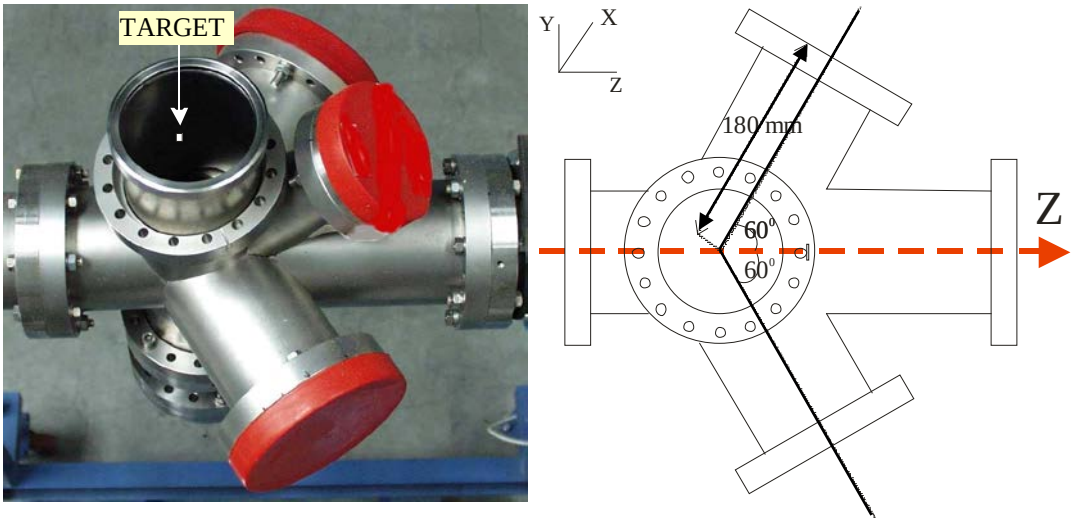

Fig. 3.5 *A photograph of the target chamber (G2 geometry) and a schematic design of the same (top view only) indicating the angles of the in-plane detector ports.*

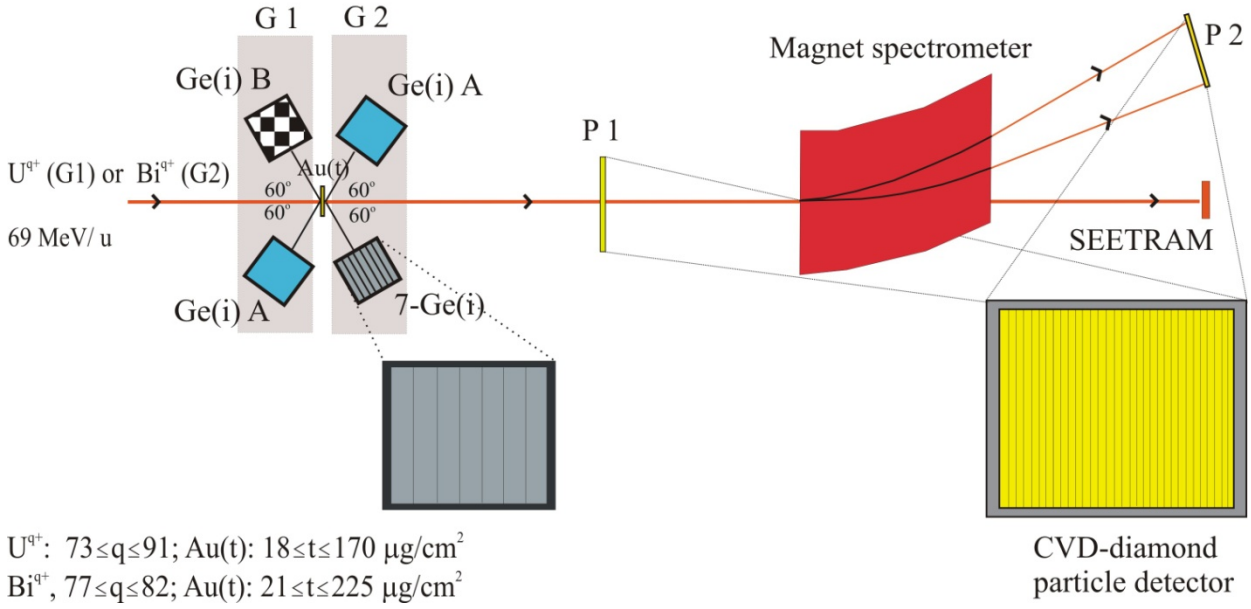

Fig. 3.6 *A schematic diagram of the experimental set up where geometries of both the experiments are represented by G1 (backward angles for U-ions) and G2 (forward angles for Bi-ions). The corresponding positions for the CVD-diamond particle detector are given by P1 and P2, respectively.*

Because of its special geometry, the target chamber could also be installed in a 180^{o} rotated (along Z-axis) position for the reasons explained above. The two coplanar ports for the Ge(i) detectors were then at 120^{o} with respect to the beam direction and the off plane (Y-Z plane) port at an angle of 135^{o} (used for the Si(Li) detector) with respect to the beam. The chamber was used in this setting for the experiment with U-ions and is indicated by the rectangle G1 in Fig. 3.6.

The target ladder consisting of 8 possible target positions was connected to a step motor, facilitating measurements with a maximum of 7 targets without a break of vacuum. Self-supporting Au targets produced by the GSI target laboratory with an open size of 8-10 mm in diameter were used and mounted perpendicular to the beam direction. The thinnest targets had to be produced on thin C backings (10 or 15 $\mu g/cm^2$) where the Au surface faces the incoming beam.

All the step motors connected to the screens and the target ladder were connected to a controller, remote controlled through the Labview software [71]. Fig. 3.6 also shows the two positions of the particle detector P1 and P2 corresponding to the geometries G1 (U-ion) and G2 (Bi-ion) for the two experiments. The ejectiles after interaction with the target were detected by the one dimensional, position-sensitive, Chemical Vapour Deposition (CVD)-diamond particle detector as described below.

ii) Particle detector set-up

The CVD-diamond detector was placed in air behind a thin 25 μm stainless steel window, either after the target chamber (position P1) or after the magnet spectrometer (at position P2) for the two different experiments as explained above (see Fig. 3.4 and 3.6). The CVD-diamond particle detector was used for normalization of x-ray yields of the collision partners in both the experiments. It was also used as a beam monitor for the beam transport through the Cave-A beam line. The detail features of the detector are described in Section 3.2.3 ii) a) below.

For the U-ion experiment (geometry G1, Fig. 3.4, 3.6), the particle detector was placed 79 cm behind the target chamber (position P1, Fig. 3.4, 3.6). In this position it registered the whole of the beam intensity after interaction with the target and functioned basically as a particle counter. The position sensitiveness was not put to use in this experiment. For the Bi-ion experiment (geometry G2, Fig. 3.4, 3.6), the detector's one dimensional position sensitiveness was used for measuring the charge state distribution of the ejectiles. Hence, the particle detector was placed after the magnet spectrometer of Cave-A (at position P2, Fig. 3.3, 3.6) in its focal plane.

iii) The magnet spectrometer

The magnet spectrometer in Cave-A consists of a dipole and two quadrupoles. The dipole having a deflection angle of 14.5°, facilitates the separation of various charge states of the ejectiles which are detected by a position-sensitive detector placed in the focal plane of the spectrometer. The Lorentz force balanced by the centrifugal force control the motion of the projectile ions (charge particles) in the magnetic field which is directed perpendicular to the motion of the particle. While passing through a magnetic field B, ions of different charge states are dispersed to different trajectories in the deflection plane. The distance x between two different charge states of the ion at the focal plane is given by:

$$x = D\ \frac{\Delta q}{q}$$

Here D is the dispersion (in the units of mm/%) of the dipole magnet for a known distance behind the dipole and $\Delta q/q$ is the difference in the charge states in %. For example, for a change of charge state from H-like to He-like in Bi-ions Δq = 1, hence $\Delta q/q$ = 1/82 = 1.2%. So for a typical dispersion (D) of say 8.35 mm/%, the distance to the next charge state would be $x = (\Delta q / q)$. D = 1.2 x 8.35 = 10.02 mm. The ion beam can be focused in the plane of deflection by the quadrupoles of the magnet spectrometer. The focusing is needed for separation of the different ejectile charge states behind the dipole magnet in a position-sensitive detector. Ion-optics calculations were performed in advance for the whole beam line including the spectrometer using the program MIRKO [72], and the settings were also controlled by MIRKO during beam adjustments.

3.2.3 Detectors for the experiment

i) X-ray detectors

a) Ge single crystal x-ray detector [Ge(i)]

The K x-rays of the collision partners were detected by two coplanar Germanium detectors. For the U-ion experiment two single crystal Ge(i) detectors were used (Ge(i)-A and Ge(i)-B, see Table 3.1 a) whereas for the Bi-ion experiment, the Ge(i)-A and another seven segmented Ge(i) detector, the [7-Ge(i)] was used (Table 3.1 b).

b) 7 stripe Ge x-ray detector [7-Ge(i)]

This position-sensitive detector with dimensions of 25x25x12 mm^3 has 7 independent adjacent Au-stripes of 3.57 mm width each oriented along the Y direction (c.f. Fig. 3.6) with an angular accuracy of better than 1 degree. The entrance window on the detector is 0.4 μm Ge and the

Table 3.1 a) *Specifications of x-ray detectors used in U-ion experiment (G1 geometry).*

Specification	**Ge(i)–A**	**Ge(i)-B**	**Si(Li)**
Model Number	CANBERRA GL0515R-7935	CANBERRA GL1010R	ORTEC 10180
Bias supply	-3000 V	-2000 V	-1000V
Shape	round	round	round
Active area	500 mm^2	1000 mm^2	80 mm^2
Active diameter	25.5 mm	35.7 mm	10 mm
Crystal thickness	15 mm	10 mm	5 mm
Crystal to window distance	5 mm	10 mm	10 mm
Be window thickness	0.15 mm	0.5 mm	0.0125 mm
Energy resolution at 13.942 keV. Am^{241} source and 4 μs shaping time	250 eV	300 eV	308 eV

Table 3.1 b) *Specifications of x-ray detectors used in the Bi-ion experiment (G2 geometry).*

Specification	**Ge(i)-A**	**7-Ge(i)**	**Si(Li)**
Model number	CANBERRA GL0515R-7935	INTERTECHNIQUE EGPS 25x25-12-N7	EURISYS
Bias supply	-3000 V	+1200V	-1000V
Shape	round	square	round
Active area	500 mm^2	(7x3.57)x25= 625 mm^2	200 mm^2
Active diameter	25.5 mm	length and breadth = 25mm	8 mm
Crystal thickness	15 mm	12 mm	5 mm
Crystal to window distance	5 mm	9 mm	7 mm
Be window thickness	0.15 mm	0.2 mm	40 μm
Energy resolution at 13.942 keV. Am^{241} source and a 4 μs shaping time.	250 eV	560 eV	338 eV

entrance window of the cap is 0.2 mm Be. Each stripe is connected to a cooled, built in preamplifier all of which work simultaneously. Along with all these specifications by the manufacturer, the cross-talk between the stripes has been quoted to be less than 0.1%. This detector was placed in one of the two coplanar ports (at an angle of 60^o to the beam) for the Bi-ion experiment (geometry G2). Placed in this position the observation angles of the detector were in the range from 53.9^o to 74.2^o in steps of approximately 3.6^o each.

c) Silicon Lithium x-ray detector [Si(Li)]

The L x-rays of the collision partners were detected by a lithium drifted silicon detector [Si(Li)]. Two different detectors were used for the experiments with U- and Bi-ion as projectiles, their specifications are given in Table 3.1 a) and b) respectively.

ii) Particle detectors

a) The CVD-diamond particle detector

Measurement of the charge state distribution and charge exchange cross-sections for heavy-ion heavy-atom collisions require a large area, position-sensitive detector with a high, known detection efficiency. For the special case investigated in this work (beam intensities of 10^7-10^9 particle/s at an energy of ~70 MeV/u) a fast, radiation hard position-sensitive detector is needed. A detector made out of polycrystalline chemical vapour deposited diamond (CVD-diamond) was specially developed at GSI and can satisfy the above requirements [73, 74]. This is based on the specific property of diamond: fast signal build up caused by equally high mobility for positive and negative charge carriers and the unusually high dislocation energy.

A front view of the particle detector is shown in Fig. 3.7 a) and the electronics used for the CVD read out are shown in Fig. 3.7 b). This detector has an active area of 60x40 mm^2 and is 200 μm thick. The one dimensional position sensitiveness is provided by the 32 gold stripes (thickness 100 nm) deposited on top of the CVD-diamond layer. Each strip is 1.8 mm broad with a 0.2 mm inter stripe distance and has an independent read-out coupled to a preamplifier. A bias of typically -300 V was given to each stripe. The preamplifier signals have been selected by a level discriminator. The threshold of the level discriminator was set to cut the electronic noise as well as the small amplitude cross-talk signals. A cross-talk may be produced specially if an ion hits the detector in between the stripes. For such a case signals in adjacent stripes originate from the same particle.

The present investigation holds the importance of being the very first measurement to test the charge collection and particle counting efficiency of this detector for high intensity, very heavy–ions of below 100 MeV/u. As a normalization detector (U-ion experiment), the CVD-diamond detector

registered the whole of the beam intensity whereas for measuring the charge state distribution (Bi-ion experiment), it detected typically more than 90% of the total beam intensity at one time. The single stripe as well as the total detector count rate were monitored during the experiments.

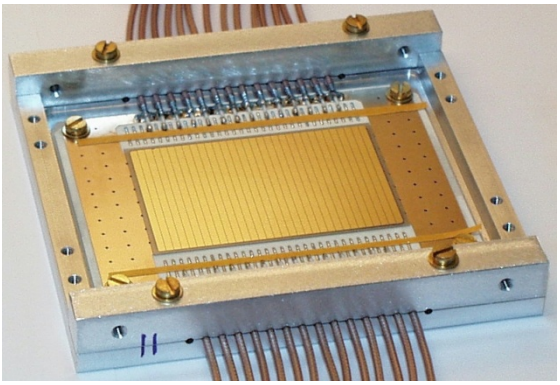

Fig. 3.7 a) *Front view of the position-sensitive CVD-diamond particle detector.*

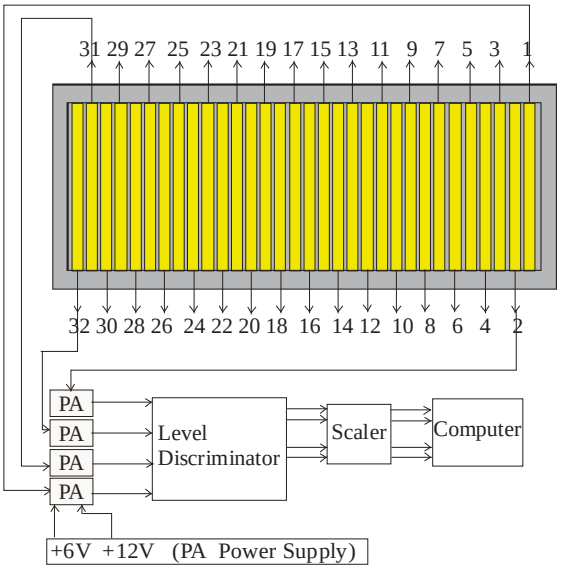

Fig. 3.7 b) *Electronics for the CVD-diamond detector. PA is the pre-amplifer, one for each stripe.*

The tremendous energy deposition of low energy heavy ions in the diamond poses a problem for a high detection efficiency. During the experiment with the U-ion beam of 69.1 MeV/u i.e. in total 16.45 GeV, the ions lost a total of 5.4 MeV during interaction with the thickest Au target (170 μg/cm^2) and subsequently a total of 908 MeV in the 25 μm stainless steel window. Further, a total of 6.29 MeV is lost in the Au layer of 100 nm which is deposited on top of the diamond layer in the detector. Finally, U-ejectiles of 15.5 GeV impinge on the diamond layer of 200 μm thickness

depositing approximately a total of 4.5 GeV of energy there. These calculations were done according to SRIM [75]; slightly different values were obtained from ATIMA [69]. The amount of deposited energy influences the charge collection efficiency of the detector. Due to the intrinsic characteristics of diamond, mainly its polycrystalline structure which creates traps for charge carriers, the pulse height distribution of the signals is very broad leading to only a limited energy resolved information.

b) SEETRAM- Secondary Electron Emission TRAnsmission Monitor

A secondary electron emission transmission detector (SEETRAM) [76] was used in the Bi-Au experiment besides the CVD-diamond particle detector as a second beam intensity monitor after interaction with the target. It is basically a particle detector which uses the phenomenon of secondary electron emission from a thin foil. Subsequently, the emitted electrons are focused to multi channel plates (MCP) to count the number of particles (ions) impinging on it. The aim in the present measurement was to determine the efficiency of the CVD-detector by comparison with the SEETRAM. The CVD-detector was developed for experiments with heavy-ions of few hundred MeV/u. Up to the present experimental investigation, no quantitative information was available regarding the efficiency of the detector with very heavy ions below 100 MeV/u. It was thus necessary to measure the efficiency of the CVD-detector with a second detector whose efficiency is known. The SEETRAM with its indirect measurement of the projectile-ions is well known as a non-destructive transmission detector with almost 100% detection efficiency for moderate count rates and lower ion energies [76]. The count rate capability being limited only by its MCP.

Working principle of SEETRAM

The projectile ions produce free electrons after interaction with the C-foils and the ones flying off in the direction of an “accelerating grid” are accelerated towards it. These accelerated electrons are bent by an angle of 90º towards a microchannel plate (MCP) by an electrostatic mirror consisting of an inner and outer grid maintained at a potential difference between them. The equations of motion for a charged particle in an electric field govern the stream of electrons, their penetration depth in the electrostatic mirror depending upon the potential of the accelerating grid and the electrostatic mirror. Hence the time of flight for different electrons to the MCP is equivalent. The signals are collected by an anode and recorded by the data acquisition system.

Mechanical design of the detector

The detector was placed in vacuum at the zero degree exit of the dipole in the beam line (Fig. 3.4) with the electrostatic mirror facing the ejectiles. Fig. 3.8 a) shows a schematic diagram of the

prism shaped detector. The microchannel plate (MCP) and the anode (separated by an insulator) form one side of the detector. Two carbon foils (held in a frame) along with the adjoining accelerating grid (G) form another side of the detector. An electrostatic mirror (oriented at 45°) faces the accelerating grid and constitutes the third side of the detector. Fig. 3.8 b) shows a photograph of the SEETRAM detector. The two C-foils of thickness 15-20 μg/cm^2 each are separated from each other by the 0.2 mm thickness of their frame. These two foils installed in this way ensure a higher mechanical stability than a single foil of 30-40 μg/cm^2 thickness. The effective area of the C-foils available for irradiation by the ejectiles is 30 x 60 mm^2 and the opening area of the electrostatic

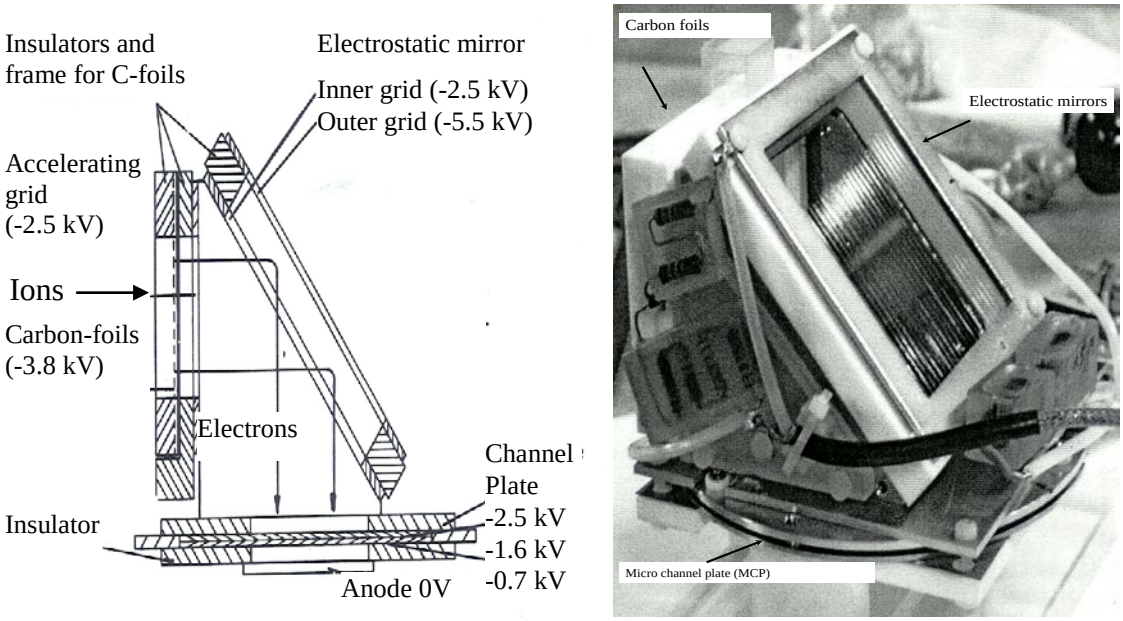

a) b)

Fig. 3.8 a) *Schematic design of SEETRAM.* b) *Photograph of SEETRAM.*

mirror's grid is 60 x 65 mm^2. This ensures that all the electrons moving towards the accelerating grid and the electrostatic mirror are bent towards the microchannel plate having an effective area of 75 mm^2. The base plate and the insulator (with an opening of 40 x 70 mm^2) are installed in such a way that all the electrons emitted from the foils and bent by the electrostatic mirror reach the MCP.

c) Comparison of CVD-diamond and SEETRAM detector efficiencies

The basic working of principle for both the detectors is different however their efficiencies can be compared normalized to a common value. The CVD-diamond detector detects the charge created by the projectile ions in the bulk of the detector directly while the SEETRAM detects the

secondary electrons (via MCP) released from a C-foil due to the passage of projectile ions (ejectiles) through them.

Highly charged heavy-ions at intermediate energies (E<100 MeV/u) produce a large amount of primary charge inside a diamond. When the range of the ions is equal to or less than the thickness of the diamond detector, bulk polarization effects could take place which could lead to a strong variation in the signal pulse height produced by ions having equal energies. This in turn can induce detection efficiency losses. Less ionizing particles (e.g. high energy protons and C-ions) have been used in the past to test the detection efficiency, time resolution and radiation hardness with excellent results [77]. The CVD-diamond detector has also showed a high detection performance for heavy ions of few hundred MeV/u [78]. During the present investigation, the detector performance has been tested for the first time with highly charged, very heavy-ions at intermediate energies (E ~ 69 MeV/u) having an extreme ionizing power. The total count rate registered by the CVD-diamond detector has been compared to the count rate of SEETRAM in order to determine the detection efficiency of the former at these energies.

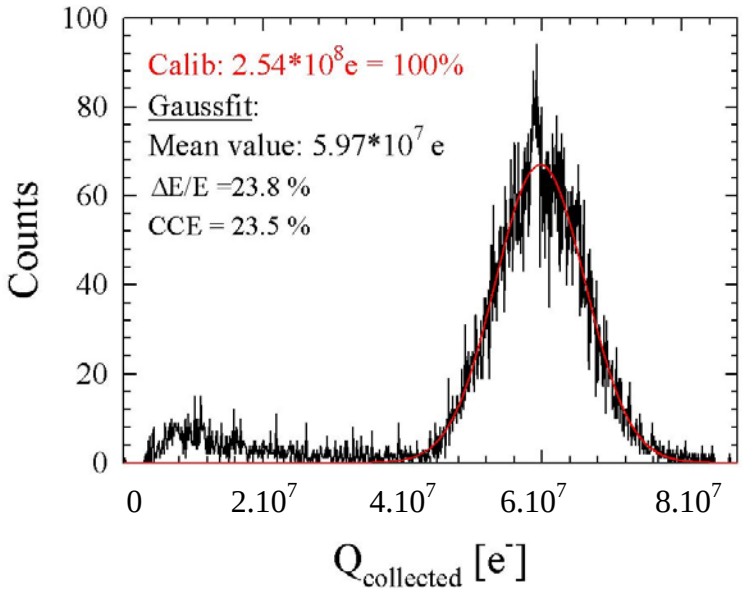

Fig. 3.9 *Pulse height distribution for the collected charge (Q) in the CVD-diamond detector measured with an incoming Bi-ion beam of 69.2 MeV/u. CCE is the charge collection efficiency. Energy resolution ΔE/E of the CVD detector is equivalent to the charge resolution of ΔQ/Q (FWHM).*

Fig. 3.9 shows the pulse height distribution of the CVD-diamond detector measured with an incoming Bi-ion beam of 69.2 MeV/u. The counts are measured as a function of the collected charge "Q", the charge being measured in units of $1e^-$ charge. The calibration of charge collection efficiency was such that a detection of 2.54 x 10^8 electrons would denote a collection efficiency of 100%. Mean

value of the charge collected "$Q_{collected}$" per ion in units of 1 electron charge (e^-) was 5.97 x 10^7. The charge collection efficiency (CCE) is ~24% which is apt enough for a 100% particle counting efficiency as it is well above the noise level. The Full Width at Half Maximum (FWHM) of the distribution $\Delta Q/Q$ is ~23.8% and corresponds to the energy resolution $\Delta E/E$ of the detector. For earlier measurements with few hundred MeV/u heavy-ions, a poor energy resolution of only 60% was observed [79]. The remarkably good separation between the noise and the real signals indicate that practically all the real events are detected even after the low electronic level discrimination introduced later.

Fig. 3.10 shows the schematics of the experimental arrangement for the comparison of efficiencies of CVD-diamond detector and SEETRAM. A Bi^{81+}-ion beam of 69.2 MeV/u has been bombarded on Au and C foils of different thicknesses t ($12 \leq t$ in $\mu g/cm^2 \leq 225$). The CVD-diamond detector was placed in air at the focal plane of the magnet spectrometer (Fig. 3.4, 3.6, position P2). The SEETRAM was installed in vacuum at the zero degree exit of the dipole magnet (see Fig. 3.4). The ejectiles were consequently detected by the CVD-diamond detector after charge state separation by the magnet spectrometer or alternatively by the SEETRAM after switching off the magnetic field. Hence, any measurement by SEETRAM was independent from that of the CVD-detector.

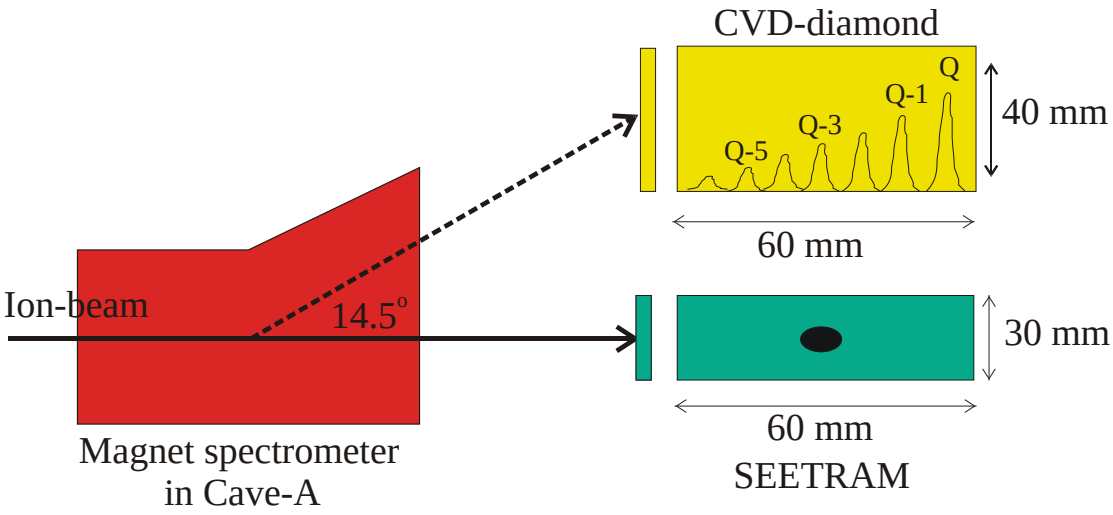

Fig. 3.10 *Schematics of the experimental arrangement at Cave-A for the comparison of CVD-diamond detector and SEETRAM detection efficiencies.*

For very thick targets a large number of charge states are created after interaction with the target yielding a very broad spectrum. By changing the magnetic field of the magnet spectrometer in small steps, it was possible to detect all the separated charge states of the ejectiles on the CVD successively. The position of at least one charge state in the spectrum from the new magnet setting

was kept as overlapping with the charge state distribution spectra from the previous setting of the magnet. It was shown that 90% of the primary beam could be measured at once in one setting of the magnet spectrometer. Hence, it was ensured that almost all the particles were counted. For the measurement with SEETRAM, an optical setting of the quadrupoles of the spectrometer was chosen such that the entire beam impinged on the surface of the detector, the beam was 3 mm broad and 20 mm in height (Fig. 3.10).

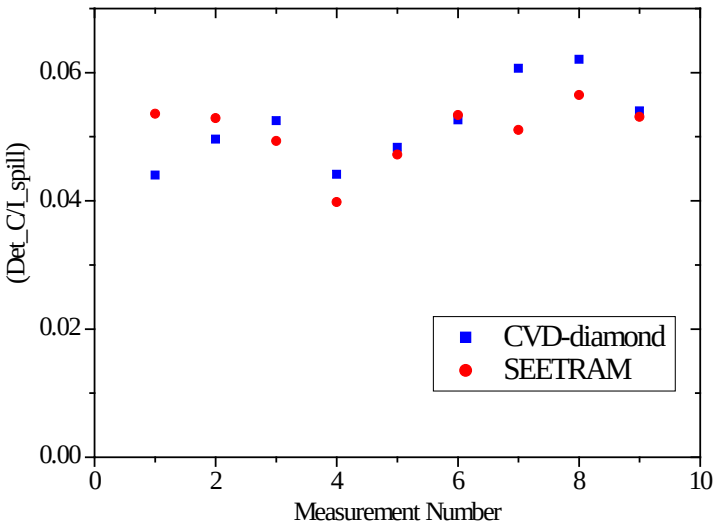

Fig. 3.11 *A comparison of CVD-diamond particle detector and SEETRAM efficiencies.*

To compare the efficiencies of the two detectors, normalization to an initial beam intensity was required. As explained earlier in Section 3.2.1, the beam on exit from the SIS is passed through a stripper (Fig. 3.3) and only one of the charge states created during this interaction impinges on the target. As a result the actual intensity of the ions after the stripper is much lower than the intensity of the beam measured in SIS. For an estimation of the detection efficiency, the number of detected ions integrated over a few seconds (Det_C) have been normalized to the total number of ions stored in a spill in the SIS (I_spill).

Fig. 3.11 for example shows this ratio (Det_C/I_spill) plotted against "measurement number" for both the detectors. A measurement number comprises two independent successive measurements for each detector both normalized to the corresponding SIS spills. The first four points correspond to the 21 $\mu g/cm^2$ thick Au target and the rest to the 225 $\mu g/cm^2$ thick Au target. The value of the calculated ratio in Fig. 3.11 is appreciably smaller than the real detection efficiency of the two detectors due to normalization on the total beam intensity stored in the SIS but not on the intensity of the ions impinging on the target. According to the calculations presented in Fig. 3.3 for the charge

state evolution in the stripper, the beam intensity on the target was only a small fraction of the total beam stored in the SIS. With the observations shown in Fig. 3.11 it can be concluded that both the detectors are equally efficient. Since the SEETRAM is known for its 100% detection efficiency, the efficiency of the CVD-particle detector is also concluded to be 100% for the used count rates and energies of the projectile-ions. The variations in Fig. 3.11 have been observed for all the target thicknesses investigated, it is concluded that this is due to the statistical fluctuation in the number of particles extracted from the SIS.

3.3 DATA ACQUISITION AND ANALYSIS

The online and offline data acquisition system used have been described briefly in Section 3.3.1 along with electronics set up for the experiments. The data analysis has been detailed in Section 3.3.2 to 3.3.5. As mentioned earlier, two different types of Germanium detectors; the single crystal Ge(i) and the seven stripe Germanium [7-Ge(i)] have been used for recording the K x-ray data. These detectors had large solid angles and the highly intense low energy L x-rays had to be cut out by strong aluminium absorbers to reduce the count rate. The Si(Li) detector with smaller solid angle and without any absorber has been used for recording the L x-ray data of the collision partners. The CVD-diamond particle detector has been used for detecting the ejectiles. Different procedures have been followed for the offline analysis of these data. The x-ray emission cross sections can be calculated from the x-ray yields, target thickness, number of particles incident on the target, efficiency and dead time of the x-ray and particle detector, solid angles subtended by both types of detectors at the target and the dead time of the data acquisition system. The shifts in the energies of the x-ray transitions and the intensity ratios of the x-ray yields can be obtained almost directly from the deconvoluted x-ray spectra. The details of analysis are discussed below.

3.3.1 Data acquisition system and electronics set up

The standard data acquisition system used at GSI is the multibranch system (MBS) [80]. It is based on real time operating System i.e. LynxOS. The CAMAC trigger module of GSI was used along with M68k CPU i.e. CVC99 (CVC: Camac VSB Computer). The net work data flow was via fast or Gigabit Ethernet switches. An easy data interface (TCP) exists for on-line analysis. A remote visualization of the data was done with online data acquisition systems like GOOSY and Go4 [81]. The offline data analysis was done with Go4. More details of MBS and Go4 can be found in the

respective internet sites quoted. The electronics set up for the two experiments performed differed from each other slightly. The more complex set up for the Bi-Au experiment is shown in Fig. 3.12.

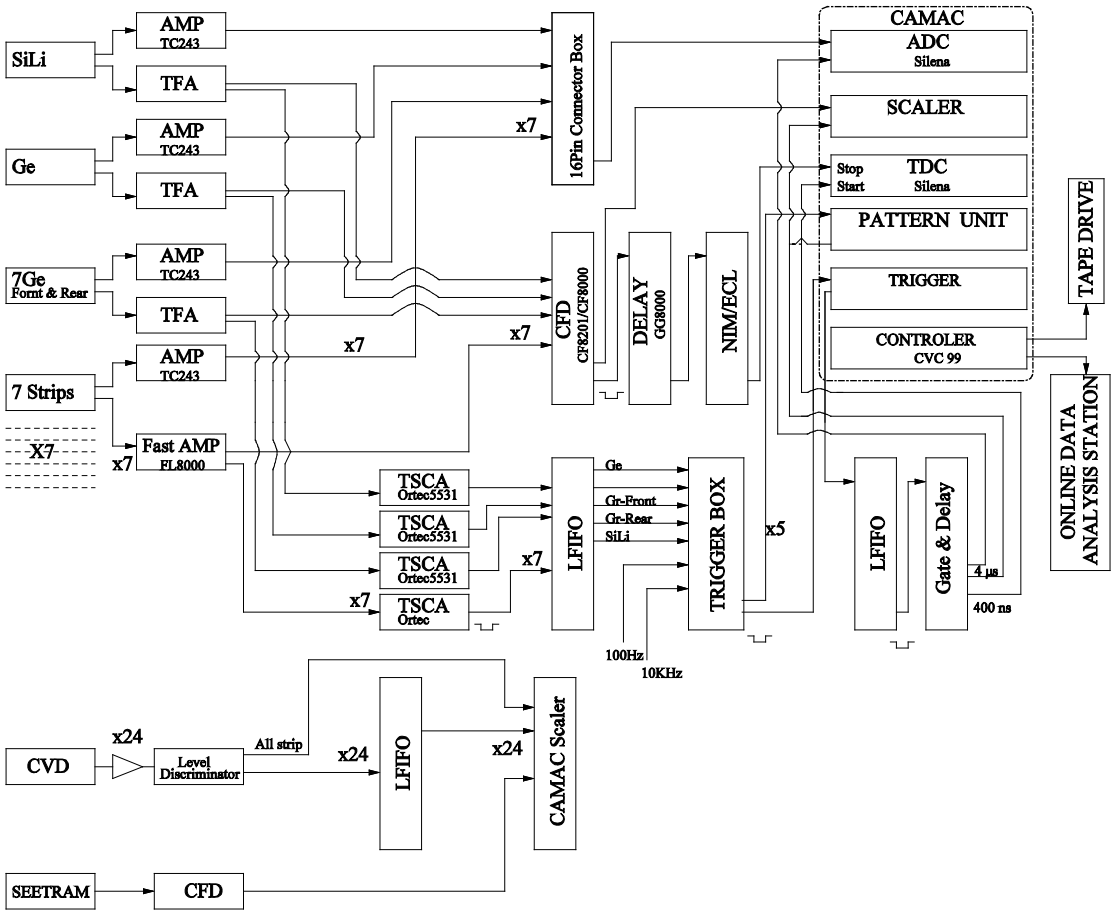

Fig. 3.12 *A schematic diagram of the electronics set up for the Bi-Au experiment.*

3.3.2 Energy and efficiency calibration of the x-ray detectors

The energy calibration of the x-ray detector is important for the identification of x-ray emission from the collision partners. A good energy resolution of the detector is also required to measure the shift in energy of x-ray transitions with respect to standard single hole values [23]. The efficiency of a x-ray detector in the energy range of interest has a direct bearing on the calculation of x-ray emission cross sections of the collision partners. The energy calibration of the Ge(i), 7-Ge(i) and the Si(Li) detector was performed before and after the experiment by using standard radioactive sources of ^{57}Co, ^{133}Ba, ^{152}Eu and ^{241}Am placed at the target position within the target chamber. With the prior knowledge of the energies of x-ray and γ–ray transitions occurring in these radioactive

sources, a linear fit for calibration was obtained and used for the identification of the projectile and target x-rays in the recorded spectra.

Special care was taken in the determination of the efficiency of the Ge(i) and 7-Ge(i) and the Si(Li) detectors. The intrinsic efficiency of all the detectors was measured in the laboratory by using standard radioactive sources in the same geometry by the procedure described by Pajek *et al.* in [82]. The measured x-ray yields corresponding to various x-ray and γ-ray lines from the radioactive source were converted into the intrinsic detector efficiency by using the formula:

$$\varepsilon_{x_i} = \frac{Y_{x_i}}{N \times I(x_i)}$$

where Y_{x_i} = Number of photons observed correspondingly to ith x-ray / γ-ray peak/s,

N = Number of disintegrations/second of the source at the time of measurement,

$I(x_i)$ = Intensity of ith x-ray/ γ-ray peak per decay of the source.

The relative intensities of different x-ray lines for ^{57}Co and ^{241}Am sources were taken from Dias and Renner [83] and Cohen [84] respectively. The experimental data was then fitted with a polynomial [85] to obtain the intrinsic efficiency. The geometrical factor of $\Omega/4\pi$, for the solid angle (Ω) of the detectors in 4π was included later to calculate the experimental efficiency curve for each detector separately. Fig. 3.13 shows the intrinsic efficiency of the 'A' Ge(i) detector used in both the experiments.

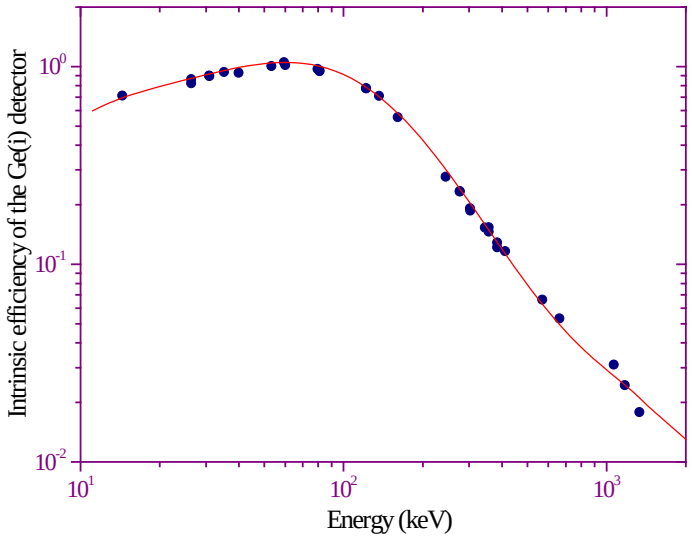

Fig. 3.13 *The intrinsic efficiency of the 'A' Ge(i) detector.*

In addition to the procedure mentioned above the efficiency of the Si(Li) detector was determined additionally through the use of the detector parameters such as the Si sensitive and dead layers, thickness of Au contact layer and the Be window as described by Pajek *et al.* [82]. The

attenuation of the x-rays in these different layers was calculated (using XCOM [86] computer code) and the corrected theoretical efficiency curve was obtained which took into account the x-ray absorption in the Be window of the target chamber separating the Si(Li) detector from the target chamber and the air gap between the Be window and the detector too. The calculated efficiency curve was least square fitted and normalized to the measured experimental values to obtain the efficiency in the region of interest.

3.3.3 Doppler shift and Doppler correction

The projectile-ions used in the present investigation move with relativistic velocities (v ~ 40% of c, the velocity of light). As a result the x-rays emitted from these projectiles are strongly Doppler shifted when observed in the laboratory (lab) frame. The Doppler shift can be calculated from the following formula:

$$E_{lab} = \frac{E_0}{\gamma\,(1-\beta\,\cos\theta_{lab})}$$

where $\beta = v/c$ and $\gamma = 1/\sqrt{1-\beta^2}$ is the Lorentz factor. E_0 is the energy for the projectile x-rays in the emitter frame or emitting system, E_{lab} is the Doppler shifted x-ray energy detected in the laboratory system, θ_{lab} is the angle between the emitted x-ray and projectile in the laboratory system. The ratio of E_{lab}/E_0 depicts the Doppler shift. For example Fig. 3.14 shows the Doppler shift for 69.2 MeV/u U^{q+}- or Bi^{q+}-ions as a function of θ_{lab} varying from 50° to 130°. This gives an idea about how the two experimental geometries in the backward (G1) and forward (G2) directions (Fig. 3.6) affect the x-ray energies observed in the laboratory system.

A correction for the Doppler shift requires a precise determination of β as well as of θ_{lab}. The uncertainty in θ_{lab} is much larger because of a large opening for the observation angle of the x-ray detectors. The uncertainties in β and θ_{lab} introduce an uncertainty ΔE_0 in emitter frame energy E_0. The ratio $\Delta E_0/E_0$ is called Doppler broadening. The solid angles in the laboratory and the emitter system follow the relation:

$$\frac{d\Omega_0}{d\Omega_{lab}} = \frac{1}{\gamma^2(1-\beta\cos\theta_{lab})^2}$$

and this factor is used for the calculation of projectile x-ray emission cross sections. The values of this factor for the two experiments performed are given in Fig. 3.14.

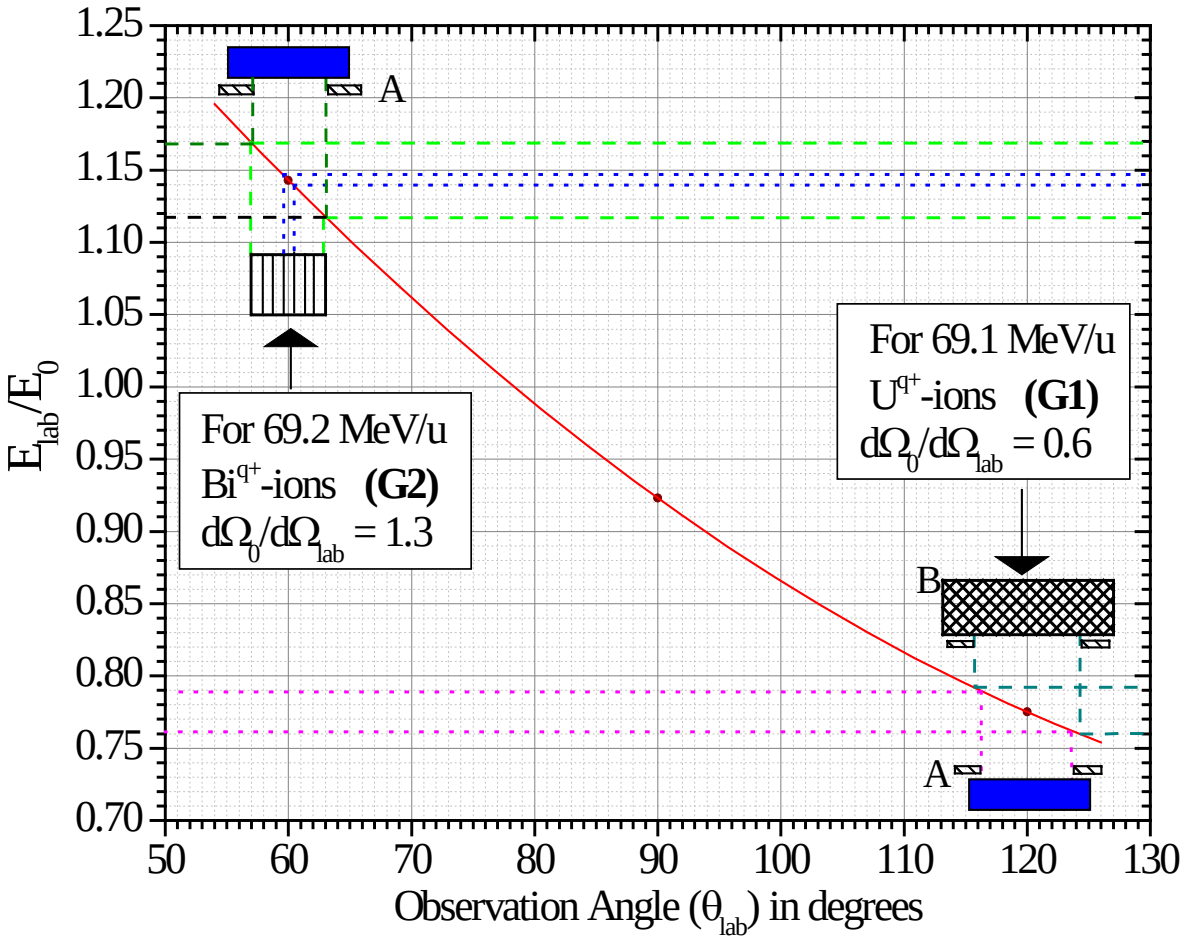

Fig. 3.14 *Doppler shift (E_{lab}/E_0) as a function of observation angles ranging from 50° to 130° for 69.2 MeV/u U^{q+}- or Bi^{q+}-ions. The x-ray detector positions for both geometries G1 and G2 are indicated.*

Based on theoretical values of E_{lab}/E_0 for the velocity of the projectile-ion (v_{ion}) chosen, a simulated x-ray spectra was emulated for both the stationary target (Au) x-rays and the Doppler shifted projectile (U or Bi) x-rays in the laboratory system. It was found that for 69.2 MeV/u U and Bi–ions the projectile K x-rays would be well separated in energy from the Au K x-rays if the detectors are placed in the forward direction (60º) i.e. geometry G2, Fig. 3.6. The Doppler broadened U or Bi K x-rays would then get a forward boost and hence a clear separation from the Au K x-rays. The geometry G2 was used for Bi-ion experiment.

For the U-ion experiment, U-targets along with the Au targets were intended to be bombarded in order to investigate completely-symmetric systems. The geometry G1 (Fig. 3.6) would facilitate a clear separation of the projectile (U) K x-rays from the target U K x-rays. Consequently, the chamber was placed with its detector ports at backward angles. Limitations of the beam time did not enable a complete measurement with the U targets and hence could not be included in the present investigation.

3.3.4 X-ray peak fitting and analysis procedure

The measured x-ray spectra were analyzed by the Gaussian peaks subtracting a suitable background using a least square fitting iterative method. The position, intensity and width of the peaks are the three adjustable parameters used for this iterative method. As a first step, the various peak energies are fixed corresponding to the standard x-ray transition energies taken from the tables of Bearden [23] corrected for the Doppler effect if required. These fixed energies of the K or L x-ray lines were then allowed to vary so that the various peaks fit in the entire spectrum. The fitting procedure gives intensities and lab energies (as well as widths) for the prominent lines. From the intensities absolute x-ray cross sections and intensity ratios have been deduced. The position (i.e. energy shifts) give in addition an information on multiple ionization during the emission of x-ray lines.

3.3.5 Calculations of experimental results

i) X-ray energy shifts

The shifts in the characteristic x-ray energies have been calculated with respect to the standard atomic values [23]. The error in the energy shifts include mainly the error in energy calibration, fitting procedure (statistics), energy resolution of the detector and by the kinematics of the collision system. The dominant uncertainty for the projectile x-ray lines arises from the uncertainty in the Doppler correction. In most other cases the statistics is the limiting factor.

ii) X-ray intensity ratios

The intensity ratios for various K and L x-ray lines were calculated by using the formula:

$$\frac{\sigma^{X}_{Li}}{\sigma^{X}_{Lj}} = \frac{Y_{Xi}}{Y_{Xj}} \frac{\varepsilon_j}{\varepsilon_i}$$

here "i" and "j" refer to different K ($K\alpha_1$, $K\beta_2$ etc.), or L x-ray lines ($L\alpha$, $L\beta_1$ etc.), Yx_i is the yield of K or L x-ray for the i^{th} x-ray line, ε_i is the efficiency of the x-ray detector for the i^{th} line. The intensity ratios calculated for a particular incoming charge state (q) of the projectiles and for a particular target thickness (t) do not require any absolute normalization. Hence these ratios can be determined with greater accuracy than the absolute x-ray emission cross sections because the sources of error arise mainly from the counting statistics. However, for an intensity ratio involving projectile and target x-ray lines, the Doppler correction for the solid angle has to be included additionally.

iii) Normalization procedure and dead time correction

As mentioned above in Section 3.2.2 (ii) two different procedures were followed for the normalization of the x-ray yields in the two experiments (U-Au and Bi-Au) by the CVD-diamond particle detector. The dead time correction to the experimental data included the dead time correction for the x-ray and particle detectors as well as the dead time correction for the data acquisition system. The latter overpowered the former; details will be discussed in the relevant chapters 4 and 5 respectively.

iv) X-ray emission cross sections

The x-ray yields are related to the x-ray emission cross sections by the relation:

$$\sigma_i^x = \frac{Y_{x_i}}{t\ \varepsilon_{x_i} N_p} \frac{\Gamma_x}{\Gamma_P}\ \Gamma\ \cdot \frac{d\Omega_0}{d\Omega_{lab}}$$

where σ_i^x = x-ray production cross section (i = Kα, Kβ, Lα etc.),

Y_{x_i} = x-ray yield under the ith x-ray peak,

t = target thickness in atoms/cm^2,

ε_{x_i} = detection efficiency of the x-ray detector accounting for the absorption of the x-rays in the chamber window and solid angle subtended by the detector at the target,

N_p = number of ejectiles after interaction with the target,

Γ_x and Γ_p = dead time corrections for the x-ray and charged particle detectors,

Γ = dead time correction for the data acquisition system,

$\frac{d\Omega_0}{d\Omega_{lab}}$ = correction to the solid angle due to Doppler effect.

The solid targets are considered to be thin if they satisfy the single collision condition conditions for the projectile-ions traversing through them. The single collisions essential for atomic physics processes investigated can be obtained approximately by extrapolating the target thickness dependence of the normalized x-ray yields to “zero” target thicknesses.

CHAPTER IV

A SLIGHTLY ASYMMETRIC SUPERHEAVY COLLISION SYSTEM: U^{q+}-Au

4.1 INTRODUCTION

This chapter deals with the first exploratory experiment performed for this study. A U-Au (Z_1 = 92, Z_2 = 79) collision system was investigated for 69.1 MeV/u, highly charged U^{q+} projectiles ($73 \leq q \leq 91$) bombarding on thin Au targets ($18 \leq t$ in $\mu g/cm^2 \leq 170$). This exploratory experiment was planned in a simple way avoiding too much complexity in the experimental set up and data analysis. For close collisions affecting inner shells, the quasiadiabatic collision regime prevails as the adiabaticity factor $\eta_{K\text{-}U} = (v_{ion}/v_{K\text{-}U})^2$, for the U K-shell is ≤ 0.33 and similarly $\eta_{K\text{-}Au} \leq 0.45$ for the Au K-shell. For H-like U projectiles i.e. for an U-ion with an incoming K vacancy, the collision conditions for the projectile charge are beyond the equilibrium charge state which is about 86+ at this energy [59]. Section 4.2 describes the experimental details and Section 4.3 deals with the K x-ray emission from the U-Au collision system. Details regarding the K x-ray spectra, energy shifts of the K x-ray transitions, their intensity ratios and K x-ray emission cross sections have been covered in the subsections of Section 4.3 viz. 4.3.1 to 4.3.4 respectively. The charge state and target thickness dependences of the x-ray emission cross sections have been detailed in Section 4.3.4. Section 4.4 deals with the L x-ray emission from the collision system for completeness although this is not a main aim of this work. Section 4.4.1 to 4.4.3 reports on the L x-ray spectra, shift in the energy of the L x-ray transitions, intensity ratios and the L x-ray emission cross sections along with their dependences on projectile charge state and target thickness. The charge exchange cross sections have been discussed in Section 4.5.

4.2 EXPERIMENTAL DETAILS

A general description of the experimental set-up with the details regarding the position of targets and detectors has been given in Chapter 3, Section 3.2.2. A charge state selected, well collimated, U^{q+}-ion beam [q = 91, 90, 88, 86 and 73] of 69.1 MeV/u impinged on thin Au targets of thickness t [t = 18, 50 and 170 $\mu g/cm^2$, the thinnest one having a thin carbon backing of 15 $\mu g/cm^2$]. For q = 73, the 18 $\mu g/cm^2$ target was not used for observations only due to time constraints. Fig. 4.1

shows a schematic diagram of the experimental set up with a view from the top (G1 geometry, see Section 3.2.2) and Fig. 4.2 shows a photograph of the experimental set-up.

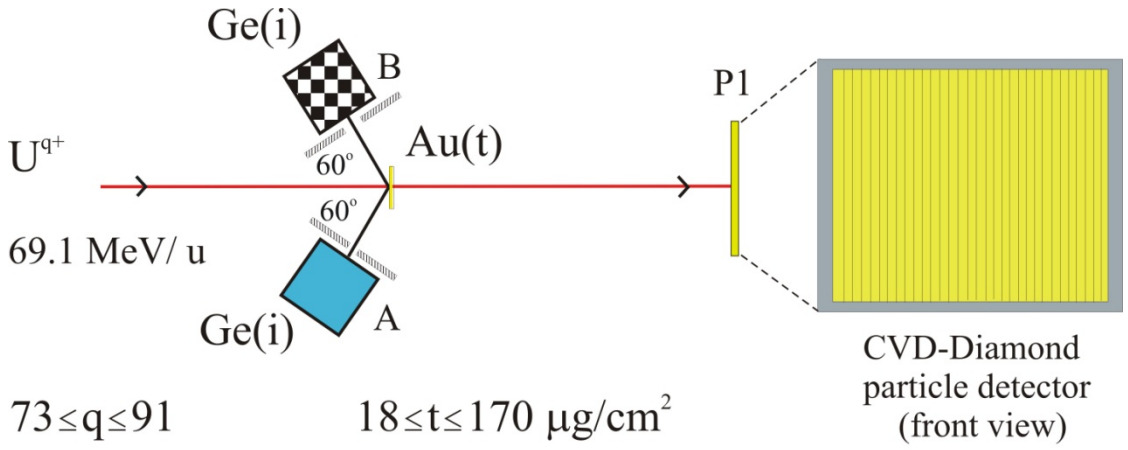

Fig. 4.1 *Schematic diagram of the experimental set up with a view from the top. The two single crystal Ge(i) detectors, A and B were placed at backward angles of ± 120°. The collimators for the two x-ray detectors are indicated in the figure, the solid angle of detector B being larger. The front view of the CVD-diamond particle detector at position P1 is depicted as blown up on the right side. The Si(Li) detector viewing the target region out of plane from above (135°) is not shown in the figure.*

With the target foils positioned normally to the beam direction, the x-rays emitted from the collision partners were detected by the two intrinsic, single crystal Ge(i) detectors positioned in the same plane at an angle of 120° to the beam direction (backwards). The two Ge(i) detectors A and B had Ta collimators of 4 and 3 mm thicknesses with rectangular openings of 5.8x38 mm^2 and 7.7x38 mm^2 respectively. The resulting geometry allowed solid angles of 0.051 sr and 0.089 sr respectively which were 0.4% and 0.7% of 4π. A Si(Li) detector was used for the detection of L x-rays of the collision partners and was installed at 135° with respect to the beam direction in the 45° port of the chamber (backwards), off plane with respect to the Ge(i) detectors (Fig. 4.2). The Si(Li) detector had a much smaller solid angle of 0.004 sr. The details of the physical characteristics of the x-ray detectors have been given in Table 3.1 a) of Chapter 3.

Behind the target, the ion beam was monitored by the one-dimensional, position-sensitive, CVD-diamond particle detector (discussed in detail in Chapter 3, Section 3.2.2 (ii) and 3.2.3 (ii a)) [87, 88] for normalization of the x-ray emission with the number of ejectiles. As mentioned in Chapter 3, this particle detector was installed approximately 70 cm behind the target. A schematic diagram of the particle detector is shown on the right hand side of Fig. 4.1.

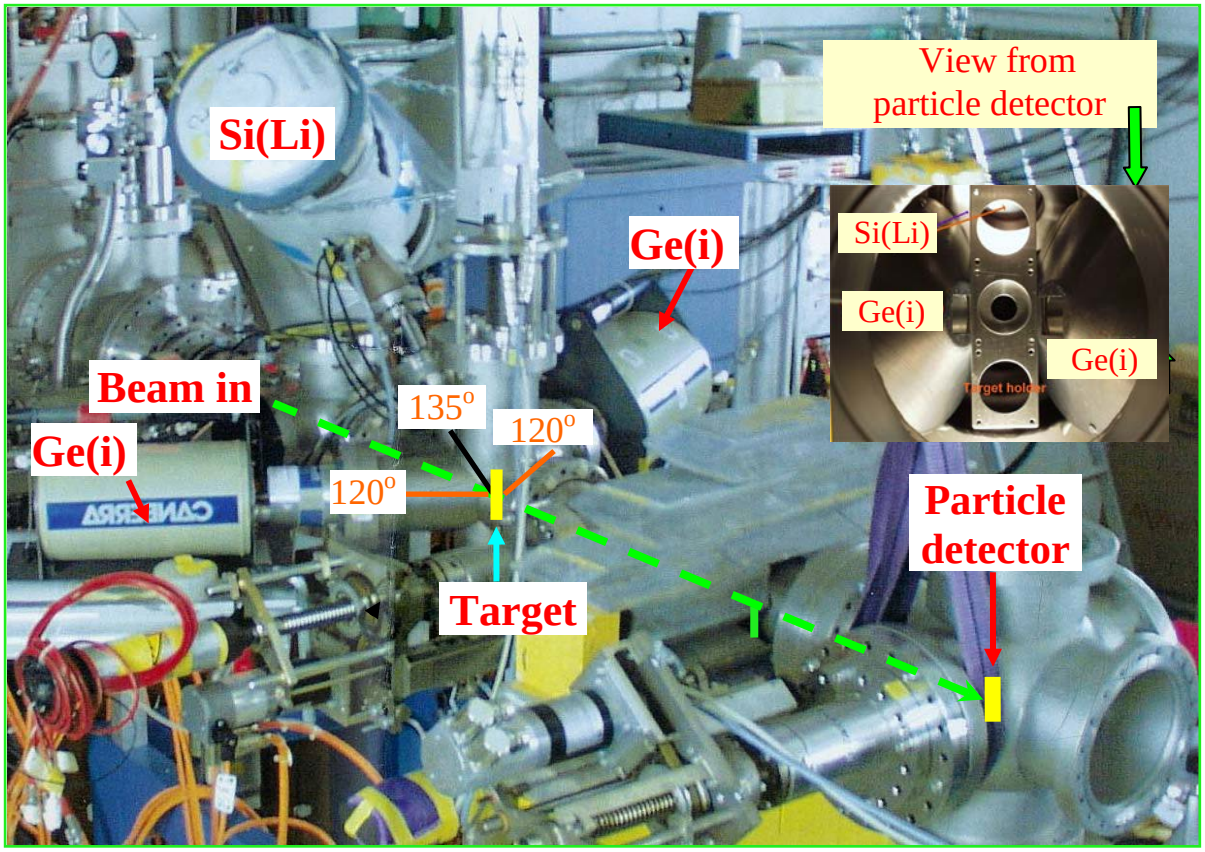

Fig. 4.2 *Photograph of the experimental set-up showing the two Ge(i) x-ray detectors A and B at angles of 120° and the Si(Li) x-ray detector placed off plane at an angle of 135° with respect to the beam direction (indicated in the figure). A view of the target area from the particle detector position is shown on top right of the figure with the Si(Li) detector (top) and the two Ge(i) detectors viewing the target in close proximity.*

4.3 K X-RAY EMISSION IN U^{q+}- Au COLLISIONS

4.3.1 The K x-ray spectra

Fig. 4.3 depicts K x-ray spectra (laboratory frame) measured by the Ge(i) detector "A" showing a smaller Doppler broadening (c.f. Fig. 4.1) for the 50 μg/cm^2 thick Au target bombarded by U^{q+}-ions (q = 73, 90 and 91). The counts are normalized relative to the number of ejectiles detected by the particle detector through the procedure described in Section 4.3.4. The counts however are not shown normalized with respect to target thickness. The different characteristic x-ray lines of the collision partners have been labelled in the figure and the overlapping of the different x-ray lines is evident. The Ta collimators used in front of the detectors are the origin for the Ta-Kα_1,α_2 and Kβ_1 fluorescence x-ray lines visible in the spectra. These fluorescence lines result due to the ionization/excitation of the Ta induced by the radiation from the interaction area. These lines also

serve as a check on the energy calibration of the x-ray spectra. The procedure for energy calibration has been explained in Chapter 3, Section 3.3.2.

The figure shows the effect of projectile incident charge state 'q' on the K x-ray spectra of the collision partners for a particular thickness 't' of the Au target. It can be clearly observed that the normalized K x-ray yields are highly sensitive to the charge state 'q'. On a comparison of spectra for

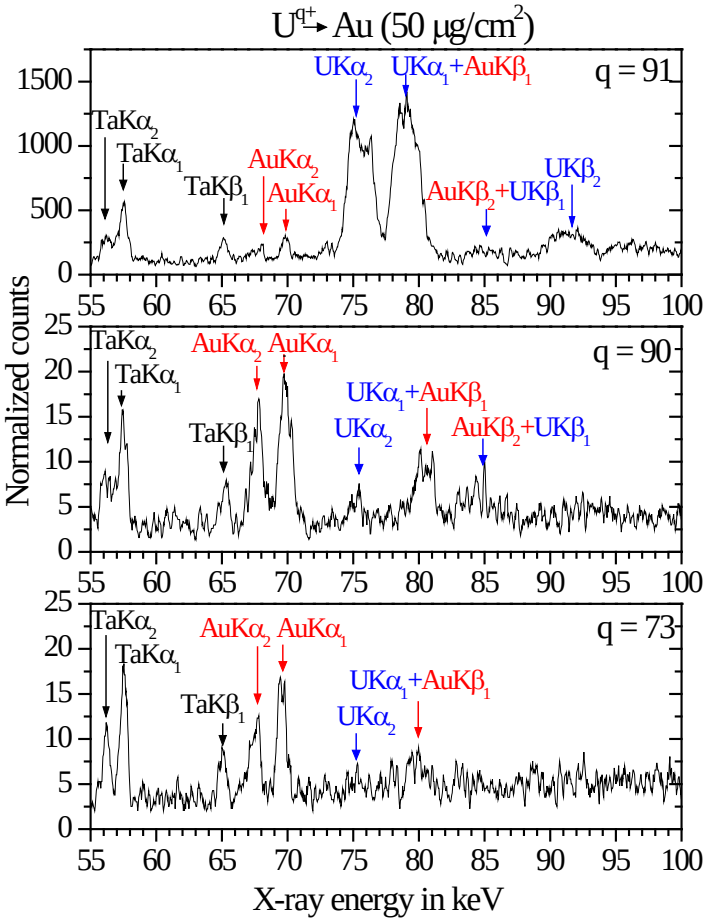

Fig. 4.3 *K x-ray spectra (laboratory frame) measured by the Ge(i) "A" detector for the 50 μg/cm² thick Au target bombarded by U^{q+}-ions (q = 73, 90, 91). The counts are normalized relative to the number of ejectiles.*

q = 90 and q = 73, one can observe only a slight increase in the yields of U- and Au-K x-rays with increasing q. A q = 91 and 90 for U^{q+} projectiles correspond to an open and closed K-shell of the U respectively in the incoming channel of the collision. A comparison of the corresponding spectra reveals firstly that for q = 90, the Au-K x-rays are relatively much more intense than the U-K x-rays. However, for q = 91 these intensity ratios show a reversal and there is a dramatic increase in the yields of the U-K x-rays as compared to that of the Au-K x-rays. Secondly, for q = 91, the normalized yields of both U and Au are considerably higher than their values corresponding to q = 90 and 73. The x-ray spectra were deconvoluted to yield Au-K and U-K x-rays separately by the x-ray line fitting procedure

described in Chapter 3, Section 3.3.4. For the spectra corresponding to q = 91, the extraction of U-Kα_1 yield from the mixed line of U-Kα_1+Au-Kβ_1 did not pose a problem because the U lines are an order of magnitude more intense than the Au-Kβ_1 lines. Elsewhere, the x-ray emission rates from Scofield [64] and the area under the Au-Kα_1 line were used to estimate the number of counts under the Au-Kβ_1 line. A similar procedure was followed for the extraction of U-Kβ_1 yield from the mixed line of Au-Kβ_2+U-Kβ_1.

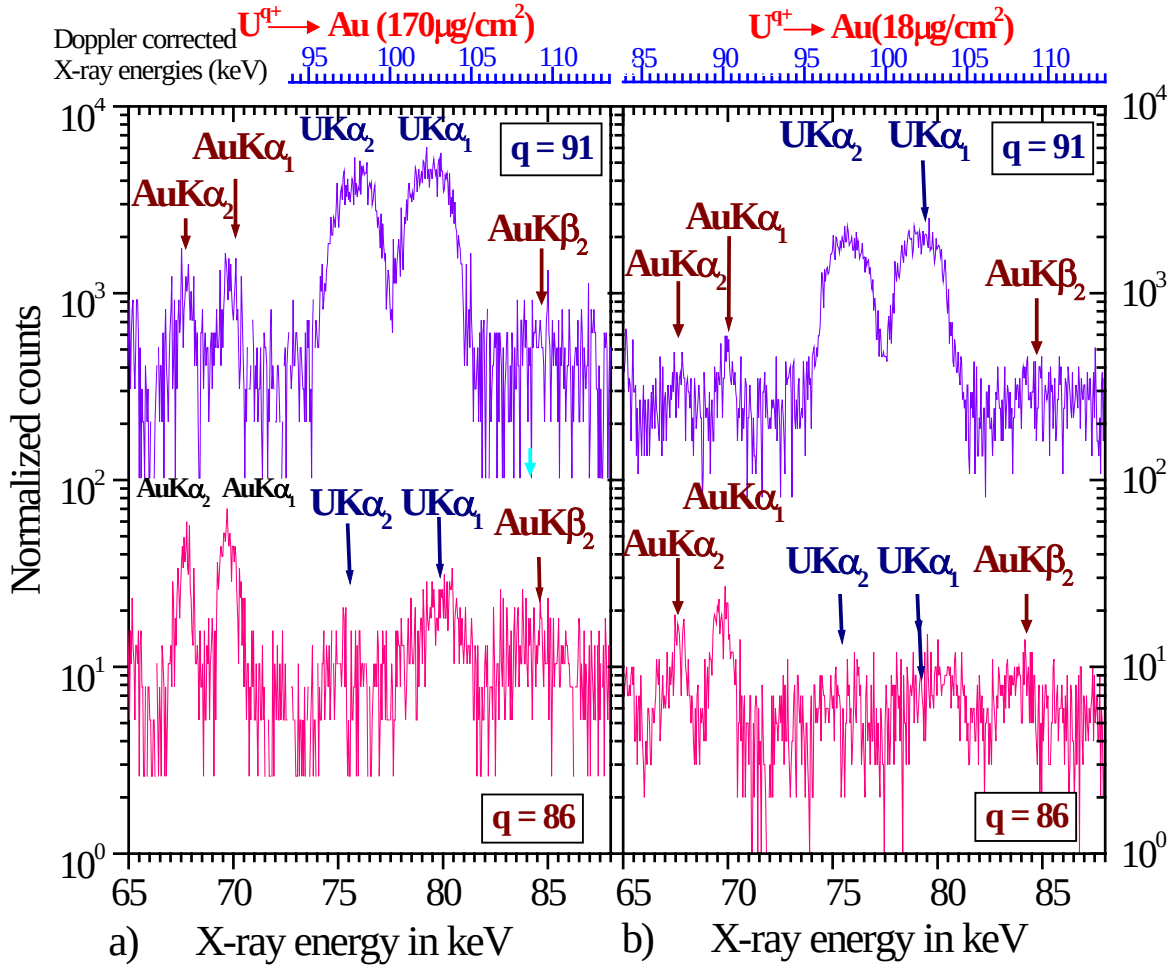

Fig. 4.4 *K x-ray spectra (laboratory frame) for U^{91+} and U^{86+}-ions (top and bottom respectively) incident on a) the thickest Au target (170 μg/cm^2) and b) the thinnest one (18 μg/cm^2). The counts are normalized relative to the number of ejectiles. The energy scale for the emitter frame of the relativistic U-ions is given on top.*

Fig. 4.4 depicts a closer look at the K x-ray spectra (semi-log plot) measured in the laboratory by the "A" Ge(i) detector for $U^{91+,\ 86+}$-ions incident on the thickest (170 μg/cm^2) Au target (part a) and on the thinnest (18 μg/cm^2) one (part b). The figure shows both the charge state 'q' effect and the target thickness 't' effect on the K x-ray spectra of both the collision partners. The counts are normalized relative to the number of ejectiles however they are not depicted normalized with respect to target thickness. The projectile K x-ray spectra are observed as Doppler shifted in the laboratory

frame. The phenomenon of Doppler shift has been explained in detail in Chapter 3, Section 3.3.3. The Doppler corrected U-K x-ray energies in the emitter frame can be obtained from the scale given at the top in both the spectra.

A comparison of the spectra with respect to 'q' shows a strong influence of the same on x-ray emission. As has also been observed in Fig. 4.3, for a projectile with an incoming K vacancy (q = 91, i.e. open K-shell), one can again observe clearly a reversal in the relative intensities of the U-K and Au-K x-rays as compared to those without an incoming K vacancy (q = 86 i.e. for a closed K-shell). For q = 91, the Au-K x-rays show a much smaller increase in yield as compared to the U-K x-rays. This observation is independent of the thickness of the target as is evident by a comparison of Fig. 4.4 a) and b).

The Au-K emission is with very high probability, the result of a close collision whereby Au-K vacancies are created. For H-like projectiles, the Au-K vacancies might also result from a sharing of the vacancies brought to the collision system in the incoming channel. The Au-K x-ray emission is not remarkably influenced by the incoming charge state of the projectile as long as the projectile K-shell is closed. On the other hand, during distant collisions, electron capture dominates for a highly charged projectile. Although capture takes place for all the incident charge states 'q' of the projectile; for q = 91, the captured electrons become visible through the now available radiative decay channel to the projectile K-shell leading to the observed high U-K x-ray emission yields. For lower incoming charge states this decay channel is closed. For these charge states only capture to the M- and higher shells can manifest itself through L x-ray emission. Moreover, according to theoretical approaches like the Eikonal [53] for H-like U (q = 91), the cross section for capture is maximum from target L shell to the projectile M shell (refer Fig. 4.23, details in Section 4.5). For all q investigated (q = 73, 86, 88, 90 and 91) the projectile always has vacancies in M and higher shells.

4.3.2 Shift in the energy of the K x-ray transitions

As has been explained in Chapter 2, multiple ionization during heavy-ion heavy-atom collisions leads to an energy shift of the x-ray lines compared to single hole standard atomic values (E_o) (taken from Bearden [23]). Fig. 4.5 a), b) shows the centroid energies ($E_{obs.}$) of $K\alpha_1,\alpha_2$ x-ray transitions in the laboratory frame (LAB) for Au and in the emitter frame (E.F.) for U respectively. They are expressed as a function of the incident charge state (q) of the U^{q+}-ions for the three different Au thicknesses investigated (18, 50 and 170 $\mu g/cm^2$). The standard values (E_o) for the energies of these x-ray transitions have been indicated by solid lines in the plot corresponding to 18

μg/cm^2 Au target. The errors in U-K$\alpha_{1,2}$ energies are larger than the ones for Au as for U x-ray emission, large systematic errors have to be taken into account due to the Doppler shift correction required for relativistic projectiles and the uncertainty in the observation angle which is in the region of 3^o (see the systematic error in the figure indicated by an arrow). This error arose from the fact that the targets loaded on the ladder were positioned about 2 mm upstream from the chamber centre. Both Au- and U-K$\alpha_{1,2}$ x-ray transitions are observed at higher energies as compared to the standard values [23].

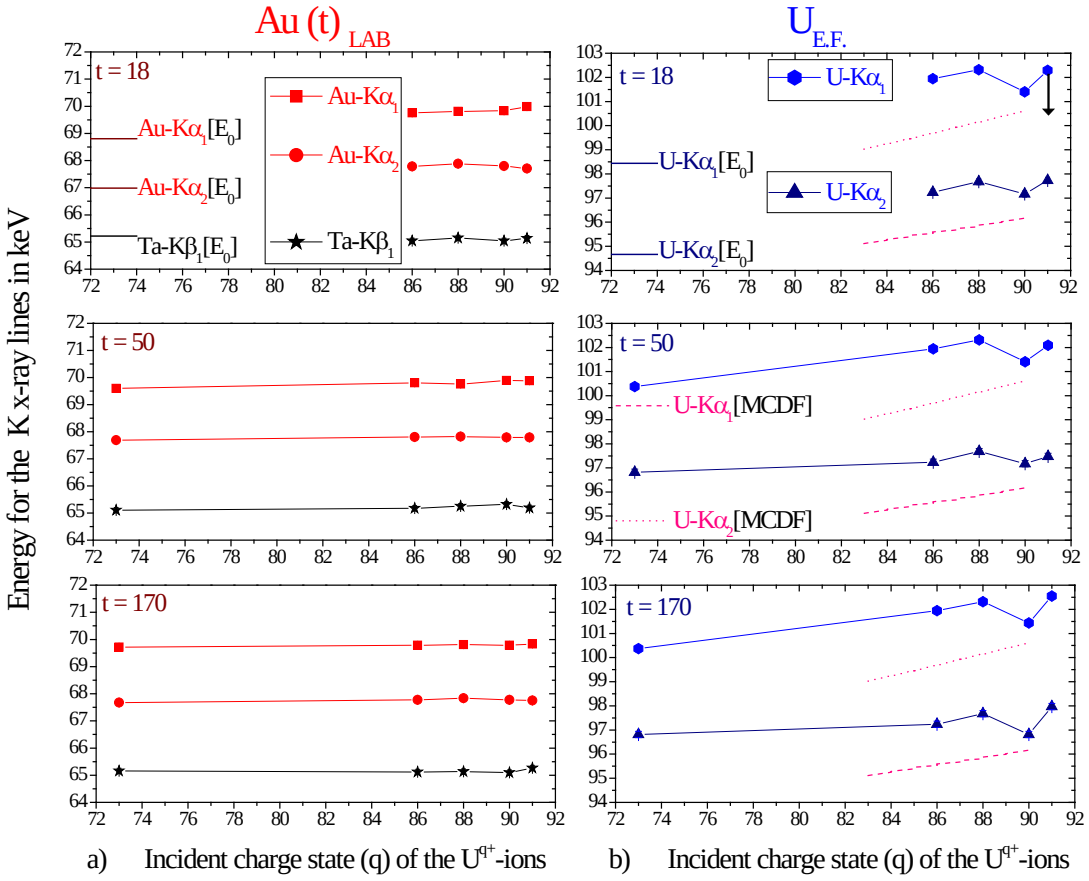

Fig. 4.5 *Centroid energies ($E_{obs.}$) of K x-ray transitions as a function of the incident charge state (q) of the U^{q+}-ions.* a) *for Au-K$\alpha_{1,2}$ in the laboratory frame (LAB)* b) *for U-K$\alpha_{1,2}$ in the emitter frame (E.F.). The corresponding standard values of Bearden (E_o) [23] have been indicated by solid lines in the uppermost plot. Thickness of Au target (t) is in μg/cm^2. Statistical errors are smaller than the size of the symbols. The lines through the data points are drawn to guide the eye. MCDF calculations [90] for U-ion are depicted with dotted and dashed lines. The uncertainty due to the Doppler correction is given by an arrow in the uppermost plot of U for q = 91.*

The U^{q+}-ion is multiply ionized in the incoming channel itself for all the q investigated (q=73 to 91) having M-shell vacancies in all the cases and hence a large number of outer shell spectator vacancies. These vacancies persist during the collision and hence during x-ray emission in the projectile. The simultaneous creation of outer shell spectator vacancies (L, M, N etc.) in Au is evident

from above observation. Both U- and Au-K x-ray transition energies increase with increase in 'q' with the former showing a larger increase. The Ta-Kβ_1 fluorescence line has been plotted to show the good agreement between its standard values and those observed experimentally.

The dotted and the dashed lines in the plots for U [see Fig. 4.5 b)] correspond to Multi Configuration Dirac Fock calculations [89] performed for U-ions [90] using GRASP92 code [91] for Kα_1,α_2 energies respectively. The energy of these x-ray transitions have been calculated for the ground state configuration of the highly charged ions with one excited electron. A particular vacancy distribution in the shells has been considered. For a final charge state of q = 90, 7 vacancies were assumed in the L-shell and the number of vacancies were decreased in steps of 1 with q also decreasing in steps of 1. Thus for a final charge state of q = 83, calculations were done for a full L shell (zero vacancies). The electrons were distributed in the 2s and the 2p shells as per the Hund's rule. Corresponding to a particular q, the values plotted in Fig. 4.5 b) are an average of values for all possible electronic configurations (3 values for q = 88, 87, 86, 85; 2 for q = 89, 84; 1 each for q = 90 and 83). For a highly charged U-ion, the observed energy shifts can be compared with these calculations as ionization/excitation will probably lead to similar configurations as discussed above. Since the experimental U-K x-ray transitions are observed at much higher energies compared to even these calculations [90], it might be caused by the uncertainty in the observation angle mentioned earlier. It is to be noted that the slope of the experimental and theoretical values is almost the same. The increase in shift per additional vacancy observed experimentally coincides with the calculations indicating that most probably the projectile captures only a single electron in a distant collision.

The 'q' dependence of these transition energies becomes clearer in a relative representation, by a comparison of these values with standard ones (E_o). For clarity, Fig. 4.6 shows the shift in the centroids of Au and U-K x-ray lines relative to standard values and normalized to them as a function of 'q' for all the three Au thicknesses investigated. These relative shifts $(E_{obs}-E_o)/E_o$ give the change in screening (change in the corresponding Z_{eff}) caused by the multiple ionization. The lines drawn are linear fits to the data. A linear fit to the Au- and U-Kα_1,α_2 corresponding to 18 $\mu g/cm^2$ thick Au target has been done with the same parameters as that for t =170 $\mu g/cm^2$. It has been estimated that the Au-K x-ray transitions show a relative shift increasing with q from 1% to 2% on an average whereas the U-K x-ray transitions show a larger relative shift increasing from 2% to 4% and therefore a steeper slope, not considering the uncertainty in the Doppler correction. For these projectiles moving at relatively high velocities this might be due to the greater initial ionization in the higher projectile shells which survive collisions in the solid to some extent. The steeper slope for the projectiles with increasing q points to a higher ionization in the L shell leading to an increased

change in the screening. The $K\alpha_2$ lines of U and Au exhibit a relatively smaller shift as $2p_{1/2}$ electrons are involved in the transition instead of $2p_{3/2}$.

Fig. 4.7 depicts the centroid energies of U- and Au-K x-ray transitions as a function of the Au target thickness (t) in the laboratory frame. Within the large experimental uncertainties, a target thickness dependence of the shifts for these Au- or U-K x-ray transitions could not be observed. This may indicate that as the projectile penetrates the solid target, its vacancy distribution does not vary considerably, i.e. the projectile vacancies have a definite probability to survive in the bulk material.

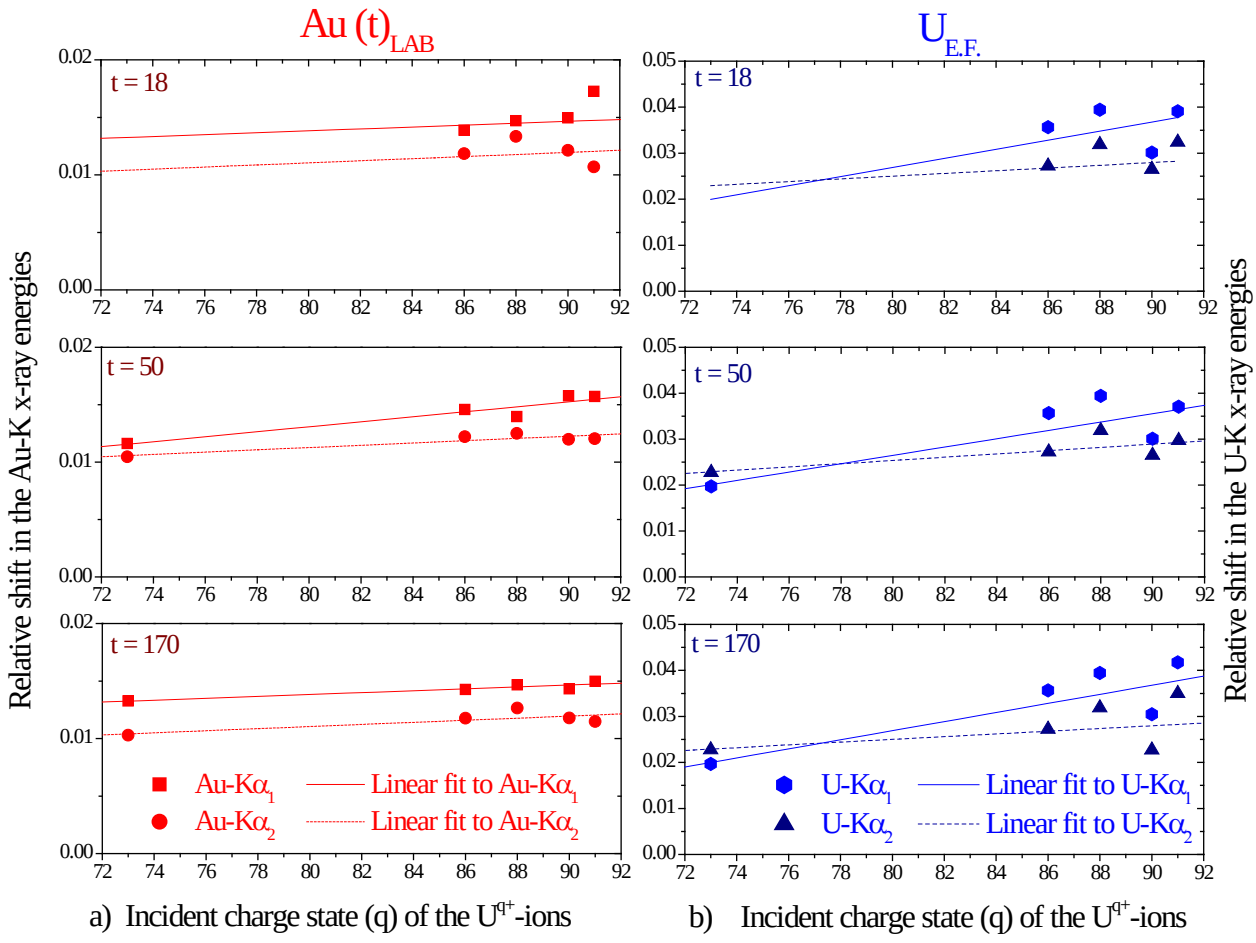

Fig. 4.6 *Relative shift $(E_{obs.}-E_o)/E_o$ in K x-ray transitions (centroids) normalized to standard values (E_o) [23], as a function of the incident charge state (q) of the U^{q+}-ions a) for Au in the laboratory frame (LAB) and b) for U in emitter frame (E.F.). Au target thickness (t) is in $\mu g/cm^2$. Statistical errors are smaller than the size of the symbols. Lines drawn are linear fits to the data. Note the different ordinate scales for a) and b).*

4.3.3. Intensity ratios for K x-rays

During heavy-ion heavy-atom collisions, the simultaneous multiple ionization of many shells of the target atom leads to additional vacancies in their upper shells which modify the relative

intensities of the emitted x-ray transitions such as K and L [62]. It was intended to investigate whether the projectile incident charge state (q) and the target thickness (t) have any effect on the intensity ratios of the K x-ray transitions i.e. $K\alpha_2$ [(L_2-K or $2p_{1/2}\rightarrow 1s_{1/2}$)] and $K\alpha_1$ (L_3-K or $2p_{3/2}\rightarrow 1s_{1/2}$)] of both the collision partners. This ratio reveals the relative population of the $2p_{1/2}$ and $2p_{3/2}$ levels thus revealing the j dependent population of the L-shell. The K x-ray intensity ratios for both U and Au were deduced using the formula given in Section 3.3.5 (ii) of Chapter 3. Taking into account the uncertainties, mainly in the counting statistics and analysis procedure, the overall uncertainties in the experimental intensity ratios are estimated to be between 20-40% for the $K\alpha_1,\alpha_2$ transitions of both U and Au. The intensity ratios for the U- and Au-$K\beta_{1,2}$ transitions were not calculated due to their low intensity and higher statistical errors involved in extracting their yields from the mixed lines shown in Fig. 4.3 and 4.4.

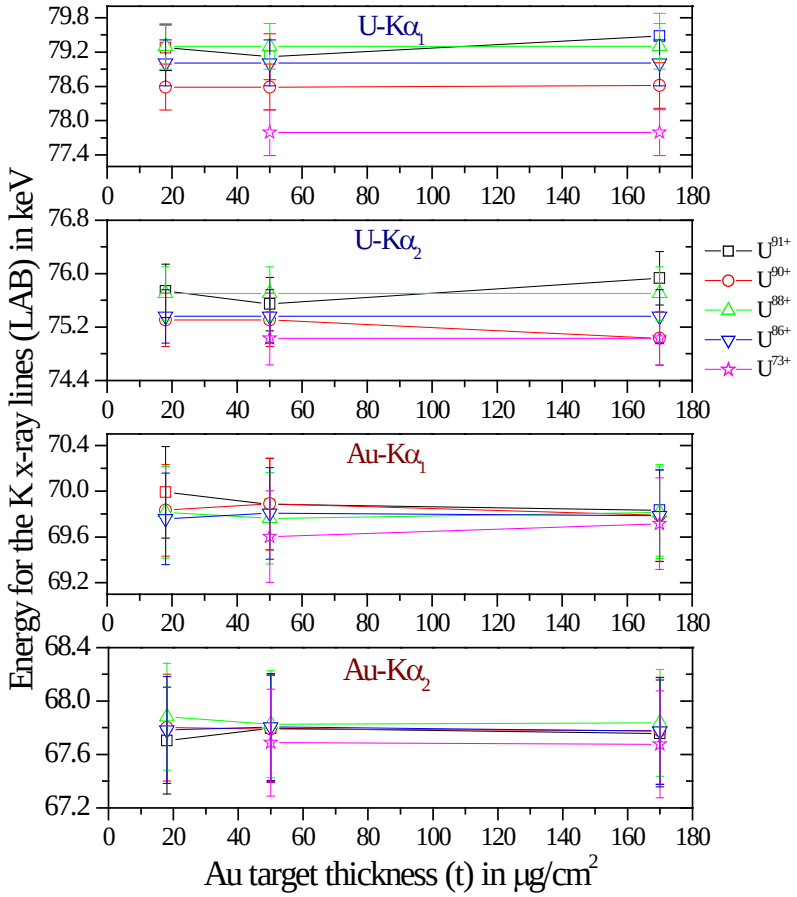

Fig. 4.7 *Centroid energies ($E_{obs.}$) of U- and Au-K x-ray transitions in the laboratory frame (LAB) as a function of the thickness (t) of the Au targets. The lines through the data points are drawn to guide the eye.*

Fig. 4.8 shows a graph of the K x-ray intensity ratios of the projectile (U) and target (Au) as a function of the projectile incident charge state (q) i.e. $K\alpha_2/K\alpha_1$ for both U and Au and for

completeness the U-Kα_1/Au-Kα_1. The figure shows that within the experimental uncertainties one cannot infer any incident charge state (q) dependence of either the U-Kα_2/U-Kα_1 or Au-Kα_2/Au-Kα_1 intensity ratio. Atomic single hole values by Scofield [64] have also been given in the figure for comparison. Scofield values assume single ionization, a comparison obviously depends on the population in both the levels concerned. So more vacancies in the inner shell increases the emission whereas a vacancy increase in the outer shell will lead to a decreased emission. This is relevant especially for comparison of inter-partner ratios (U-Kα_1/Au-Kα_1) at different q.

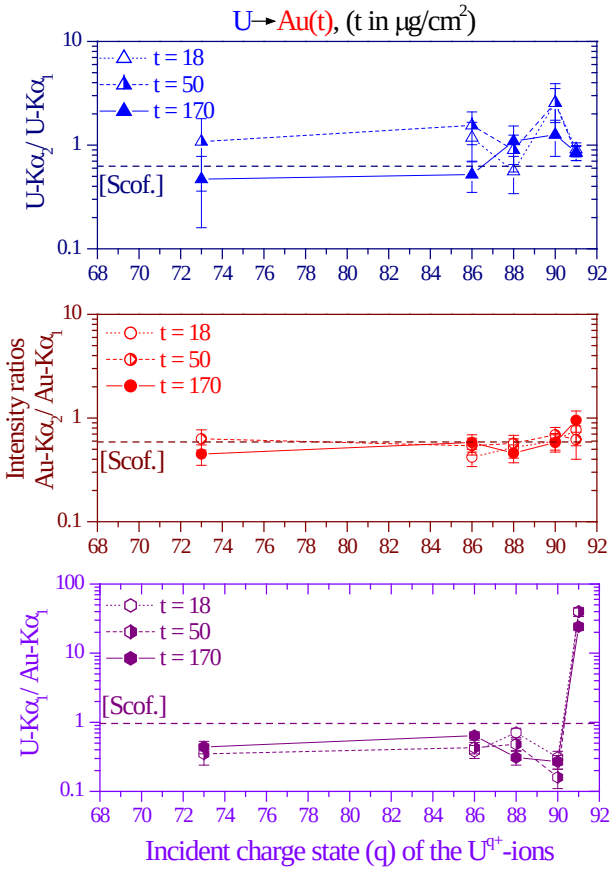

Fig. 4.8 *Measured intensity ratios (intra-partner and inter-partner) for K x-ray transitions of the projectile (U) and target (Au) as a function of the incident charge state (q) of the U^{q+}-ions. The corresponding single hole values by Scofield [64] have been indicated in the figures as [Scof.].*

Table 4.1 presents the average values for intensity ratios in a tabular form for q ≤ 90, corresponding to closed, incoming, projectile K-shell and for q = 91, the open K-shell of the incident U^{q+}-ions. The average has been calculated over all 'q' and 't' investigated. Scofield values [64] have also been given for comparison. For q ≤ 90 and q = 91 the experimental Au-Kα_2/Au-Kα_1 ratio agrees reasonably well with the single hole values of Scofield [64]. The experimental U-Kα_2/U-Kα_1 ratio is quite higher than Scofield's value for q ≤ 90 (almost double) and about 44% higher for q=91 pointing

to a possibility of higher population of the U L_2-subshell in comparison to L_3 or higher ionization of the latter (binding effect)..

Both from Fig. 4.8 as well as from Table 4.1, it is evident that the inter-particle ratio of U-Kα_1/Au-Kα_1 has a near constant value of 0.4 for the closed K-shell case ($q \leq 90$). For these charge states, the population in the $2p_{3/2}$ level of U is probably ~1/3 of that in Au. This indicates again that the projectile remembers its high ionization in outer shells even after interaction. Considering that the Au target is also highly ionized (evident by the line shifts), it can be inferred that the projectile 2p levels have a very small population. This is caused by the relatively large velocity of the projectile compared to the orbital velocity of concern ($\eta_{U\text{-}L} = 1.4$).

Table 4.1 *Average values of U and Au x-ray intensity ratios for closed ($q \leq 90$) and open ($q = 91$) U K-shell in the entrance channel. Atomic single hole values by Scofield [64] have been given for comparison. The experimental inter-partner ratios (1st line) are corrected for the relativistic solid angle transformation.*

Charge state q / Intensity ratio	**q ≤ 90**	**q = 91**	**Scofield [64]**
U-Kα_1 / Au-Kα_1	0.4 ± 0.1	34.6 ± 4.8	0.96
U-Kα_2 / U-Kα_1	1.3 ± 0.5	0.9 ± 0.1	0.625
Au-Kα_2 / Au-Kα_1	0.7 ± 0.1	0.8 ± 0.2	0.588

The ratio of U-Kα_1/Au-Kα_1 increases drastically for an open K-shell of the projectile ($q = 91$) in the entrance channel. This fact is evident from the K x-ray spectra itself shown in Fig. 4.3 and 4.4. The reasons for the increased U-K emission for $q = 91$ has been explained above. A comparison of the observed value (34.6±4.8) with the single hole value of 0.96 for U-Kα_1/Au-Kα_1 indicates the presence of other active processes mainly for U. Here the radiative decay channel to the K-shell for capture processes to higher shells becomes available. Thus this increased ratio gives mainly the probability for having a K vacancy in the projectile or target atom.

Fig. 4.9 shows the U-Kα_1/Au-Kα_1 intensity ratio as a function of the Au target thickness (t). For $q = 73$ to 90 i.e. closed U-K shell in the entrance channel, the ratio does not always show a clear 't' dependence. However for $q = 91$, a decrease in the ratio with increasing target thickness is evident. As the projectile ions pass through the bulk of the solid target, highly charged ions (U^{91+}) capture electrons by multiple collisions which gradually fill up the K-shell vacancies due to the radiative transitions, consequently, the U-Kα_1 emission decreases. After a penetration length of about 190±10 $\mu g/cm^2$ half of the projectiles have lost their initial K vacancy.

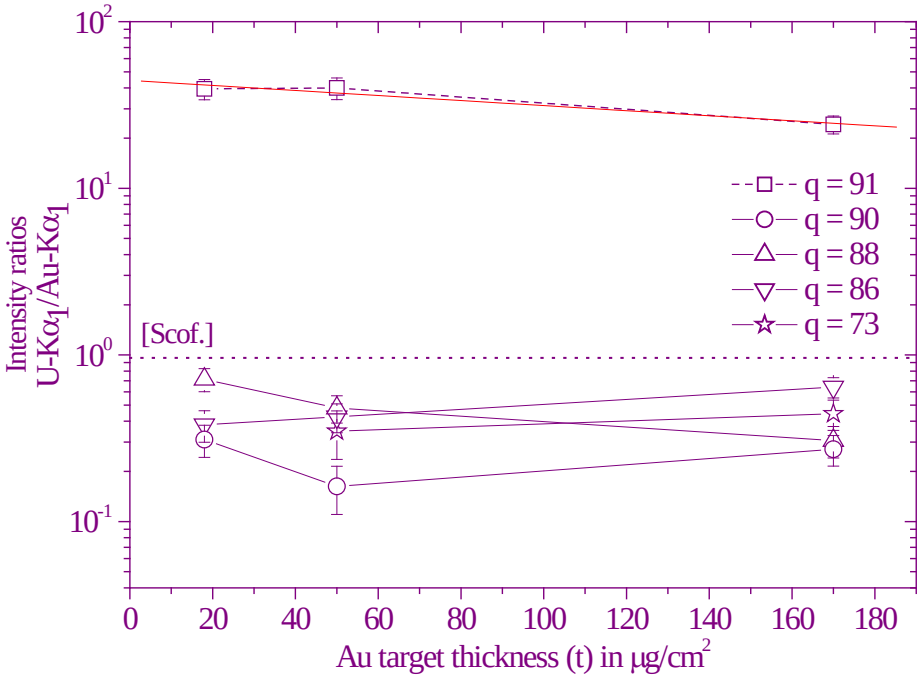

Fig. 4.9 *Measured inter collision partner intensity ratio (U-Kα_1/Au-Kα_1) as a function of the Au target thickness (t). The corresponding single hole values by Scofield [64] have been indicated in the figures as [Scof.].*

4.3.4 K x-ray emission cross sections

The K emission cross sections for both the projectile and target x-rays have been calculated using the formula given in Chapter 3, Section 3.3.5 (iv) and have been extracted by normalizing the measured x-ray yields to the number of ejectiles monitored by the CVD-diamond detector.

Normalization procedure and dead time correction

For this experiment, the CVD-diamond detector had not been placed after the magnet spectrometer and hence no information on charge state distribution of the ejectiles was obtained. All the ejectiles impinged directly on the detector and the particle rate varied between 9.0×10^6 to 1.0×10^8 as measured by the scaler connected to the CVD. 16 stripes out of 32 of the CVD-detector were used in this experiment. The detector had an individual read out for each of the 16 stripes (say b_1- b_{16}) which were later summed up to (say) 'b'. Another signal was recorded which was an "OR" for the 16 stripes (say 'a') and 'b' was found to be higher than 'a'. The percentage difference between the 'b' and 'a' gives an estimation of the double counting/cross-talk involved due to high projectile integral count rates (~10^8 particles/s) and it has been found to vary between 4-20%. Although the CVD-particle detector is believed to have a near 100% efficient counting capabilities at this energy,

however, for these count rates, the double counting phenomenon/cross talk might have lead to an overestimation of the particle count rate.

The beam position on the particle detector was monitored by recording the spectra of particle counts vs detector stripe number. In order to find out whether the beam shifted its position on the target during the measurements, such spectra were recorded in small time windows and compared to each other. It was found that the maxima of the beam spot fell between 5^{th} to 8^{th} stripes. The FWHM of the distribution or the diameter of the beam on the CVD fluctuated between 1.9 and 2.8 stripes i.e. ~4 mm and 6 mm respectively. Hence the use of 16 stripes was found sufficient for measuring the total number of ejectiles.

The dead time of the data acquisition system overpowered that of the individual x-ray detectors in this experiment, the dead time for the latter being not large due to their small solid angles. The ratio of the number of events accepted to the total number of events is given as $\frac{\Sigma N_i}{\Sigma N_i . i}$ where i is the number of channels in the scaler spectra and N_i is the number of counts in the i^{th} channel. Hence the x-ray yields were corrected for the dead time of the acquisition system by multiplying the yields with the reciprocal of the above quantity.

The ion beam intensity had an approximate uncertainty of ~10% as estimated from the particle detector, the efficiency of the Ge(i) detectors ~3%, solid angles ~5% and target thickness ~5%. Apart from these uncertainties, the data acquisition system constrained the efficient counting of the emitted x-rays leading to systematic uncertainties of the order of 30% at maximum. Due to the experimental boundary conditions (varying spill structure) of the ion beam, high systematic errors of a factor of 2 (at an average) had to be taken into account. The K x-ray emission cross sections along with their uncertainties are presented in Fig. 4.10 as a function of the projectile incident charge state (q) and as a function of the Au target thickness (t) in Fig. 4.11.

Charge state dependence of the cross sections

Fig. 4.10 a) shows the q dependence of Au-Kα_1,α_2 emission cross sections for 18, 50 and 170 $\mu g/cm^2$ target thicknesses and Fig. 4.10 b) depicts the same for U-Kα_1,α_2. It is clear from the figure that for projectiles carrying a K vacancy prior to the collision (U^{91+}), the projectile K x-ray emission increases substantially above its value for the closed K-shell (U^{90+}) and a similar trend is shown by the Au-K emission although by an order of magnitude to a lesser extent.

During distant collisions for highly charged projectiles (i.e. when the inner shells of the two collision partners do not overlap each other), the electrons are captured from the target to the higher

vacant shells of the projectile. For projectiles having K vacancies prior to the collision (U^{91+}) radiative stabilization of the captured electrons to the half empty K-shell leads to the observed increase in the U-K x-ray emission. A capture cross section of an order of a megabarn has been observed for these projectiles (typical electron capture interaction distance is estimated later in Chapter 6).

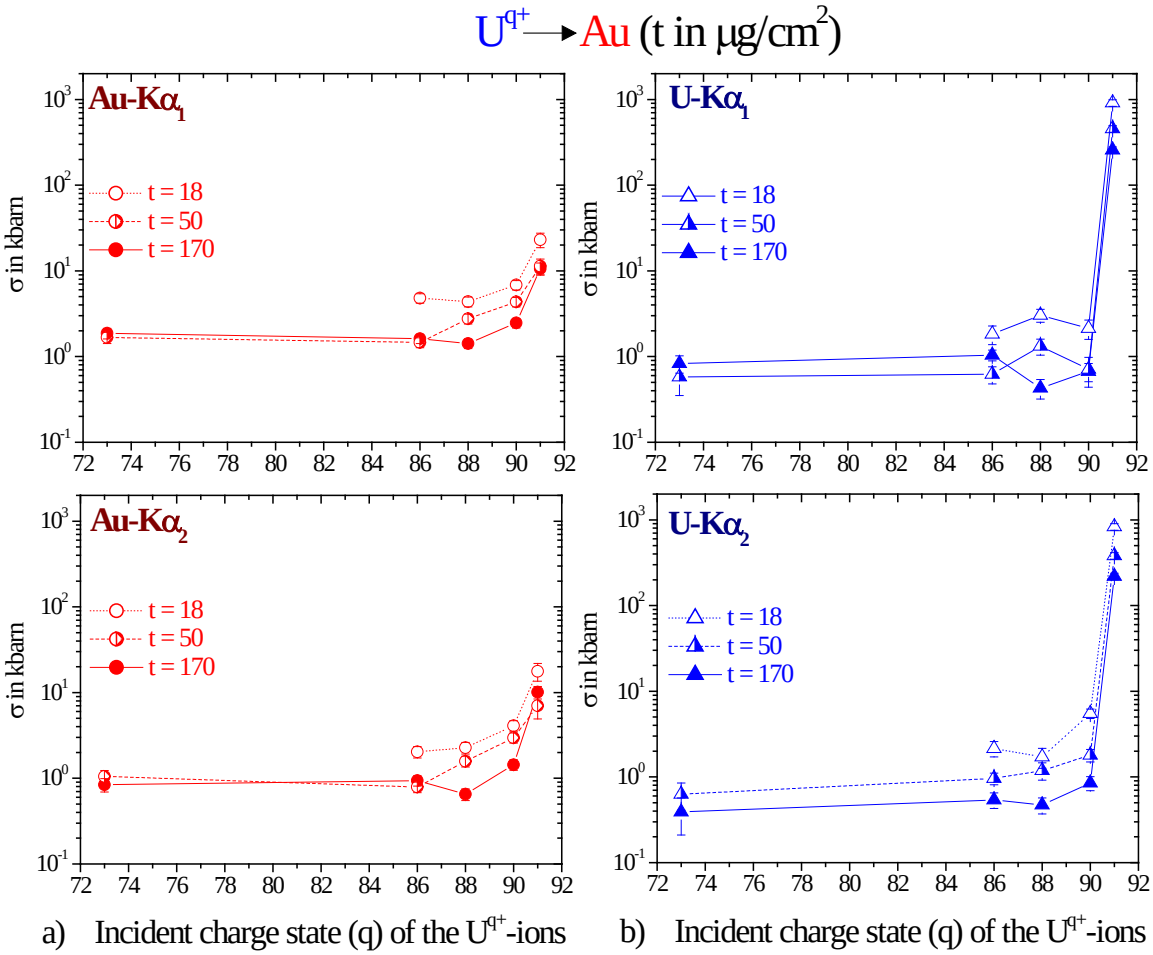

Fig. 4.10 *$K\alpha_1$ and $K\alpha_2$ emission cross sections (top and bottom respectively) as a function of incident charge state (q) of the U^{q+}-ions* a) *for the target Au,* b) *for the projectile U. Au target thickness (t) is in $\mu g/cm^2$.*

The increase in the Au-K emission (of the order of 10 kbarns) gives access to the vacancy transfer in the collision molecule i.e. in close collisions. For H-like projectiles (U^{91+}), the increase in Au-K x-ray emission cross section relative to its value for q=90 points to an additional vacancy production mechanism such as coupling of K-shells of both the collision partners (the K-K sharing process [92]). For projectiles with incoming L(j=1/2) vacancies (e.g. U^{90+}), a slight increase in the Au-K emission might also be observed for U^{90+} in comparison to its value for U^{88+}. This slight increase indicates the possibility of a coupling between the L-shell of the projectile and the K-shell of the target atom in close collisions, the so called L-K shell coupling [93]. The cross sections stay nearly constant for lower incident charge states (ranging from 73+ to 86+). The above features are exhibited

for the entire range of target thicknesses investigated. Further discussion and inferences from the 'q' dependence of the cross sections and calculation of interaction distances for K-K sharing and L-K shell coupling are given in Chapter 6.

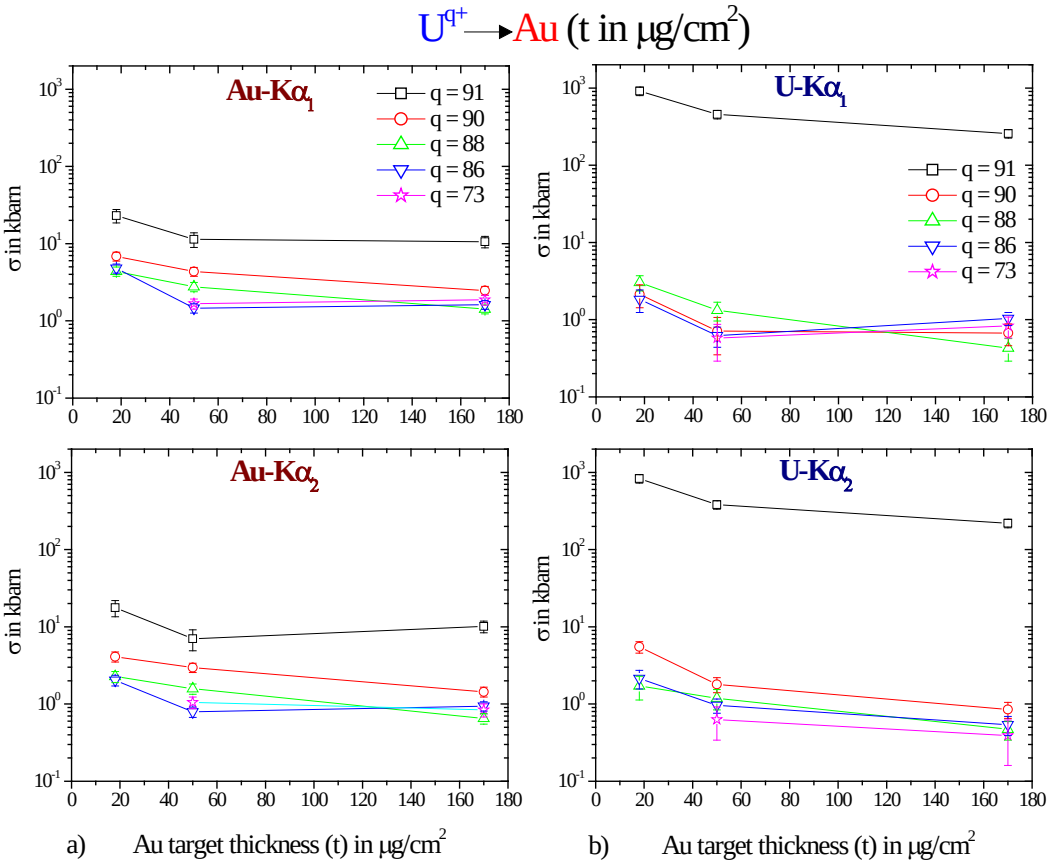

Fig. 4.11 *Kα₁ and Kα₂ x-ray yields (cross sections) top and bottom respectively, as a function of the target thickness (t)* a) *for the target Au,* b) *for the projectile U.*

Target thickness dependence of the cross sections

The target thickness (t) dependence of the Au-Kα_{1,α_2} and U-Kα_{1,α_2} emission cross sections are presented in Fig. 4.11 a) and b) respectively. The figure shows clearly that as the target thickness increases, the U-Kα_{1,α_2} emission cross sections show a pronounced decrease; to some extent a similar trend may be seen for the Au-K cross sections also. Since a true cross section does not depend on target thickness the cross sections shown here are actually absolute yields and the true cross section can be calculated by extrapolating these values to zero target thickness, i.e. to approximate cross sections at single collision conditions. It is observed that within the given large uncertainties, the decrease in yield is remarkable for q = 91 as compared to the other incident charge states of the projectile (q = 73 to 90).

From the target thickness dependence of the absolute yields, cross sections corresponding to "zero" target thickness have been extrapolated. This has been done by assuming an exponential decrease of the K x-ray cross sections approaching ultimately the values corresponding (approximately) to those for the equilibrium charge state of the projectile (e.g. to a few kb for U-K$\alpha_{1,}$ see Fig. 4.11 b). More details regarding the cross sections for near "zero" target thicknesses along with their significance for the present investigation are discussed in Chapter 6. For the projectile having an open K-shell (q = 91), the decrease in the U-K emission indicates the filling up of vacancies as the projectile penetrates the solid. From a rough exponential fit we may deduce that after a penetration length of about 95±10 μg/cm^2 half of the ions have lost their initial K vacancy. Due to the large systematic uncertainties in absolute cross sections this value is still in acceptable agreement with the half thickness (190±10 μg/cm^2) extracted from the intensity ratios above. Moreover, a slight decrease is observed also for the Au-K x-rays probably due to the K-K vacancy sharing.

4.4 L X-RAY EMISSION IN U^{q+} - Au COLLISIONS

4.4.1 The L x-ray spectra

The L x-ray spectra from the collision partners U and Au were recorded by the Si(Li) detector and both the Ge(i) detectors "A" and "B" (refer Fig. 4.2 and Section 4.2). The spectra were analysed mainly by the Si(Li) detector placed at 135° (off plane) with respect to beam direction for the reasons mentioned in Chapter 3, Section 3.3. Fig. 4.12 shows the L x-ray spectra recorded by the Ge(i) "A" detector for U^{86+}-ions incident on Au targets of various thicknesses (t = 18, 50 and 170 μg/cm^2). The top most spectra has to be compared with the corresponding one in Fig. 4.13 for U^{86+}-ions incident on 170 μg/cm^2 Au target recorded by the Si(Li) detector. A comparison of these two spectra reveals the advantages of the Si(Li) detector's resolution over the Ge(i). The U-Lα_1 line visible separately in the Si(Li) spectra is merged with the Au-Lβ_1 line in the Ge(i) spectra. Due to the different observation angles, 135° for Si(Li) (off-plane) and 120° for Ge(i) (in-plane), the projectile x-ray lines are observed with different Doppler shifts and hence different energies in the two spectra. The L x-ray spectra are interpreted with respect to both the incident charge state (q) effect as well as the target thickness (t) effect on the spectra.

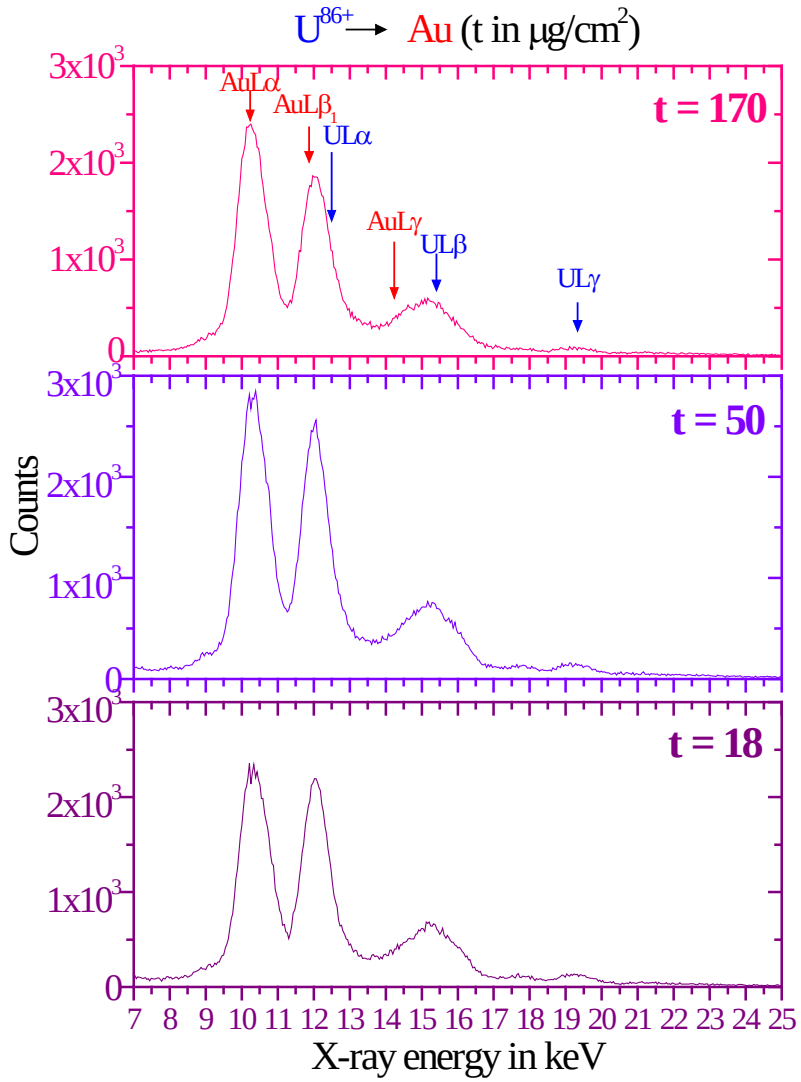

Fig. 4.12 *The L x-ray spectra for U^{86+}-ions incident on Au targets of various thicknesses (t = 18, 50 and 170 μg/cm^2) recorded by the "A" Ge(i) detector positioned in-plane at 120°. The characteristic lines for both U and Au are marked.*

4.4.2 Shift in the energy of the L x-ray transitions

Effect of the projectile incident charge state (q)

Fig. 4.13 shows the L x-ray spectra recorded for the thickest Au target (170 μg/cm^2) for all the incident charge states (q) of the U^{q+}-ion beam viz. (q = 73, 86, 88, 90 & 91). Although the standard energy values [23] of both Au and U are such that only the Au-Lγ lines would overlap with the U-Lα lines, however due to the backward observation angle of 135° for Si(Li), the U-L x-ray spectra almost completely overlap the Au-L x-ray spectra.

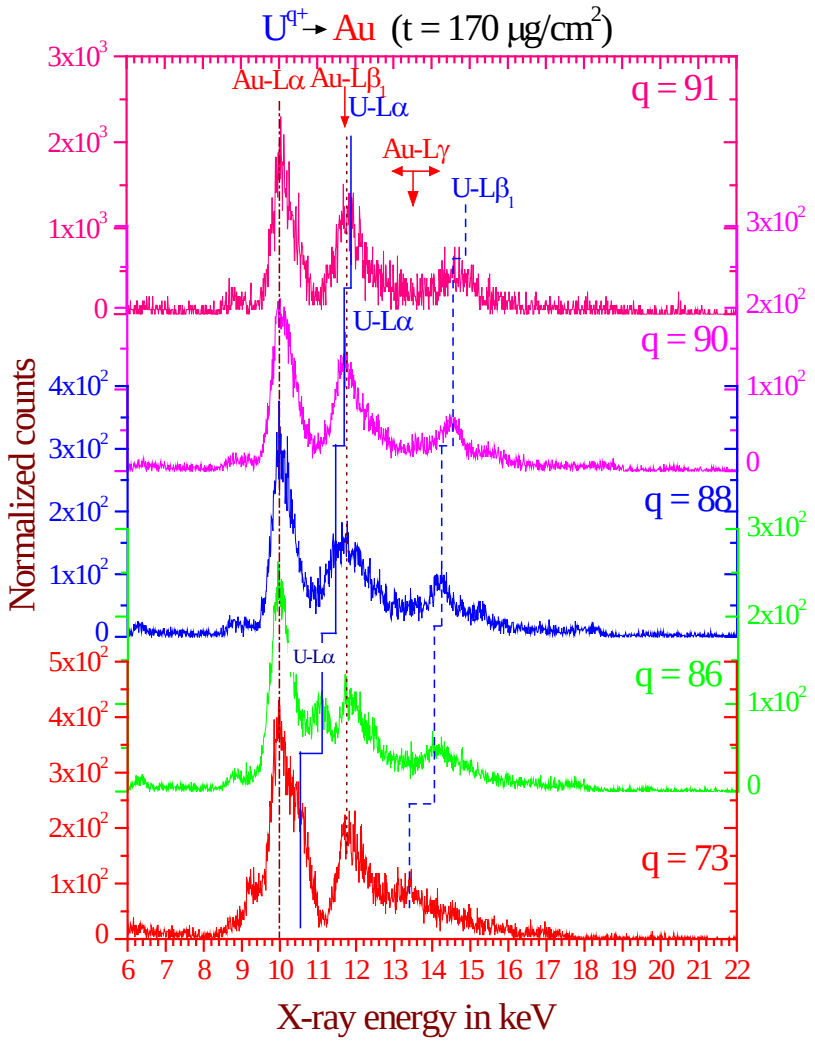

Fig. 4.13 *A comparison of L x-ray spectra for U^{q+}-ions (q = 73, 86, 88, 90, 91) incident on the thickest Au target (170 μg/cm²) recorded with the Si(Li) detector. The solid and the dashed lines indicate the shift of the U-Lα and U-Lβ$_1$ lines towards higher energies. The dash-dot and the dotted lines show the near constant energy of Au-Lα and Au-Lβ$_1$ lines respectively. (The scale for normalized counts corresponding to q = 86 and 90 are indicated on the right). The counts are normalized relative to the number of ejectiles.*

The influence of q on the L x-ray spectra is evident from Fig. 4.13. As q increases from 73 to 91, a line which first appears merged with the Au-Lα line as a hump on the right side for q = 73, shifts progressively to higher energy values (shift being indicated by the solid line). This line is visible individually, only in the spectra corresponding to q = 86. Probably only a x-ray line corresponding to the projectile can shift to higher energies as q increases and this line has been identified as the U-Lα. The distortion of the Au-L x-ray spectra due to the progressive shift of the U-L x-ray lines towards higher energies is evident from the spectra. The Au-L x-rays do not show a pronounced shift towards higher energies with the increase in the charge state as is evident by looking at the dash-dot and dotted

lines passing through Au-Lα, $L\beta_1$ respectively as compared to U-L x-ray lines. The strong increase in the centroid energy of the U-L x-ray transitions with increasing q, indicate the presence of increased number of projectile vacancies in L shell itself and partially in higher shells too.

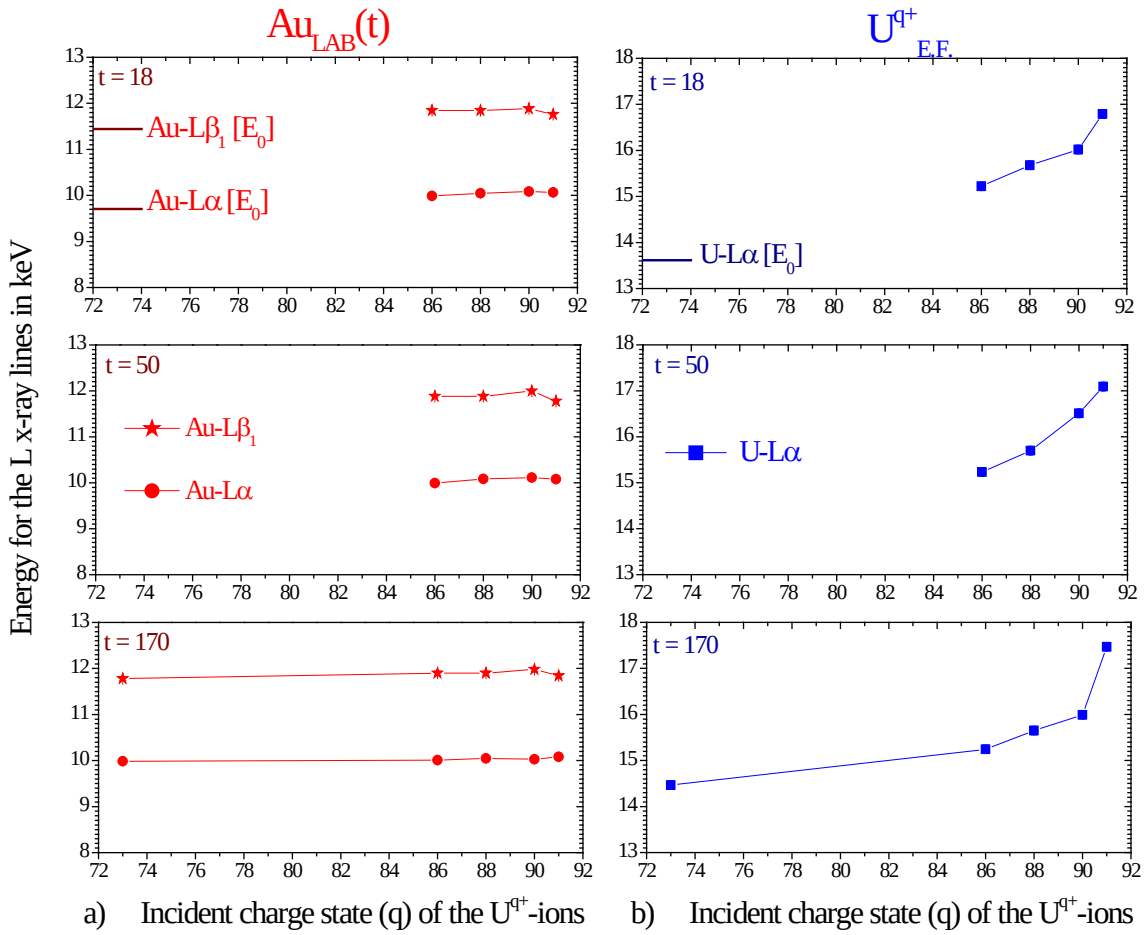

Fig. 4.14 *Centroid energies ($E_{obs.}$) of L x-ray transitions as a function of the incident charge state (q) of the U^{q+}-ions, a) for Au-Lα,β_1 in the laboratory frame (LAB) and b) for U-Lα in the emitter frame (E.F.). The corresponding standard values of Bearden (E_o) [23] have been indicated by solid lines in the uppermost plot. Au target thickness (t) is in $\mu g/cm^2$. The lines through the data points are drawn to guide the eye. Statistical errors are smaller than the size of the symbols.*

The centroid energies of Au-Lα,β_1 x-ray transitions in the laboratory frame (LAB) and of U-Lα in the emitter frame (E.F.) as a function of the incident charge state (q) have been shown in Fig. 4.14 a) and b) respectively. The energies have been plotted for all the three Au target thicknesses investigated (18, 50, 170 $\mu g/cm^2$). The standard values E_o [23] for the energies of these x-ray transitions have been indicated by solid lines in the plot corresponding to 18 $\mu g/cm^2$ Au target. The systematic errors in U-Lα energies are larger than the ones for Au-Lα due to the uncertainty in the detector's observation angle.

As has also been observed for the K x-rays, the Au-Lα, $L\beta_1$ are observed at higher energies with respect to standard values confirming multiple ionization. The same is also true for U-Lα, however the shifts are larger due to the presence of projectile L vacancies. As shown already in Fig. 4.14, the centroid positions of U-L x-rays show appreciable q dependence, increasing with increase in q.

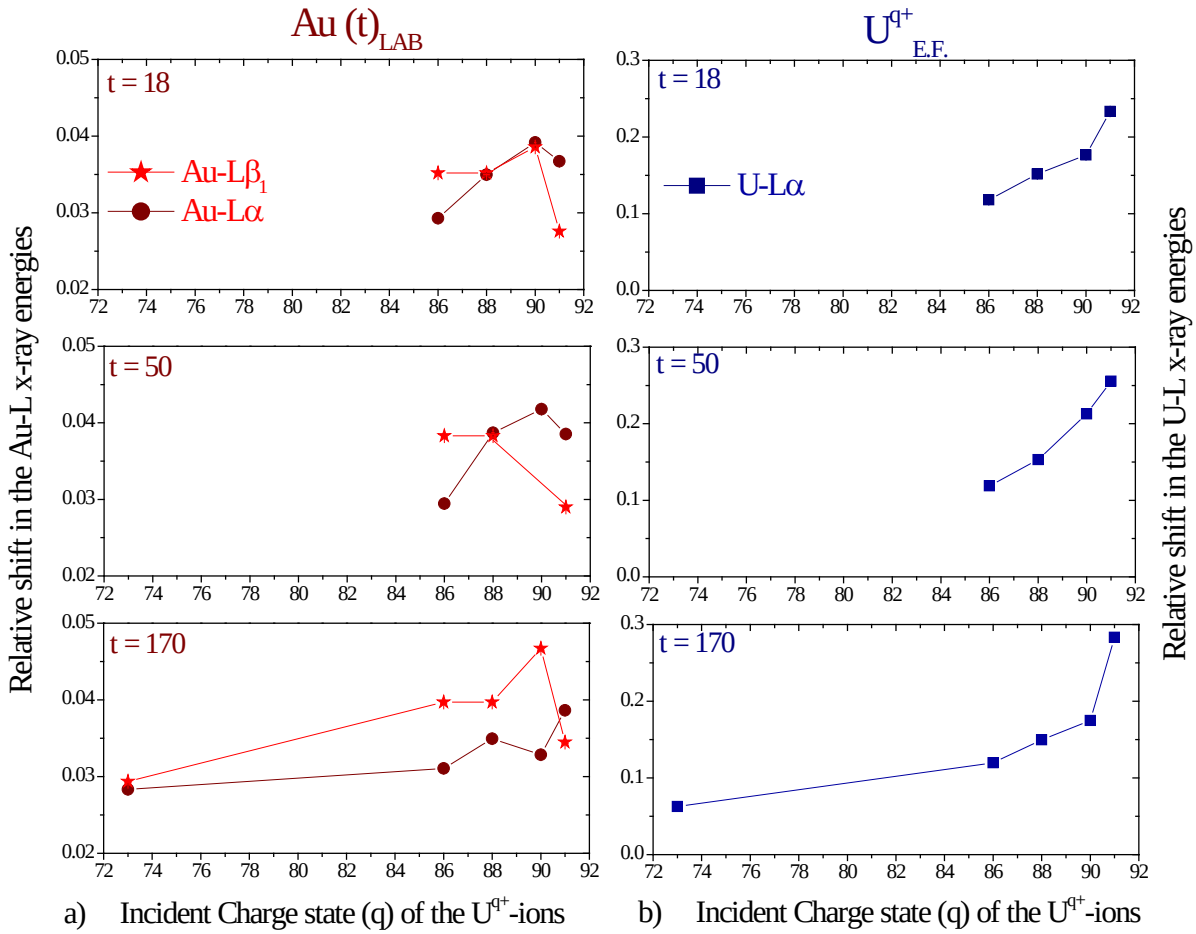

Fig. 4.15 *Relative shift* $(E_{obs.}-E_o)/E_o$ *in L x-ray transitions (centroids) with respect to and normalized to standard values* (E_o) *[23] as a function of the incident charge state (q) of the* U^{q+}*-ions,* a) *for Au-*$L\alpha,\beta_1$ *in the laboratory frame (LAB) and* b) *for U-*$L\alpha$ *in the emitter frame (E.F.). Au target thickness (t) is in* $\mu g/cm^2$*. Statistical errors are smaller than the size of the symbols. Lines are drawn to guide the eye. Note the drastically different scales for the Au and U.*

The relative shift $(E_{obs.}-E_o)/E_o$ with respect to and normalized to standard values (E_o) in the centroids of Au and U-L x-ray lines are shown respectively in Fig. 4.15 a) and b) as a function of the incident charge state q for all Au target thicknesses investigated. It can be observed that the relative shifts for U are appreciably stronger than that for Au. As mentioned in Section 4.3.1, the Eikonal approximation [53] predicts that the cross section for capture from the Au-L shell to the U-M shell is maximum. The excitation and/or ionization of the target L-shell along with the capture of its electrons

to the outer shells of the projectile is probably one of the reasons for the production of the vacancies in the target L-shell. Due to fast electron rearrangement in the outer shells of the target atom, multiple ionization is less pronounced as compared to that in the outer shells of the fast projectile. Hence for the target (Au), the centroid positions are less affected by the presence of vacancies in the projectile in the incoming channel of the collision.

It is observed that the L x-ray intensity for U is comparatively □ very less intense U-Au, possibly it also indicates that electrons captured to the M and N shells of U are probably reionized quickly leading to fewer transitions to the L shell. The higher shifts observed for the projectile are caused by its higher ionization which survives the collision partially. For an incoming K vacancy, a further drastic increase in the shifts is observed due to the change in inner shell screening.

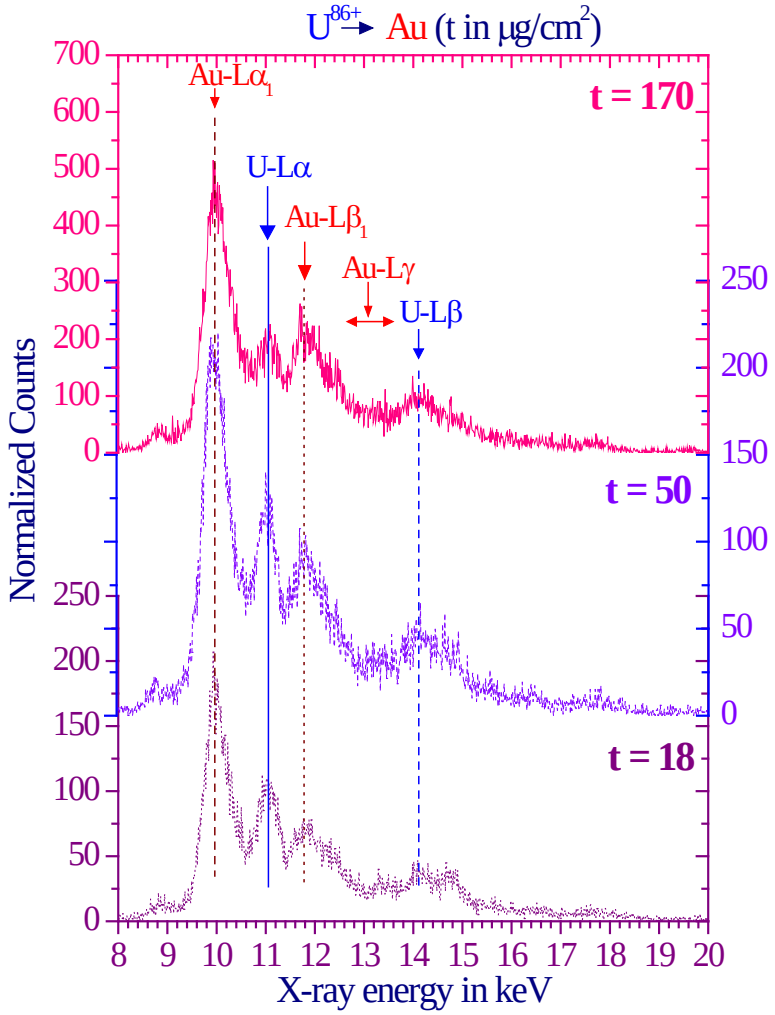

Fig. 4.16 a) *A comparison of L x-ray spectra depicting the centroid positions of x-ray transitions with increasing Au target thicknesses (t = 18, 50 and 170 μg/cm^2) for U^{86+}-ions, The counts are normalized relative to the number of ejectiles. The scale for normalized counts corresponding to t = 50 is indicated on the right axis. As in Fig. 4.13, the solid and the dashed lines indicate the positions of the U-Lα and U-Lβ$_1$ lines respectively. Those for Au-Lα and Au-Lβ$_1$ lines are indicated by dash-dot and dotted lines respectively.*

Effect of the target thickness (t)

Fig. 4.16 a) and b) depict the L x-ray spectra of U^{86+}- and U^{91+}-ions incident on Au targets (for all the different thicknesses investigated) respectively. The spectra do not display a pronounced shift in the centroid energies of the intense lines such as either the Au-Lα or the U-Lα. The solid and the dashed lines indicate the positions of the U-Lα and U-$Lβ_1$ lines respectively. Those for Au-Lα and Au-$Lβ_1$ lines are indicated by dash-dot and dotted lines respectively. Any possible dependences on the target thickness cannot be inferred from the spectra.

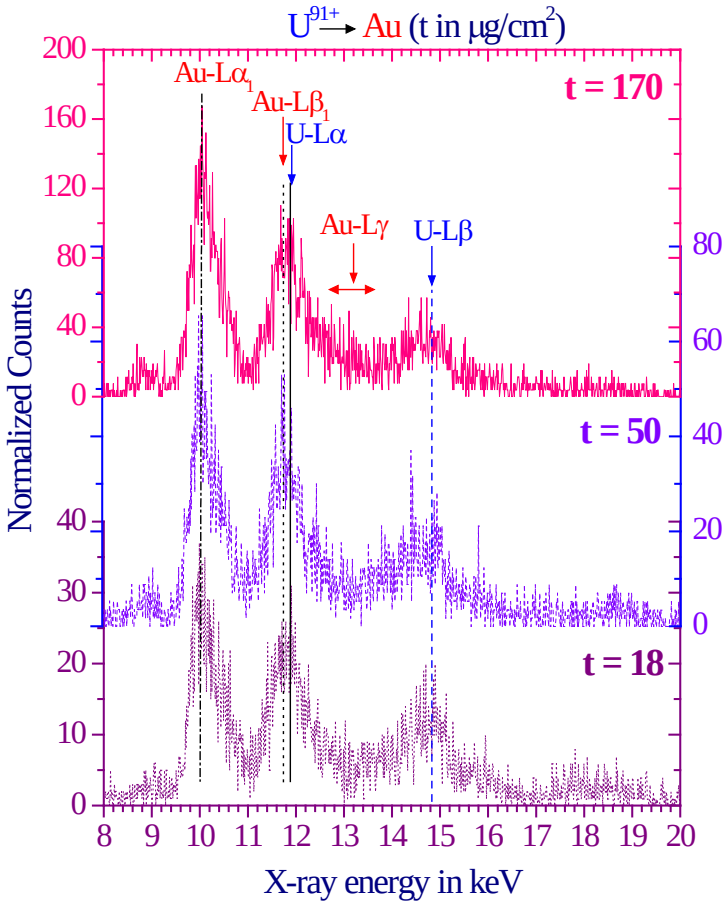

Fig. 4.16 b) *Same as Fig.4.16 a) but for U^{91+}-ions.*

Fig. 4.17 shows the centroid energies of Au-Lα,$β_1$ in the laboratory (LAB) frame and U-Lα in the emitter frame (E.F.) as a function of 't' the target thickness. Within the large uncertainties the Au-Lα,$β_1$ do not indicate any 't' dependence in their energies and so do U-Lα. This observation is similar to that for target thickness dependence of K x-ray transitions (Section 4.3.2, Fig. 4.7). Fig. 4.18 depicts the relative shifts in the centroid energies of Au-Lα,$β_1$ and U-Lα as a function of 't' and the observations of Fig. 4.17 are reiterated here. Systematic errors (less than 10%) are not shown in the above figures.

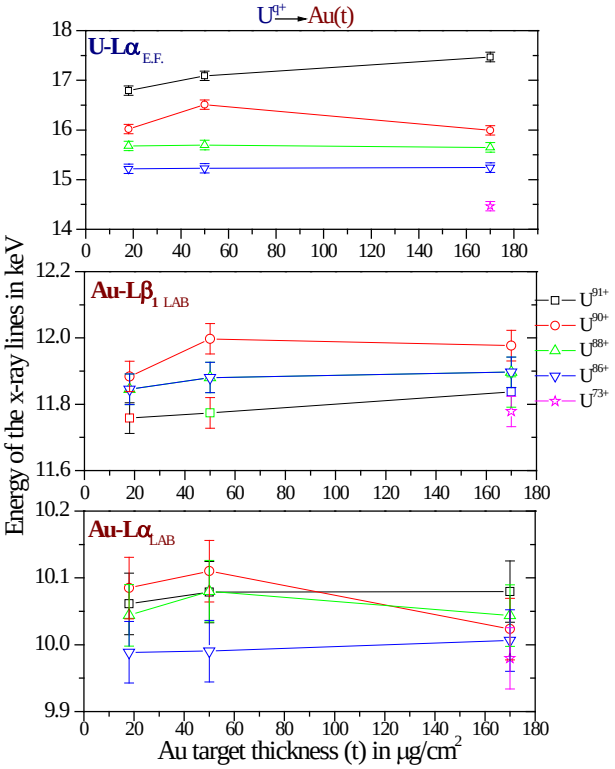

Fig. 4.17 *Centroid energies ($E_{obs.}$) of Au-L x-ray transitions in the laboratory frame (LAB) and of U-Lα in the emitter frame (E.F.) as a function of the Au target thickness (t). Lines through the data points are drawn to guide the eye. Systematic errors (<10%) are not shown here.*

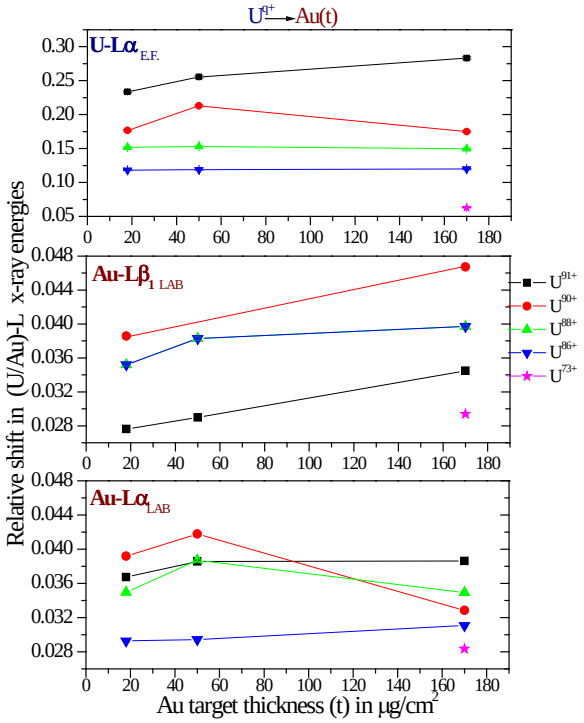

Fig. 4.18 *Relative shift ($E_{obs.}$-E_o)/E_o in L x-ray transitions (centroids) with respect to and normalized to standard values (E_o) [23] as a function of Au target thickness (t) for Au-Lα,β_1 in the laboratory frame (LAB) and for U-Lα in the emitter frame (E.F.). Statistical errors are smaller than the size of the symbols. Main uncertainties are due to systematic errors (<10%, not shown here). Lines are drawn to guide the eye. Note the different scales for U-Lα and that for Au-Lα,β_1.*

4.4.3 Intensity ratios for L x-rays

The utility of x-ray line intensities ratios in investigating the relative population of the levels from where they originate has been discussed in the Section 4.3.3 for the K x-ray transitions of the collision partners. Following the formula given in Section 3.3.5 (ii) of Chapter 3 the L x-ray intensity ratios of U and Au have been deduced from the spectra for the higher intensity lines only such as $L\alpha,\beta_1$ for Au and $L\alpha$ for U. Fig. 4.19 shows the projectile incident charge state (q) dependence of the intra-partner and inter-partner intensity ratios viz. Au-$L\alpha$/Au-$L\beta_1$, U-$L\alpha$/Au-$L\alpha$ for all the target thicknesses investigated. The corresponding single hole values by Scofield [64] have also been indicated the figure as [Scof.]. The former ratio has a higher value and the latter a lower value compared to the single hole values.

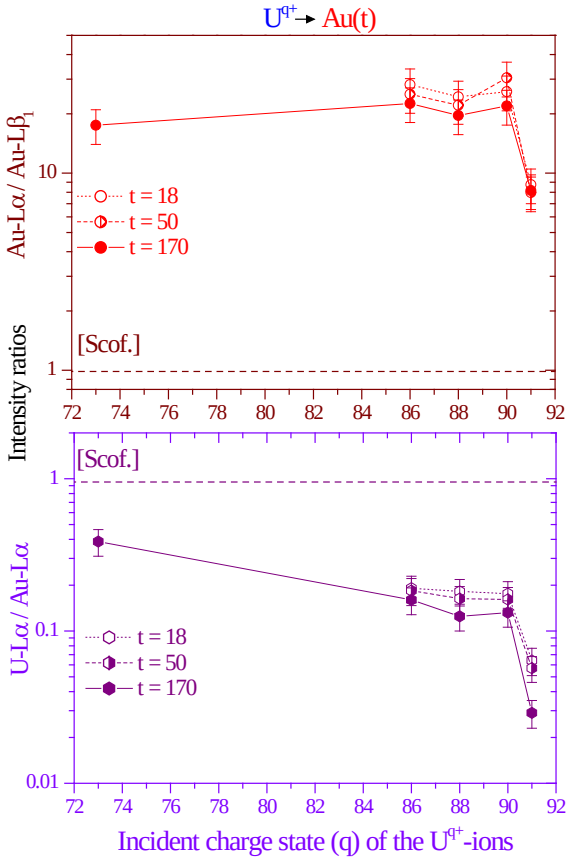

Fig. 4.19 *Measured intensity ratios (intra partner and inter-partner) for L x-ray transitions of the projectile (U) and target (Au) as a function of the projectile incident charge state (q). The corresponding single hole values by Scofield [64] have been indicated in the figures as [Scof.]. Lines through the data points are drawn to guide the eye.*

Within the experimental uncertainties Au-$L\alpha$/Au-$L\beta_1$ do not show any q dependence for the closed K-shell case ($q \leq 90$). However for the open K-shell ($q = 91$) the ratios decreases implying a

preference of M_4-L_2 transition ($L\beta_1$) over $M_{4,5}$-L_3 ($L\alpha$) transition. This further indicates a preference of L_2-K transition ($K\alpha_2$) over L_3-K transition ($K\alpha_1$) which has been indeed found to be the case (see Fig. 4.8). The loss from Au L-shell is probably more from the L_3 subshell than the L_2 subshell in the latter case. Compared to the neutral atom case (Scofield values) L_3 vacancy production seem to be a lot more efficient than the L_2 one.

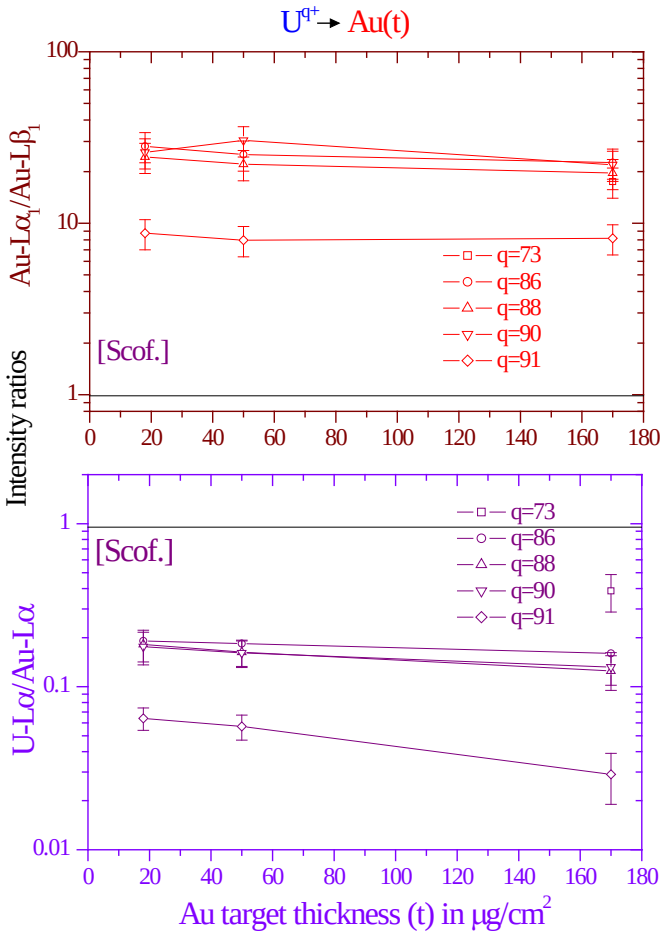

Fig. 4.20 *Measured intensity ratios (intra partner and inter-partner) for L x-ray transitions of the projectile (U) and target (Au) as a function of the target thickness (t) in μg/cm². The corresponding single hole values by Scofield [64] have been indicated in the figures as [Scof.]. Lines through the data points are drawn to guide the eye.*

Fig. 4.20 shows the above mentioned intensity ratios of Fig. 4.19 as a function of target thickness. Both the intra-partner or inter-partner intensity ratios show no explicit 't' dependence except for U-Lα/Au-Lα for q=91, an observation similar to the one for the K x-ray intensity ratios (see Fig. 4.9). For q=91 a slight decrease is observed in this ratio with increasing 't'. As 't' increases there is a gradual filling up of U-L shell vacancies leading to decreased U-Lα emission. However considering the data for lower projectile charge states further investigations need to be performed. It is

indeed interesting to note that after about 200 μg/cm^2, half of the projectiles have changed their relevant electron/vacancy distribution.

4.4.4 L x-ray emission cross sections

The L x-ray emission cross sections have been calculated from the measured L x-ray yields, efficiency of the Si(Li) corresponding to the L x-ray line energies, its solid angle and the solid angle transformation required for the projectile x-rays, known target thicknesses, number of normalizing ejectiles measured by the particle detector and the dead time correction required for the Si(Li) and the data acquisition system. The formula used was the one discussed in Section 3.3.5 (iv), Chapter 3. As has been noted by Fig. 4.13 and 4.16 the U-L x-ray spectra are almost completely overlapped by the Au-L x-ray spectra. Hence emission cross sections for only Au-Lα and U-Lα can be calculated with reasonable uncertainties although the entire spectrum was deconvoluted into U- and Au-L x-ray lines.

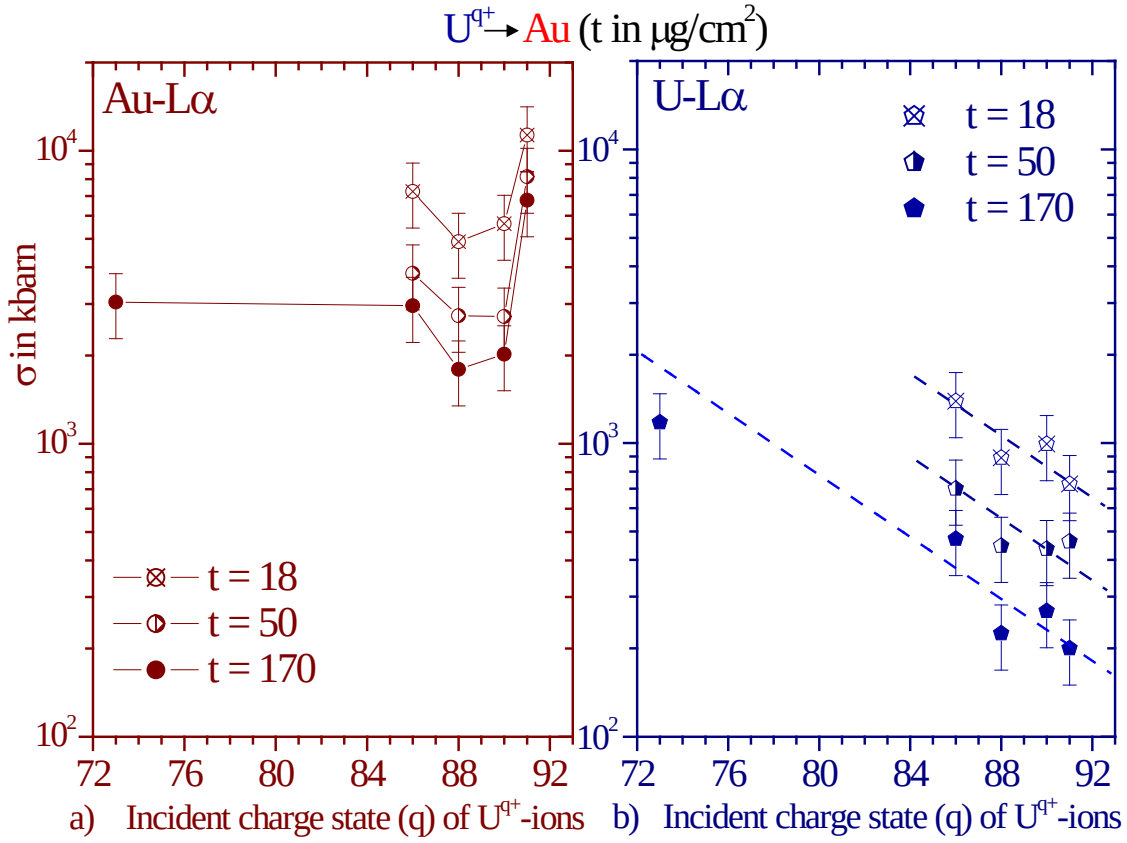

Fig. 4.21 *Lα x-ray emission cross sections of Au (part a) and U (part b) as a function of incident charge state (q) of the U^{q+}-ions for all target thicknesses (t, in μg/cm^2) investigated. Lines are drawn through the Au data points to guide the eye, for U data for t=170 has been fitted linearly to show the decrease of cross sections.*

Fig. 4.21 a) and b) shows the x-ray emission cross sections of Au- and U-Lα as a function of the incident charge state (q) respectively. The data has been plotted for all the target thicknesses investigated. One can observe a slight increase in the Au-Lα for q=91, as compared to its value for q = 86, 88 and 90. For t=170 μg/cm^2, one may observe that Au-Lα shows a slight decrease with increasing q, increasing again for an open U-K shell. On the other hand U-Lα cross sections display a definite q dependence, decreasing with the increase in q. Presently, the decrease is difficult to explain. However looking at the comparable cross sections for U and Au, electron capture seems to be a dominant process especially from Au-L to U-M shell leading to L x-ray emission in both the partners. The extent to which the matching of the K- and L-shells changes and hence the cross sections has to be investigated further. Moreover, an excitation of available projectile L electrons to higher shells in distant collisions may contribute to the U-L emission and its decrease with increasing initial charge state.

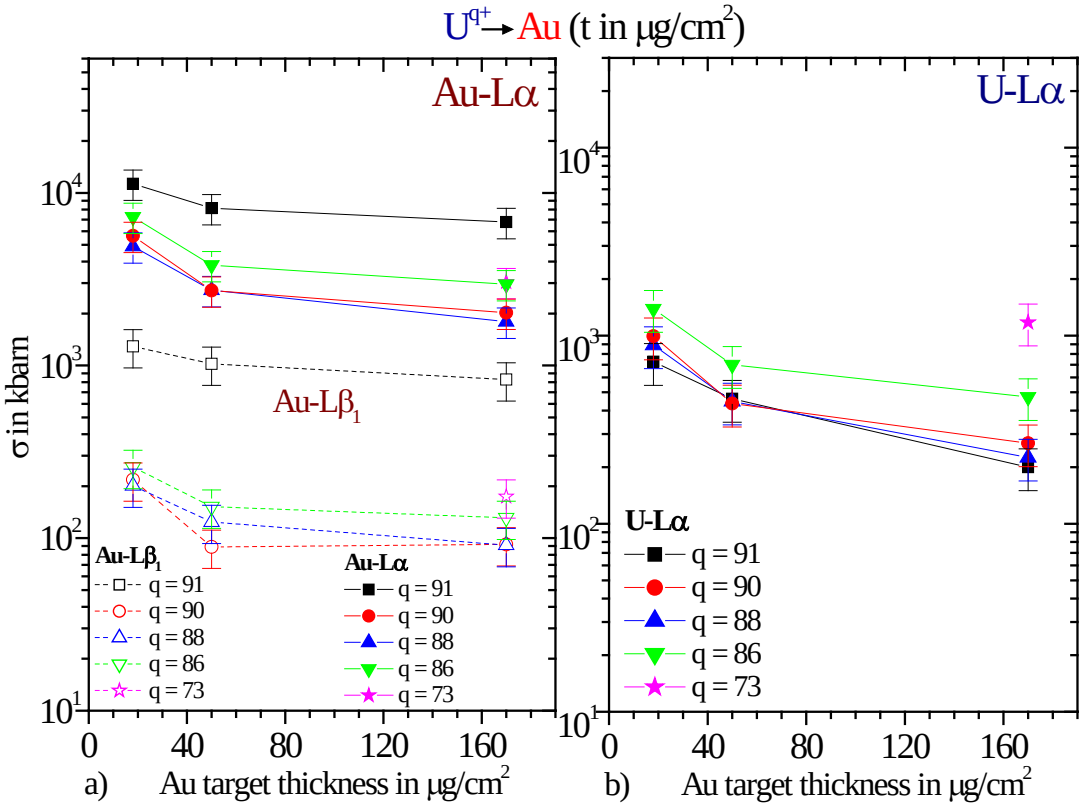

Fig. 4.22 *Lα and Lβ$_1$ x-ray yields (cross sections) of Au (part a) and U (part b) as a function of target thickness (t) corresponding to q = 73, 86, 88, 90 and 91. Lines through the data points are drawn to guide the eye.*

Fig. 4.22 depicts the x-ray cross sections of Au-Lα,β$_1$ and U-Lα in part a and b respectively, as a function of the Au target thickness (t) corresponding to all the charge states investigated. Both

Au-Lα,β_1 and U-Lα show a decrease in the yield with increasing target thickness. A comparison of Fig. 4.22 with that of Fig. 4.11 (for K x-ray transitions) may indicate that both K and L x-rays show to some extent a similar trend for initially closed K-shell projectiles; however, the thickness dependence is stronger for the L x-ray emission. The reasons for this observation are not fully understood, and the effect has to be investigated further in the future, the self absorption in the target may play a role here. Here, additionally solid state effects as e.g. surface effects or the built up of wakes in the bulk may contribute (see e.g. [94]). However, this part is not important for our main goal, the study of quasimolecular inner shell processes.

4.5 CHARGE EXCHANGE CROSS SECTIONS

The process of electron capture has been discussed in Chapter 2. Since a charge state distribution was not measured, the charge exchange cross sections could only be calculated either by using model approximations or deduced from the projectile x-ray emission cross sections for projectiles having incoming K vacancies. During distant collisions, the U^{91+}-ions (incoming projectile K-vacancy) capture electrons in the outer shells. Fig. 4.23 gives a graph of electron capture cross sections deduced from x-ray emission cross sections, by the Eikonal approximation of Eichler [53] and the semi-empirical, non-relativistic, scaling prescription for non radiative capture (NRC) by Schlachter *et al*. [50].

The curves indicate the distribution of cross sections corresponding to electron capture from the different Au-shells (K, L, M and N) to various empty U-shells (K to T). The total of σ_{cap} from Au shells (K to N) to a particular U-n^{th} shell (K to T, to be read from abscissa) is also depicted ((#) thick solid line). A total of cross sections from a Au-n^{th} shell (K, L, M and N to be read from top axis) to U K to T shells has been also shown ((*) thin solid line). It can be observed that the probability of capture is maximum from the Au L- and M-shells. This suggests that electrons are preferentially captured to the M- and N-shells of U with a maximum for the U-M shell. Values for total electron capture cross section according to the semi-empirical, non-relativistic scaling prescription for non radiative capture (NRC) by Schlachter *et al.* [50] have also been included for U^{q+} (q = 86 to 91) and they do not vary much with q. Values of σ_{cap}^{L} and σ_{cap}^{M} deduced from x-ray emission cross sections are indicated in the figure along with σ_{cap}^{Tot}. The K emission cross sections for open incoming K-shell (q = 91) corresponding to "zero" target thickness were used for determining the σ_{cap}^{Tot}. This corresponds to the sum of all U-K x-ray cross sections extrapolated to the value corresponding to a

single collision i.e. “zero” target thickness (details below). For closed incoming projectile K-shell (q=73 to 90), the measured U-L x-ray emission cross sections provide an estimate of the capture into U M-shells (for higher lines into N, .. , .. shells).

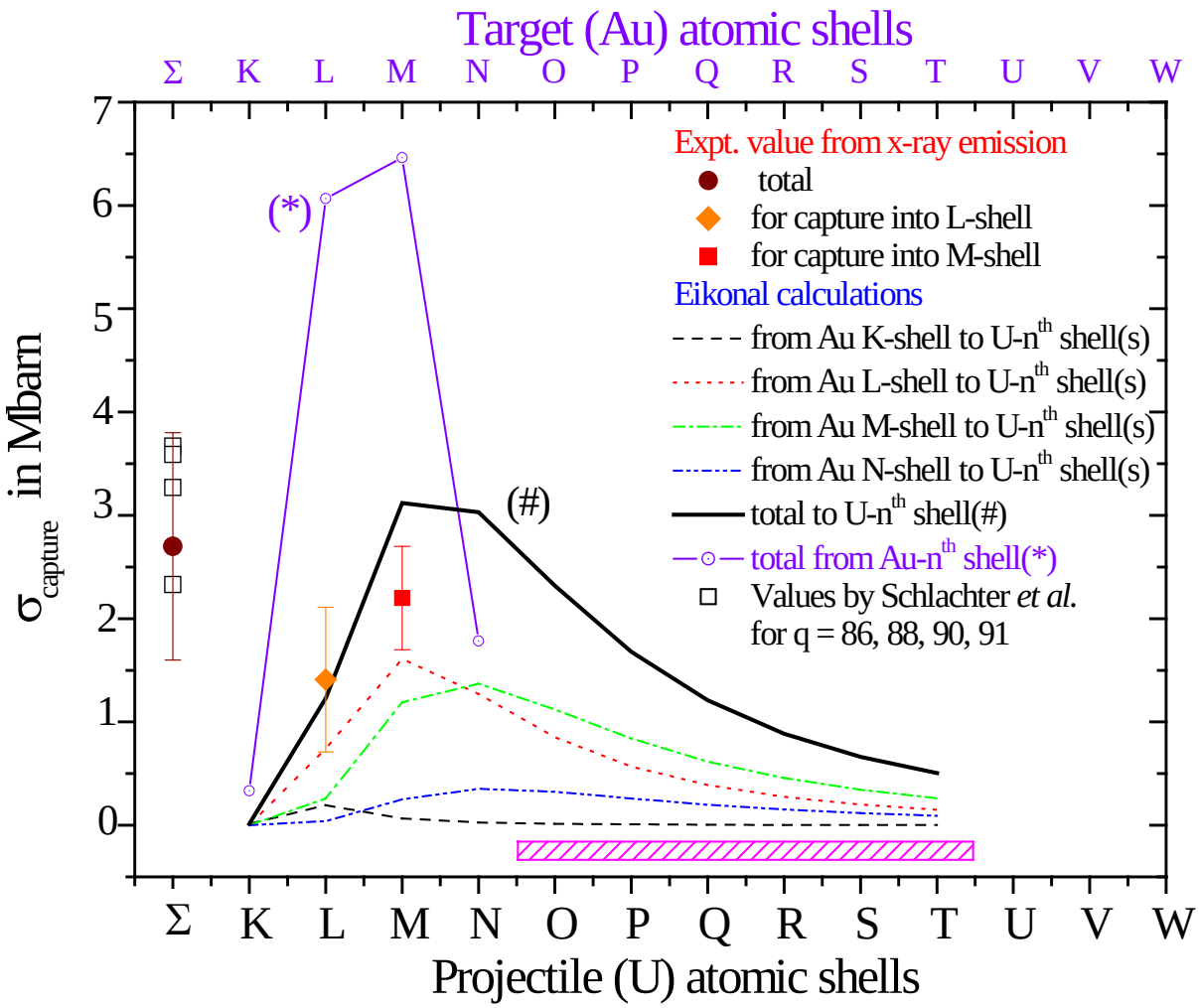

Fig. 4.23 *Shell differential electron capture cross sections vs. the atomic shells of the projectile (U) calculated theoretically and from experimentally measured values. The curves signify the distribution of the cross sections according to Eikonal [53] from Au K, L, M and N shells to various projectile shells (shown on the abscissa) and their total. (#):-* σ_{cap}^{Tot} *from Au K, L, M and N-shells to a U-n*th *shell (K to T) (to be read from abscissa). (*):-* σ_{cap}^{Tot} *from a Au-n*th *shell (K to N) (to be read from axis on top) to all U-shells (K to T). The Schlachter [50] values are a total for q = 86, 88, 90 and 91. The experimentally determined values of* σ_{cap}^{L}, σ_{cap}^{M} *and* σ_{cap}^{Tot} *from x-ray emission cross sections (*$K\alpha_{1,2},\beta_{1,2}$ *for q = 91and* $L\alpha,\beta_1$ *for q<91) are also included.*

Estimating the U-Lα and U-Lβ_1 cross sections for single collision conditions i.e. corresponding to ‘t=0’ and summing up, the σ_{cap}^{M} is calculated to be about 2.2 Mb (closed incoming K-shell). For an open incoming projectile K-shell (q=91), the U-L radiation is reduced (see Fig. 4.21) compared to its

values for the closed case (q=73 to 90) as part of the captured M-shell electrons decay directly to the K-shell (leading to U-Kβ emission). This reduction can be calculated from the cross sections for U-Lα as a difference between its values at q=73 to 90 and that corresponding to q=91. The σ_{cap}^{M}-reduction is thus estimated to be about 0.5 Mb. These results provide an estimate of projectile subshell population. For a predominance of single capture with an open U K-shell, it is expected to find an increase in the shifts in centroid energies of L x-rays which is indeed the case (see Fig. 4.14, 4.15). The U-K radiation for an open incoming K-shell comprises also capture to U-L and higher shells (including cascades). The U-Kα_1 cross section corresponding to its value for t=0 provides an estimate. In order to account for all the K x-ray decay channels i.e. α_1, α_2, β_1, β_2 a multiplicative factor, maximum of about "3" (see Table 6.2) has to be taken into account. This yields a total capture cross section of σ_{cap}^{Tot} = 2.7 Mb. Subtracting the U-L cross sections i.e. σ_{cap}^{M} (including the reduction) from σ_{cap}^{Tot}, one gets the capture to the U-L shell i.e. σ_{cap}^{L} = 2.7-2.2+0.5= 1.4 Mb. Above are shell differential results deduced from measured x-ray cross sections.

Table 4.2 *Total electron capture cross sections for 69 MeV/u Uranium on Gold target calculated by Schlachter et. al. formula [50], the Eikonal approximation [53] and the values determined from measured projectile x-ray emission cross sections. The* σ_{cap}^{L}, σ_{cap}^{M} *represent the calculated cross section for electron transfer from target K to N shells into the projectile L and M shells respectively.* $\sigma_{cap}^{Tot}(1)$ *represents the electron capture from the target K to N shells into the projectile K to N shell.* $\sigma_{cap}^{Tot}(2)$ *is the electron capture cross section from the target K to N shells into all K to T projectile shells. The experimental values* σ_{cap}^{Expt-X} *are deduced from the projectile x-ray emission yields.*

Projectile incident charge state (q)	σ_{cap}^{Th} **in Mb**					σ_{cap}^{Expt-X} **in Mb**		
	Schlachter *et al.* [50]	**Eikonal approximation [53]**				σ_{cap}^{L}	σ_{cap}^{M}	σ_{cap}^{Tot}
		σ_{cap}^{L}	σ_{cap}^{M}	σ_{cap}^{Tot} (1)	σ_{cap}^{Tot} (2)			
91	3.67	1.23	3.12	7.39	14.6	1.41 ± 0.7	2.2 ± 0.5	2.7 ± 0.1
90	3.59							
88	3.27							
86	2.33							

Table 4.2 gives the electron capture cross sections calculated by the Eikonal approximation, by the semi-empirical prescription of Schlachter *et al.* [50] and σ_{cap}^{L}, σ_{cap}^{M} and σ_{cap}^{Tot} deduced from measured x-ray emission cross-sections. It is to be noted that σ_{cap}^{Tot} estimated through U K x-ray emission cross sections (for open K-shell in the entrance channel) can only reflect one electron capture. In case there is multi electron capture or successive capture in different collisions, it will be reflected in σ_{cap}^{M} which is capture into M and higher shells. Within our experimental uncertainties the total capture cross section is comparable to the value by Schlachter. A total of the Eikonal cross sections for capture from Au K-, L-, M- and N-shells to U-shells (K-T considered) yield a value of 14.6 Mb. The Bohr's criterion of $v_{ion} = v_e$, shows that the collision velocity is already larger than the velocity of electrons in the U-M shell. Hence, some of the electrons captured to the M-shell are probably reionized quickly by further collisions if they do not cascade down via the L- to K- shell. All the shells above U-M are probably vacant and hence the bulk of the curves for O and higher shells can be safely neglected (shaded rectangle at the bottom of the figure) in calculating the total capture to U n^{th}-shell. According to Eikonal, the total capture from Au (K- to N-shells) to U K- to N-shells (column 1) yields a value of 7.39 Mb which is more than double the value of σ_{cap}^{Tot} deduced from x-ray emission cross sections (2.7±0.1 Mb). The value of σ_{cap}^{L} determined from x-ray emission agrees well with the predictions of Eikonal (solid line), however Eikonal overestimates the experimental σ_{cap}^{M}. These values provide only a general picture of the capture process in the slightly asymmetric collision system under investigation and more accurate data are required for a rigorous comparison.

Although Eikonal predicts a maximum capture to the U-M shell, U-Kβ_1 (M_3-K transition) has not been observed with appreciable intensity for all q = 73 to 90 (Fig. 4.3 and 4.4). For q = 73 to 90 this K-decay channel is closed and the L radiation provides the requisite information. The U-Lα emission cross section is in the order of 1.2 Mb indicating capture to the U M-shell and its cascading (cf. Figs. 4.21 and 4.22). Additionally, it can be seen from Fig. 4.21 that the Au-L emission is considerably larger (from a factor of about 3 to an order of magnitude) than the U-L emission. However, it is comparable in magnitude to that of U-Kα manifesting the capture from the Au-L shell and further indicating that for the Au-L shell ionization is the dominant channel compared to loss to the projectile (capture). Moreover, the Eikonal approach is known to overestimate cross sections for the considered case.

CHAPTER V

A NEAR SYMMETRIC SUPERHEAVY COLLISION SYSTEM: Bi^{q+}- Au

5.1 INTRODUCTION

Based on the exploratory studies described in Chapter 4 for a slightly asymmetric, superheavy collision system, the present investigation applies refined experimental techniques to study under equivalent conditions, a near symmetric superheavy collision system. The new system of Bi-ions (Z_1 = 83) bombarding on Au target (Z_2 = 79) has a nuclear charge of the united atom (u.a.) [7] as $Z_{u.a.} = Z_1+Z_2 = 162$. In this study the ejectiles behind the target were charge state analysed magnetically and additionally a granular x-ray detector was used to reduce the uncertainties caused by the Doppler effect on the x-ray energies (broadening, line overlap and shifts) without reducing the total detection solid angle. As for the asymmetric collision case, the initial aim of this study was to confirm the previous observation that an incoming inner shell projectile vacancy will survive with a high probability the penetration of thin layers of solid matter and hence, those projectiles colliding with thin target foils can be used for exploring superheavy quasimolecules. Consequently, the first goal was to deduce the charge state evolution and charge exchange cross sections of a relativistic heavy ion (Bi^{q+}) penetrating through a very thin solid foil (Au). The charge state evolution in a solid target depicts to some extent the conditions for the incoming channels, for quasimolecular collisions inside the solid as a function of penetration depth. Further, the charge exchange cross sections could be correlated with x-ray emission cross sections determined for the collision system. The central goal of an elucidation of coupling mechanisms of inner shells in the superheavy quasimolecules was subsequently fulfilled. Collisions with a projectile having an incoming K vacancy (Bi^{82+}) were of particular interest as this implies a high charge state far off the equilibrium. For close collisions and inner shells (K) the adiabatic collision regime prevails as the adiabaticity factor η for K-shells [$\eta_K = (v_{ion}/v_{K\text{-}e})^2] \leq 0.5$. In the present investigation in contrast to the one reported in Chapter 4, more targets of different thicknesses were used at the cost of fewer charge states studied.

5.2 EXPERIMENTAL DETAILS

A general description of the experimental set-up with the details regarding the position of targets and detectors has been given in Chapter 3, Section 3.2.2. A charge state selected Bi^{q+}-ion

beam (q = 82, 81 or 77) of 69.2 MeV/u was well collimated before it bombarded on thin Au targets with thicknesses (t) of 21, 42, 79, 150 and 225 μg/cm^2 (the thinnest ones, 21 and 42 μg/cm^2 targets had ultra thin carbon backings of 11 and 12 μg/cm^2 respectively). The Au layer faced the incoming beam.

A schematic diagram of the experimental set-up with a top view is shown in Fig. 5.1 and a photograph of the same is shown in Fig. 5.2. The target foils were positioned perpendicular to the beam direction. The emitted projectile and target x-rays emitted were detected by two intrinsic Ge detectors (mainly for the K x-rays) and by a Si(Li) detector (for the L x-rays). Following the G2 geometry mentioned in Chapter 3, Section 3.2.2, the Ge detectors, a normal and a granular one were positioned in one plane (on both sides of the beam axis) at 60^o (forwards) to the beam direction and the Si(Li) detector was positioned at 45^o, off plane relative to the two Ge detectors (the latter shown

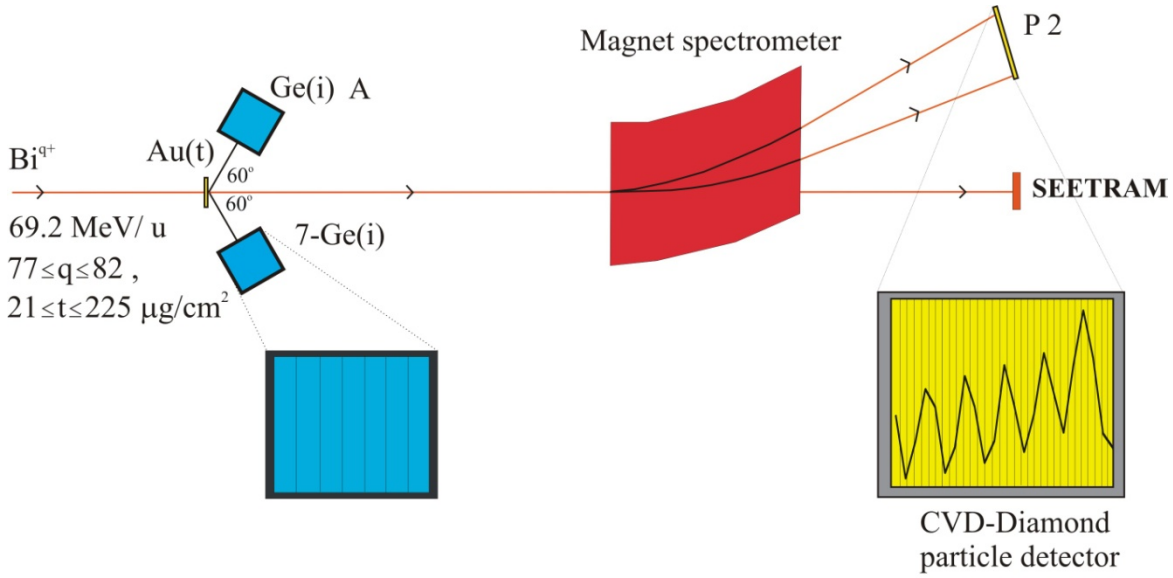

Fig. 5.1 *A top view of the schematic experimental set up with the two Ge(i) x-ray detectors, the magnet spectrometer and the position-sensitive, CVD-diamond particle detector at position P2. The granular arrangements (stripes) for the 7-Ge(i) and the CVD detector are indicated at the bottom. The spectra shown on the CVD is the charge state distribution of the ejectiles. The alternate position for the particle detector "SEETRAM" is shown.*

only in Fig. 5.2). Both the germanium detectors had aluminium absorbers of 500 μm and 1 mm thicknesses respectively in front to reduce the high count rate of the L x-rays as compared to the K x-rays of main interest. The single crystal Ge detector [Ge(i)] had a 4 mm thick Ta collimator with an aperture of 5.8x38 mm^2. The 7-Ge(i) detector (an enlarged front view is shown at the bottom right in Fig. 5.1) had its observation angles (polar) in the range of 53.9^o to 74.2^o. Each stripe had an

observation angle of 3.6°. The active solid angles of the Ge(i) and the whole of the 7-Ge(i) detector were 0.049 sr and 0.199 sr respectively (0.4% and 1.6% of 4π respectively). Each stripe of the 7-Ge(i) subtended a much smaller solid angle of 0.029 sr (0.2 % of 4π).

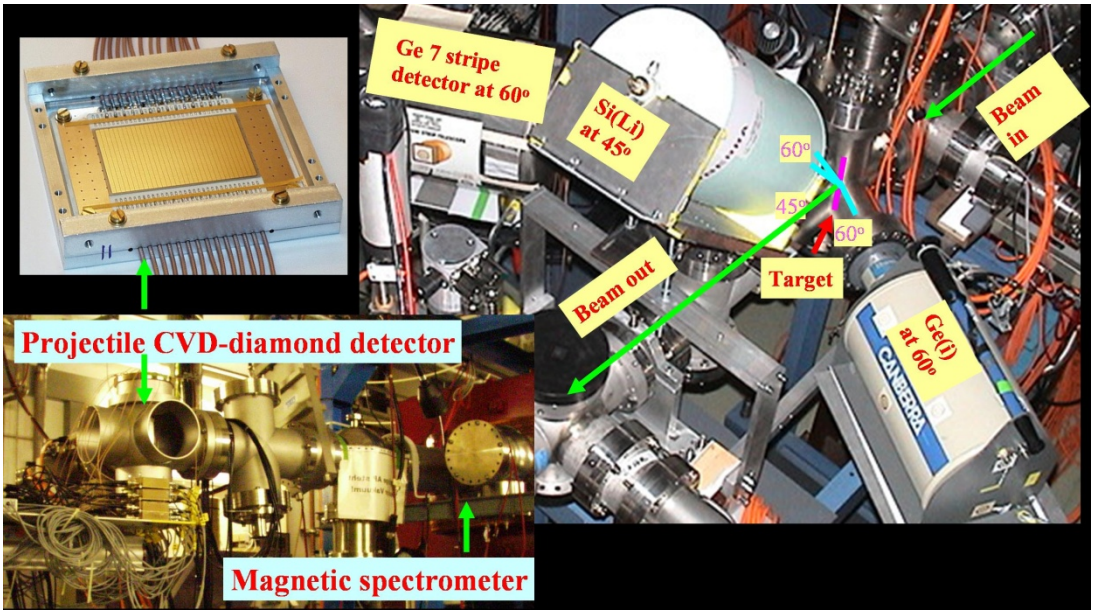

Fig. 5.2 *A photograph of the target area for the experimental set-up showing two Ge(i) x-ray detectors, the Si(Li) x-ray detector on the right hand side (the beam is coming from top right); the magnet spectrometer and the position of the CVD-diamond particle detector after the magnet spectrometer is shown on the left side at the bottom. An enlarged view of the particle detector has been shown in the inset (top left).*

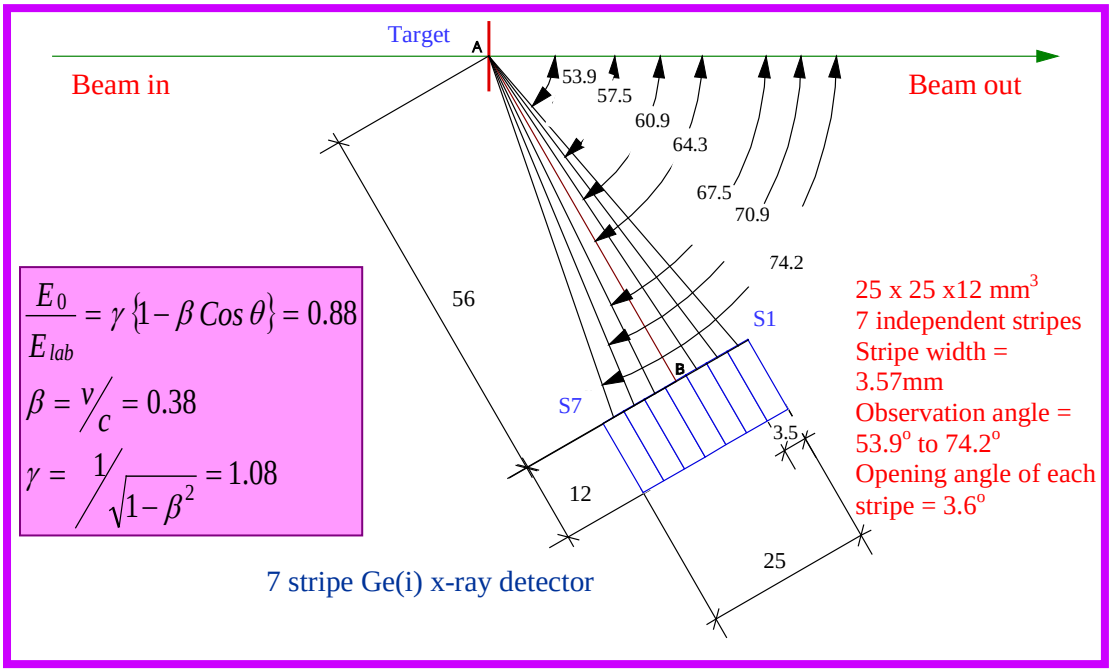

Fig. 5.3 *A schematic diagram of the 7-Ge(i) x-ray detector showing the observation angles of each stripe. Detector specifications are indicated on the right and the Doppler correction values are indicated on the left.*

Fig. 5.3 shows a detailed schematic diagram of the 7-Ge(i) detector and the observation angles of each stripe. The values of β and γ required for the calculation of the Doppler correction factor (E_0/E_{lab}) are also indicated in the figure (see Section 3.3.3, Chapter 3). The standard Ge(i) detector was used mainly for a check on the redundancy of the data. Its large solid angle allowed the measurements at much higher statistics compared to any single stripe of the 7-Ge(i). However, the 7-Ge(i) detector had an advantage over the Ge(i) regarding the smaller solid angle opening of each stripe as well as the unique possibility of using the phenomenon of angle dependent Doppler shift to deconvolute the projectile K x-rays from the target K x-rays separately. The details are discussed in Section 5.3.1. Fig. 5.4 shows a complete x-ray spectra recorded by the 1st, 4th and 7th stripes of the 7-Ge(i) detector for Bi^{77+}-ions incident on 42 μg/cm^2 Au target. The regions of Bi-K and Bi-L x-rays and Au-K x-rays have been indicated in the figure. More details of the spectra follow in the subsequent sections.

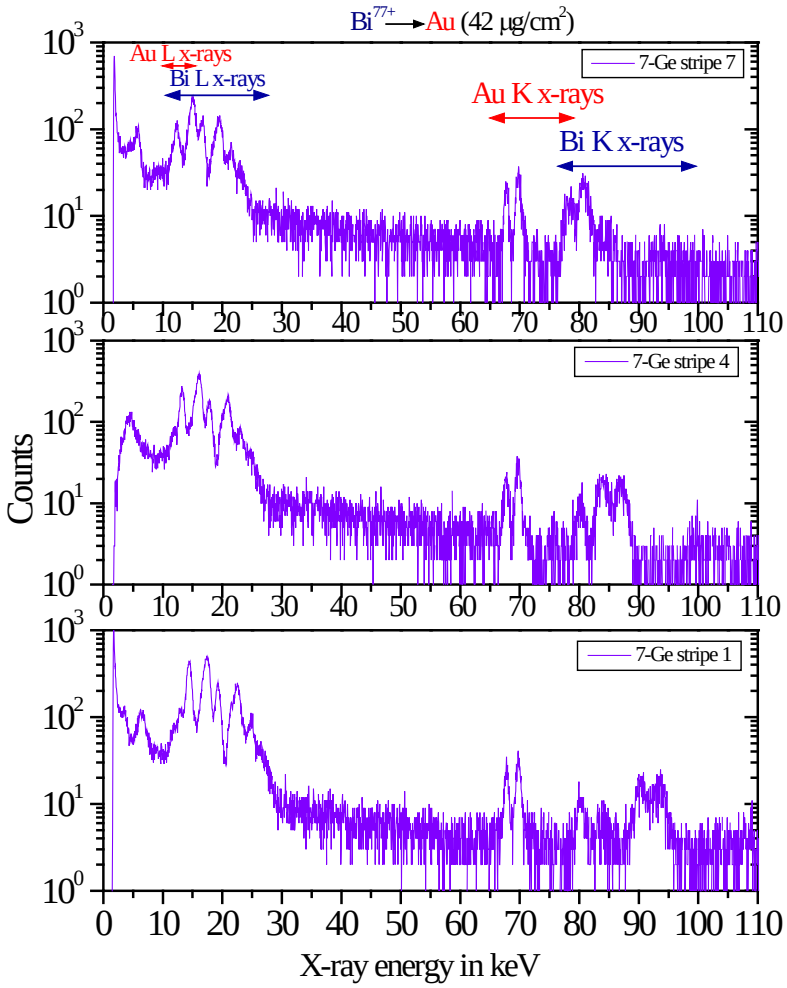

Fig. 5.4 *X-ray spectra recorded by the 1st, 4th and 7th stripes of the 7-Ge(i) detector for Bi^{77+}-ions incident on 42 μg/cm^2 Au target in the laboratory frame. Counts are not normalised to the ejectiles. The regions of Bi-K, Bi-L and Au-K x-rays have been indicated in the figure.*

The Si(Li) detector had an opening of 2.8^{o} for the observation angle and a solid angle of 0.006 sr (0.04% of 4π), it was mainly used for the detection of the L x-rays of the collision partners discussed in Section 5.4. The ejectiles after being charge state analyzed by a magnet spectrometer were detected by the one-dimensional, position-sensitive CVD-diamond particle detector the details of which have been already given in Chapter 3 Section 3.2.3 (ii), and a photograph of the same in Fig. 3.7 a). The charge state distributions and their evolution with the target thickness measured using this detector as well as charge exchange cross sections are presented in Section 5.5.

5.3 K X-RAY EMISSION IN Bi $^{q+}$- Au COLLISIONS

5.3.1 The K x-ray spectra

Fig. 5.5 a) shows the K x-ray spectra (in logarithmic presentation) measured in the laboratory system by the different stripes of the 7-Ge(i) detector for Bi^{82+}-ions incident on the thinnest Au target (21 $\mu g/cm^2$). Considering the previously treated asymmetric case, the Bi-K emission is expected to overwhelm the target K emission due to the initially open projectile K-shell. The x-ray peaks for Au-Kα_2 and Au-Kα_1 transitions of the target which is stationary in the laboratory frame display the same energy for all the stripes of the detector. Those for Bi-K$\alpha_{1,2}$ and Bi-K$\beta_{1,}$ K$\beta_{3,5,2,4}$ are moving in the laboratory frame and appear at different energies in each stripe because of the observation angle dependent Doppler shift (for details see Chapter 3 Section 3.3.3). The laboratory frame spectra of Fig. 5.5 a) are corrected for Doppler shift and depicted in Fig. 5.5 b). In this representation the projectile (Bi) K x-rays are observed at the same energy in the moving (emitter) frame and hence coincide for all the stripes. The x-ray peaks for the Bi are observed as broadened due to the Doppler effect.

For all ‘q’ and ‘t’ combinations investigated, the projectile K x-ray spectra observed in the laboratory frame overlapped those of the target K x-rays for certain stripes of the detector (stripe 2 to stripe 7), for e.g. the Au-Kβ x-rays are overlapped by the Bi-K$\alpha_{1,2}$ x-rays in Fig. 5.5 a) for stripe 4 onwards. For such cases the non-overlapped spectrum of Au target K x-rays observed in stripe 1 was considered as a reference spectrum and a non-overlapped spectrum for Bi K x-rays in stripe 2 to 7 was obtained by subtraction of the reference spectrum from each stripe spectrum (except stripe 1). Hence two separate set of spectra were obtained, one each for Au and Bi in the laboratory frame. The Bi K x-rays were then corrected for Doppler shift as shown in Fig. 5.5 b). The spectra obtained by the above two methods were added up independently resulting in separate emitter frame K-spectra for each collision partner. A total yield for the Au and Bi K x-rays was then deduced for all the ‘q’

and‘t’ combinations investigated. The use of the 7-Ge(i) detector thus enabled a very clear separation of the projectile x-ray spectra from the target x-ray spectra. Such a possibility did not exist with any single crystal Ge(i) detector used in this experiment as well as with the previous experiment of U^{q+}-ions incident on Au (discussed in Chapter 4). From Fig. 5.5 it is clear that for q = 82 (open K-shell of the projectile) the Au-K x-rays are observed to have a much smaller intensity as compared to the Bi-K x-rays.

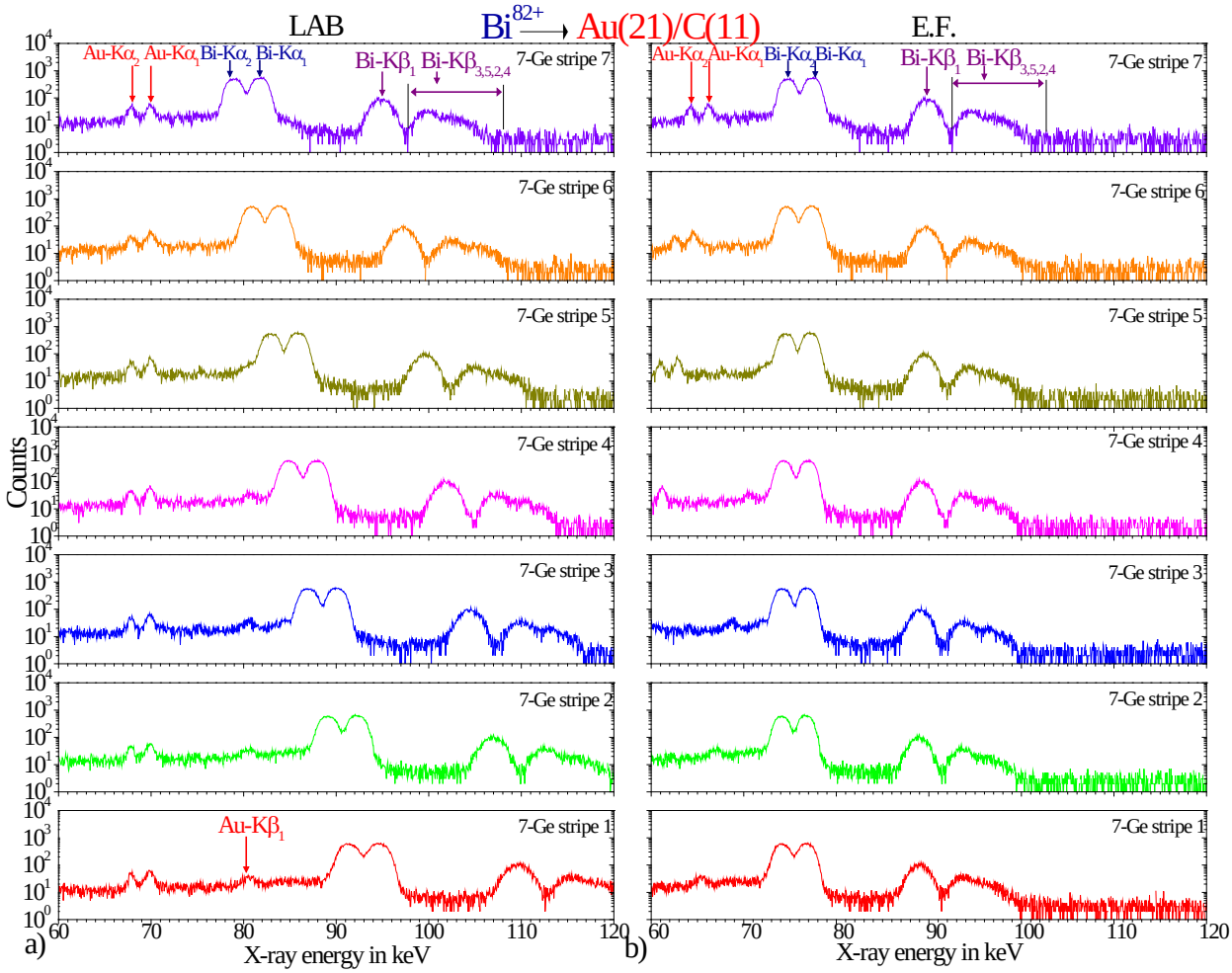

Fig. 5.5 a). *K x-ray spectra (log. scale) measured in the laboratory frame (LAB) by different stripes of the 7-Ge(i) detector for Bi^{82+}-ions incident on 21 $\mu g/cm^2$ thick Au target on a carbon backing of 11$\mu g/cm^2$.* b) *The spectra shown in* a) *are depicted here in the emitter frame (E.F.) of the projectile after being corrected for Doppler shift. Counts are not normalised to the number of ejectiles.*

Fig. 5.6 shows the laboratory frame K x-ray spectra (in linear representation) for Bi^{81+}-ions, i.e. with a full incoming K-shell, incident on the thickest Au target (225 $\mu g/cm^2$) measured by the first, fourth and seventh stripes of the 7-Ge(i) detector. Due to the closed, incoming, projectile K-shell, the K x-ray emission is expected to be of comparable magnitude for both the collision partners. The observation regarding the energy positions of Au-K$\alpha_{1,2}$, Bi-K$\alpha_{1,2}$ and Bi-K$\beta_{1,2,3,4,5}$ x-ray peaks

is identical to that of Fig. 5.5 a). The dashed lines in Fig. 5.6 indicate the position of the target x-rays and the slanted dotted lines represent the position of the projectile x-rays moving towards lower energies for greater observation angles of the stripes (with respect to the beam direction). A comparison of Fig. 5.5 and 5.6 (log. and lin. representation respectively) reveals that the x-ray emission from Bi^{q+}-Au collision system depends significantly on the incident charge state 'q' of the projectile as in the asymmetric case discussed previously.

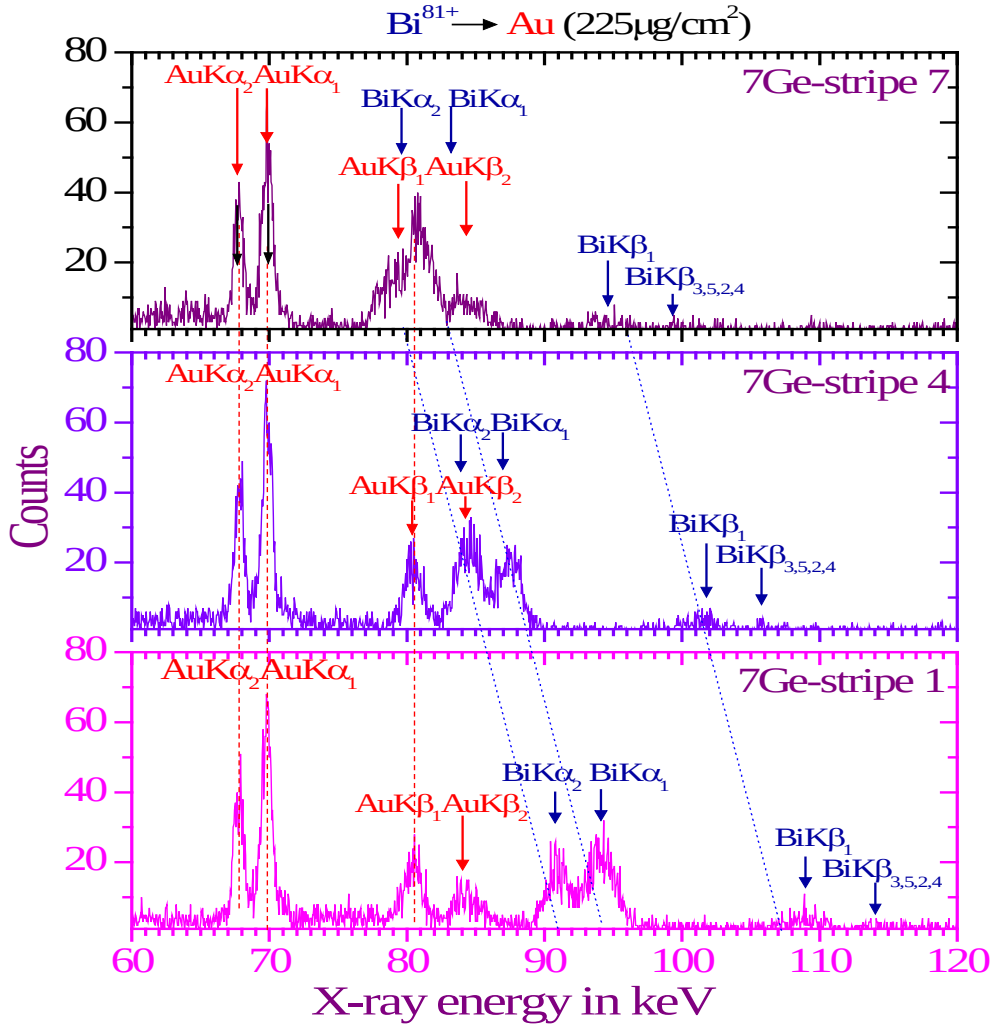

Fig. 5.6 *K x-ray spectra (laboratory frame) measured by the 1st, 4th and 7th stripes of the 7-Ge(i) detector for 69.2 MeV/u Bi^{81+}-ions incident on the 225 μg/cm² thick Au target.*

To clarify this observation further, Fig. 5.7 shows a comparison of the K x-ray spectra with counts normalized relative to the beam intensity for Bi^{q+}-ions (q = 82, 81 and 77) incident on the thickest Au target (225μg/cm²) and measured by the 1st stripe of the 7-Ge(i) detector. The spectra depict clearly the comparison between the relative intensities of the Bi (projectile) and Au (target) K x-rays for each 'q' of the projectile. It can be observed that the intensity of the Bi K x-rays increase drastically relative to that of the Au ones, as q increases from a closed (q = 77, 81) to an open K-shell

(q = 82) condition. For q = 82, the copious emission of Bi-K x-rays relative to the Au-K x-rays has been mentioned above. So there is a reversal in the relative intensities of the projectile and target while moving from a closed to an open K-shell condition of the projectile. This observation is identical to that for U-Au collision system reported in Chapter 4 Section 4.3.1

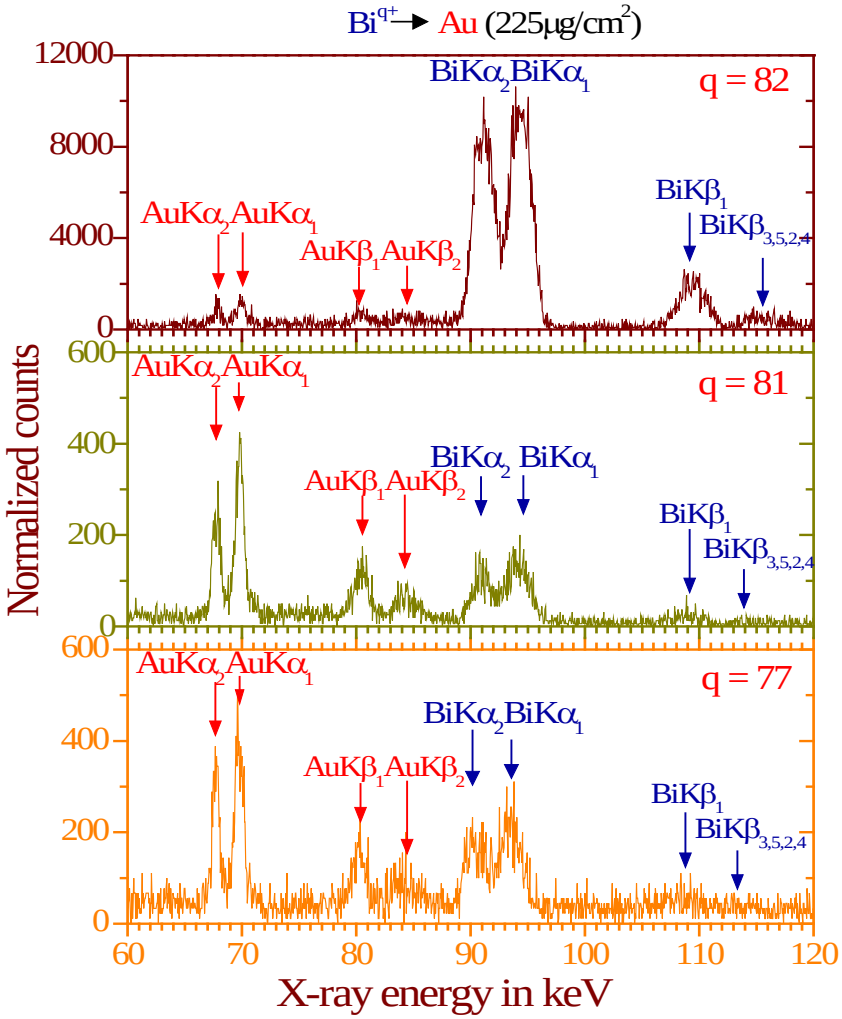

Fig. 5.7 *A comparison of the K x-ray spectra for Bi^{q+}-ions with q = 82, 81 and 77, incident on 225 μg/cm² thick Au target. The counts are normalized relative to the number of ejectiles. (Note: for the spectra corresponding to q = 82, the scale is a factor of 16 larger than others).*

5.3.2 Shift in the Energy of the K x-ray transitions

The reasons for the shift in the energies of the x-ray transitions compared to standard atomic values (single hole) of Bearden (E_o) [23] has been already explained in Chapter 2 and Chapter 4. Fig. 5.8 a), b) shows the centroid energies ($E_{obs.}$) of $K\alpha_{1},\alpha_{2}$ x-ray transitions in the laboratory frame

(LAB) for Au and in the emitter frame (E.F.) for Bi respectively, as a function of the incident charge state (q) of the Bi^{q+}-ions.

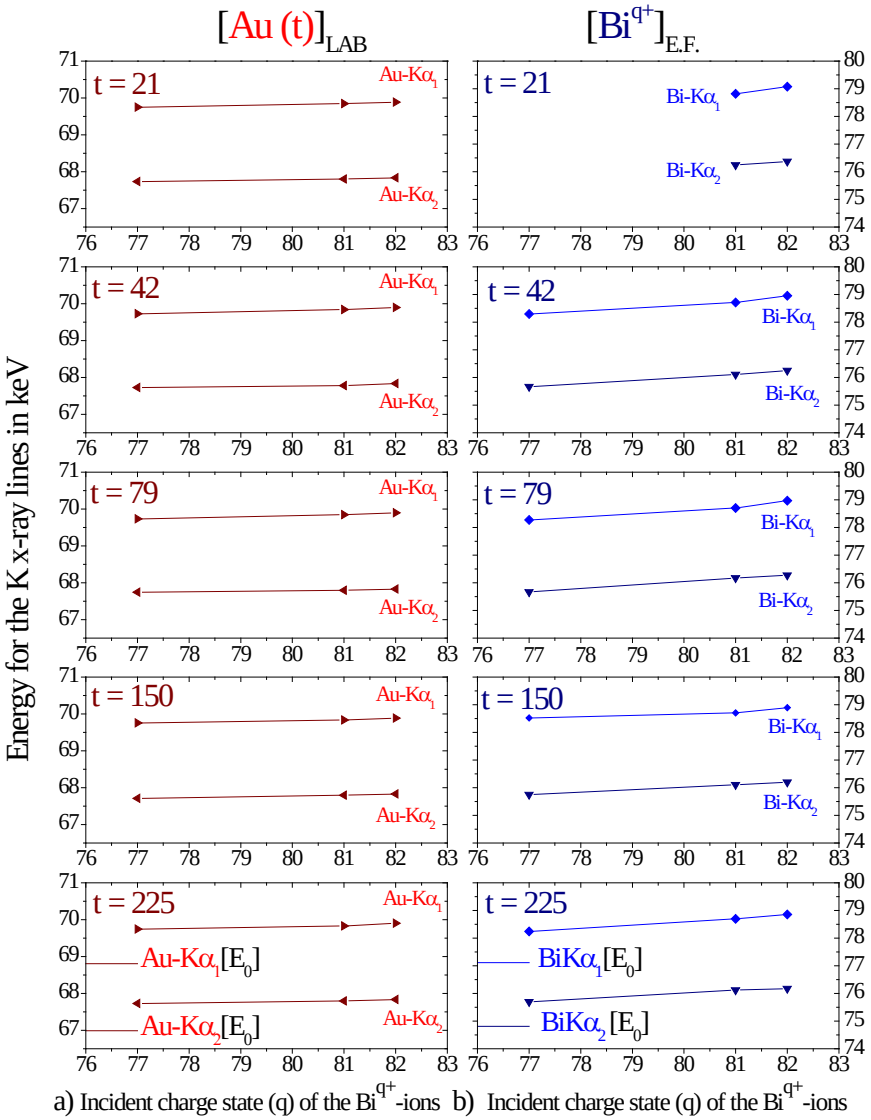

Fig. 5.8 *Centroid energies ($E_{obs.}$) of K x-ray transitions as a function of the incident charge state (q) of the Bi^{q+}-ions.* a) *for Au-K$\alpha_{1,2}$ in the laboratory frame (LAB) and* b) *for Bi-K$\alpha_{1,2}$ in the emitter frame (E.F.). The corresponding standard values of Bearden (E_o) [23] have been indicated by solid lines in the lowermost plot. Thickness of Au target (t) is in $\mu g/cm^2$. Statistical errors are smaller than the size of the symbols. The lines through the data points are drawn to guide the eye.*

The plots have been shown for all the Au target thicknesses investigated (t = 21, 42, 79, 150 and 225 $\mu g/cm^2$). The solid lines on the y axis of the lowermost plot indicate the standard values of Bearden (E_o) [23] for the x-ray energies. The uncertainties in Bi-K$\alpha_{1,2}$ centroids are larger than the ones for Au as a systematic error has to be introduced due to the uncertainty in the observation angle and the required Doppler shift correction mentioned also for U x-ray transitions (Section 4.3.2).

However in the present case, the observation angles are a lot more precisely known than in the asymmetric collision case (U-Au) treated in the previous chapter. It is because of the redundant information available from the x-ray granular detector [7-Ge(i)]. The total errors are smaller than the size of the symbols.

It is clear from the figure that both the Au and Bi-Kα_1,α_2 x-ray transitions are observed at higher energies (E_{obs}) as compared to the standard values (E_o) [23]. For all 'q' investigated, the Bi^{q+}-ion is multiply ionized in the incoming channel itself having L shell vacancies in all cases and hence has a large number of outer shell spectator vacancies. During collision, the projectile seems to remember (to some extent) its initially high ionization in outer shells and hence the observed shifts in the x-ray transitions. The figure also points out to the creation of multiple vacancies in the upper levels (L, M, N etc.) of Au. The Bi-Kα_1,α_2 plot shows a more pronounced slope with increasing 'q' as compared to that of Au for all target thicknesses investigated. This observation is also identical to that of U-Kα_1,α_2 plots (Fig. 4.5 b).

Just as for the U-Au collision system, relative shifts (($E_{obs.}$-E_o)/E_o) provide more information for this collision system also. Fig. 5.9 shows these relative shifts for Au (part a) and for Bi (part b) as a function of 'q' for all 't' investigated. The uncertainties in the values for Au are smaller than that for Bi for the reasons mentioned above, however, they are smaller than the size of the symbols in the figure for both Au and Bi. The lines drawn are linear fits to the data.

The relative shifts in the Au- and Bi-Kα_1,α_2 x-ray lines are observed to become larger with increasing q. Bi-Kα_1,α_2 x-ray lines exhibit a stronger q dependence than Au x-ray lines. With increasing q, the Au-Kα_1 and Bi-Kα_1 x-ray transitions show a relative shift of 1.1-1.6 % and 1.5-2.5 % respectively. The increase in the relative shifts of Au is about half as much as that for Bi indicating a correspondingly lower multiple ionization as compared to Bi. For the Kα_2 lines there is a slightly smaller but quite similar behaviour as instead of $p_{3/2}$, $p_{1/2}$ electrons are involved in the transition. These observations are identical to that observed for U-Au collision system in Fig. 4.6 a), b), Chapter 4. The reasons for this dependence have been explained there already and are valid for this collision system also.

Here it is emphasized that for the Au targets, the relative shifts with their absolute values and slopes coincide (within the experimental uncertainties) for the symmetric (Bi-Au) and asymmetric (U-Au) collision case; this points to comparable multiple ionization in both collision cases. However, for the U-ion projectile case, a stronger dependence on 'q' has been observed than that for the Bi projectiles. For the U-ion case, the uncertainty caused by the observation angle (target position shift) yielded in unreasonable high shifts which were also not supported by the calculations of shifts (see

Fig. 4.5). From this observation and the more precise measurements of the Bi-Au case, it may be concluded that the relative U-ion shifts given (Fig. 4.6) should possibly be reduced by a factor of 0.6. Anyhow, it is clear that the projectile ions show a stronger relative shift (compared to the target atoms) and a steeper slope with q at the high charge states investigated for the reasons explained earlier. This is due to the greater initial ionization in the higher projectile shells surviving to some extent, collisions in the solid at the relatively high ion velocities.

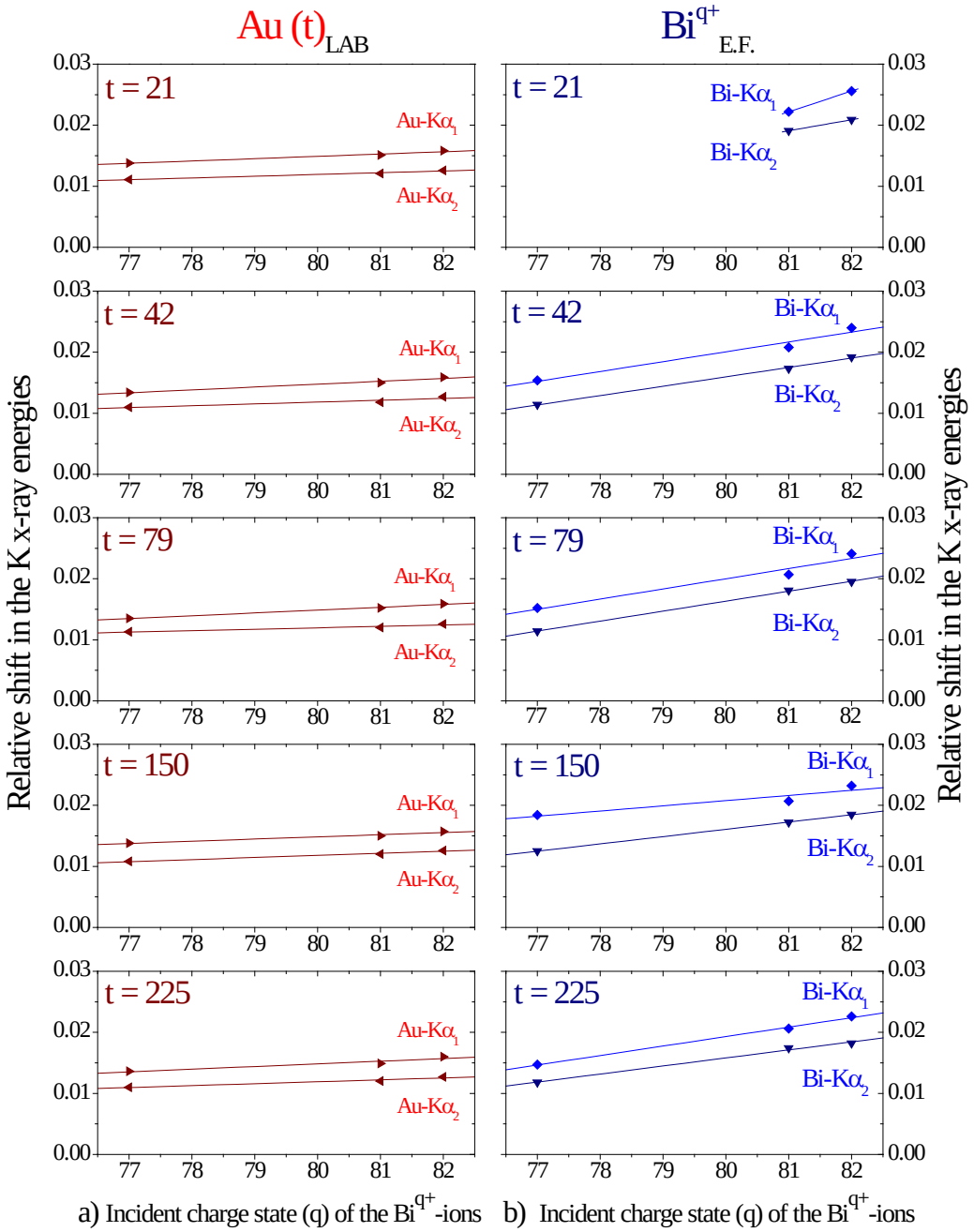

Fig. 5.9 *Relative shift $(E_{obs}-E_o)/E_o$ in K x-ray transitions (centroids) normalized to standard values (E_o) [23], as a function of the incident charge state (q) of the Bi^{q+}-ions,* a) *for Au in the laboratory frame (LAB) and* b) *for Bi in the emitter frame (E.F.). Thickness of Au target (t) is in $\mu g/cm^2$. Statistical errors are smaller than the size of the symbols. Lines drawn are linear fits to the data.*

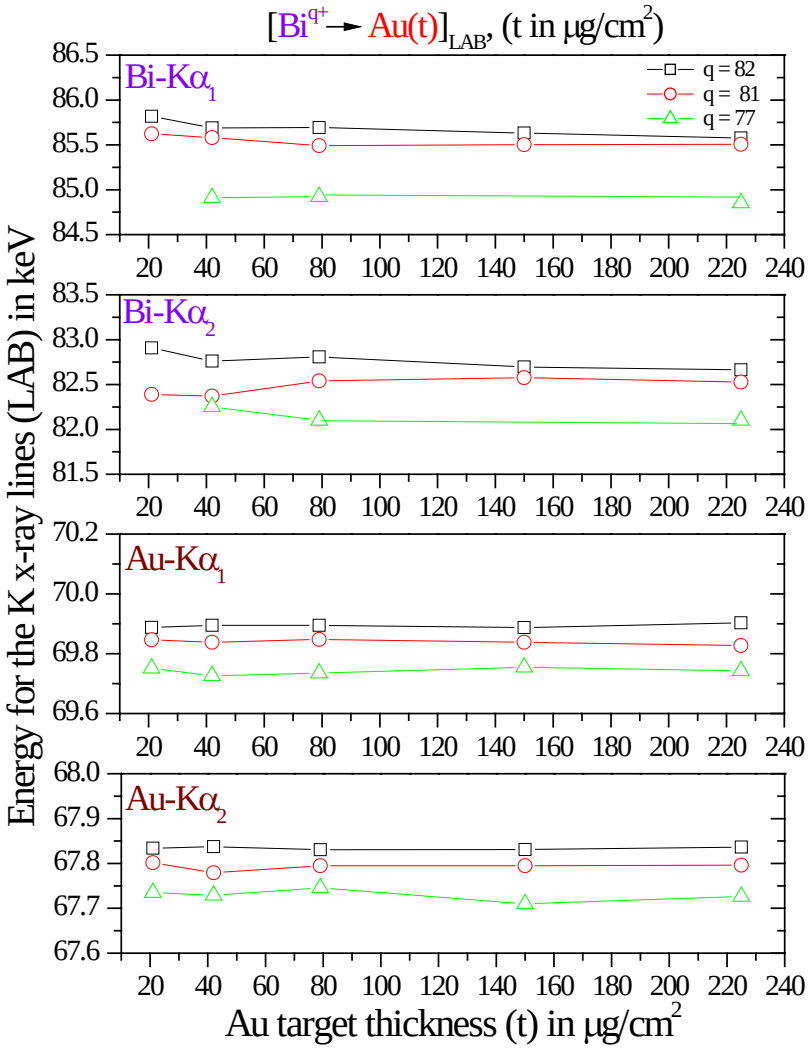

Fig. 5.10 *Centroid energies (E_{obs}) of Bi- and Au-K x-ray transitions in the laboratory frame (LAB) as a function of the thickness (t) of the Au targets. Statistical errors are smaller than the size of the symbols. The lines through the data points are drawn to guide the eye.*

Fig. 5.10 depicts the centroid energies of Bi- and Au-K x-ray transitions as a function of the Au target thickness (t) in the laboratory frame. Within the experimental uncertainties a target thickness dependence of these Au- or Bi-K x-ray transitions could not be observed except possibly in the open K-shell case for Bi-K x-rays. This observation is also identical to that for U-Au collision system (Fig. 4.7, Chapter 4) and the inferences too: the ionization in higher shells seems to survive with a high probability while penetrating the solid target foils.

5.3.3 Intensity ratios for K x-rays

The reasons for the modification of the intensities of the K x-ray transitions have been discussed in Chapter 2 and 4. Assuming a single ionization of the target atom, branching ratios have

been calculated theoretically by Scofield [64] for a full occupation of the shells. A variation of the occupation numbers will change the intensity ratios correspondingly. Therefore a comparison of the measured K x-ray intensity ratios and the calculated branching ratios reveals how the intensity ratios of the K x-ray lines get changed due to multiple ionization and how the population ratio of the $2p_{1/2}$ and $2p_{3/2}$ levels changes. The intensity ratios have been calculated using the formula given in Section 3.3.5 (ii) of Chapter 3 and the overall uncertainties were ~10%. The ratios of only the intense x-ray lines i.e. $K\alpha_{1},\alpha_{2}$ of both Bi and Au have been calculated. Table 5.1 presents the average values for these for $q \leq 81$, corresponding to closed, incoming, projectile K-shell and for $q = 82$, the open K-shell of the incident Bi^{q+}-ions. Single hole values [64] have also been given in the table for comparison. The values have been averaged over all 'q' and 't' investigated.

Table 5.1 *Average values of Bi and Au x-ray intensity ratios for closed ($q \leq 81$) and open ($q = 82$) projectile K-shell in the entrance channel. Single hole values by Scofield [64] have been given for comparison. The experimental inter-partner ratios (1^{st} line) are corrected for the relativistic solid angle transformation.*

Charge state q / Intensity ratio	**$q \leq 81$**	**$q = 82$**	**Scofield [64]**
Bi-$K\alpha_1$ / Au-$K\alpha_1$	0.9 ± 0.1	23.7 ± 6.5	0.989
Bi-$K\alpha_2$ / Bi-$K\alpha_1$	0.6 ± 0.1	0.9 ± 0.05	0.598
Au-$K\alpha_2$ / Au-$K\alpha_1$	0.6±0.03		0.588

Fig. 5.11 shows the Bi and Au intensity ratios as a function of the incident charge state 'q' for all t investigated. The Bi and Au $K\alpha_2/K\alpha_1$ ratio does not show any q dependence and agrees reasonably well with the Scofield values (Table 5.1) except for the Bi $K\alpha_2/K\alpha_1$ ratio showing a slight q dependence on opening the incoming K-shell. Since this ratio reveals the population distribution of the $2p_{1/2}$ and $2p_{3/2}$ levels, it seems that this distribution is unaffected by the presence of vacancies in the incoming channel of the collision. For the open K-shell case, the projectile $p_{3/2}$ electrons seem to be more affected than the $p_{1/2}$ ones. These observations and the following are identical to that observed for U-Au collision system.

For a closed shell case (q = 77 to 81) the Bi-$K\alpha_1$/Au-$K\alpha_1$ ratio is slightly lower than the Scofield's value and does not vary with q. For this case the relative population of $2p_{3/2}$ level of Bi seems to be almost the same as that of Au $2p_{3/2}$ level. The inner shell vacancies created during close collisions may be transferred to the Bi and Au-K shells in the outgoing part of the collision and it may influence this ratio additionally. The implications of this are discussed in Chapter 6. For an open

K-shell of Bi (q = 82), the Bi-Kα_1/Au-Kα_1 inter-partner ratio increases by more than an order of magnitude. This is also demonstrated by the K x-ray spectra shown in Fig. 5.7. A similar observation for U-Au collision system is reported in Fig. 4.8, Chapter 4. The reasons for increased Bi K emission have been explained above. As the experimental value is much larger than the Scofield value it indicates that a different production channel becomes available. The presence of a K vacancy there enables the observation of an electron captured to higher shells through its radiative decay to the K-shell.

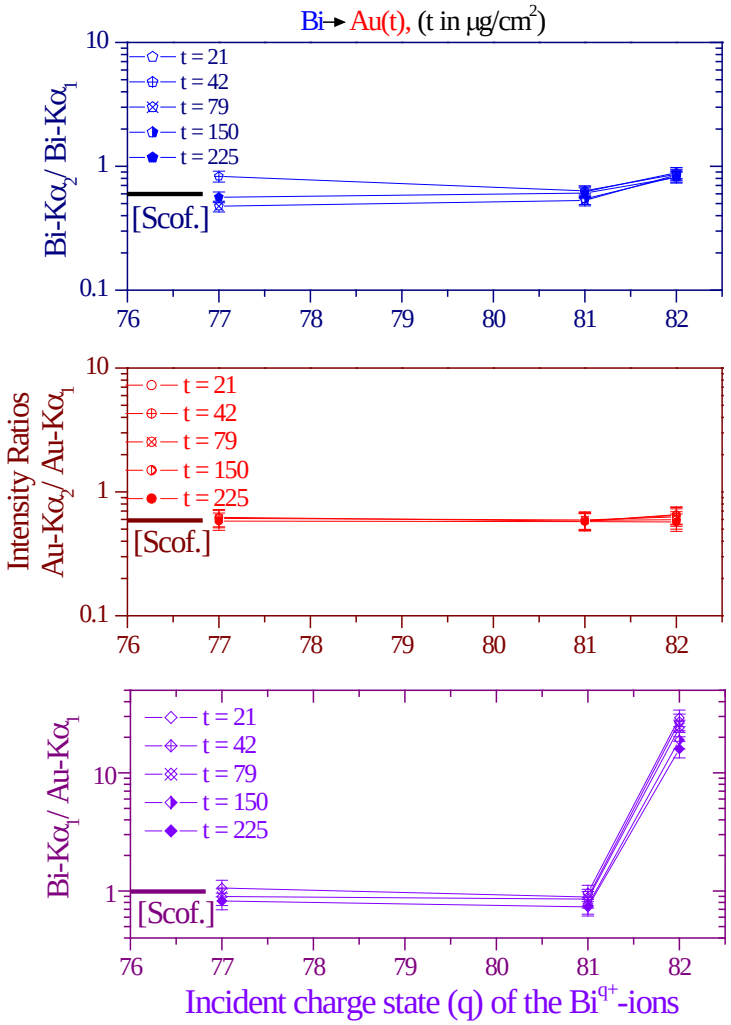

Fig. 5.11 *Measured intensity ratios (intra-partner and inter-partner) for K x-ray transitions of the projectile (Bi) and target (Au) as a function of the projectile incident charge state (q). The corresponding single hole values by Scofield [64] have been indicated in the figures as [Scof.].*

Fig. 5.12 shows the measured Kα_2/Kα_1 intensity ratio for Bi and Au and the Bi-Kα_1/Au-Kα_1 inter-partner ratio as a function of the target thickness t for all $q_{incident}$ investigated. The single hole values are also given in the figure as [Scof.]. Both Bi and Au Kα_2/Kα_1 ratios do not show any target thickness dependence indicating that population ratio between the $2p_{1/2}$ and $2p_{3/2}$ levels created during

collisions is not altered while the projectile penetrates through the thickness of the solid target. The Au ratios agree well with the single hole values pointing towards a similar population ratio in the 2p levels as in a singly ionized atom.

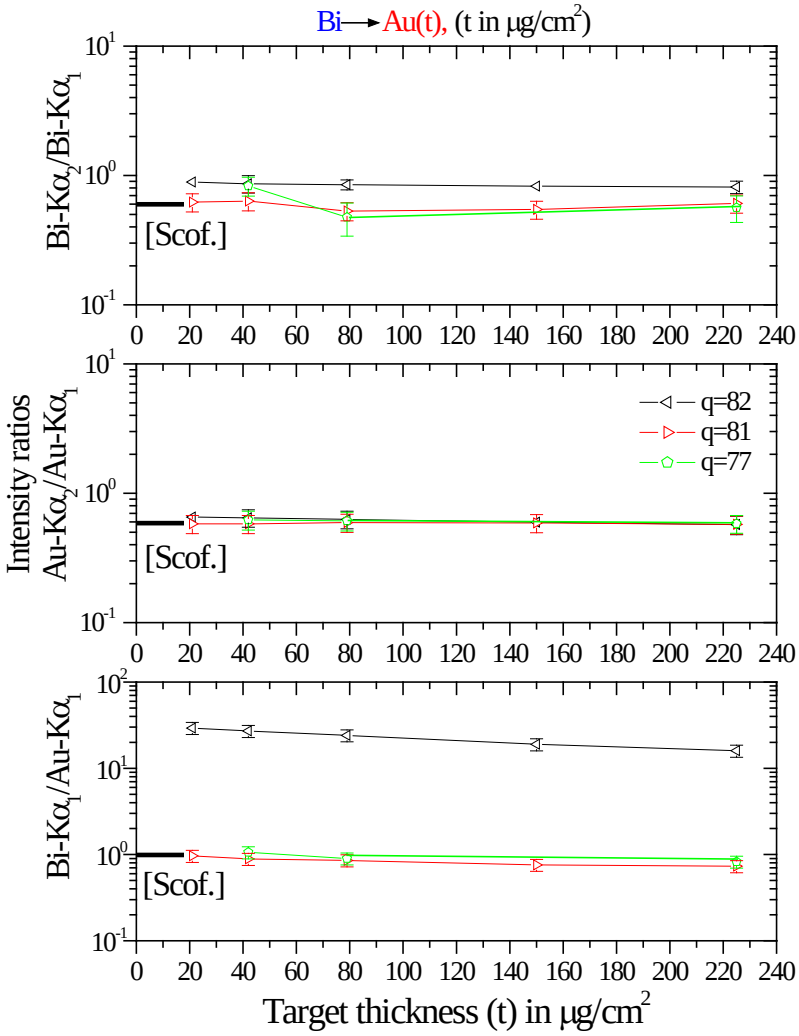

Fig. 5.12 *Measured intensity ratios (intra-partner and inter-partner) for K x-ray transitions of the projectile (Bi) and target (Au) as a function of the Au target thickness (t). The corresponding single hole values by Scofield [64] have been indicated in the figures as [Scof.].*

A highly charged Bi-ion might capture electrons in distant collisions yielding to a slightly higher population preference for the $p_{1/2}$ level compared to the ratio in singly ionized atoms. The inter-partner Bi-Kα_1/Au-Kα_1 ratio does not show a target thickness dependence for a closed K-shell and agrees reasonably well with the Scofield values. For an open K-shell situation (q = 82), however, this inter-partner ratio decreases with increasing t. These observations are similar to the ones observed for U-Au collision system (Fig. 4.9). Since the high inter-partner ratio can be used as a measure for the existence of projectile vacancies, the decrease of this ratio gives directly the percentage of projectile ions losing their initial K vacancy with target thickness. From the

(exponential) decrease of this ratio, the thickness of the target corresponding to which half of the projectiles lose their initial K vacancy can be inferred. This yields a value of about 230±30 μg/cm^2. Here it is emphasized that these (intra spectra) intensity ratios are independent of any normalization problems. These estimations have been compared in Chapter 6 with other results.

5.3.4 K x-ray emission cross sections

The x-ray spectra were deconvoluted to yield Au K and Bi K x-rays separately by the procedure explained in Section 5.3.1. Total yields for the Au and Bi K x-rays were obtained by adding up the two set of spectra independently. The K x-ray emission cross sections for both Bi and Au were calculated by the formula discussed in Chapter 3, Section 3.3.5 (iv).

Normalization procedure and dead time correction

The x-ray yields of both Bi and Au have been normalized to the number of ejectiles recorded by the CVD-diamond particle detector which was used after the magnet spectrometer to measure the charge state distribution of the ejectiles. The total number of normalizing ejectiles was obtained from a sum of the intensities of all the charge state fractions for each charge state distribution measurement. The details regarding the procedure of obtaining the intensities have been covered later in Section 5.5 of this chapter. The dead time correction of the data acquisition system was much larger than the dead time of the individual x-ray detectors and corrections for the same were made by the same procedure as explained in Section 4.3.4 of chapter 4.

Charge state dependence of the cross sections

Fig. 5.13 shows the K$\alpha_{1,2}$ emission cross sections as a function of the projectile incident charge state (q) for Au (part a) and Bi (part b) corresponding to all the Au thicknesses investigated. The Au- and Bi-K$\alpha_{1,2}$, cross sections show a slight increase in the values for q = 81 (just closed projectile K-shell) relative to those for q = 77 (near equilibrium charge state). These observations are identical to the ones for U-Au collision system detailed in Section 4.3.4. The inferences drawn there are applicable to this collision system also. For q = 82 (open projectile K-shell), both the Bi and Au cross sections show a considerable increase relative to their values at q = 81. However, the increase in the Bi-K$\alpha_{1,2}$ cross sections is dramatic. For q = 82, the increase in the Bi-K emission cross sections indicates a predominance of electron capture from the target to the higher projectile shells and their radiative stabilization to the K-shell, whereas the increase in Au-K emission gives access to

the vacancy transfer in the collision molecule. The electron capture cross sections for Bi-Au collision system is of the order of 1-2 megabarns and a typical electron capture interaction distance has been estimated later in Chapter 6. The increase in the Au-K emission is of the order of 50 kbarns for an open K-shell condition. For this collision system inferences are not deduced for incoming L (j=1/2) vacancies in the projectile as it requires a larger number of data points for initial L-shell vacancies. All the observations are applicable for all the target thicknesses investigated. Estimation of interaction distances for K-K sharing are given in Chapter 6 along with further discussions and inferences.

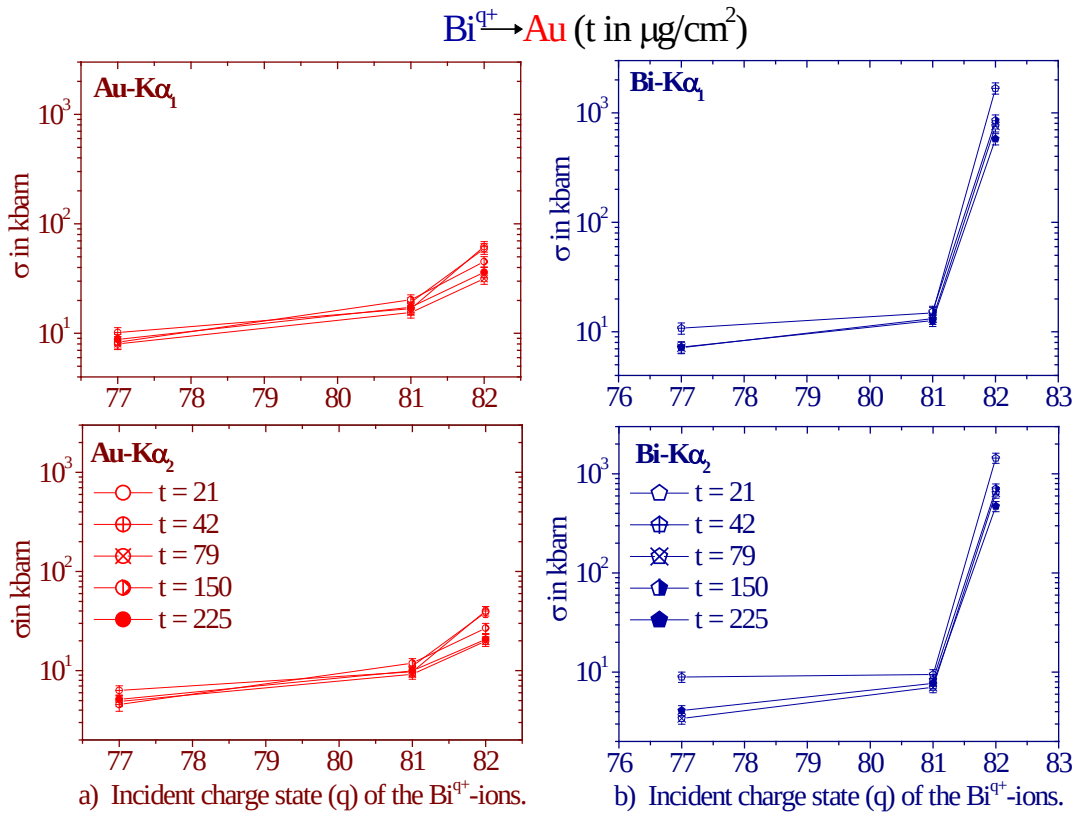

Fig. 5.13 *Kα$_1$ and Kα$_2$ emission cross sections (top and bottom respectively) as a function of projectile incident charge state (q),* a) *for the target Au and,* b) *for the projectile Bi. Au target thicknesses (t) is in μg/cm^2.*

Target thickness dependence of the cross sections

Fig. 5.14 shows the Kα$_{1,2}$ x-ray cross sections for the target Au (part a) and projectile Bi (part b) as a function of the Au target thickness (t). The cross sections for single collision condition can be obtained by an extrapolation of the shown values which are actually the absolute yields (a true cross section is known to be independent of target thickness). It can be observed that for an incoming K vacancy (q = 82), the Bi-K and Au-K x-ray cross sections decrease with increasing target thickness. This

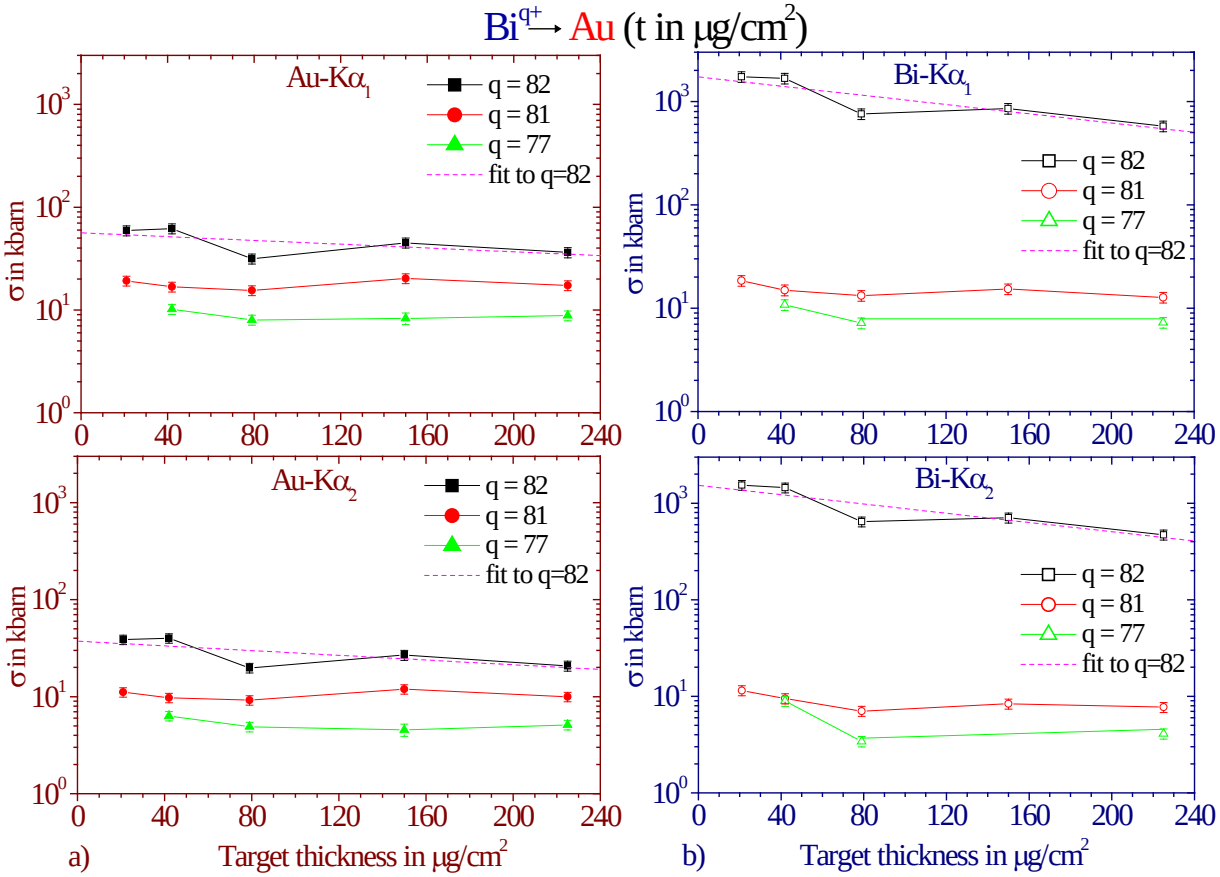

Fig. 5.14 *$K\alpha_1$ and $K\alpha_2$ x-ray yields (cross sections) top and bottom respectively, as a function of the target thickness (t)* a) *for the target Au and* b) *for the projectile Bi for all the charge states (q) investigated. The dotted line passing through Au and Bi-$K\alpha_{1,}\alpha_2$ values for q = 82 are the exponential fits to extract the single collision cross sections.*

seems to be due to the gradual filling of the projectile K-vacancies in the solid target during passage in the bulk. The decrease for Bi-K cross sections is much steeper than that for Au. For Bi^{81+} (He-like), comparatively only a slight decrease with target thickness can be observed; and for Bi^{77+} the data are not good enough to deduce a real variation with target thickness. Assuming an exponential reduction of the vacancy in the bulk for the H-like case, exponentials have been fitted to the data for each value of q (shown in Fig. 5.14) by the same procedure as done for U-Au collision system (Fig. 4.11, Chapter 4). The inferences drawn there are applicable here also. The exponentials fitted to the data of Bi-$K\alpha_{1,2}$ for q = 82 are identical to each other and so are approximately the ones for Au-$K\alpha_{1,2}$. The ones fitted to the data corresponding to q = 81 and 77 have a different, almost negligible slope. These exponentials can be extrapolated to zero target thickness and then the corresponding values represent the real cross sections for approximate single collision conditions in the solid targets. From the least square fit to the projectile K x-ray emission a penetration thickness of about 164±29 μg/cm^2 is obtained where half of the projectiles have filled up their initial K vacancies. The

true, “single collision” cross sections are summarized in Table 6.1. A detailed interpretation and explanation is given in Chapter 6.

5.4 L X-RAY EMISSION IN Bi $^{q+}$-Au COLLISIONS

5.4.1 L x-ray spectra

Although the L x-ray spectra was recorded by both Si(Li) and the Ge(i) detectors, it was analysed only from the Si(Li) spectra. Strong absorbers had to be used in front of the Ge(i) detectors to cut out the high intensity of the low energy L x-rays. Moreover, thresholds of the amplifiers connected to these detectors had to be high in order to cut off the unwanted noise generated from the experimental electronics. In this process low energy x-rays (M x-rays) were partially cut out for certain stripes of the 7-Ge(i) detector. Spectra recorded by first, fourth and seventh stripes of the 7-Ge(i) detector for Bi^{81+}-ions incident on 42 μg/cm^2 target are shown in Fig. 5.15. These spectra, strongly suppressed by absorbers, are to be compared with a similar spectra recorded by Si(Li) for the same ‘q’ and ‘t’ shown in Fig. 5.16. Inferences from L x-ray spectra can be drawn by looking for the effect of varying ‘q’ and ‘t’ on the energy shifts, intensity ratios and the x-ray emission cross sections for both the collision partners.

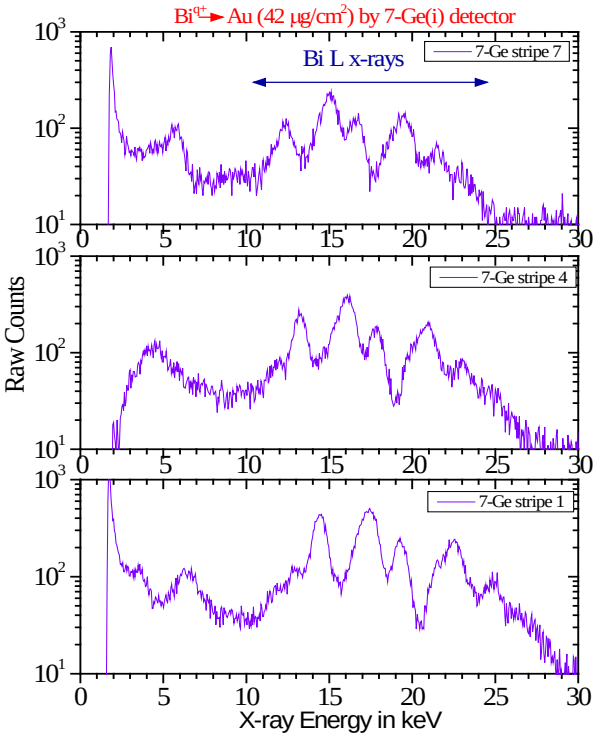

Fig. 5.15 *L x-ray spectra recorded by first, fourth and seventh stripes of the 7-Ge(i) detector for Bi^{81+}-ions incident on 42 μg/cm^2 thick Au target in the laboratory frame.*

5.4.2 Shift in the energy of the L x-ray transitions

Effect of the projectile incident charge state (q)

Fig. 5.16 shows a comparison of the L x-ray spectra for 42 μg/cm^2 thick Au target bombarded by Bi^{q+}-ions for q = 77, 81 and 82 and Fig. 5.17 shows the same comparison but for the thickest Au target investigated i.e. 225 μg/cm^2. The spectra depict the counts normalized relative to the number of ejectiles. The peaks of Au and Bi L x-rays are indicated in the figure. Because of

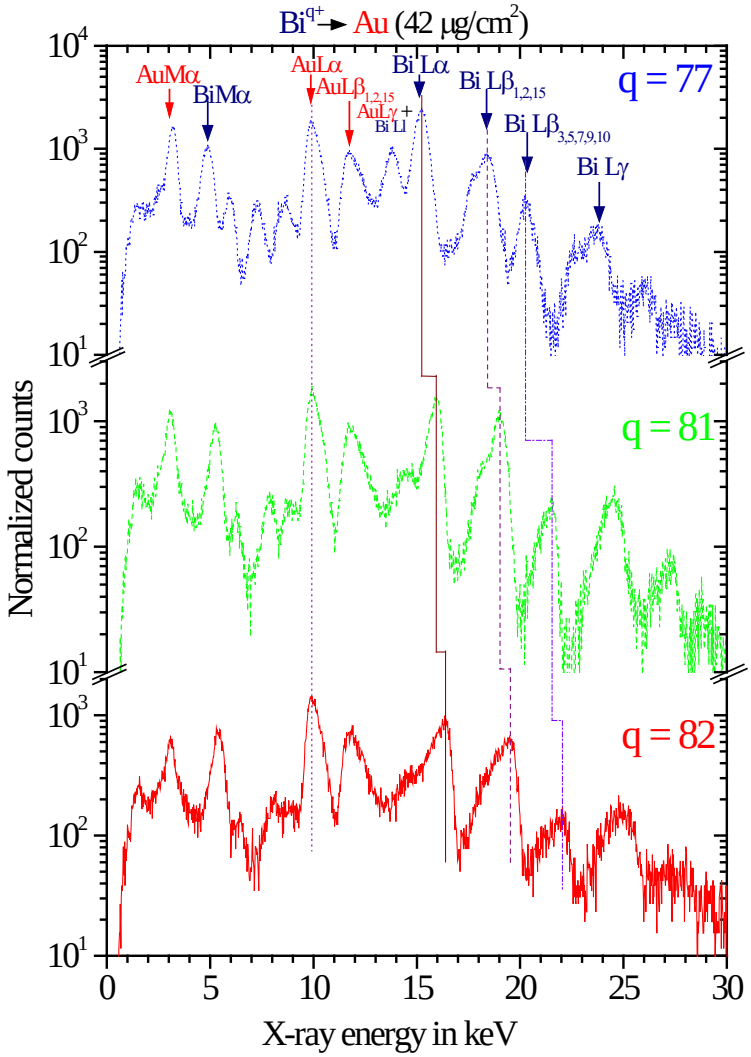

Fig. 5.*16 L x-ray spectra (laboratory frame) for 42 μg/cm^2 thick Au target bombarded by Bi^{q+}-ions for q = 77, 81 and 82. The counts are normalized relative to the number of ejectiles. The dotted line shows the near constant energy of Au-Lα line. The solid, dashed, dash-dotted lines show the shift in the energy of the Bi-L x-ray lines labelled in the figure.*

Doppler shift at 45° Bi-L x-rays are separated to a large extent from the Au-L. However, the Bi-L*l* x-rays are observed overlapped with Au-Lγ x-rays in the figure. The energy resolution of Si(Li) detector contributes to the observed composite peak of Lβ$_{1,2,15}$ for both Au and Bi and as well as for

Bi-L$\beta_{5,7,9,10.}$ The Au and Bi-Lγ x-rays are not resolved clearly into separate peaks and are observed as mere humps. The Au and Bi-Mα x-rays have also been identified in the figures.

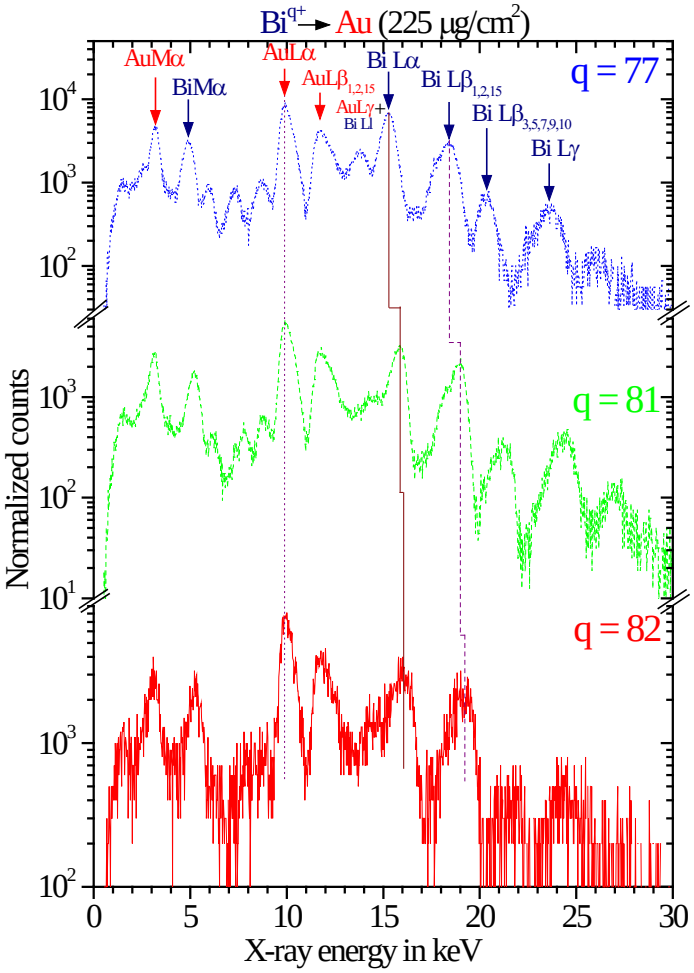

Fig. 5.17 *L x-ray spectra (laboratory frame) for 225 μg/cm^2 thick Au target bombarded by Bi^{q+}-ions for q = 77, 81and 82. The counts are normalized relative to the number of ejectiles. The dotted line shows the near constant energy of Au-Lα line. The solid and dashed lines show the shift in the energy of the Bi-L x-ray lines labelled in the figure.*

The Au target L x-rays are observed at almost the same energy for all the three spectra corresponding to q = 77, 81 and 82 in Fig. 5.16 and 5.17. No remarkable energy shift with increasing charge state 'q' is observed for these x-rays from the spectra. The dotted line in the figures demonstrates the near constant energy of the Au-Lα x-rays. The Bi-L x-rays on the other hand show a remarkable shift in energy towards higher values with increasing q. The solid line through the Bi-Lα x-rays for q = 77 to 82 indicates the shift in energy exhibited by these x-rays with increasing q. Similarly, the dashed line depicts the energy shift experienced by the L$\beta_{1,2,15}$ x-ray peak and the dashed-dotted line represents the same for Bi-L$\beta_{3,5,7,9,10}$ x-rays.

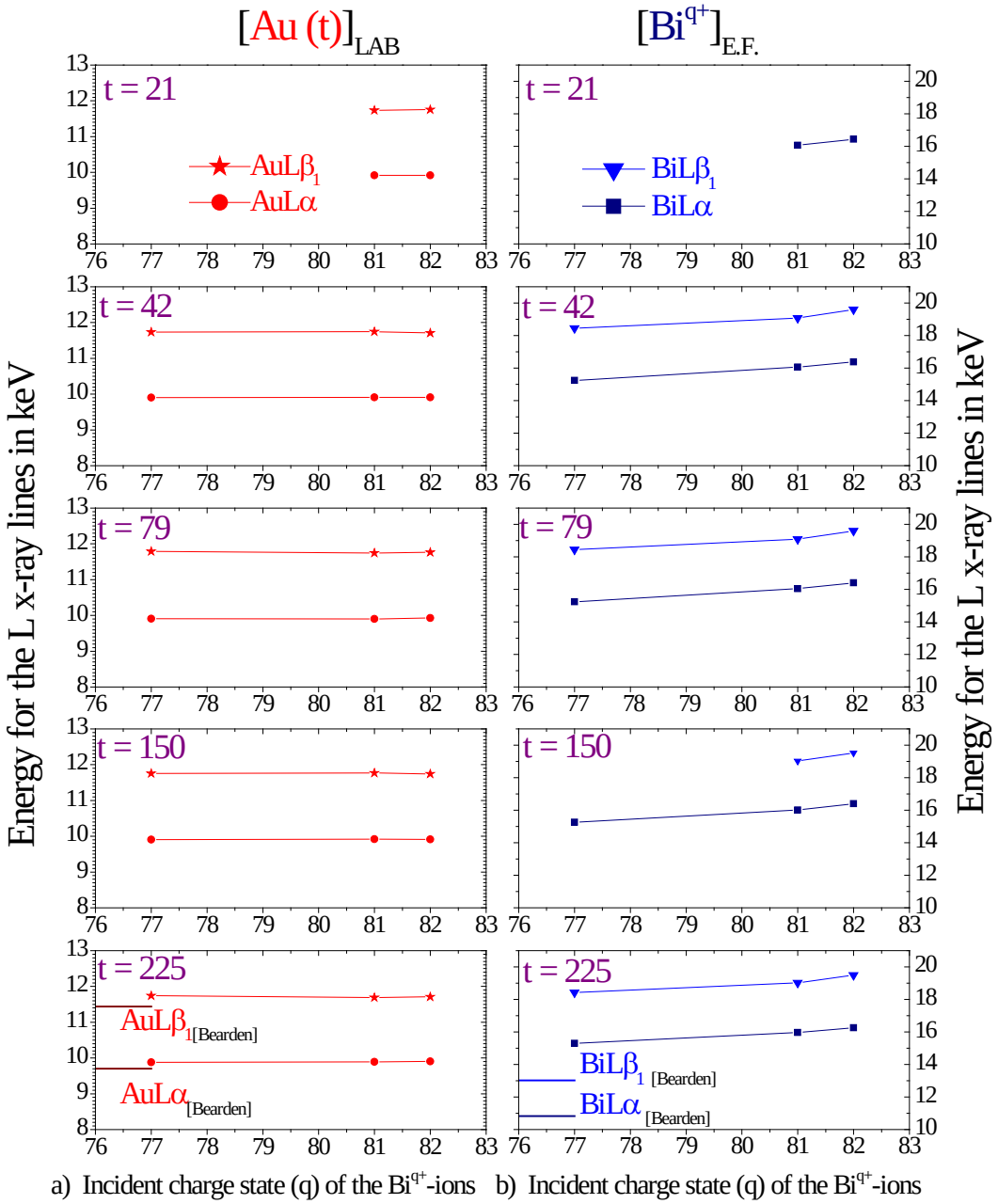

Fig. 5.18 *Centroid energies ($E_{obs.}$) of L x-ray transitions as a function of the incident charge state (q) of the Bi^{q+}-ions.* a) *for Au-Lα,β_1 in the laboratory frame (LAB) and* b) *for Bi-Lα,β_1 in the emitter frame (E.F.). The corresponding standard values of Bearden (E_o) [23] have been indicated by solid lines in the lowermost plot. Au target thickness (t) is in $\mu g/cm^2$. The lines through the data points are drawn to guide the eye. Statistical errors are smaller than the size of the symbols.*

Fig. 5.18 shows the centroid energies of the Au and Bi-Lα,β_1 x-ray peaks in the laboratory and emitter frame respectively with respect to 'q' for all the target thicknesses investigated ($21 \leq t \leq 225$ $\mu g/cm^2$). The graph confirms the observations made earlier. The reasons for shift in energy of x-rays due to change in binding energy by multiple spectator vacancies has been explained in Chapter 2. For Bi^{q+}-ions with an incoming K vacancy (q = 82), the change in the binding energy is the largest

and hence the observed shifts are largest in this case. Fig. 5.19 shows the relative shift $(E_{obs}-E_o)/E_o$ in above mentioned L x-ray transitions and reiterate the observations and inferences.

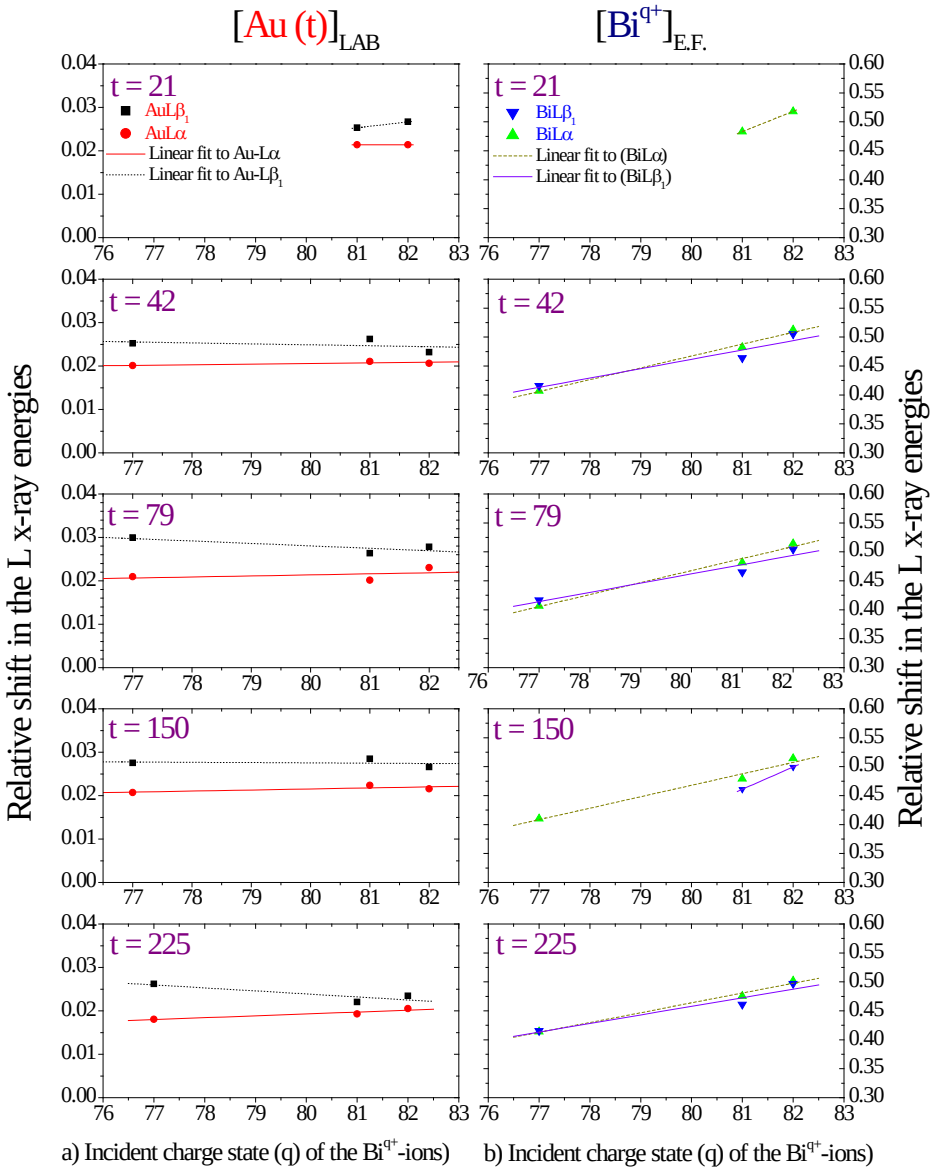

Fig. 5.19 *Relative shift $(E_{obs}-E_o)/E_o$ in L x-ray transitions (centroids) with respect to and normalized to standard values (E_o) [23], as a function of the incident charge state (q) of the Bi^{q+}-ions* a) *for Au-Lα,β_1 in the laboratory frame (LAB) and* b) *for Bi-Lα,β_1 in emitter frame (E.F.). Au target thickness (t) is in $\mu g/cm^2$. Lines drawn are linear fits to the data. Statistical errors are smaller than the size of the symbols. Note the drastically different scales for the Au and Bi.*

Effect of the target thickness (t)

The L x-ray spectra also show a target thickness dependence apart from the q dependence discussed above. Fig. 5.20 for instance shows a comparison of the energy calibrated L x-ray spectra for Bi^{81+}-ions incident on Au targets of various thicknesses investigated viz. 21, 42, 79, 150 and 225 $\mu g/cm^2$. The counts are normalized relative to the number of ejectiles for these laboratory frame

spectra. A similar comparison for Bi^{82+}-ions carrying a K vacancy is shown in Fig. 5.21. The Mα peak and the L x-ray peaks of Au and Bi are labelled in the figures. The shaded region with negatively sloping lines indicate the region of Au L x-rays and that with positively sloping lines indicate the Bi-L x-rays in both the figures. The dotted line through the Au-Lα peaks in Fig. 5.20 and 5.21 does not indicate a noticeable energy shift with target thickness.

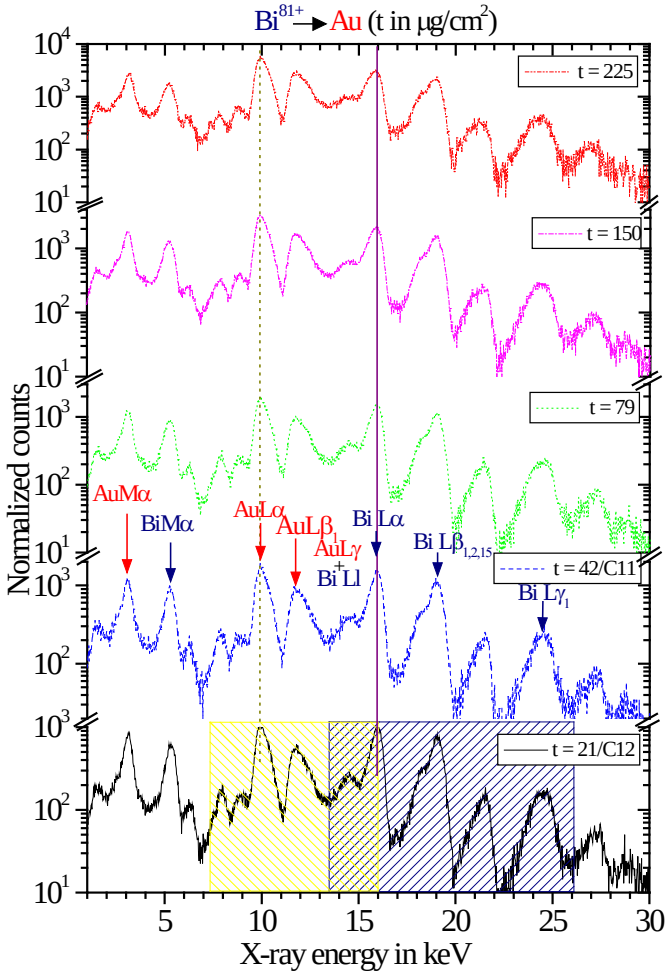

Fig. 5.20 *A comparison of the L x-ray spectra (laboratory frame) for Bi^{81+}-ions incident on Au targets of various thicknesses investigated viz. 21, 42, 79, 150 and 225 μg/cm^2. The counts are normalized relative to the number of ejectiles. The shaded rectangles show the region of L x-ray lines for Au by right, down slanting lines and for Bi by left, down slanting lines. The dotted and the solid lines represent the near constant energy of Au-Lα and Bi-Lα lines with increasing target thickness.*

For Bi^{81+}-ions in Fig. 5.20, the solid line through the Bi-Lα peaks also does not indicate any remarkable energy shift with target thickness. This observation remains the same for Bi^{77+}-ions also. However for Bi^{82+}-ions (Fig. 5.21) the dashed and the solid line through Bi-Lα indicate a shift in energy towards higher values with decreasing target thickness. The dashed line corresponds to the energy of Bi-Lα for 225 μg/cm^2 thick Au target and the solid line for 21 μg/cm^2 thick target. With

increasing target thickness, the projectiles lose their K vacancy partially and hence, the average shift decreases in that case for the projectile lines. The increasing line width points to the same fact.

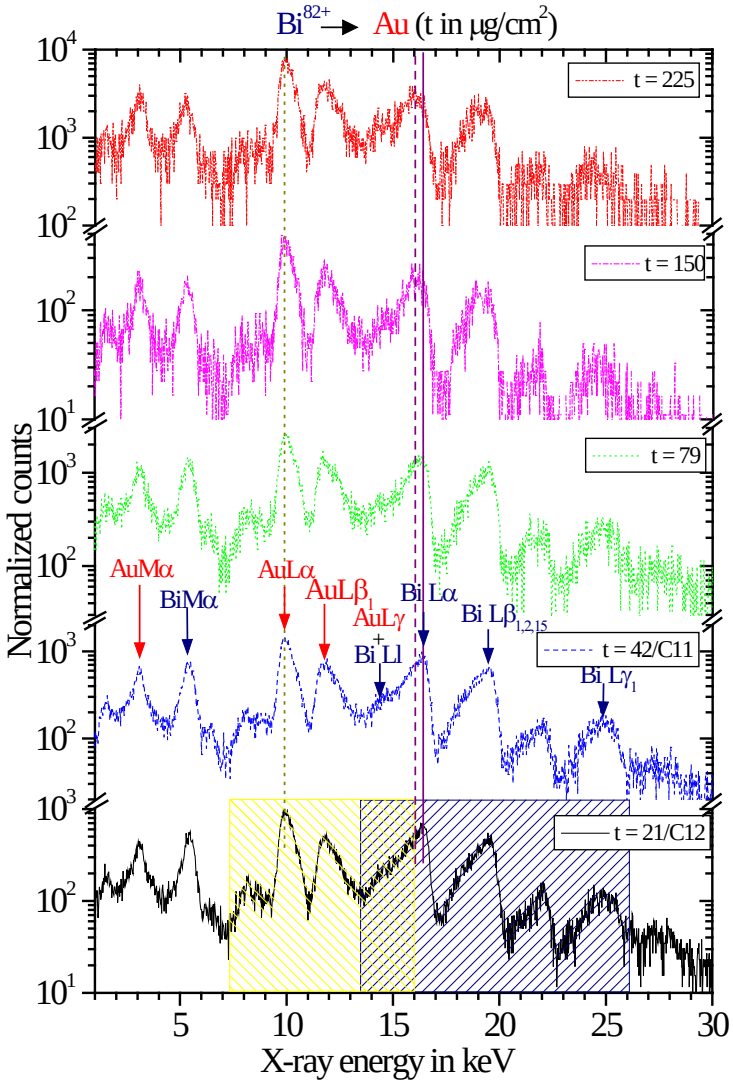

Fig. 5.21 *A comparison of the L x-ray spectra (laboratory frame) for Bi^{82+}-ions incident on Au targets of various thicknesses investigated viz. 21, 42, 79, 150 and 225 μg/cm^2. The counts are normalized relative to the number of ejectiles. The shaded rectangles show the region of L x-ray lines for Au by right, down slanting lines and for Bi by left, down slanting lines. The dotted line represents the near constant energy of Au-Lα. The solid and dashed lines depict for Bi-Lα the slight dependence of the shift with increasing target thickness.*

Fig. 5.22 a) shows the centroid energies ($E_{obs.}$) of Au-Lα,β_1 in the laboratory frame (LAB) and that of Bi-Lα,β_1 in the emitter frame (E.F.) as a function of the Au target thickness (t). The standard values (E_o) of Bearden [23] are indicated in the figure for comparison. Fig. 5.22 b) shows the relative shift (E_{obs}-E_o)/E_o in these L x-ray transitions (centroids) with respect to and normalized to standard values (E_o) [23], as a function of the Au target thickness (t). These L x-ray transitions for both Au and Bi do not show any truly remarkable target thickness dependence. Fig. 5.22 b) only reiterates this observation, however one has to note the different scales for the Au and Bi in this figure indication higher shifts for the projectile than that for the target.

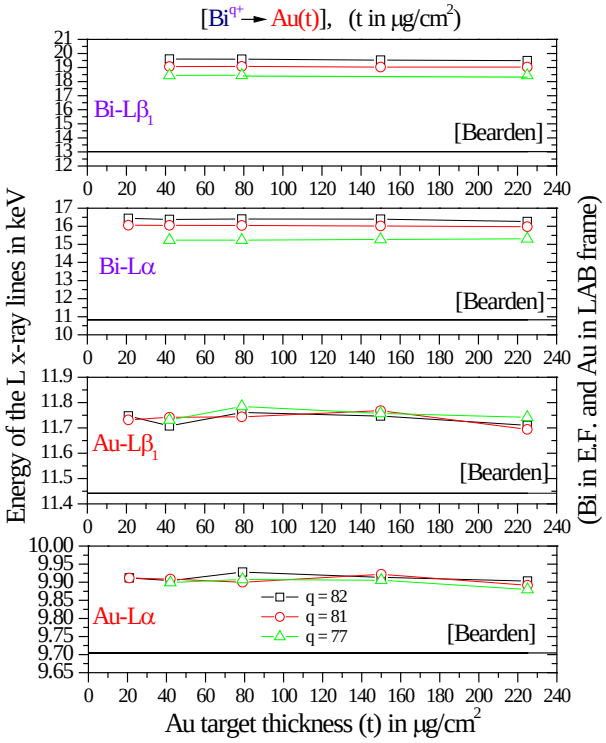

Fig. 5.22 a) *Centroid energies ($E_{obs.}$) of L x-ray transitions of Au-Lα,β_1 in the laboratory frame (LAB) and of Bi-Lα,β_1 in the emitter frame (E.F.) as a function of the Au target thickness (t). The standard values (E_o) of Bearden [23] are indicated in the figure. Statistical errors are smaller than the size of the figure. The lines through the data points are drawn to guide the eye.*

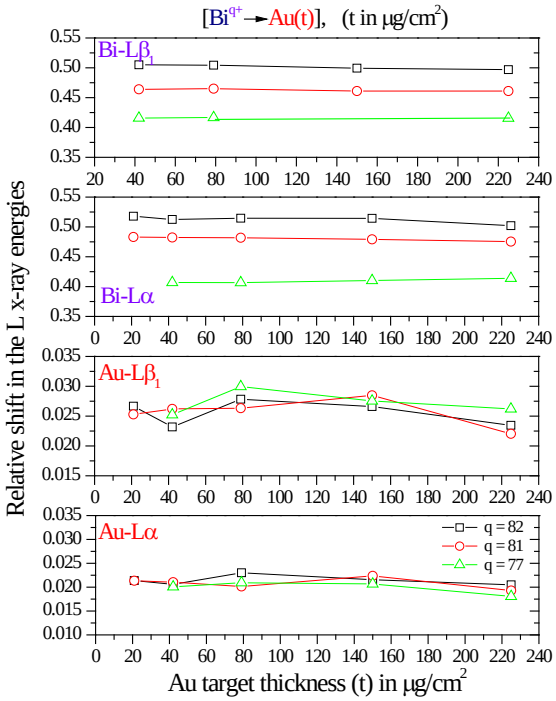

Fig. 5.22 b) *Relative shift (E_{obs}-E_o)/E_o in L x-ray transitions (centroids) with respect to and normalized to standard values (E_o) [23], as a function of the Au target thickness (t) for Au-Lα,β_1 in the laboratory frame (LAB) and for Bi-Lα,β_1 in emitter frame (E.F.). Lines through the data points are drawn to guide the eye. Statistical errors are smaller than the size of the symbols. Note the different scales for the Au and Bi.*

5.4.3 Intensity Ratios of L x-rays

It can be observed from Fig. 5.16 (42 μg/cm^2 Au target) that for the spectra corresponding to q = 77, the peak height of the Bi-Lα x-ray line is higher than that of the Au-Lα and for the spectra corresponding to q = 81, 82 it is vice versa. Any possible influence of the energy differential self absorption in the target has not been considered here. The observation for spectra corresponding to q = 81, 82 for 225 μg/cm^2 Au target is the same as that for 42 μg/cm^2 as can be seen in Fig. 5.17. For this thickest target, the q = 77 spectra shows a smaller intensity of Bi-Lα compared to Au-Lα in contrast to the observation for 42 μg/cm^2 Au (Fig. 5.16).

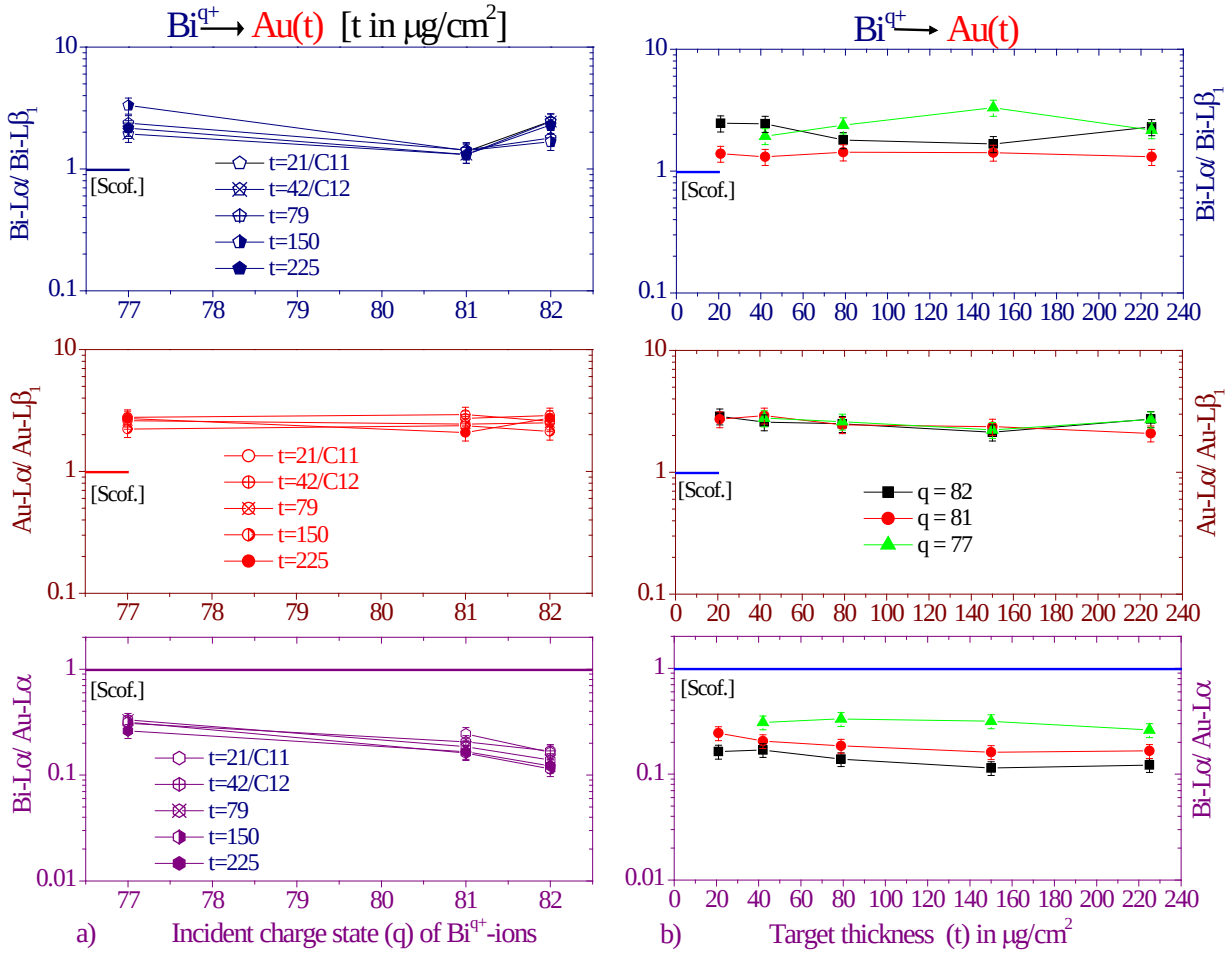

Fig. 5.23 *Measured L x-ray intensity ratios (intra-partner and inter-partner) of the projectile (Bi) and target (Au) as a function of* a) *projectile incident charge state (q) and* b) *target thickness (t). The corresponding single hole values by Scofield [64] have been indicated in the figures as [Scof.]. Lines through the data points are drawn to guide the eye.*

Fig. 5.23 shows graphs of Au-L and Bi-L x-ray intensity ratios viz. Bi-Lα/Bi-Lβ$_1$, Au-Lα/Au-Lβ$_1$ and Bi-Lα/Au-Lα as a function of 'q' and 't'. The inter-partner ratio is corrected for the

solid angle transformation, and hence deviates from the direct observation in the spectra by a factor of 0.623. For q = 77, the inter-partner ratio Bi-Lα/Au-Lα is higher than its value for q = 81 or even for q = 82; this ratio decreases considerably with increasing q. The strong decrease for q = 82 may be caused by the fact that for closed K-shell (q = 77, 81) condition of the projectile, more transitions to L-shell (from the Bi-M) take place in comparison to the case when the Bi^{q+} possesses an open K-shell (q = 82) and M electrons can directly decay to the K-shell. Although q = 81 is also a closed K-shell condition, the half filled L-shell of Bi^{q+} for q = 77 leads to more $M_{4,5}$–L_3 (Lα) transitions than that for q = 81 (L-shell completely empty). Fig. 5.23 b shows that the intensity ratio of Au-Lα/Au-$L\beta_1$ and Bi-Lα/Bi-$L\beta_1$ does not show any remarkable q dependence, the statistics of the spectra limits the observation of any such dependence within errors.

Concerning the M radiation, Fig. 5.16 depicts that for spectra corresponding to q = 82, the Bi-Mα x-ray intensity is more than that of Au-Mα. One cannot observe such a trend for other spectra in Fig. 5.16 or 5.17. As q increases from 81 to 82, the yield ratio of Au-Mα/Bi-Mα decreases indicating a "relative" larger yield for the Bi-Mα x-ray emission. With increasing target thickness (see Fig. 5.17) this ratio increases, possibly caused by the loss of projectile vacancies. However, one has to take into account a shift with q especially for the projectile Mα radiation, changing the intensity ratios by a change of the detector efficiencies.

5.4.4 L x-ray emission cross sections

Since the L x-ray measurement by the Si(Li) was simultaneous to that for the K x-rays described in Section 5.3, hence the normalization procedure followed for the K x-rays and L x-rays is identical. The procedure has been described in detail in Section 5.3.4 above. The emission cross section data for L x-rays of Bi and Au have been calculated by the formula discussed in Chapter 3, Section 3.3.5 (iv).

Fig. 5.24 displays the emission cross sections for Lα and $L\beta_1$ (the most intense L x-ray peaks) for Au in part a and for Bi in part b as a function of q for all target thicknesses investigated. The part a indicates that the Au-Lα and $L\beta_1$ do not show any strong q dependence within the experimental errors, although there might be a tiny tendency of a decrease with increasing q. On the other hand Bi-Lα and $L\beta_1$ cross sections show a definite q dependence, these cross sections decrease with increase in q, in particular for an open projectile K-shell. For q = 82 (open K-shell) the decreased cross sections may indicate that even though electrons are captured to outer vacant shells, the radiative decay has preference to fill first the half empty K-shell. As a result fewer electrons are

present in the M and N shells to decay down radiatively as L x-rays. Here, it is necessary to mention that the results for the asymmetric collision system (U-Au; Section 4.4.3) gives similar dependences for U-Lα although the Au-Lα shows somewhat different dependences which have to be analyzed in the future. In particular energy differential absorption in the target should also be considered here for accuracy.

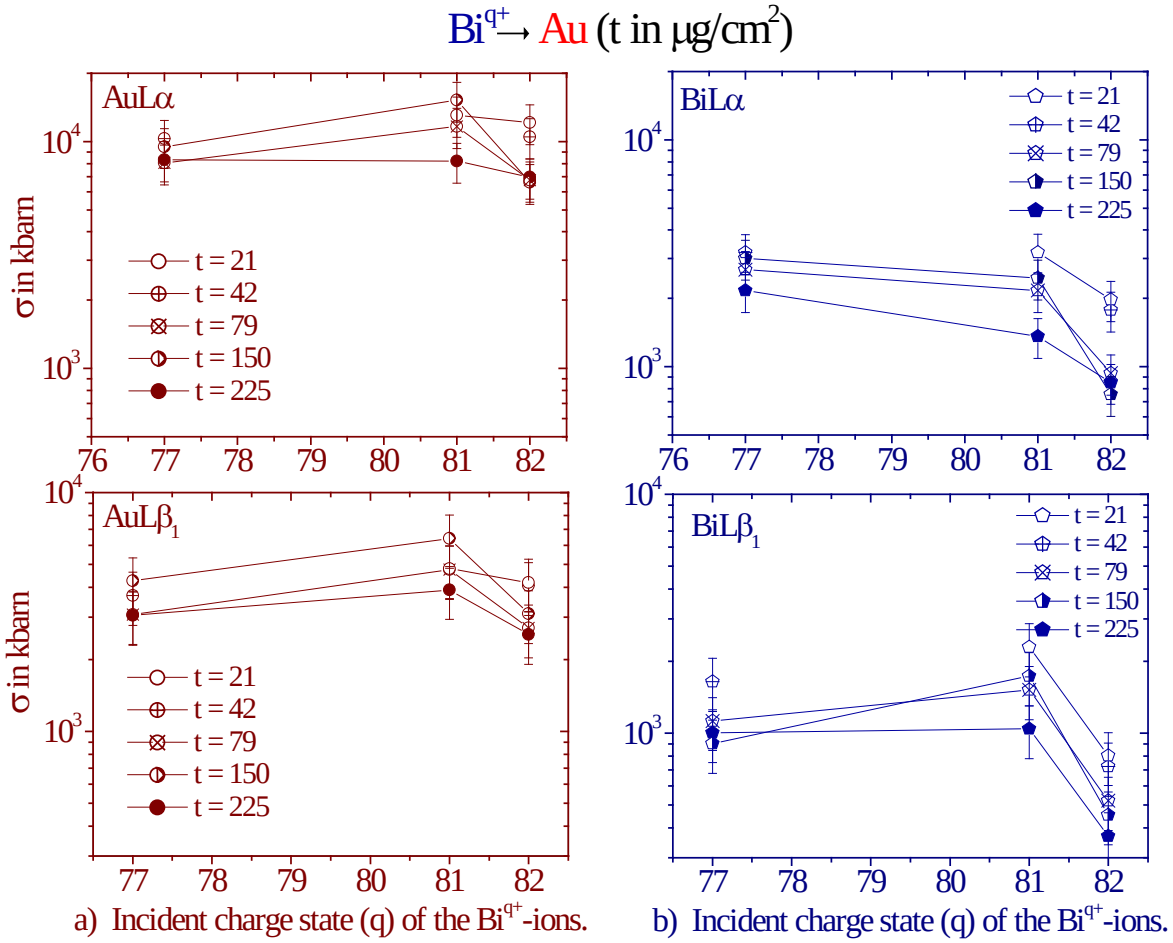

Fig. 5.24 *Lα and Lβ$_1$ x-ray emission cross sections of Au (part a) and Bi (part b) as a function of incident charge state (q) of the Bi^{q+}-ions for all target thicknesses (t, in μg/cm^2) investigated. Lines through the data points are drawn to guide the eye.*

Fig. 5.25 depicts the x-ray yields of Au and Bi-Lα and Lβ$_1$ in part a and b respectively as a function of the Au target thickness (t) corresponding to all q investigated. The Au-Lα and Lβ$_1$ yields show a small decrease with t, whereas the Bi-Lα and Lβ$_1$ data show a stronger but still moderate decrease in the yield with increasing target thickness. This may point to a gradual filling of the projectile vacancies while moving through the solid foil. On comparison of Fig. 5.25 with Fig. 5.14 for K x-ray transitions it is clear that both K and L x-rays show an opposing trend with the yields for the K x-rays being the largest for q = 82 whereas lowest for L x-rays for the same q, cf. Figs. 5.24

and 5.13. Also here, it has to be noted that the dependences for the asymmetric collision system are definitely a lot stronger (Figs. 4.21 and 4.22). .

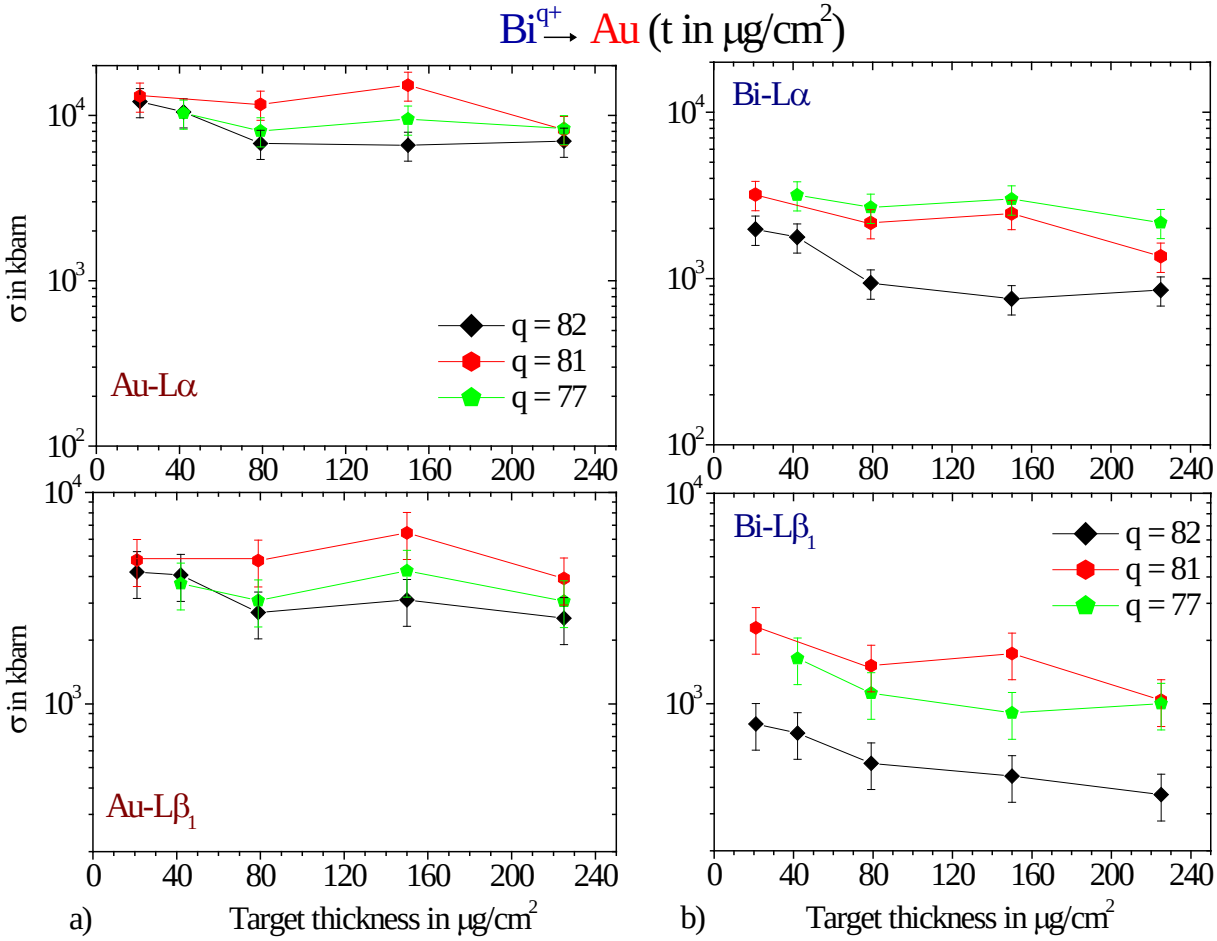

Fig. 5.25 *Lα and Lβ₁ x-ray yields (cross sections) of Au (part a) and Bi (part b) as a function of target thickness (t) corresponding to q = 71, 81 and 82. Lines through the data points are drawn to guide the eye.*

5.5 CHARGE EXCHANGE

5.5.1 Charge state distribution and evolution

For this investigation, the CVD-diamond, position-sensitive particle detector has been used for the measurement of charge state distributions (spread over 24 adjacent stripes) after the magnet spectrometer (Fig. 5.1). The charge state evolution and charge exchange cross-sections has been deduced from the charge state distributions. The detector facilitated normalization of the x-ray emission cross sections too. The position of the detector enabled the detection of five primary charge states of the emerging Bi^{q+}-ions. The actual charge state distribution of the ejectiles was broader than

the active area of the position-sensitive detector. A detector with 55 stripes would be required in principle to record the complete charge state distribution at once (see Fig. 5.26). However, it was possible to draw a "composite charge state distribution" by changing the magnetic field of the spectrometer to appropriate values for successive measurements of groups of 5 charge states. This was followed by normalization of overlapping charge states and all the lower ones (Bi^{q-4}, Bi^{q-5}, Bi^{q-6} etc.).

Such a distribution has been obtained for each measurement (change of $q_{incident}$ as well as target thickness t) except for the Bi^{77+} bombarding on Au targets of 21 and 42 μg/cm^2 thicknesses. This process has been repeated until the intensity of $Bi^{q\text{-lowest}}$ has been negligible compared to the $Bi^{q\text{-incident}}$. Each charge state fraction of the ejectiles was spread out over 3-4 stripes of the particle detector and the various fractions separated clearly from each other with the counts of the valley being negligible compared to that of the peak.

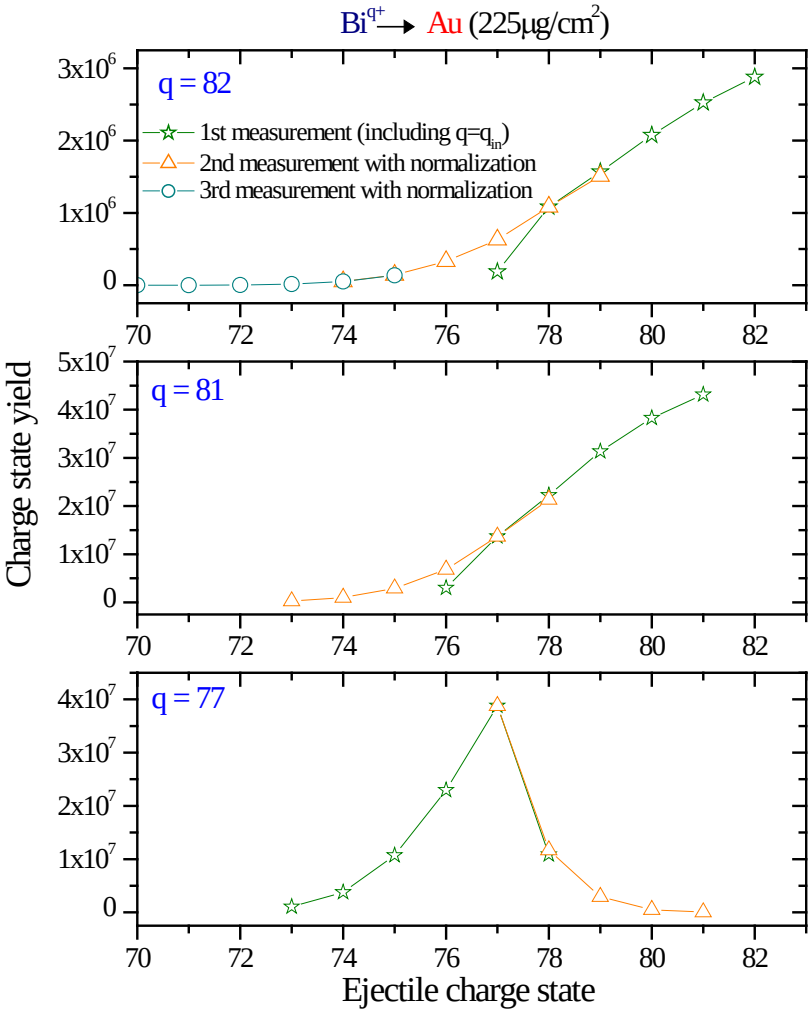

Fig. 5.26 *Area under the peaks for each ejectile charge state vs the outgoing charge states detected by the CVD-diamond, position-sensitive detector for* $Bi^{82+,81+,77+}$*-ions incident on 225 μg/cm*^{2} *Au target.*

Fig. 5.26 shows the area under the peaks for each charge state of the ejectiles vs the outgoing charge states as observed by the particle detector. These yields have been shown for each incident charge state (q = 77, 81, 82) of the Bi^{q+}-ions after penetrating the thickest Au target (225 μg/cm^2). The lines connecting the data are drawn to guide the eye. The curves for q = 82 and 81, show the tail of a distribution with a possible maximum around q = 82 and 81 respectively. This asymmetric distribution is in contrast with the symmetric one for q = 77 having a maximum at q = 77.

Charge state distribution

Fig. 5.27 shows a composite charge state distribution for the particle detector for $Bi^{82+,81+,77+}$-ions incident on 79 μg/cm^2 Au based on charge spectra measured by the particle detector. The dashed lines indicate the lower (for $Bi^{82+,81+}$) or higher (for Bi^{77+}) charge state ensembles observed with the shift of the spectrometer magnetic field. The overlapping of at least one of the charge states (measured with the shift of the magnetic field) with one of the primary charge distribution on the detector is presented in the figure, the former being normalized to latter. About 60% of the ions with q_{in} = 77 and 81 retain their charge state while passing through 79 μg/cm^2 thick Au target and about 30% do so for q_{in} = 82. The strong logarithmic scale is to be noted.

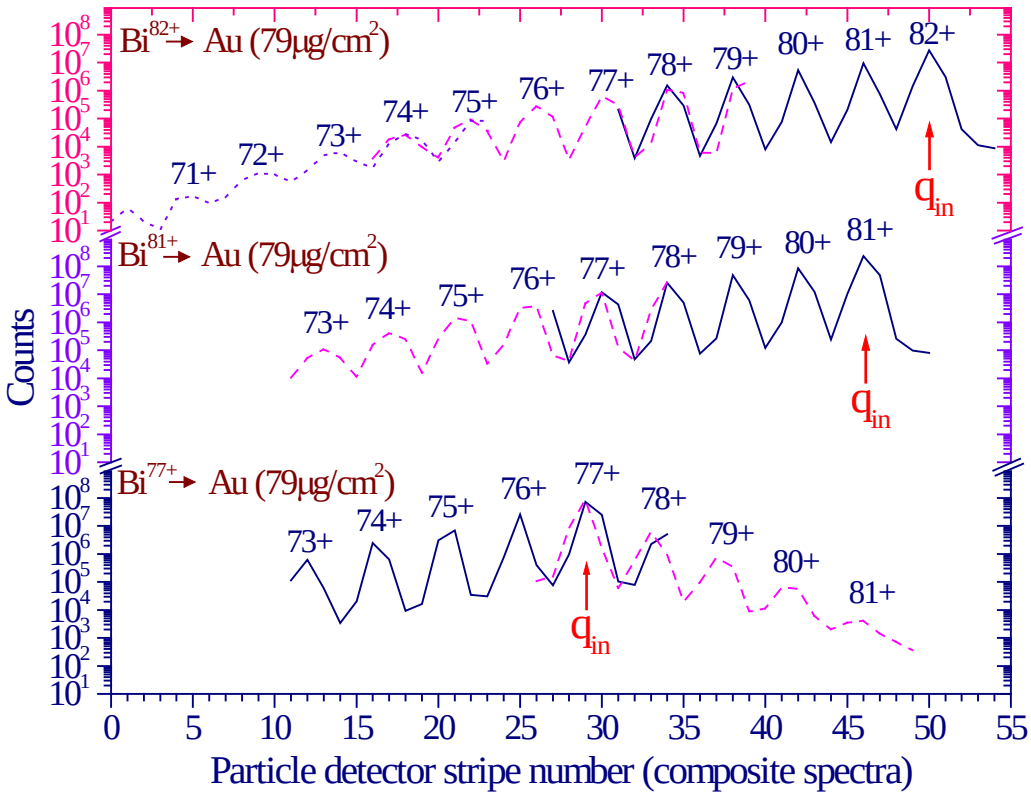

Fig. 5.27 *"Composite charge state distribution" measured by the CVD-diamond, position-sensitive, particle detector for $Bi^{82+,81+,77+}$-ions incident on 79 μg/cm^2 Au target. Note the compressed log-scale.*

The survival probability of the initial charge state of the projectile becomes clearer by the following comparison of target thickness dependence of the charge state distribution. Fig. 5.28 a), b) shows the composite charge distribution in the particle detector for $Bi^{82+,81+}$-ions incident on Au targets of two extreme thicknesses, 21 and 225 μg/cm^2 respectively. The two spectra for different thicknesses look quite similar, except for the initial charge state fraction. For the thin target the initial charge state fraction is roughly an order of magnitude larger than that for the thick one (logarithmic display is condensed for the former case in Fig. 5.28 a). Hence, for the thin target the incoming charge fraction survives with a high probability. From the composite distributions it can be deduced that the equilibrium thickness is larger than 225 μg/cm^2. This assumption can be cross checked by comparing the experimental charge state evolution through the thickness of the target with calculations as is discussed later in this section.

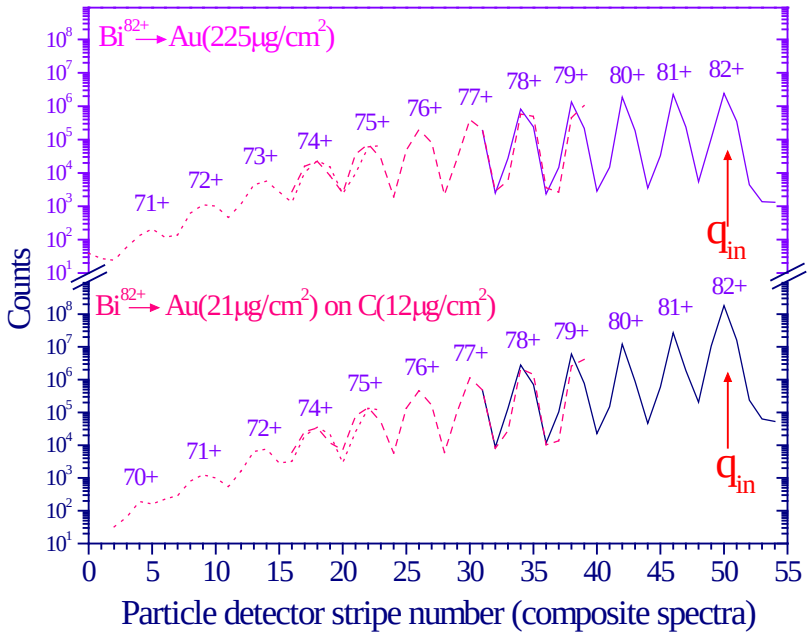

Fig. 5.28 a) *"Composite" charge state distribution measured by the CVD-diamond, position-sensitive, particle detector for Bi^{82+}-ions incident on Au targets of two extreme thicknesses, 21 and 225 μg/cm^2 respectively.*

Fig. 5.28 c) shows the same spectra as above for Bi^{77+}-ions incident on the thickest (225 μg/cm^2) and the thinnest Au target investigated (79 μg/cm^2). For q = 82, 81 it can be observed that more than 90% of the projectile incident charge state survives in the thinnest target (21 μg/cm^2) and about 30% in the thickest target (225 μg/cm^2). For q = 77, about 60% of the ions remain having the initial charge state fraction. Both the figures 5.27 and 5.28 verify that vacancies existing in the inner shells of the projectile (incoming channel of the collision) have a definite probability to survive while penetrating thin solid targets.

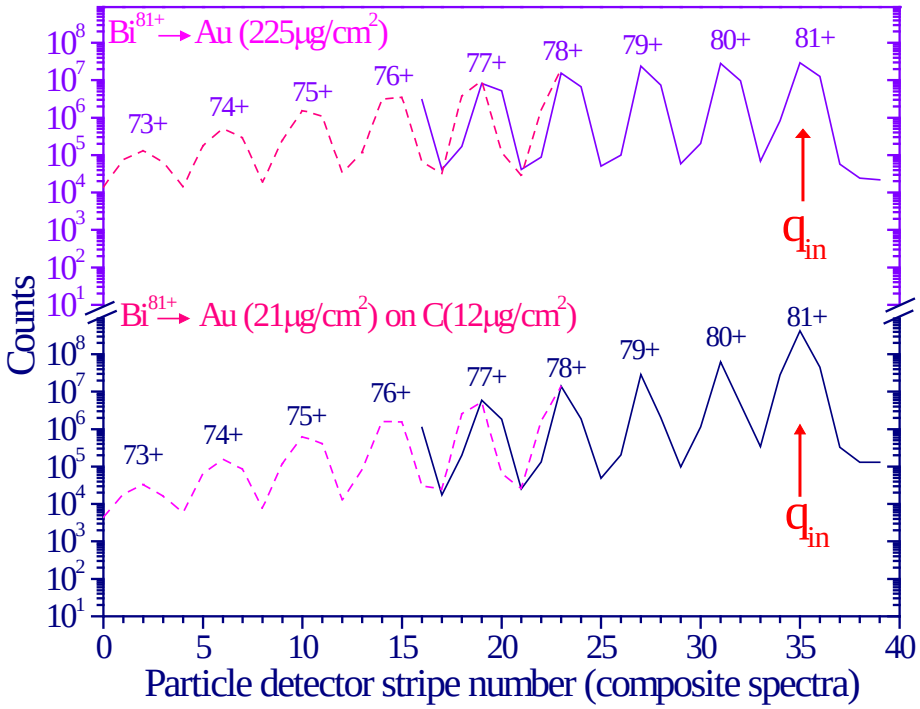

Fig. 5.28 b) *"Composite" charge state distribution measured by the CVD-diamond, position-sensitive, particle detector for Bi^{81+}-ions incident on Au targets of two extreme thicknesses, 21 and 225 μg/cm² respectively.*

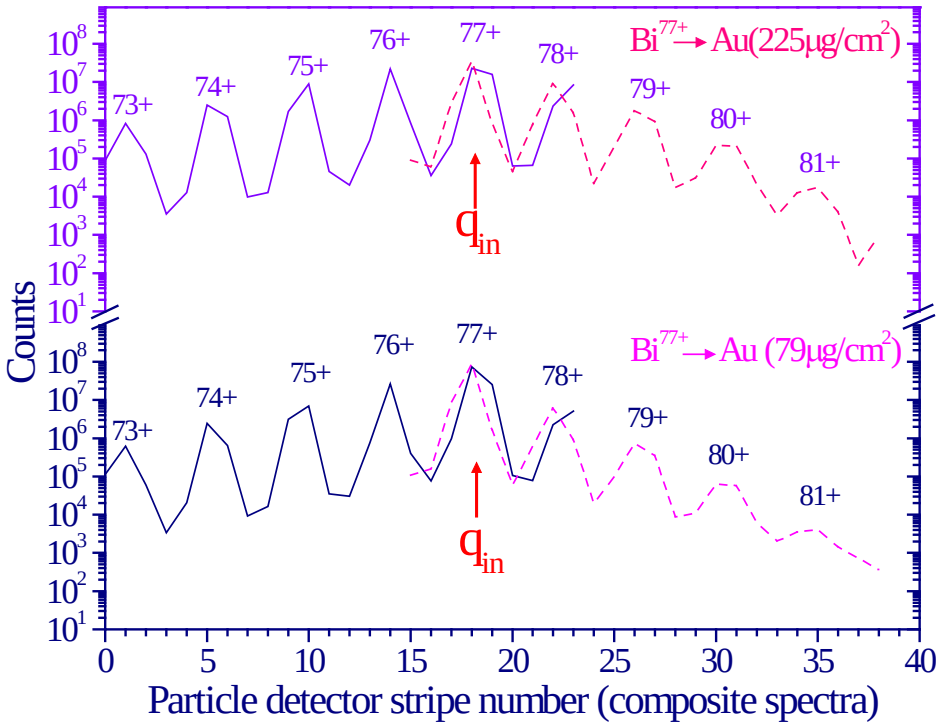

Fig. 5.28 c) *"Composite" charge state distribution measured by the CVD-diamond, position-sensitive, particle detector for Bi^{77+}-ions incident on Au targets of two thicknesses investigated, 79 and 225 μg/cm² respectively.*

Charge state evolution

The intensity of each charge state i.e. the number of ejectiles corresponding to each charge state, N^{q+} was calculated by adding up the number of counts corresponding to each stripe displaying the fraction. The counts corresponding to the stripe representing the minima between the two charge state peaks was divided equally between the two fractions. It was observed that the charge state fractions obtained with the shift of the magnetic field and later normalized with the overlapping charge states constituted 1-10% of the total number of counts for the Bi^{82+}, 8-30% for the Bi^{81+} and 6-17% for the Bi^{77+}. Here, the lower percentage corresponded to the thinnest target and the higher to the thickest Au target. Thus it can be concluded that the primary charge distribution obtained on the position-sensitive, CVD-diamond particle detector constituted the main contribution to the total number of ejectiles and the normalized fractions constituted a small percentage of the same. Hence the uncertainty in the total number of ejectiles introduced due to the shift of the magnetic field and normalization is small.

Fig. 5.29 a), b) and c) shows the charge state fractions i.e. the ratio of the number of particles corresponding to a particular charge state (N^{q+}) with respect to the total number of particles (N_{tot}) (i.e. N^{q+}/N_{tot}) as a function of Au target thicknesses (t) in μg/cm^2 for $Bi^{82+,81+,77+}$-ions. The symbols in this figure present the experimental values and the lines are calculations performed using the GLOBAL code [68].

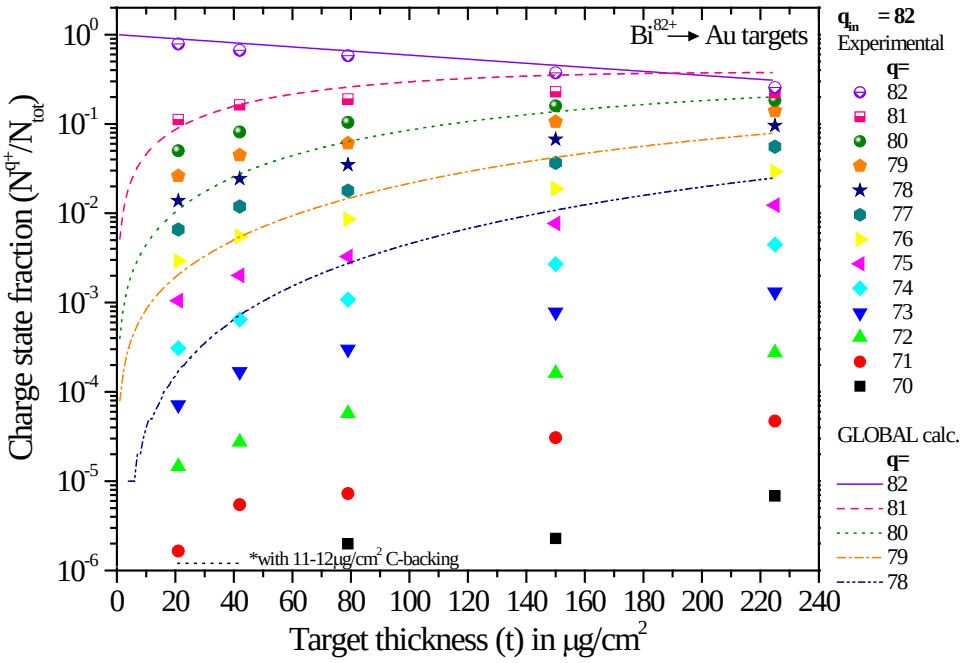

Fig. 5.29 a) *Charge state fractions N^{q+}/N_{tot} of Bi^{82+}-ions as function of the Au target thickness: N^{q+} refers to the number of ejectiles for a particular charge state 'q' and N_{tot} to the total number of ejectiles. The experimental data are denoted by symbols and the lines are calculations performed using the GLOBAL code [68].*

From Fig. 5.29 a) for $q_{incident}$ = 82, it can be deduced that the calculations by GLOBAL agree to some extent with the experimental data for charge state evolution corresponding to q = 82 and 81 (solid and dashed line respectively). For q = 80 and for lower charge states, the calculations by GLOBAL underestimate the measured cross sections. The underestimation is larger for thinner targets. The calculations for charge states lower than 78 have not been shown in the figure as the underestimation of the experimental data increases there. For $q_{incident}$ = 81 (Fig. 5.29 b), the observations are similar. The GLOBAL values agree reasonably with the experimental data for q = 81, 80 and underestimate for other, lower charge states. For $q_{incident}$ = 77 (Fig. 5.29 c), the experimental data does not agree well with the calculations. The curves underestimate the experimental data for q = 75, 76, more for smaller thicknesses than at higher ones. For q=78, 79, 80 and 81, the trend of overestimation is the same as mentioned above. This also indicates that the equilibrium thickness lies higher than 225μg/cm^2.

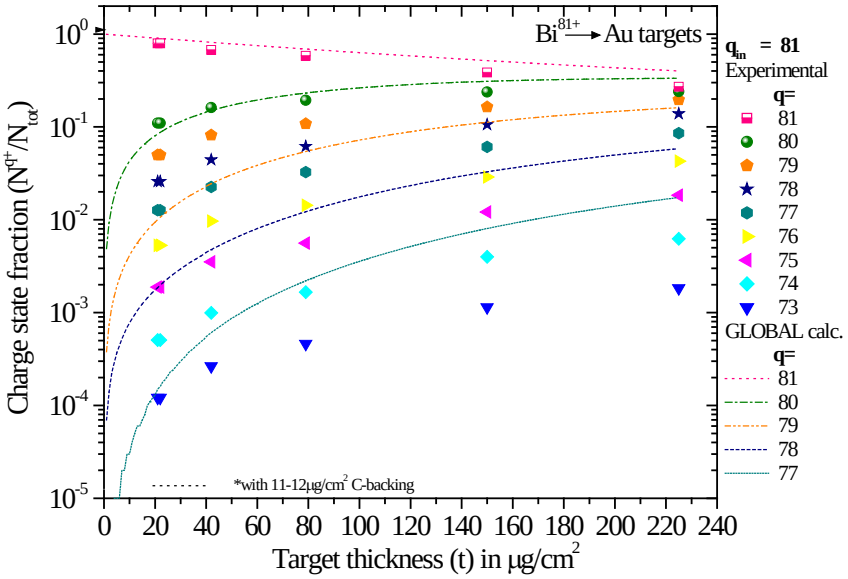

Fig. 5.29 b) *Charge state fractions N^{q+}/N_{tot} of Bi^{81+}-ions as function of the Au target thickness: N^{q+} refers to the number of ejectiles for a particular charge state 'q' and N_{tot} to the total number of ejectiles. The experimental data are denoted by symbols and the lines are calculations performed using the GLOBAL code [68].*

From the Figures 5.29 a) - c) the most important issue, the survival of the primary projectile vacancy can be deduced. In particular the half thickness $t_{1/2}$ where the fraction for the initial charge dropped to 50% can be extracted. For Bi^{82+} ions (open K-shell) the half thickness $t_{1/2}$ in the Au layer is about 150 μg/cm^2, for Bi^{81+} (just closed K-shell) already about 170 μg/cm^2, and for Bi^{77+} (near equilibrium) 200 μg/cm^2. Hence for the ion energies used here, thin Au target foils can be used for studying inner shell process in close quasimolecular collisions with well defined entrance channels.

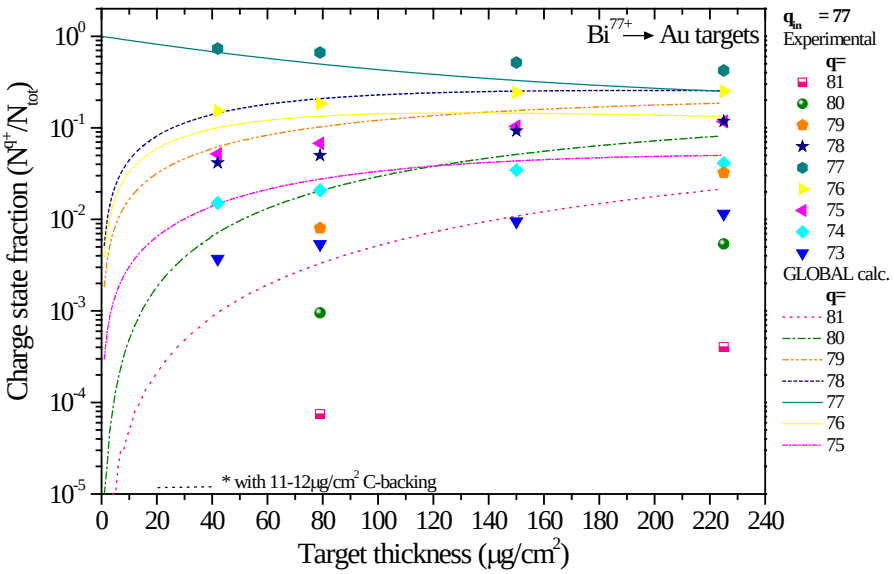

Fig. 5.29 c) *Charge state fractions N^{q+}/N_{tot} of Bi^{77+}-ions as function of the Au target thickness: N^{q+} refers to the number of ejectiles for a particular charge state 'q' and N_{tot} to the total number of ejectiles. The experimental data are denoted by symbols and the lines are calculations performed using the GLOBAL code [68].*

5.5.3 Charge exchange cross sections

Charge exchange cross sections have been determined experimentally from the charge state distribution (Fig. 5.28 a) and the dependence of charge state fractions on target thickness (Fig. 5.29 a). During distant collisions, the Bi^{82+}-ions (incoming projectile K-vacancy) capture electrons in the outer shells. The total electron capture cross section can be calculated from the target thickness dependence of the ratio N^{82+}/N_{tot}. The curve corresponding to N^{82+}/N_{tot} in Fig. 5.29 a) has been fitted with an exponential function of the form:-

$$y = A\ (\exp^{-\sigma t})$$

Here σ is the total electron capture cross section and was found to be equal to $4.3 \cdot 10^{-18}$ cm^2 or 4300 kbarn. This value has been compared with the calculations from two different approaches, the Eikonal approach of Eichler [53] and the semi-empirical, non-relativistic scaling prescription for non radiative capture (NRC) by Schlachter *et al.* [50] (see below).

Additionally σ_{cap} has been deduced from the measured values of x-ray emission cross sections for capture to L-, M-shell and a total. For closed incoming projectile K-shell (q=77, 81), the measured Bi-L x-ray emission cross sections provide an estimate of the capture into Bi M-shells (for higher lines into N, ... shells). Estimating the Bi-Lα and Bi-$L\beta_1$ cross sections for single collision conditions i.e. corresponding to t=0 (see Fig. 5.24) and summing up, the σ_{cap}^{M} is calculated to be

about (3.35)+(1.9) ≈ 5.25Mb. For an open incoming projectile K-shell (q=82), the Bi-L radiation is reduced (see Fig. 5.24) compared to its values for the closed case (q=77, 81) as part of the captured M shell electrons decay directly to the K-shell (leading to Bi-Kβ emission). This reduction can be calculated from the cross sections for Bi-Lα, as a difference between its value for q=81 and q=77 to the corresponding value for q=82. This gives a σ_{cap}^{M}-reduction to be about 1.5 Mb. Correspondingly one can note that the shifts in L x-rays increase for an open Bi K-shell as is expected with a predominance of mostly single capture. The Bi-K radiation for an open incoming K-shell comprises capture to Bi-L and also higher shells (including cascades). The Bi-Kα_1 cross section corresponding to t=0 can be used to estimate this value. However a multiplicative factor of about "3" (maximum, see Table 6.2) has to be taken to account for all the decay K channels i.e. Kα_1, Kα_2, Kβ_1 and Kβ_2. This yields a total capture cross section of σ_{cap}^{Tot} = 5.1Mb. Subtracting the Bi-L cross sections i.e. σ_{cap}^{M} (and accounting for the reduction) from σ_{cap}^{Tot}, one gets the capture to the Bi-L shell. Hence, σ_{cap}^{L} = 5.1-5.3+1.5 =1.24 Mb. Above are shell differential results deduced from measured x-ray cross sections.

Fig. 5.30 summarizes the electron capture cross sections just as done for U-Au collision system (Fig. 4.23, Chapter 4). The cross section distribution according to Eikonal approximation for capture from Au (K, L, M and N) shells to vacant shells of Bi (K to T) is indicated by the curves. The calculations show that the total cross section for capture from target L and M shells (to be read from top of the figure) is most probable (thin solid line with empty circles denoting the four values (*)). The total cross section distribution (thick solid line (#)) for capture into all K to T Bi shells suggests a preferential capture to the L, M and N shells with a maximum for the Bi-M shell. Values for total electron capture cross sections according to Schlachter *et al.* [50] are indicated as empty squares in the figure. These values do not differ appreciably from each other when calculated for different incident charge states of the projectile. The experimental value of the σ_{cap}^{Tot} (~4300 kbarn) determined from the charge state evolution (for q = 82) is indicated in the figure along with those deduced from x-ray emission cross sections (described above). The Schlachter values are only slightly underestimating the experimental data. The σ_{cap}^{L} and σ_{cap}^{M} determined from x-ray emission give a general idea of the capture process in these near symmetric collision systems and more accurate data are required for a rigorous comparison.

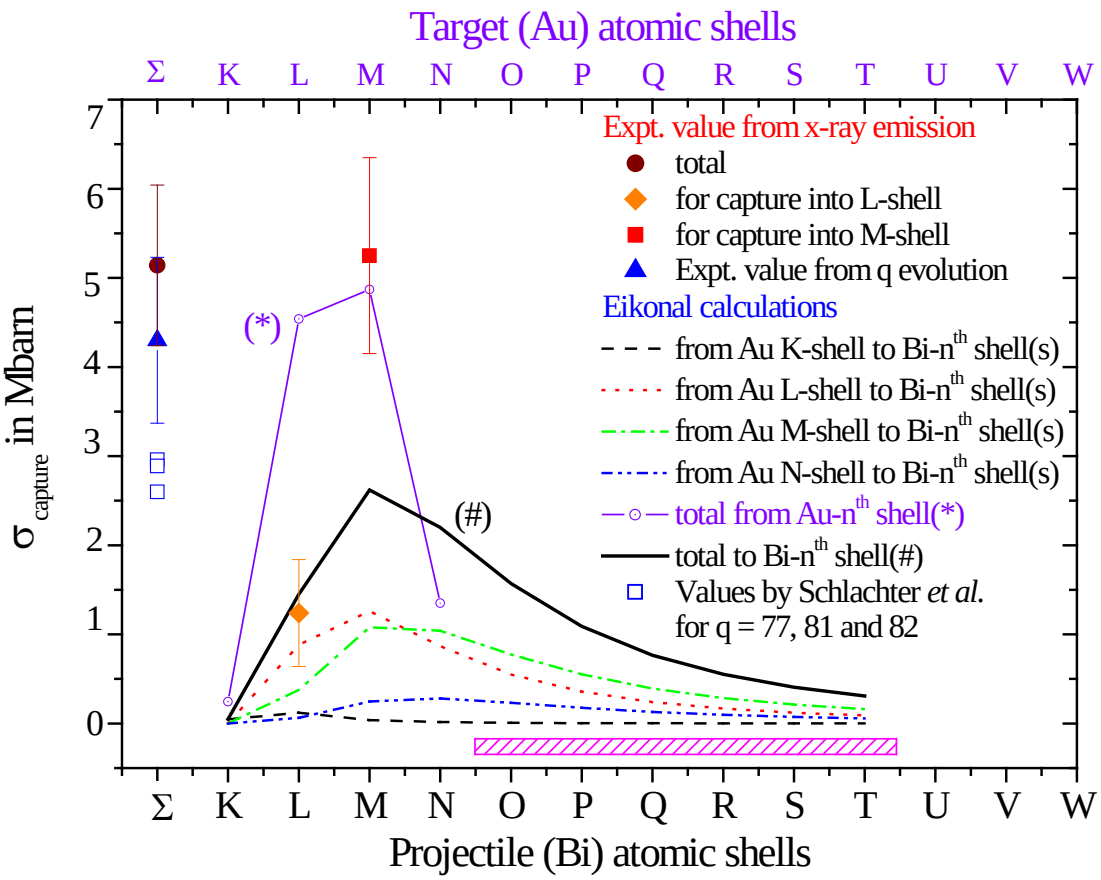

Fig. 5.30 *Shell differential electron capture cross sections vs the atomic shells of the projectile (Bi) calculated theoretically and from experimentally measured values. The curves signify the distribution of the cross sections according to Eikonal [53] from Au K, L, M and N shells to various projectile shells (shown on the abscissa) and their total. (#):-* σ_{cap}^{Tot} *from Au K, L, M and N-shells to a Bi-n*th *shell (K to T), (to be read from abscissa). (*):-* σ_{cap}^{Tot} *from a Au-n*th *shell (K to N) (to be read from axis on top) to all Bi-shells (K to T). The Schlachter [50] values are a total for q = 77, 81 and 82. The experimentally determined values of* σ_{cap}^{L}, σ_{cap}^{M} *and* σ_{cap}^{Tot} *from x-ray emission cross sections (*$K\alpha_{1,2}$,$\beta_{1,2}$ *for q=82 and L*α *for q<82) are included along with the value deduced from measured 'q' state evolution.*

Table 5.2 gives a comparison of the above mentioned experimental and theoretical values. The total capture to Bi K to N-shells (6.32 Mb see column 5) is in good agreement with the σ_{cap}^{Tot} deduced from x-ray emission cross sections (5.1 Mb) and in fair agreement with that from q state evolution (4.3 Mb). A total of the Eikonal cross sections for capture from Au K, L, M, N shells to Bi (K to T shells) yield a value of 11.4 Mb. As has been mentioned earlier, σ_{cap}^{Tot} estimated through Bi K x-ray emission cross sections (for open K-shell) reflects only one electron capture and not multi electron capture or successive capture in different collisions. The latter is manifested through σ_{cap}^{M} (including capture into higher shells). The higher values of σ_{cap}^{M} are probably due to this reason and

this has to be investigated further. However, without further studies a conclusion cannot be drawn. As per the Bohr's criterion mentioned earlier in Chapter 4, the collision velocity of Bi-ions is larger than the velocity of electrons in the Bi-L shell. In principle the electrons captured to N and higher shells will be reionized quickly (before being able to cascade down to inner shells) and hence the bulk of the curves for O and higher shells can be safely neglected (shaded rectangle at the bottom of the figure) in calculating total capture to Bi n^{th} shell reducing Eikonal value considerably to about 6.3 Mb.

Table 5.2 *Total electron capture cross sections for 69 MeV/u Bismuth on Gold target calculated by Schlachter et. al. formula [50], the Eikonal approximation [53] and the values determined from measured projectile x-ray emission cross sections. The* σ_{cap}^{L} , σ_{cap}^{M} *represent the calculated cross section for electron transfer from target K to N shells into the projectile L and M shells respectively.* $\sigma_{cap}^{Tot}(1)$ *represents the electron capture from the target K to N shells into the projectile K to N shells.* $\sigma_{cap}^{Tot}(2)$ *is the electron capture cross section from the target K to N shells into all K to T projectile shells. The experimental values* σ_{cap}^{Expt-X} *are deduced from the projectile x-ray emission yield and the* σ_{cap}^{Tot-q} *from the charge state distribution.*

Projectile incident charge state (q)	σ_{cap}^{Th} **in Mb**					σ_{cap}^{Exp} **in Mb**			
	Schlachter *et al.* [50]	**Eikonal approximation** [53]				σ_{cap}^{L-X}	σ_{cap}^{M-X}	σ_{cap}^{Tot-X}	σ_{cap}^{Tot-q}
		σ_{cap}^{L}	σ_{cap}^{M}	σ_{cap}^{Tot} (1)	σ_{cap}^{Tot} (2)				
82	2.96	1.45	2.62	6.32	11.4	1.24±0.6	5.3±1.1	5.1±0.9	4.3±1.0
81	2.89								
77	2.60								

The Eikonal approximation predicts a maximum capture to the Bi-M shell and Bi-Kβ_1 (M_3-K transition) emission has been observed with a low intensity only for q = 82. For q = 77 and 81 this K-decay channel is closed and the L radiation provides the requisite information. The Bi-Lα cross section is in the order of 3 Mb confirming the possibility of capture to the projectile M shell (cf. Figs. 5.24 and 5.25). Additionally, it can be seen from Fig. 5.24 that the Au-L emission is considerably larger (factor of about 3) than the Bi-L emission. However, it is comparable in magnitude to that of Bi-Kα manifesting the capture from the Au-L shell and further indicating that for the Au-L shell, ionization is the dominant channel compared to loss to the projectile (capture).

CHAPTER VI

COUPLING DISTANCES IN SUPERHEAVY COLLISION SYSTEMS

6.1 INTRODUCTION

The details and results of the experiments performed with very heavy, extremely charged projectile-ions at SIS for a slightly asymmetric (U-Au) and a near symmetric (Bi-Au) very heavy collision systems have been given in Chapter 4 and 5 respectively. A general discussion of the results obtained is given in Section 6.2. Section 6.3 presents a summary of the results of this investigation. The projectile and target x-ray lines' energy shifts and intensity ratios are given in Section 6.3.1 and 6.3.2 respectively. The results of x-ray cross section measurements for both K and L x-ray emission are summarized in Section 6.3.3. Section 6.3.4 explains the charge state dependence of the x-ray cross sections. Section 6.3.5 comments on the survival probability of the "prior to collision" inner shell (K) vacancies for projectiles penetrating a solid. The interpretations from the results of charge state evolution and charge exchange cross sections measured or calculated for the collision systems is given in Section 6.3.6. Section 6.4 offers an explanation of the observations made from x-ray emission on the basis of the quasimolecular model. Section 6.4.1 uses the level diagrams evaluated on the basis of the quasimolecular model to interpret the results. Section 6.4.2 provides an estimation of the interaction distances for "electron capture", for "K-K transfer" (vacancy transfer between projectile K-shell and target K-shell) and for "L-K coupling" (coupling between the L-shell of the projectile and K-shell of the target). Section 6.5 derives a correlation between the interpretations from K and L x-ray emission and those from charge state evolution and charge exchange cross sections of the collision systems. Thus a comprehensive picture of the processes taking place during heavy-ion, heavy-atom collisions in the light of the above discussion and interpretations is presented along with conclusions.

6.2 DISCUSSION OF RESULTS

In general ion-atom interaction involves two different regimes, distant collisions showing evidently large cross sections and close collisions with smaller cross sections. Both regimes leave different fingerprints in the x-ray emission therefore, the details of the interaction mechanisms can be

understood from the collision induced x-ray radiation. The reported results on x-ray emission give information mainly on three different subjects:

- On the excitation status of the collision partners while the projectile penetrates the foil. After the interaction it is manifested by the observed transitions, their energy shifts and intensity ratios (see Section 6.3.1 and Section 6.3.2).
- On the probability of survival of a projectile vacancy while penetrating a solid foil (see Section 6.3.5) from the variation of the x-ray emission, particularly that of cross sections with foil thickness (see Section 6.3.3). This can also be deduced from the complimentary, direct measurements on charge exchange (see Section 6.3.6).
- On the interaction mechanisms for the two regimes, capture and loss for distant collisions and inner shell interaction for close collision processes, mediated especially by the variation (increase) of cross sections with the incoming charge state (q) of the projectile. (For K and L cross sections see Section 6.3.3 and 6.3.4).

The two interaction regimes

The distant collisions involve outer and to some extent intermediate shells also leading to charge exchange, i.e. loss and capture of electrons. For highly charged projectiles electron capture is a dominant phenomenon. The projectile L x-rays reflect capture to excited states – and if there is already an incoming projectile K vacancy, the same is true additionally for the K radiation too. In the latter case, both K and L radiation shed light on the population distribution of the projectile due to the captured electron. The situation is different for the initially neutral target atoms in the bulk. For this case, loss and multiple ionization (as well as excitation) in outer (and intermediate) shells are the dominant processes. The electrons lost from the target are captured into the projectile to some extent. As a result the target radiation may provide some additional information on the target levels contributing to the electron capture by the projectile. However this effect might be completely overwhelmed by the intense target ionization.

After the strong perturbation due to the collision is over, the target atom has the possibility to rearrange itself quickly with the existing electrons in its environment. However the swift projectile does not have sufficient number of electrons in the proper phase space for its rearrangement. This indicates that post collision, the projectile remembers its initial charge state distribution (more so in outer levels) to a large extent whereas the target still reflects its status in the bulk. This general difference in the outer and medium shell population is also reflected mainly by the energy shifts at variance for both the collision partners. To some extent the intensity ratios are also helpful in

determining the final electron population distribution. (For shifts and intensity ratios see Section 6.3.1 and Section 6.3.2).

For close collisions the inner shells of both partners interact with each other and overlap transiently to form a quasi-molecule. After the collision, the K radiation of both partners give information on inner shell ionization/excitation and interaction mechanisms. In particular coupling mechanisms between inner shells of both partners can be probed if special/chosen incoming channels are varied (i.e. opened/closed). Nevertheless, the difference in the post collision outer shell population for projectile- ion and target atom becomes evident by investigating the energy shifts for the inner shell transitions of both partners at variance.

Opening an incoming channel for inner shell excitation leads usually to an increase in K radiation for both the collision partners. However, if an incoming K vacancy is provided in the projectile, the increase in K projectile radiation caused by the inner shell interaction is completely overshadowed by the distant collision processes. For an open projectile K-shell, the capture to higher shells manifests its existence suddenly by K radiation and this has a large cross section. Hence, for an incoming projectile K vacancy the increase in target K radiation indicates the inner shell interaction whereas the increase in projectile K radiation is dominated by capture, a distant collision process.

Finally, the main goal has been to get information on the inner shell interaction mechanisms (see Section 6.4) after having established that projectiles will retain their inner shell (K) vacancies while penetrating a solid foil with a certain high probability. Thus from target thickness dependence of the x-ray emission, cross sections for zero target thicknesses can be extracted, i.e. cross sections under single collision conditions. With these cross sections and with the help of appropriate “level diagrams” (see Section 6.4.1) finally the following coupling distances (Section 6.4.2) could be extracted using some approximate values for coupling strengths and compared to level crossing regions in the level diagrams:

- K-K sharing – deduced from K emission of both collision partners for closed, incoming projectile K-shell and its increase from the target K radiation for one incoming projectile K vacancy.
- L-K shell coupling – deduced from observed increase in K x-ray cross sections of both collision partners with the increase of incoming j=1/2 vacancies in the projectile.

Only oversimplified models could be used for this interpretation as presently no full dynamic coupled channel calculations exist.

- A rough interaction distance for capture was also deduced from the increase in projectile K emission carrying a vacancy in the incoming channel.

6.3 SUMMARY OF RESULTS

6.3.1 Energy shifts for K and L x-ray emission

The shifts in the energies of the K and L x-ray transitions towards higher values have been investigated for both U-Au and Bi-Au collision systems. The reasons for the energy shifts have been explained in Chapter 2. The energy shifts were estimated for the collision systems to obtain additional information on the distribution of population in the higher/outer shells. Although the present investigation was not designed for precision energy shift measurement, nevertheless their rough values for K and L x-ray emission reveal interesting trends shedding light on the collision processes relevant for outer shells. The centroid energies of Au-Kα_{1},α_{2} (lab frame) and U-Kα_{1},α_{2} (emitter frame) as a function of the projectile incident charge state 'q' has been shown in Fig. 4.5 a and b respectively for all target thicknesses investigated in comparison to the standard, single hole values of Bearden [23]. Similarly, Fig. 5.8 a, b shows the centroid energies of Au-Kα_{1},α_{2} (lab frame) and Bi-Kα_{1},α_{2} (emitter frame) respectively as a function of q. The corresponding shifts relatively normalized to the standard values have been shown in Fig. 4.6 for U-Au collision system and in Fig. 5.9 for the Bi-Au collision system.

As a summary the relative shifts of Au-Kα_{1},α_{2} (lab frame) and that of U- and Bi-Kα_{1},α_{2} (emitter frame) are shown in Fig. 6.1 a), b) respectively as a function of the projectile incident charge state (q). All the Au-, U- and Bi-K x-ray transitions are observed at higher energies as compared to the standard values (see Fig. 4.5 and Fig. 5.8) confirming increasing multiple ionization (with spectator vacancies in the upper levels) in all of them. The Au-K x-ray transitions show only a slight q dependence whereas both U- and Bi-Kα_{1},α_{2} show a distinct dependence, the shifts increasing with increasing q. The Au-K x-ray transitions show a relative shift of 1-2% for U-ions and 1-1.5% for Bi-ions, increasing slightly with an increase in q. On the other hand, U-K x-ray transitions show a larger relative shift of 2-4% as compared to 1-2.5% for Bi-K x-ray transitions both increasing with an increase in q. It is clear that even for lower q, multiple vacancies exist in the outer/higher shells during x-ray emission for all q investigated. The U- or Bi–ions are laden with a large number of outer shell spectator vacancies in the incoming channel of the collision itself and the Au target gets multiply ionised due to either electron capture in a distant collision as the projectile approaches it or

due to (ionisation/excitation) during the collision.

During close collisions, the multiple vacancies in the higher shells increase with an increase in the q and the projectile somehow recalls its initial high ionization in the outer shells. The distant

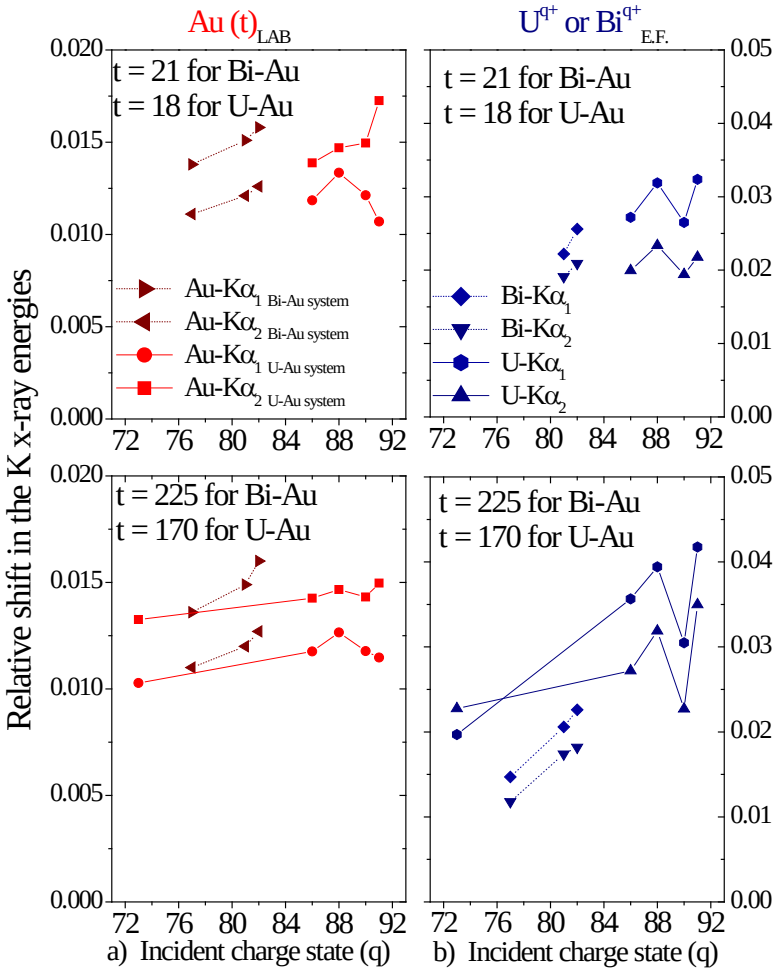

Fig. 6.1 *Relative shift $(E_{obs.}-E_0)/E_0$ in K x-ray transitions (centroids) with respect to and normalized to standard values (E_0) [23], as a function of the incident charge state (q) of the projectile ions a) for Au in the laboratory frame (LAB) and b) for U and Bi in emitter frame (E.F.). Thickness of Au targets (t) is in $\mu g/cm^2$. Statistical errors are smaller than the size of the symbols. Lines through the data points are drawn to guide the eye. (Note the factor of two change in ordinate scale for target and projectile.)*

collisions seem to result into mainly one electron capture although multiple electron capture remains as a possibility too. The increase in the relative shifts of Au are nearly half as that of U or Bi indicating that Au is probably multiply ionized to a lesser extent as compared to U or Bi. As the relative shifts of Au $K\alpha_{1},\alpha_{2}$ for both the near symmetric (Bi-Au) and slightly asymmetric (U-Au) collision case coincide with each other within the experimental uncertainties, it can be concluded that the target K shifts do not depend sensitively on the projectile Z in the considered small range of Z.

The target thickness dependence of Au-, U- and Bi-K x-ray transition energies has been shown in Fig. 4.7 (for U-Au) and in Fig. 5.10 (for Bi-Au) collision systems. Within the large

experimental uncertainties a target thickness dependence of Au-, U- or Bi-K x-ray transitions was not observed indicating that the vacancy distribution (beyond the K-shell) of a highly charged projectile does not change considerably while penetrating thin solid targets. This may point also to a definite survival probability of inner shell vacancies in the solid targets.

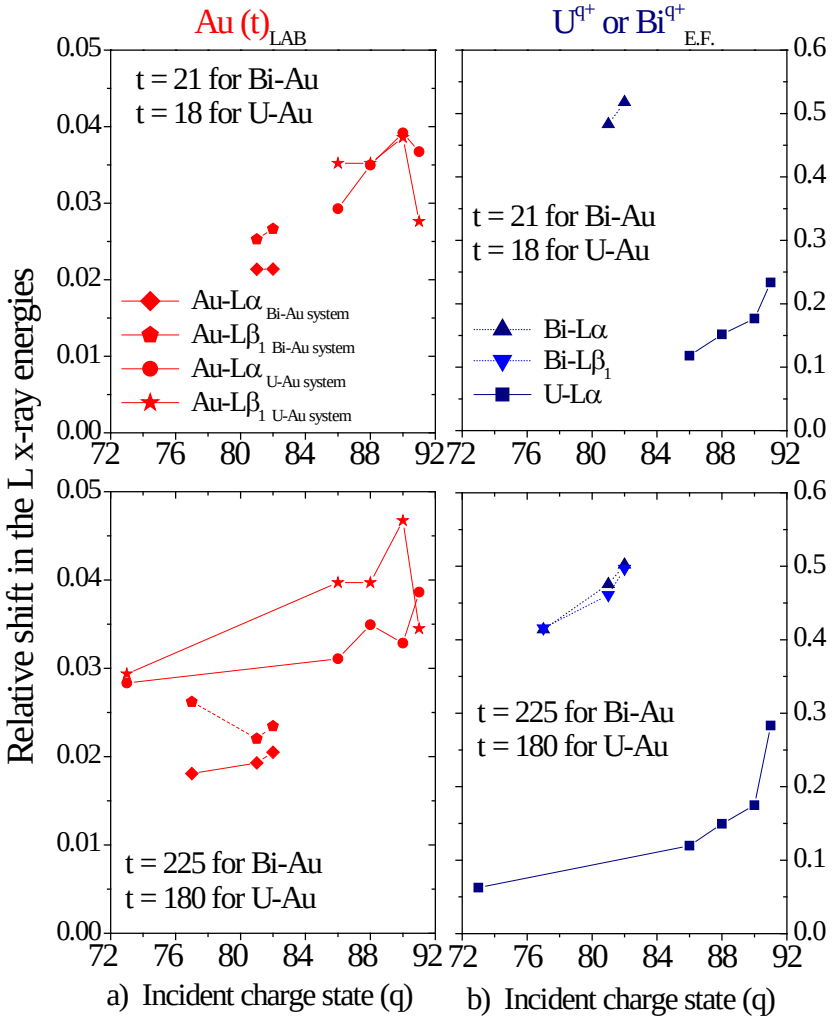

Fig. 6.2 *Relative shift ($E_{obs.}$-E_0)/E_0 in L x-ray transitions (centroids) with respect to and normalized to standard values (E_0) [23], as a function of the incident charge state (q) of the projectile ions a) for Au in the laboratory frame (LAB) and b) for U and Bi in emitter frame (E.F.). Thickness of Au targets (t) is in $\mu g/cm^2$. Statistical errors are smaller than the size of the symbols. Lines through the data points are drawn to guide the eye. (Note the drastically different scales in the shifts for projectile and target system).*

For completeness Fig. 6.2 gives the relative shifts for the L x-rays a) for the target, b) for the projectiles. Due to the high ionization, the relative L shift is larger than that for the K radiation. Moreover, due to the stronger binding energy in the U-case compared to Bi-projectiles, the shift in both cases differ from each other as expected. The energy shifts give information on the charge and excitation status of each collision partner after the interaction. Inferences can be drawn both from K and L x-ray shifts. It has been observed that:

- With increasing q both the shifts increase, slightly for target and drastically for projectile indicating increasing (multiple) ionization for both the partners.
- With increasing target thickness the shifts (projectile and target) do not show any appreciable dependence
- The $K\alpha_1$ shift for U-, Bi- and Au is observed to be larger than the $K\alpha_2$ shift. The L(j=3/2) wave function (responsible for $K\alpha_1$ transition) is more extended in space than the L(j=1/2) (responsible for $K\alpha_2$ transition) one; the latter one measures more the inner screening, the first one is more sensitive to L shell spectators
- Projectile shifts are larger than the target shifts (by a factor of 2 for K x-ray shifts for U-Au and by a factor of 7-25 for L x-ray shifts of U and Bi respectively) showing the memory effect in the outer shells of projectile and target electron population and indicating the high projectile ionization in the L and higher shells.
- The U and Bi-K energy shifts show a fair agreement with each other however the Bi-L x-ray energy shifts are much larger (almost a factor of 2) than the corresponding values for U-L values due to the difference in L-binding energies.

6.3.2 Intensity ratios for K and L x-ray emission

The drawback of total cross sections is the systematic uncertainties especially if only a few points are available. Intensity ratios between x-ray lines in one spectrum are not sensitive to those errors which are responsible for absolute values. Hence the projectile K to target K intensity ratio gives a precise measure of the emission variation with projectile incident charge state ‘q’ and target thickness ‘t’. The additional vacancies created in the upper shells can modify the yield of the inner shell x-ray transitions such as K and L. The intensity ratios provide additional information on the outer shell vacancy distributions during x-ray emission. Both the K and L x-ray intensity ratios were investigated for the prominent lines of the collision partners in light of their q and t dependence. Details have been covered in Section 4.3.3, Chapter 4 for U-Au and in Section 5.3.3, 5.4.3, Chapter 5 for Bi-Au collision system.

The $K\alpha_2/K\alpha_1$ ratio reveals the relative population of the $2p_{1/2}$ and $2p_{3/2}$ levels within a collision partner and the $L\alpha/L\beta_1$ intensity ratio provides supplementary information for the same. Neither the projectile (U or Bi) nor the target (Au) $K\alpha_2/K\alpha_1$ ratios showed any remarkable q or t dependence (see Fig. 4.8 and Fig. 5.11). This indicates that probably the final population ratio of the $2p_{1/2}$ and $2p_{3/2}$ levels is not sensitive to the change in the incident charge state of the projectile. Table

6.1 gives average values of U, Bi and Au x-ray intensity ratios for closed and open projectile K-shell in the entrance channel. Single hole values by Scofield [64] have been given for comparison. The value of Au-Kα_2/Kα_1 ratio within experimental uncertainties agrees reasonably well with the single hole values of Scofield for both closed and open projectile K-shell in the entrance channel. The projectile Kα_2/Kα_1 ratios for Bi agrees well with the Scofield value for closed K-shell case whereas for U it is almost double (not considering the large errors in that case). For open projectile shell for this ratio, both U and Bi exhibit a higher value as compared to that of Scofield, 44% for Bi and 50% for U.

Table 6.1 *Average values of U, Bi and Au x-ray intensity ratios for closed and open projectile K-shell in the entrance channel. Single hole values by Scofield [64] have been given for comparison. The experimental inter-partner ratios are corrected for the relativistic solid angle transformation.*

Proj. K-shell / Intensity ratio	**Closed**	**Open**	**Scofield [64]**
	q ≤ 90	**q = 91**	
U-Kα$_1$ / Au-Kα$_1$	0.4 ± 0.1	34.6 ± 4.8	0.96
U-Kα$_2$ / U-Kα$_1$	1.3 ±0 .5	0.9 ± 0.1	0.625
Au-Kα$_2$ / Au-Kα$_1$	0.7 ± 0.1	0.8 ± 0.2	0.588
	q ≤ 81	q = 82	
Bi-Kα$_1$ / Au-Kα$_1$	0.9 ± 0.1	23.7 ± 6.5	0.989
Bi-Kα$_2$ / Bi-Kα$_1$	0.6 ± 0.1	0.9 ± 0.05	0.598
Au-Kα$_2$ / Au-Kα$_1$	0.6 ± 0.03		0.588

The observations are entirely different for the inter-partner ratio of Kα_1 transition i.e. U-Kα_1/Au-Kα_1 and Bi-Kα_1/Au-Kα_1. This ratio has to be seen in the light of closed K-shell or open K-shell of the projectile in the entrance channel of the collision. For the closed K-shell case the ratio is smaller than the Scofield value and has almost a constant value for all q corresponding to closed K-shell. This may indicate that in a close collision more K vacancies are produced in the lighter collision partner due to the smaller binding energy. For the near symmetric Bi-Au system this ratio is close to the Scofield value pointing to equal K ionization probabilities. In the case for the U-Au system, the K ionization probabilities seem to be a factor of 3 different. The Scofield value is more

than twice the experimental value for the U-Kα_1/Au-Kα_1 ratio for the closed K-shell condition and it is only 9% higher than Bi-Kα_1/Au-Kα_1 ratio for the closed K-shell condition.

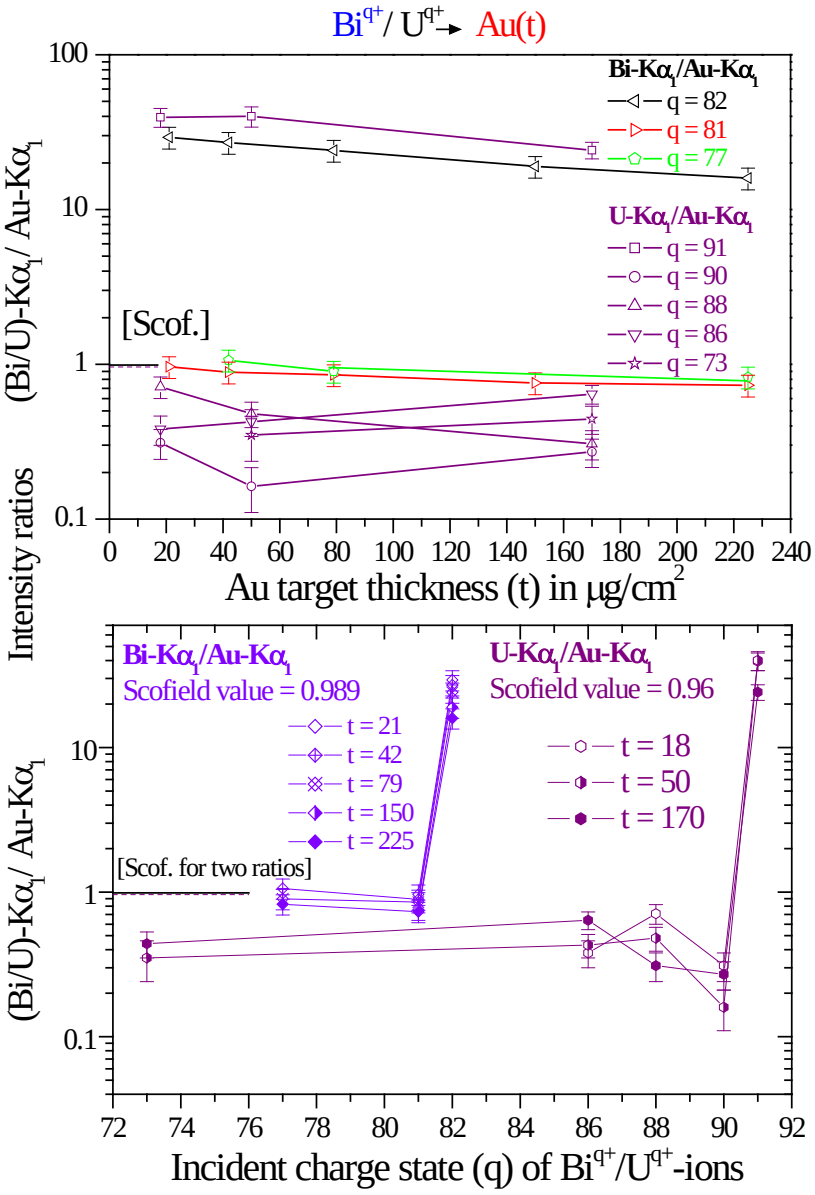

Fig. 6.3 *Inter collision partner K-line ratios (U-Kα_1/Au-Kα_1 and Bi-Kα_1/Au-Kα_1) as a function of 'q' in the bottom part and as a function of target thickness 't' in the upper part. The corresponding single hole values by Scofield [64] have been indicated in the figures as [Scof.]. Lines through the data points are drawn to guide the eye.*

For open K-shell of the projectile in the entrance channel this ratio increases dramatically for both the U-Au and Bi-Au systems. It indicates the probability of having a K vacancy in the U or Bi in the receding part of the collision. The open K-shell facilitates the observation of electron capture in higher outer shells through its radiative decay down to the K-shell. The probability for capture compared to K-shell ionization is about a factor of 30 and 70 larger for the symmetric and asymmetric case, respectively without considering the L-shell population.

Fig. 6.3 shows the inter-partner K-line ratios (U-Kα_1/Au-Kα_1 and Bi-Kα_1/Au-Kα_1) as a function of 'q' in the bottom part and their variation with target thickness 't' in the upper part. A glance at the figure shows the equivalence of the two intra-partner ratios. Since the inter-partner K line ratios are not much different from the Scofield ratio for all 'q' except for the open K-shell condition, they indicate a usual statistical population of the L sublevels for these charge states (q = 73 to 90 for U and q = 77 to 80 for Bi). The dramatic change for this ratio after opening the projectile K-shell (q = 91 for U and q = 81 for Bi) points to the different interaction mechanisms responsible for the target and projectile K emission.

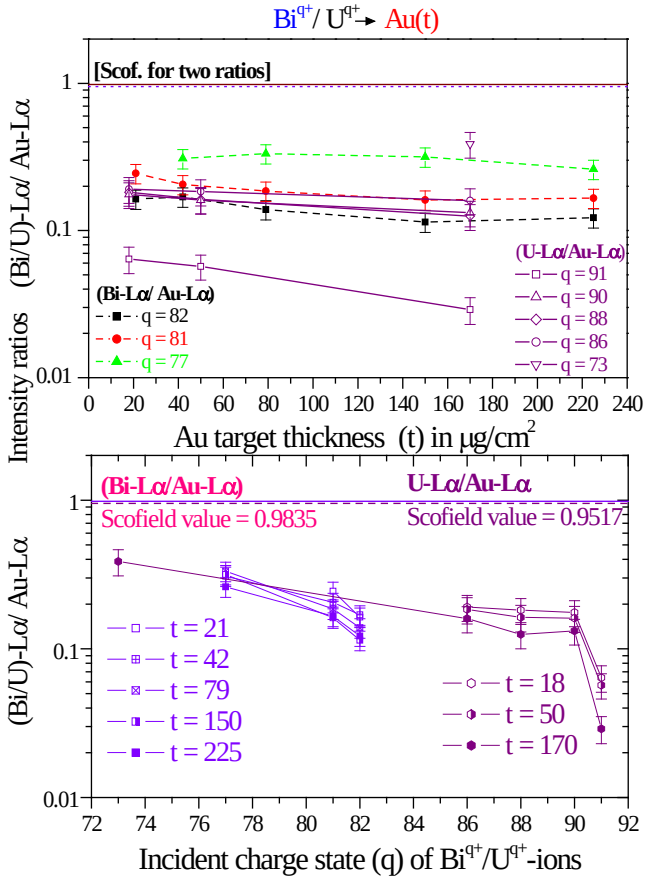

Fig. 6.4 *Inter collision partner L-line ratios (U-Lα/Au-Lα and Bi-Lα/Au-Lα) as a function of 'q' in the bottom part and as a function of target thickness 't' in the upper part. The corresponding single hole values by Scofield [64] have been indicated in the figures as [Scof.]. Lines through the data points are drawn to guide the eye.*

This inter-partner Kα_1 ratio is especially target thickness dependent as can be observed from Fig. 6.3 showing the gradual loss of projectile K vacancies with target thickness. As the projectile emission increases drastically compared to the target K emission for opened projectile K-shell, the increase in this ratio is a good indicator of the survival of the incoming projectile K vacancy probability.

For completeness the L x ray ratios are depicted in Fig. 6.4. As the highly charged projectiles have a low probability for electrons in higher shells (beyond L shell), only a low L x-ray intensity is expected (despite the possibly higher fluorescence yield) resulting in a half survival thickness of 190 and 230 $\mu g/cm^2$ for U and Bi respectively (see later). The interpartner ratio is considerably smaller (by a factor 4 for Bi and 10 for U) than predicted by Scofield. Further, this ratio decreases with increasing projectile charge and additionally for the special case of an open projectile K-shell. The latter tendency is more for the heavier projectile. A decrease can also be observed with increasing target thickness however this effect is not fully understood.

6.3.3 K and L x-ray cross sections

For both the collision systems investigated, the x-ray emission has been measured for the projectile and the target as a function of projectile incident charge state 'q' and target thickness 't'. The inferences from the K and L x-ray emission of collision partners of both the collision systems are similar in many respects and are to be interpreted in totality with some peculiarities.

U-Au collision system

The 'q' dependence of the Au- and U-Kα_{1,α_2} have been shown in Fig. 4.10 a) and b) (Chapter 4) respectively for all the target thicknesses 't' investigated. As a summary, emission cross sections for only the most intense K x-ray transition i.e. Kα_1 are presented for U and Au corresponding to the thinnest and the thickest target (t = 18 and 170 $\mu g/cm^2$ respectively) as a function of q in Fig. 6.5 a). The 't' dependence of the Au- and U-Kα_{1,α_2} emission cross sections have been presented in Fig. 4.11 a) and b) (Chapter 4) respectively. As a recapitulation, Fig. 6.5 b) depicts the U- and Au-Kα_1 emission cross sections as a function of 't' for q = 91 and 73 (highest and lowest q respectively).

Bi-Au collision system

The projectile charge state 'q' dependence of the Au- and Bi-Kα_{1,α_2} emission cross sections have been presented in Fig. 5.13 a) and b) respectively (Chapter 5) and their 't' dependence in Fig. 5.14 a) and b). Fig. 6.6 a) shows, as a summary the Au- and Bi-Kα_1 emission cross sections as a function of 'q' corresponding to the thinnest and the thickest target (t = 21 and 225 $\mu g/cm^2$ respectively). Fig. 6.6 b) shows the same as a function of the increasing 't' for q = 82 and 77 (highest and lowest q respectively).

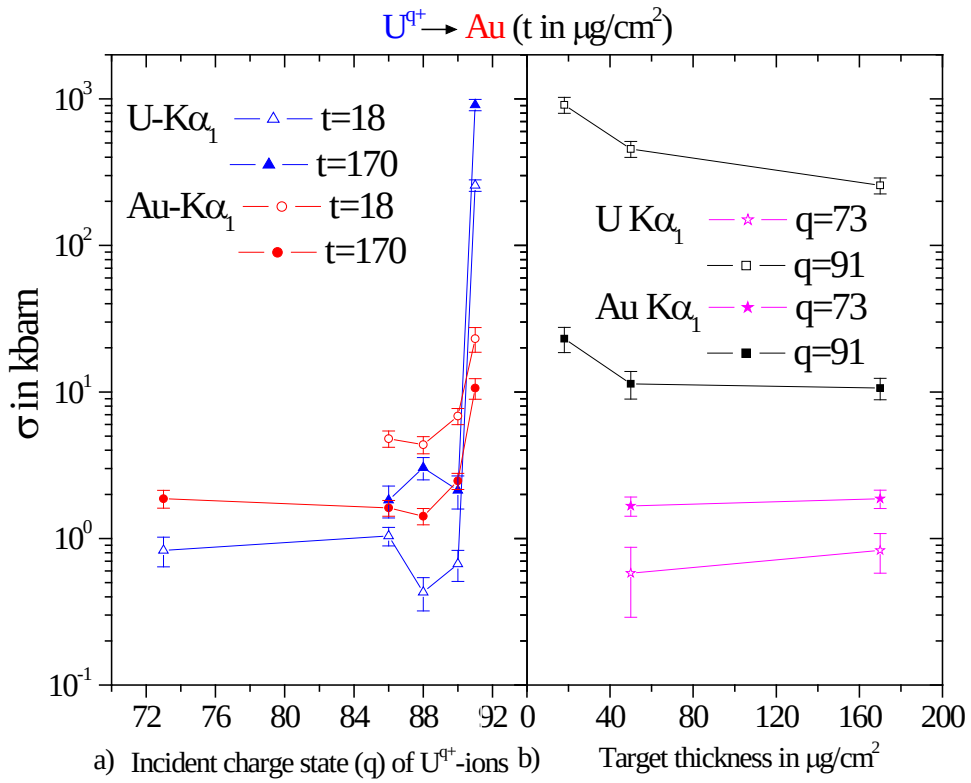

Fig. 6.5 *U- and Au-Kα_1 emission cross sections for 18 and 170 µg/cm^2 thick targets a) as a function of the incoming charge state and b) as a function of target thickness (t).*

The most striking feature for both systems is the dramatic cross section increase with the opening of the projectile K-shell (see below). Especially the projectile K x-ray emission increases by orders of magnitude indicating electron capture to higher shells and its radiative stabilization. As with increasing target thickness the probability for a survival of the projectile vacancy decreases, the projectile K emission diminishes correspondingly giving a unique access to the survival probability. The smaller increase in target K emission gives the possibility to study inner shell couplings through the involved vacancy transfer in the collision molecule. Similar findings can be observed for for the Bi-Au collision system depicted in Fig. 6.6.

For completeness the main cross sections for L x-ray emission – typically in the Mbarn region and beyond are given, in Fig. 6.7 for charge state dependence and in Fig. 6.8 for the target thickness dependence. A detailed inference/interpretation has been already given in Chapter 4 and 5 for the two systems in Section 4.4.4 and Section 5.4.4 respectively. In general it can be commented that the normalized x-ray yields decrease with target thickness pointing possibly also to a decrease of the projectile charge. The target emission compared to the projectile is less sensitive to thickness and projectile charge. The projectile yields are smaller than the target ones, particularly for the heavier ion. This is

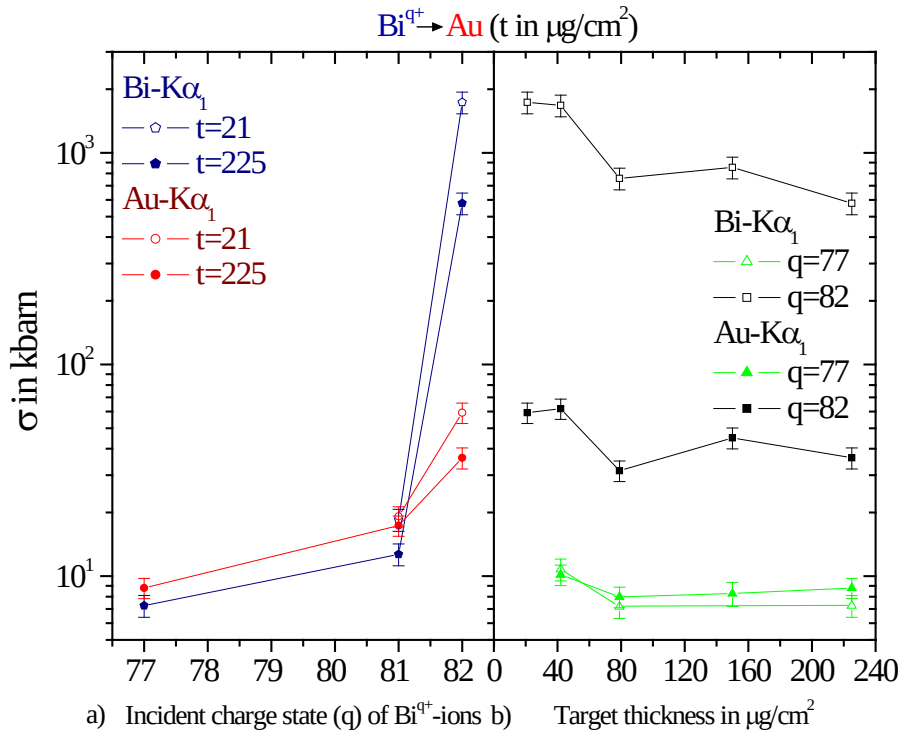

Fig. 6.6 *Bi- and Au-Kα_1 emission cross sections for t = 21 and 225 μg/cm^2 thick targets a) as a function of the incoming charge state b) as a function of target thickness.*

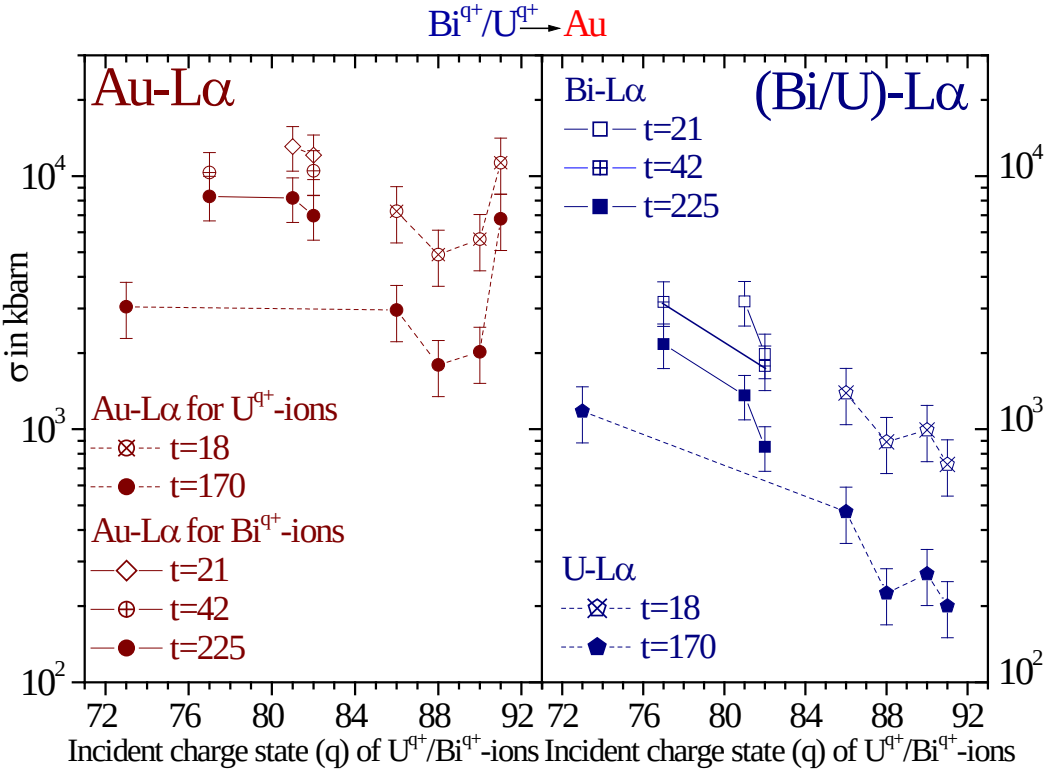

Fig. 6.7 *Emission cross sections for Bi-Lα for t = 21, 42 and 225 μg/cm^2 thick targets and for U-Lα for t = 18, 170 μg/cm^2. Au-Lα cross sections corresponding to Bi^{q+}/U^{q+} projectiles for all the above t's as a function of incident charge state (q) of the projectile-ions.*

probably a result of the reduced number of outer electrons in the projectile that are needed for filling the L shell radiatively. For a closer consideration however, further effects such as the changes in fluorescence yields have to be taken into account.

6.3.4 Charge state dependence of K x-ray emission

The charge state dependence of K x-ray emission for the projectile (U or Bi) and for the target (Au) is similar for both the collision systems. The charge state dependence has to be interpreted in the light of "open" and "closed" K shells for the projectile in the incoming channel of the collision. The interpretation from above two views has to be supplemented with a comparison of the case when the projectile has a near equilibrium charge state.

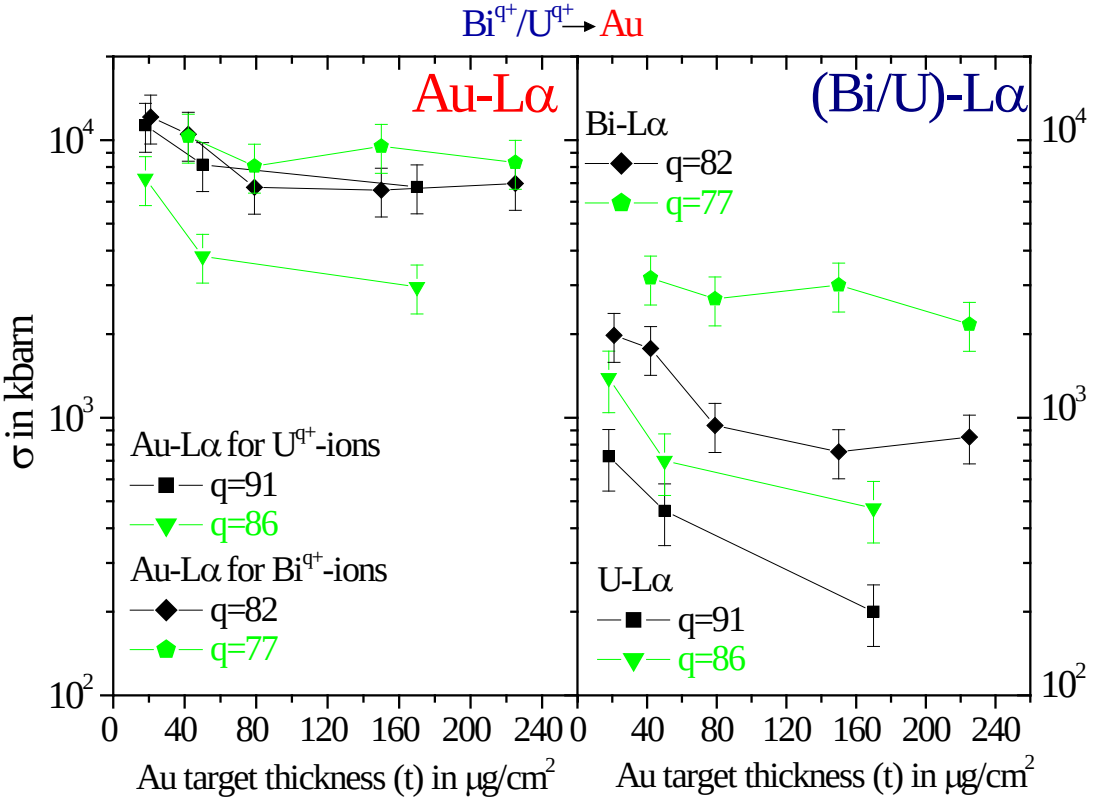

Fig. 6.8 *X-ray yields (cross sections) as a function of target thickness for Bi-Lα (for q = 82 and 77), U-Lα (for q = 91 and 86) and Au-Lα corresponding to Bi^{q+}/U^{q+} projectiles for all the above q's.*

For both the collision systems, the K x-ray emission of the projectile and the target show nearly constant values for q ranging from a near equilibrium to the case when the projectile L-shell is partly empty (i.e. from q = 73 to 89 for U-Au and q = 77 to 80 for Bi-Au). The U-Au collision system was investigated over a larger range of q (Δq =13 with smaller steps) as compared to that for Bi-Au (Δq = 6). As a result it is also possible to draw inferences from U-Au collision system for the

case when the projectile carries L (j = 1/2) vacancies in the incoming channel of the collision, the so called “closed K-shell condition”. Lastly, K x-ray emission for projectiles carrying K-shell vacancies in the collision, the so called “open K-shell” condition in comparison to the “closed” case provides a glimpse of the processes taking place in these collisions.

Comparing the Au-K x-ray emission cross sections corresponding to q = 90 and 88 for K projectiles, a slight increase may be evident for the former from Fig. 6.5 as has been reported earlier in Section 4.3.4 (Chapter 4). It is possible that the L (j=1/2) vacancies brought in by the projectile in the incoming channel get transferred partially to the K-shell of Au in outgoing channel of the collision. Such a transfer may be possible due to coupling between the L shell of the projectile and K-shell of the target at very small internuclear distances. The region of L-K shell coupling [95] between projectile and target shells can be visualized through the representation of the level diagrams discussed in Section 6.4 in detail (Fig. 6.10 and 6.11). The region of L-K coupling is indicated in the figures with rectangles numbered 2. From this observed increase in the Au-K emission it is possible to estimate the interaction distance for the L-K shell coupling and a comparison with calculations can be done (Section 6.4.2).

For both U-Au and Bi-Au collision systems, the K x-ray emission cross sections for the projectile show a marked increase in their value for an open K-shell (q = 91 for U, q = 82 for Bi) as compared to the value for a closed K-shell (q = 90 for U and q = 82 for Bi). The target (Au) K emission also shows such an increase however not as dramatic as the former. These observations have been already mentioned in (Section 4.3.4 and 5.3.4 of Chapter 4 and 5 for U-Au and Bi-Au respectively.

Although both the projectile and target K x-ray emission increases for this “open K-shell” condition but they reflect entirely different processes occurring during collision. The increase in the projectile K x-ray emission is a result of distant collision whereas the increase in target K x-ray emission is due to a close one. The former results into electron capture from the target to outer projectile shells and the latter points to an additional vacancy production mechanism such as the coupling of the K-shells of both the collision partners as the two partners recede from each other (the K-K sharing process [96]). The sharing of the K-vacancies brought in by the projectile in the incoming channel of the collision are shared with the K-shell of the target in the outgoing channel of the collision and this sharing takes place due to the close proximity of the two K levels at small inter nuclear distances. This K-K sharing can also be visualized through the level diagrams shown in Fig. 6.10 and 6.11. The region of K-K sharing is indicated there with a rectangle numbered 1.

The increase in the projectile (U, Bi) K x-ray emission for “open K-shell” relative to its value for the “closed K-shell” enables an estimation of the interaction distance for electron capture whereas

the increase in the target K x-ray emission enables an estimation of the K-K transfer interaction distance (both discussed in detail in Section 6.4.2).

It is emphasized that the observed increase in the x-ray emission with increasing 'q' depends on the target thickness, i.e. on the survival probability of the projectile K-vacancy while penetrating the target foils. The increase in the projectile (U or Bi) and target (Au) x-ray emission cross sections corresponding to incoming K or L vacancies in the projectile are to be calculated for single collision conditions. These can be reached approximately for near zero target thicknesses (discussed in detail in the following section).

6.3.5 Target thickness dependence of x-ray cross sections: Survival probability of projectile K-vacancies penetrating a solid target

As has been mentioned already in the "Introduction" (Chapter 1) to this work, the primary objective of this investigation was to find out the survival probability of "prior to collision" K-shell vacancies in the projectile while penetrating solid targets. A sufficiently long survival time would ensure the applicability of solid targets for investigating the inner shell dynamics of the superheavy quasimolecules formed transiently during collisions. Hence a target thickness dependent study of the x-ray emission of the collision partners became a prerequisite to any further measurement for the objectives of this investigation.

Fig. 6.5 b) and 6.6 b) show the target thickness dependence of the U-, Bi- and Au-Kα_1 cross sections. Since a true cross section does not depend on target thickness the cross sections shown are actually the absolute yields. Cross sections corresponding approximately to "single collision" condition can be extracted from these yields by extrapolating them to "zero" target thickness. These observations have been mentioned in Section 4.3.4 and Section 5.3.4 for U-Au and Bi-Au collisions respectively. These K x-ray cross sections show an approximate (exponential) decrease with increasing target thickness the decrease being firstly, more pronounced for the projectile than that for the target and secondly, remarkable for an "open K-shell condition" (q = 91 for U, q = 82 for Bi) as compared to "closed" or other incident charge states. The cross sections (absolute yields) decrease with increasing target thickness due to filling of the projectile K vacuum in the bulk. Assuming an exponential decrease, i.e.

$$\sigma = \sigma_0 \exp\left[-\left(\frac{\ln 2}{t_{1/2}}\right) t\right]$$

the cross sections for zero target thickness (i.e. cross sections under almost single collision conditions) have been extrapolated from these graphs. Here t is the thickness of the targets and hence

$t_{1/2}$ is half thickness for half of the projectile–ions to lose their K vacancy. The decrease of the K x-ray cross sections has been assumed to be towards the values corresponding (approximately) to those for the equilibrium charge state of the projectile (e.g. to a few kb for U-Kα_1, see Fig. 6.5).

Table 6.2 lists the increase in U-Kα_1, Bi-Kα_1 and Au-Kα_1 x-ray emission cross sections (in kbarn) per incoming projectile (K, $L_{j=1/2}$) vacancy obtained for zero target thickness i.e. approximate single collision conditions. For example with an exponential fit to the U-Kα_1 cross sections, half of the U^{91+}-ions (having an incoming K vacancy) are expected to lose their K-vacancy in a half thickness of approximately 95±10 μg/cm^2 (=$t_{1/2}$). This corresponds to a survival time ($\tau_{1/2}$) in the range of ~(4 to 5) x10^{-16}s for the U K-vacancy in the bulk at the experimental ion velocity of 0.38 c. This half-survival time is appreciably larger than that of a vacancy in a "normal" uranium atom ($\tau_{0(1/2)}$~6x10^{-18} s) [5, 6]. For Bi $\tau_{1/2}$ ~(6 to 9) x10^{-16} which is also larger than the corresponding value for a bismuth atom i.e. 9x10^{-18}s. The half thickness for Bi is 164±29 μg/cm^2. The high projectile ionization together with the size of the electron capture cross section leads to this long survival time of the projectile K vacancy in the bulk. Table 6.3 gives the values of $t_{1/2}$ (survival half thickness) and $\tau_{1/2}$ (half-survival time) of the K-shell vacancies while penetrating solid Au targets for U-Au and Bi-Au collision systems. The $\tau_{0(1/2)}$ for a vacancy in a normal U and Bi atom [5, 6] are also given for comparison.

Table 6.2 *Increase (ΔI) in U-Kα_1, Bi-Kα_1 and Au-Kα_1 x-ray emission cross sections (in kbarn) per incoming projectile vacancy (K, $L_{j=1/2}$) as well as total for all emission channels obtained for zero target thickness i.e. approximate single collision conditions. The total x-ray emission for all decay channels i.e. α_1, α_2, β_1, β_2 etc. is assumed to be approximately 3 times that of Kα_1 emission.*

Collision system	**Kα1**	**Increase of x-ray emission cross section in kbarn**			**Cross section**
		ΔI (Kα_1) / incoming K-vacancy	**ΔI (Kα_1) / incoming $L_{(j=1/2)}$-vacancy**	**ΔI (K-X^{tot}) / vacancy**	
U-Au	**U**	903 ± 165	-	~ 2709 ± 859	σ *electron capture*
	Au	20 ± 5	-	~ 60 ± 26	σ *K – K sharing*
	Au	-	1.3 ± 0.7	~3.9 ± 2.1	σ *L – K sharing*
Bi-Au	**Bi**	1714 ± 314	-	~ 5141 ± 1631	σ *electron capture*
	Au	30 ± 10	-	~ 90 ± 52	σ *K – K sharing*

The half thickness $t_{1/2}$ can be calculated by different ways such as from the decrease in the projectile and target K and L x-rays, decrease in the interpartner intensity ratio for both K and L x-ray emission, and the variation of the charge state evolution with increasing target thickness. Here only one of the different ways for determining $t_{1/2}$ has been used. The other methods give partially upto a factor of 2 larger $t_{1/2}$ values leading to correspondingly longer half survival times. However, for safety the smallest $t_{1/2}$ value has been used for comparison. The most reliable value is extracted from the interpartner $K\alpha_1$ ratio leading to $t_{1/2}$= 190±10 μg/cm^2 for U-Au system and $t_{1/2}$= 230±30 μg/cm^2 for Bi-Au system instead of 95±10 and 164±29 μg/cm^2 respectively.

Interaction distance for electron capture

During distant collisions for highly charged projectiles, the electrons are captured from the target to the higher vacant shells of the projectile (typical electron capture interaction distance has been estimated later in text). For projectiles carrying a K-vacancy prior to the collision (U^{91+} or Bi^{82+}), the radiative stabilization of the captured electrons to the K-shell leads to a copious emission of the projectile K x-rays and hence to the observed increase in the projectile-K x-ray emission (U-$K\alpha_1$ or Bi-$K\alpha_1$) (see Fig. 6.5, 6.6).

Table 6.3 *Parameters for calculation of half-survival time ($\tau_{1/2}$) of a K vacancy corresponding to half thickness of target foil i.e. ($t_{1/2}$). The half- life time ($\tau_{0(1/2)}$) for a vacancy in a normal U and Bi atom [97] are mentioned for comparison.*

Name of parameter	Parameters	U-Au system	Bi-Au system
Half thickness	$t_{1/2}$ (μg/cm^2)	95 ± 50	164 ± 29
Half-survival time	$\tau_{1/2}$ (s)	~ (4 to5)x10^{-16}	~ (6 to 9)x10^{-16}
Half-Life time	$\tau_{0(1/2)}$ of a "normal" atom [97] (s)	~ 6x10^{-18}	~ 9x10^{-18}

The electron capture cross section (σ_{cap}) can be calculated from the increase in total projectile-K x-ray emission cross sections (i.e. for all transitions to the K-shell, $K\alpha_1$, $K\alpha_2$, $K\beta_1$ and $K\beta_2$). The Bi, U and Au x-ray emission cross sections given in Table 6.2, column 3 refer to only one decay channel of the K vacancy. In order to account for the total K-vacancy production cross sections, a sum over all channels (i.e. sum over all transitions to the K-shell viz. for $K\alpha_1$, $K\alpha_2$, $K\beta_1$ and $K\beta_2$ emission) is required which adds up to an estimated factor of about 3 roughly within 25%. Hence for a total increase in the K x-ray emission, one can calculate the $\sigma_{cap} = \sim 5141\ kb$ for the Bi

K x-rays and ~ 2709 *kb* for the U K x-rays (column 5, Table 6.2). These values are compared to the theoretical calculations [50, 53] for electron capture as well as with the values obtained from the measured charge state cross sections in Section 6.3.6.

A simple geometrical picture (using a box model with a step function) has been used to estimate the interaction distance for electron capture approximately i.e.

$$\sigma_{cap} = P_{cap} \cdot \pi r_{cap}^2$$

with $P_{cap} = 1$ for $r \leq r_{cap}$ and $P_{cap} = 0$ for $r \geq r_{cap}$. From the above equation the interaction distance for electron capture, r_{cap} can be estimated to be ~12792±4055 fm for Bi-Au collision system and ~ 9286±2944 fm for the U-Au system. The corresponding arrow for the two distances are marked in the adiabatic level diagrams shown in Fig. 6.10 and 6.11.

6.3.6 Charge exchange measurements

As has been mentioned clearly in Introduction (Chapter 1) of this study, the charge exchange was investigated for the collision systems in order to fulfill the primary objective of this investigation namely the probability of survival for the incoming vacancies in the projectile while passing through solid targets. The charge exchange cross sections can either be measured directly (such as done for Bi-Au collision system) or deduced from x-ray emission cross sections (done for both U-Au and Bi-Au systems) corresponding to projectiles carrying vacancies in the incoming channel of the collision.

A charge state evolution measurement and charge exchange cross sections of a highly charged ion can be correlated with x-ray emission. This would provide an insight into the conditions of incoming channels during quasimolecular collisions inside a solid. The K x-ray emission cross sections corresponding to the projectiles carrying an incoming K vacancy are used for calculating the total electron capture cross section for both U-Au and Bi-Au collision system. As has been clarified in Section 4.3.5 (Chapter 4) these cross sections have been calculated for “zero” target thickness corresponding to approximately single collision conditions. A sum over all the possible decay channels has also been taken into account (see Section 6.3.5).

The charge state distribution was measured by a position-sensitive particle detector for the Bi-Au collision system (Chapter 5). The charge exchange cross sections were determined from the target thickness dependence of the yield of charge state fractions (N^{q+}/N_{tot}). For q = 82 corresponding to a H-like Bi (open K-shell) a total electron capture cross section could be deduced by the procedure described in Section 5.5.3 (Chapter 5). The measured values from both the above procedures have been found to be in fair agreement with each other.

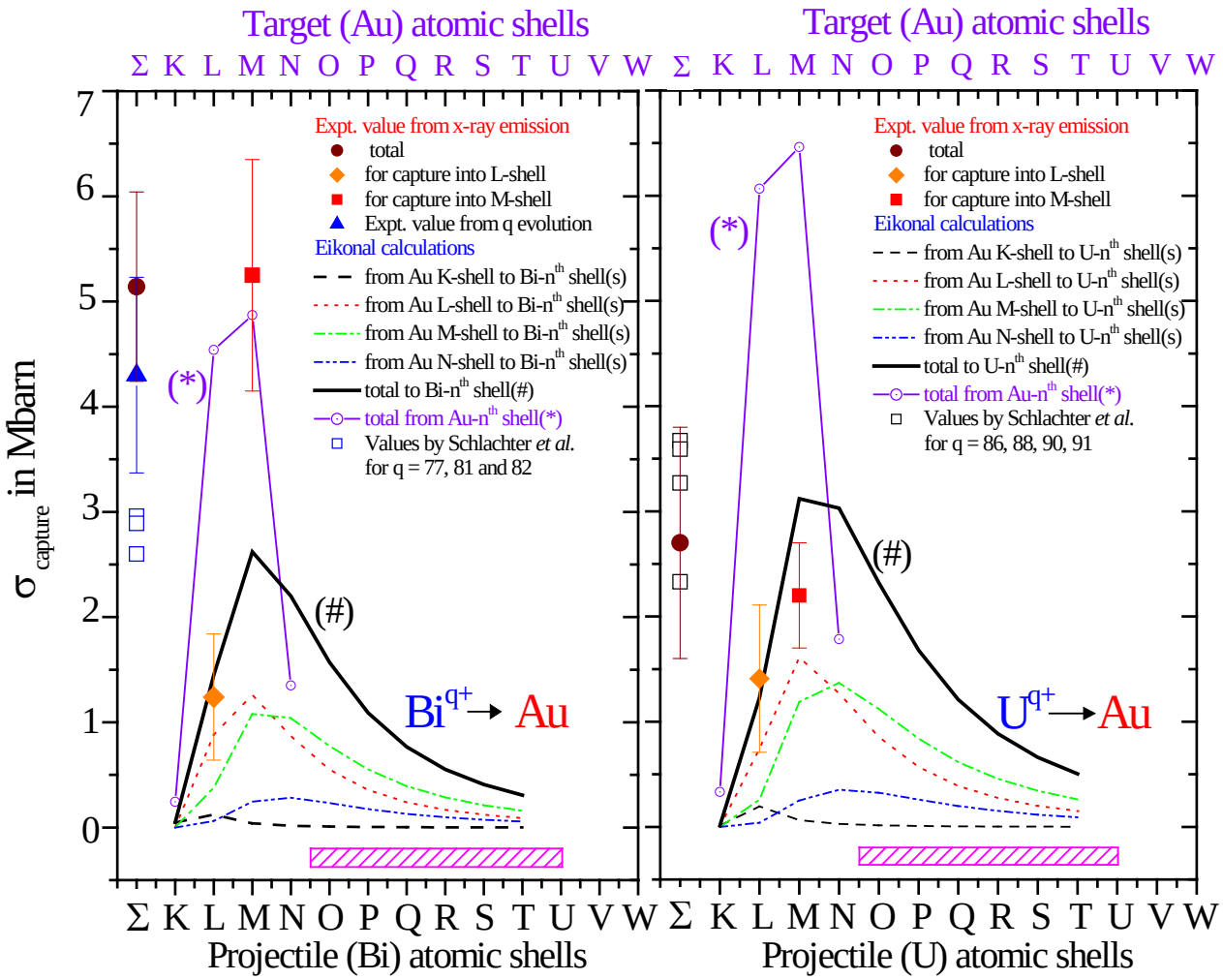

Fig. 6.9 *Shell differential electron capture cross sections vs the atomic shells of the projectile (U/ Bi) calculated theoretically and from experimentally measured values. The curves signify the distribution of the cross sections according to Eikonal [53] from Au K, L, M and N shells to various projectile shells (shown on the abscissa) and their total. (#):-* σ_{cap}^{Tot} *from Au K, L, M and N-shells to a U/Bi-n*th *shell (K to T), (to be read from abscissa). (*):-* σ_{cap}^{Tot} *from a Au-n*th *shell (K to N) (to be read from axis on top) to all U/Bi K to T shells. The Schlachter [50] values are a total for q = 86, 88, 90 and 91 for U and for q = 77, 81 and 82 for Bi. The experimentally determined values of* σ_{cap}^{L}, σ_{cap}^{M} *and* σ_{cap}^{Tot} *from x-ray emission cross sections (for q = 91 for U and for q = 82 for Bi) have also been included along with the value deduced from measured 'q' state evolution for Bi.*

Lastly a comparison of the experimentally measured values with the model calculations of Eikonal [53] and to the semi-empirical non-relativistic scaling formula for non radiative capture (NRC) by Schlachter *et al.* [50] have also been performed (details in Section 4.3.5, Chapter 4 and Section 5.5.3, Chapter 5) for both the collision systems. Fig. 6.9 shows the shell differential capture cross sections vs. the atomic shells of the projectile for U and Bi, calculated by the Eikonal approximation and by Schlachter *et al.*. The details have been covered in the respective chapters.

The curves signify the distribution of the cross section from Au K, L, M and N shells and their total according to Eikonal. The Schlachter values are a total for q = 86, 88, 90 and 91 for U and a total for q = 77, 81, 82 for Bi. The total experimentally determined value from x-ray emission cross sections (for q = 91 for U, for q = 82 for Bi) have also been included. For both the collision systems, the Eikonal predicts that the probability of capture is maximum from Au-L and -M shell to the U- or Bi-M shell. The total cross sections distribution indicated by the thick solid line (#) in both the figures indicated that the capture to projectile (U- or Bi-) M and N-shells is preferred. Additionally Bohr's criterion of $v_{ion} = v_e$ indicates that the collision velocity of both the projectiles is larger than the velocity of the electrons in the M-shell of U and Bi. Keeping in mind the intensity of the projectile $K\beta_1$ (M_3-K) line in the x-ray spectra of both U-Au and Bi-Au collision system corresponding to open K-shell condition; it can be inferred that either the electrons captured to the M-shell are re-ionized quickly or they cascade down to the L and K-shells. The cross sections according to Schlachter *et al.* have been found to agree reasonably well with the experimentally measured values (within the experimental uncertainties), more for U-Au system than for Bi-Au as indicated in the Fig. 6.9 by empty squares. It can be observed that the σ_{cap}^{M} values are higher for the near symmetric Bi-Au system in comparison to those for the asymmetric U-Au system. This probably due to the matching of the levels in the symmetric case whereby many electron are captured from the target to the projectile shells. The higher values of σ_{cap}^{M} are probably due to this reason and this has to be investigated further. σ_{cap}^{Tot} is estimated through projectile K x-ray emission cross sections (for open K-shell) and reflect only one electron capture and not multi electron capture or successive capture in different collisions. The latter is manifested through σ_{cap}^{M} (including capture into higher shells) and hence relatively higher values. In Table 6.4 the capture cross sections are summarized once more for comparison.

Table 6.4 *Total electron capture cross sections calculated by Eikonal approximation [53], the semi-empirical prescription by Schlachter et al. [50] and measured values determined both from x-ray emission cross-sections and charge state evolution.*

Collision system	**Projectile incident charge state (q)**	σ_{cap}^{Tot} **in Mb**		σ_{cap}^{Exp} **in Mb**	
		Eikonal approx. [53]	**Schlachter *et al.* [50]**	**from x-ray emission**	**from q-state evolution**
U-Au	91	7.39	3.67	2.7 ± 0.1	Not available
Bi-Au	82	6.32	2.96	5.1 ± 0.9	4.3 ± 1.0

6.4 LEVEL DIAGRAMS AND COUPLING DISTANCES FOR SUPERHEAVY COLLISION SYSTEMS

6.4.1 Level diagrams for superheavy collision systems

As has been mentioned in Chapter 1, the superheavy quasimolecules are formed transiently during collisions of heavy-atoms by high-Z projectile ions, moving slowly (v_{ion}) with respect to the orbital velocities of the electrons of concern (v_e), here the inner shell processes are governed by the adiabaticity parameter η [$=(v_{ion}/v_e)^2$] (Chapter 2). As the adiabaticity factor for the inner shells of both the investigated collision systems is smaller than 1 ($\eta \leq 0.5$ for the Bi-Au collision system and $\eta \leq 0.35$ for the U-Au collision system for the Au K-shell), both lie in the quasiadiabatic regime. Hence, the inner shell vacancy transfer can be considered / interpreted in accordance with the quasimolecular picture [7] using adiabatic level diagrams [98, 99]. Based on an earlier work, see e.g. [98], advanced SCF-DFS multielectron level diagrams for the U-Au and Bi-Au collision systems have been calculated by Anton and Fricke [99] and are shown in see Fig. 6.10 and 6.11 respectively.

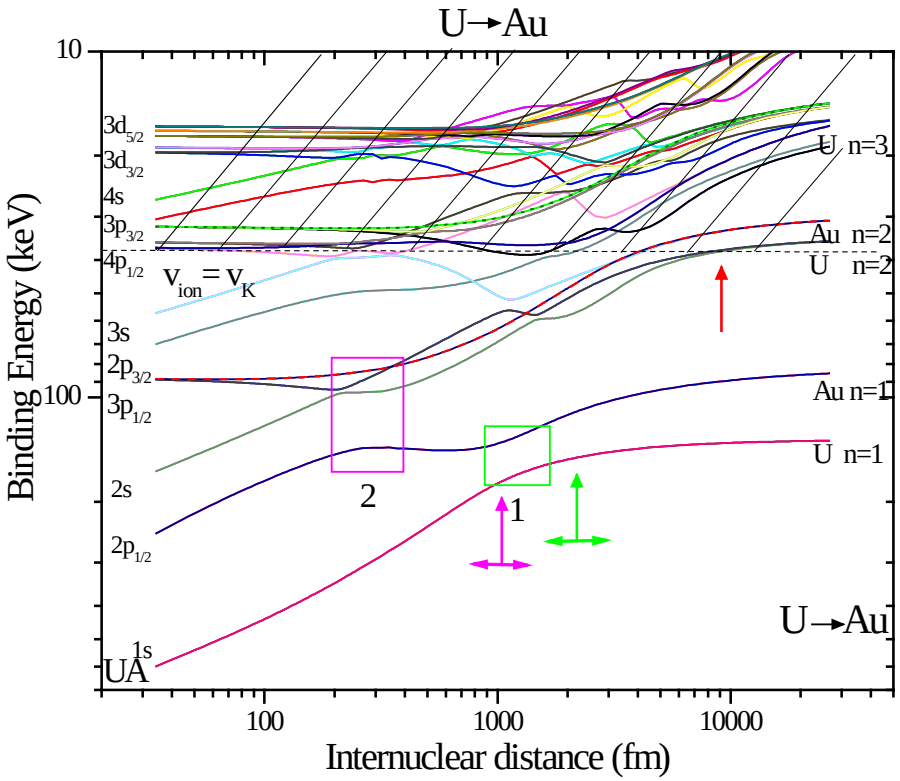

Fig. 6.10. *Adiabatic level diagram for the asymmetric U-Au collision system by [99]. All the electrons above the region for $v_{ion} = v_e$, i.e. shaded area, cannot be considered within the quasiadiabatic picture.*

According to these calculations, the interaction region of "K-K sharing" mentioned in the earlier section is indicated in Fig. 6.10 and 6.11 by rectangles numbered 1. The interaction region for "L-K coupling" (coupling between the L-shell of the projectile and K-shell of the target at small inter nuclear distances) is indicated by rectangles numbered 2. The internuclear distances for the above two processes r_{K-K} and r_{L-K} estimated from experimentally measured cross sections are indicated by arrows in the figures. The L-K shell coupling distance has not been estimated experimentally for Bi-Au collision system for the reasons clarified above. The detail discussion regarding these follows in the next Section 6.4.2. This quasimolecular picture (where the adiabatic level diagram is valid only up to the binding energy given by (v_{ion} = v_e) is not applicable to the electron capture process. The corresponding arrow for electron capture, r_{cap} estimated from measured cross sections has been indicated for presenting a complete overview only.

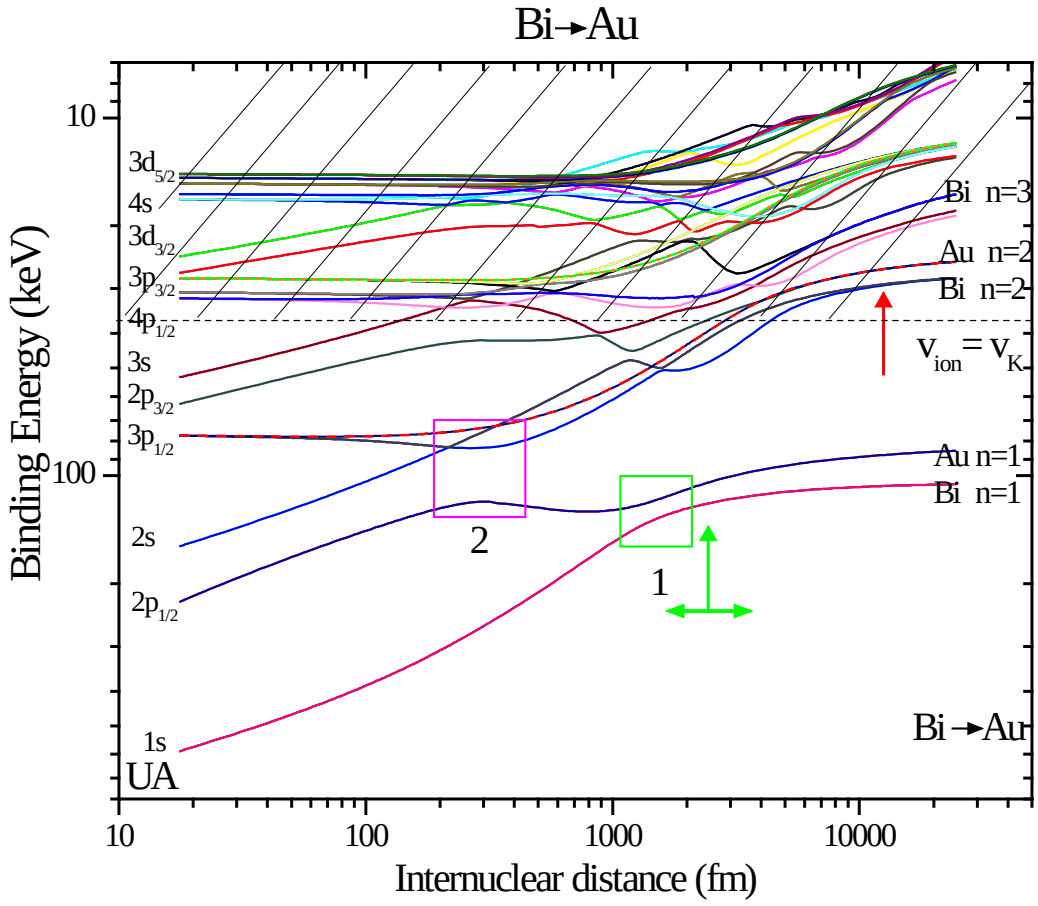

Fig. 6.11. *Adiabatic level diagram for the near symmetric Bi-Au collision system [99]. All the electrons above the region for $v_{ion} = v_e$, i.e. shaded area, cannot be considered within the quasiadiabatic picture.*

6.4.2 Coupling Distances

Table 6.5 gives a summary of the formulae for the probabilities and calculation of interaction distances for different processes viz. “electron capture”, “K-K sharing” and “L-K coupling”. The explanation of the inner shell processes is given below, electron capture has already been discussed above in Section 6.3.5.

K-K transfer

The increase in Au-K x-ray emission for incident U^{91+} or Bi^{82+}-ions indicates that during close collisions, apart from couplings, excitation and ionization active at lower incident charge states, an additional process of K-K vacancy transfer is responsible for the production of K vacancies. In close collisions, K vacancies brought in by the projectile (e.g. U^{92+}, Bi^{82+}) can be transferred to the target K-shell in the quasimolecule via the coupling of the $1s\sigma$ and $2p\sigma$ orbitals called the K-K transfer [95] (the corresponding region indicated in Fig. 6.10 and 6.11 by rectangles numbered 1). Transferred vacancies are then carried by the target K-shell in the outgoing part of the collision. These excess target K-vacancies cause an increase in the target K x-ray emission which has been observed experimentally for Au for both U- and Bi-ions carrying initial K vacancies. With a knowledge of the transfer probability, this increase in the Au-K emission allows an estimation of the internuclear interaction distance for K-K transfer using a simple model.

Table 6.5 *Probabilities and formulae for calculation of different interaction distances. For explanation of the parameters see text.*

Process	**Bi- or U-$K\alpha_1$/Au$K\alpha_1$**	**Probabilities**	**Total probability**	**Geometrical models for estimations**
e^- capture			$P_{cap} = 1 \; r \le r_{cap}$, $= 0 \; r \ge r_{cap}$.	$\sigma_{cap} = P_{cap} \,.\, \pi \, r_{cap}^2$
K-K transfer	$R = \frac{p_{K-K}}{1 - p_{K-K}}$	p_{K-K}	$P_{K-K\,(Transfer)} = 2\,p_{K-K}(1 - p_{K-K})$ for a 2 way passage	$\sigma_{K-K\,(Transfer)} = P_{K-K(Transfer)} \,.\pi \, r_{K-K}^2$
L-K coupling		p_{L-K} p_{K-K} $g = 1/2$	$P_{L-K} = 2\,p_{L-K}(1 - p_{L-K})$ for a 2 way passage	$\sigma_{L-K} = P_{L-K} \,.\, g.$ $(1 - p_{K-K}) .\, \pi \; r_{L-K}^2$

The charge state dependence of Au-Kα_1 for a closed projectile K-shell (i.e. q$\leq$90 for U and q $\leq$81 for Bi) and its drastic increase for an open projectile K-shell has been observed in Fig. 6.5 and 6.6 for the experiments with U and Bi projectiles respectively. The intensity ratio of the projectile, U- or Bi-Kα_1 with respect to the Au-Kα_1 have been given in Tables 4.1 and 5.1 respectively for both closed and open projectile shells.

First we consider the closed projectile case: Denoting the K x-ray emission ratio of heavier to lighter collision partner for closed K-shell as $R = \frac{Z_1 - K_{\alpha 1}}{Z_2 - K_{\alpha 1}}$ and assuming that the K vacancies are mainly produced via the 2pσ level, *R* can be related to the transfer probability p_{K-K} for a single way passage (outgoing) by the following relation:

$$R = \frac{p_{K-K}}{1 - p_{K-K}}$$

For U-Au system *R* = 0.4±0.1 and that for Bi-Au system *R* = 0.9 ± 0.1. For U-Au system p_{K-K} = 0.29 ±0.06 and for Bi-Au system p_{K-K} = 0.47±0.03 is deduced.

According to the Meyerhof formula [95, 100], the non relativistic probability of single transfer of a vacancy R_{Mey} can be approximately given by:

$$R_{Mey(2p\sigma-1s\sigma)} \approx \exp(-\frac{\pi \Delta Z}{v_{a.u.}})$$

where ΔZ is the difference in the atomic numbers of the two collision partners and $v_{a.u.}$ is the velocity of the projectile in a.u.. The two probabilities *R* and R_{Mey} can be compared to each other. The R_{Mey} = 0.78 for Bi-Au and is = 0.46 for U-Au. In these values no relativistic effects are included. Hence they can only be used as guide lines and agree reasonably well with the experimental values.

For an open, incoming projectile K-shell (U^{91+} or Bi^{82+}), a two way passage for the vacancy transfer (in and out) has been considered. This leads to a total probability of vacancy transfer or K-K transfer as:

$$P_{K-K\,(transfer)} = 2\, p_{K-K}\left(1 - p_{K-K}\right)$$

For U-Au it is 0.41±0.06 and for Bi-Au 0.49±0.01. Table 6.6 gives the values of all the parameters required for the calculation of interaction distances for both the systems Bi-Au and U-Au. In a simplified geometrical picture, this total probability is related to the cross section for vacancy transfer or K-K transfer by the relation:

$$\sigma_{K-K\ transfer} = P_{K-K\ transfer} \cdot \pi\, r_{K-K}^2$$

The increase in Au-Kα_1 per incident K vacancy for practical single collision conditions is indicated in Table 6.2 for both U-Au and Bi-Au collision systems as ~20 ± 5 kb and ~30 ± 10 kb respectively. Taking into account the total number of Au-K vacancies (which adds up to a factor of 3 approximately) as explained above for capture cross section case, the total cross section for K-K transfer ($\sigma_{K-K\ transfer}$) is calculated as ~60 ± 26 kb for U-Au system and ~90 ± 52 kb for Bi-Au system. Using the above simple geometrical model the interaction distance for K-K coupling (r_{K-K}) is estimated to have a value of ~2418 ± 1395 fm for the U-Au and ~2158 ± 935 fm for Bi-Au system. These estimated values for r_{K-K} are marked by the corresponding arrows in Fig. 6.10 and 6.11 respectively.

Table 6.6 *Values of all the parameters required for the calculation of interaction distances for the U-Au and Bi-Au collision systems. See text for details of parameters.*

Process	**Parameters**	**U-Au collision system**	**Bi-Au collision system**
K-K transfer	p_{K-K}	0.29±0.06	0.47±0.03
	R	0.4±0.1	0.9±0.1
	R_{Mey}	0.46	0.78
	P_{K-K}	0.41±0.06	0.49±0.01
L-K coupling	p_{K-K}	0.29±0.06	-
	p_{L-K}	< 1/2	-
	g	1/2	-
	P_{L-K}	< 1/2	-

Fig. 6.12 a) and b) show the level diagram of U-Au system (Fig. 6.10) enlarged for the K-K vacancy transfer region. Area of interaction is indicated by the circle. The passage of the incoming projectile vacancy through the molecular orbital levels has two possibilities. These two ways are shown by direction of the blue and red arrows in the two figures.

These values estimated from experimental cross sections are somewhat larger than the region of crossings (rectangles numbered 1, Fig. 6.10 and 6.11) of the 1sσ and 2pσ orbitals shown in the level diagrams. For K-K transfer the level diagrams indicate a value for interaction distance as

approximately within the range 800 to 2000 fm. Relativistic treatment of the couplings may change the result slightly. Here one has also to consider a dynamic coupling of the involved levels already outside the coupling region due to the high collision velocity. Thus slightly increasing the interaction distance. For a more detailed understanding of the inner shell coupling in the relativistic regime further dynamic calculations are required. Moreover, a more detailed consideration of the conversion from x-ray emission to vacancy cross sections has to be considered in future.

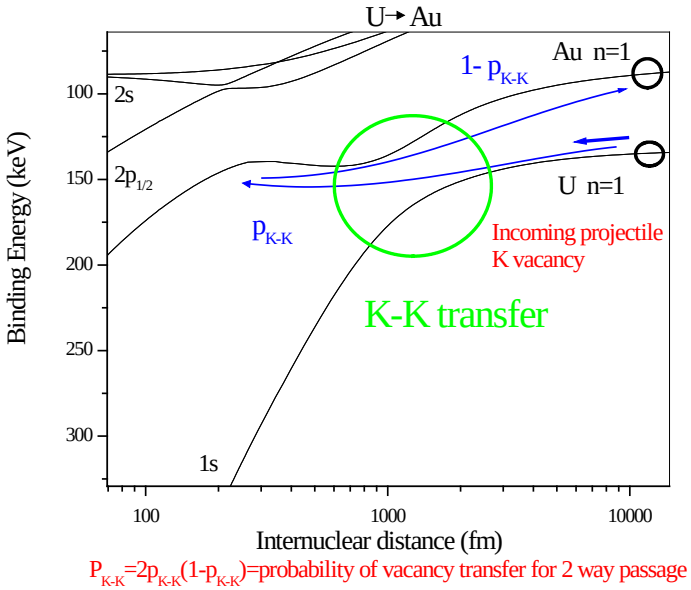

Fig. 6.12 a) *Enlarged graph of Fig. 6.10 depicting the K-K vacancy transfer region. The probability for transfer $p_{K\text{-}K}$ and the probability for not transfer $1\text{-}p_{K\text{-}K}$ are also shown for clarity (see the blue path with the arrows showing the direction of the vacancy transfer).*

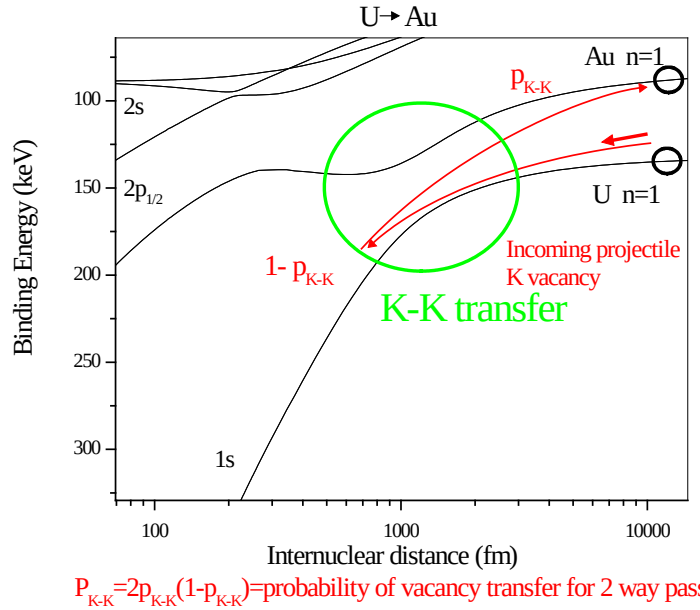

Fig. 6.12 b) *Enlarged graph of Fig. 6.10 depicting the K-K vacancy transfer region. The probability for transfer $p_{K\text{-}K}$ to U-K shell and the probability for not transfer $1\text{-}p_{K\text{-}K}$ are also shown for clarity. (see the red path with the arrows showing the direction of the vacancy transfer).*

L-K coupling

The coupling distance for the L-K shells could be calculated only and approximately for the U-Au collision system because for Bi-Au experiment there was a paucity of intermediate data points

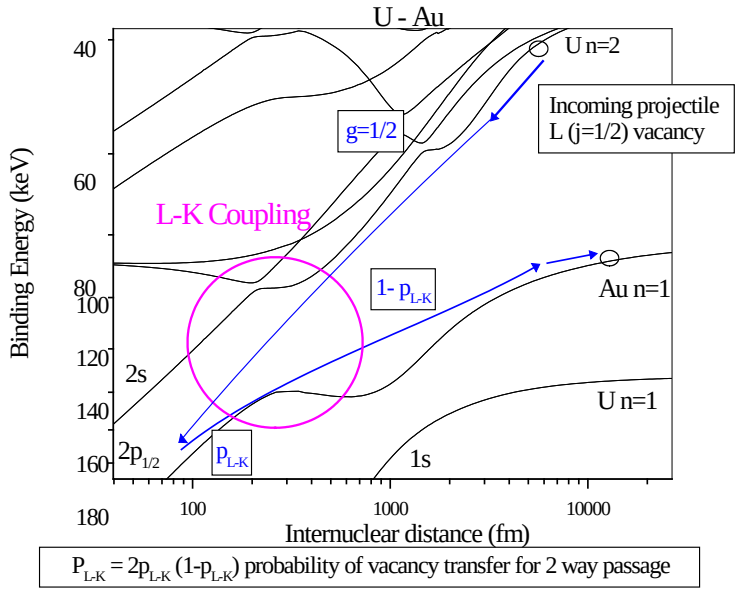

Fig. 6.13 a) *Enlarged graph of Fig. 6.10 depicting the L-K coupling region. The probability for crossing over $p_{L\text{-}K}$ and the probability for not crossing over $1\text{-}p_{L\text{-}K}$ are shown for clarity. The one possible way of passage for an incoming projectile L vacancy is shown with the blue arrow.*

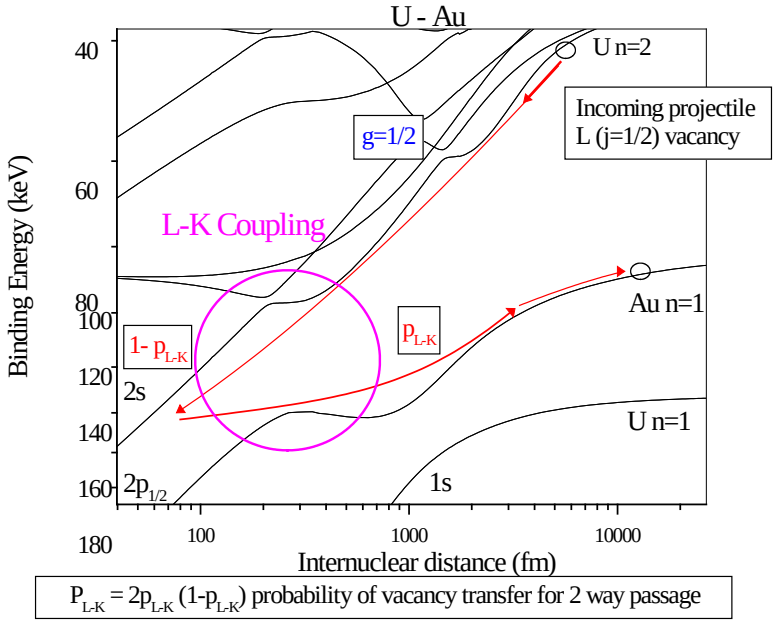

Fig. 6.13 b) *Enlarged graph of Fig. 6.10 depicting the L-K coupling region. The probability for crossing over $p_{L\text{-}K}$ and the probability for not crossing over $1\text{-}p_{L\text{-}K}$ are shown for clarity. Another possible way of passage as compared to that shown in Fig.6.13 a) for an incoming projectile L vacancy is shown with the red arrow.*

(see Fig. 6.6) whereby one could calculate emission cross sections corresponding to incoming projectile L(j=1/2) vacancies ($Bi^{80+ \text{ or lower q}}$).

Fig. 6.13 a) and Fig. 6.13 b) show the level diagram of U-Au system (Fig. 6.10) enlarged for the L-K vacancy transfer region. Area of interaction is indicated by the circle. The two ways of passage of an incoming projectile L vacancy are shown by direction of the blue and red arrows in the two figures.

For projectiles with incoming L(j=1/2) vacancies ($U^{90+, 88+}$), the vacancy may be transferred during the collision towards the united L-shell and couple at intermediate distances to the 2pσ level correlating to the Au K-shell (Fig. 6.10). In the outgoing part of the collision when the partners separate a fraction of the vacancies may be lost to the 1sσ level correlating to the projectile (U) K-shell with probability $p_{K\text{-}K} = 0.29 \pm 0.06$. The projectile vacancy may exist in either a $2s_{1/2}$ or $2p_{1/2}$ level and one can assume a simple statistical factor of a $1/2$ (= g, Table 6.6) for the population of the 2pσ level (Fig. 6.10). The passage of the initial L(j=1/2) vacancy to the target 1s level can be assumed to be a two way passage, then the total probability of transfer can be calculated as follows:

$$P_{L-K} = 2\, p_{L-K} \left(1 - p_{L-K}\right) \leq 1/2$$

This probability along with a statistical factor of g=$1/2$ gives the total probability of transfer of a L(j=1/2) vacancy to the target 1s level as $\leq 1/4$. The total increase in the Au K x-ray emission cross section (σ_{L-K}) for all the channels can be calculated from the increase per L(j=1/2 vacancy) which is with a large uncertainty ~1.3 ± 0.7 kb (Table 6.2) and multiplying it with a factor of 3 (Table 6.2, column 4) in order to include all the decay channels as explained above. This total cross section (σ_{L-K}) can be expressed as:

$$\sigma_{L-K} = P_{L-K} \cdot g \cdot (1 - p_{K-K}) \cdot \pi\, r^2_{L-K}$$

Now taking into account the L-K coupling sharing ratio P_{L-K}, the statistical factor g, the K-K sharing ratio, $p_{K-K} = 0.29$ and (σ_{L-K}), the L-K shell coupling distance (r_{L-K}) can be roughly estimated form the above equation. The r_{L-K} is obtained as ≥ 1035fm**.** The corresponding arrow is marked in the correlation diagram in Fig. 6.10. As was the case for the K-K sharing distances, this value estimated by a simplified model from experimental cross sections is really larger than the region of crossing marked in Fig. 6.10. According to the level diagram, the L-K coupling binding energy is around 120 keV with a gap of about 40 keV. This gap energy corresponds roughly to a transition energy optimally excited at the collision energy used. (cf. also the binding energy for the $v_{ion}=v_e$ limit). Hence due to the relatively large adiabaticity factor for the L-K coupling, the

corresponding levels will couple dynamically, leading to considerably larger coupling distances. It is clear that only dynamical calculations for the relativistic case and a more detailed consideration of further experiments will result in a more effective test of the coupling parameters for these superheavy collision systems. An enlarged graph of Fig. 6.10 depicting the K-K vacancy transfer and L-K coupling regions together is shown in Fig. 6.14.

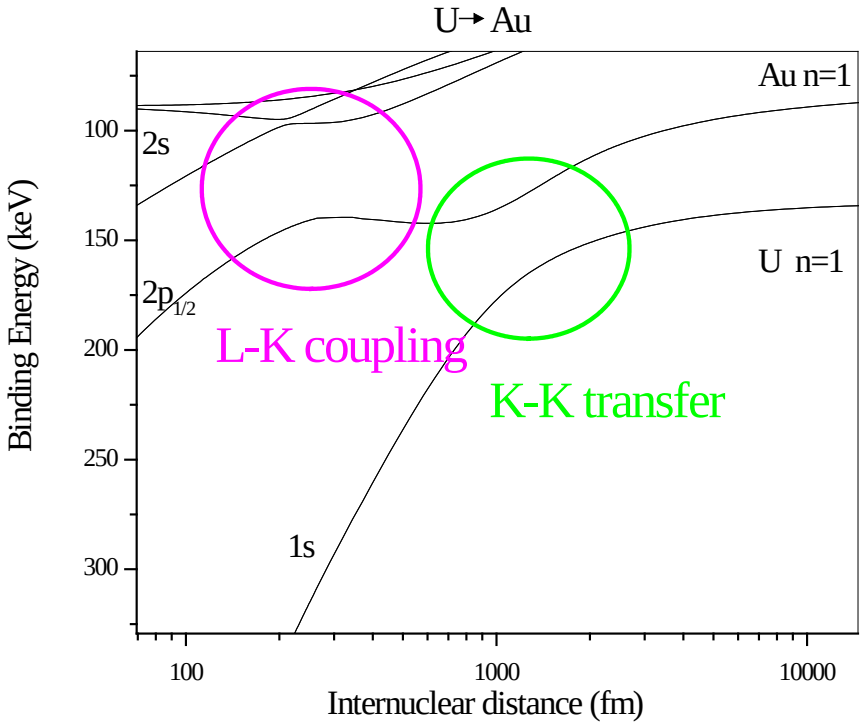

Fig. 6.14 *Enlarged graph of Fig. 6.10 depicting the K-K vacancy transfer and L-K coupling regions.*

6.5 A COMPREHENSIVE PICTURE

The target thickness dependence of the K x-ray cross sections showed clearly that for moderately slow near symmetric as well as for slightly asymmetric collisions for very heavy partners, the projectile K vacancy can survive while penetrating solid targets. The half survival time of the K vacancy (~(6 to 9) $x10^{-16}$ s for Bi and ~(4 to 5) $x10^{-16}$ s for U) in a 69.2 MeV/u, Bi^{82+}-ions and 69.1 MeV/u, U^{91+}-ions while passing a solid Au target is estimated to be appreciably larger than the lifetime of a K vacancy in a normal bismuth or uranium atom (~10^{-18} s). It was thus shown that for very thin solid targets (e.g. $t_{1/2}$ = 95±10 μg/cm^2 for U-Au system and 164±29 μg/cm^2 for Bi-Au system) the inner shells in superheavy quasimolecules can be probed. The K emission cross sections of the collision partners showed a strong dependence on the incident charge state (q) of the

projectile. The charge exchange cross sections calculated from the position resolved particle spectra concurred nicely with those calculated from the K x-ray emission.

As the collision system of U-Au ($\eta_K \leq 0.35$) and Bi-Au ($\eta_K \leq 0.5$) just fall in the quasiadiabatic collision regime an adiabatic level diagram [99] for the two systems was used for the interpretation of the data (Fig. 6.10, 6.11). As is evident from the level diagrams, the K-K vacancy sharing takes place at an appreciable shorter internuclear distance as compared to the electron capture. The interaction distance for electron capture concurs with the region where the atomic levels turn already towards molecular ones, i.e. where the corresponding shells start to overlap, the coupling between the L shells of the projectile and K-shell of the target take place during close collisions and the K-K sharing takes place where the quasimoleular 1sσ and 2pσ levels start to diverge towards the united atom system.

The increase in the Bi-, U- and Au-K x-ray emission for projectiles with initial K vacancies allowed a rough estimation of interaction distances. The interaction distance for electron capture in distant collisions, interaction distance for K-K sharing and coupling distance for L-K shells sharing during close collisions are estimated assuming simple geometrical models. Table 6.7 gives a summary of the various interaction distances estimated for the Bi-Au and U-Au collision systems. These distances were found to be somewhat larger than the ones indicated by the level diagrams (Fig. 6.10 and 6.11) possibly indicating more channels for the feeding of vacancies during collisions than assumed in our simple geometrical models. Dynamical calculations for the involved couplings in the relativistic regime as well as further dedicated measurements are needed to get more precise information on these superheavy atomic collision systems. The present investigation could only open the door to this challenging field giving a very first however exciting glance of it.

Table 6.7 *A summary of the various interaction distances estimated for the U-Au and Bi-Au collision systems.*

	U-Au collision system	**Bi-Au collision system**
r_{cap}	~ 9286±2944 fm	~ 12792±4055fm
r_{K-K}	~ 2158±935 fm	~ 2418±1395 fm
r_{L-K}	≥ 1035±517 fm	-
r_{K-K} [99] see Fig. 6.10, 6.11	~ 900-1500 fm	~ 900-2000 fm
r_{L-K} [99] see Fig. 6.10, 6.11	~ 200-400 fm	~ 200-400 fm

With the results of the present investigation, the basis for a detailed probe into the inner shells of superheavy quasimolecules is laid. In the future, lower projectile energies will have to be investigated to probe these systems at better adiabatic conditions.

CHAPTER VII

CONCLUSIONS AND OUTLOOK

7.1 SUMMARY AND CONCLUSIONS

Collisions of very heavy atoms and ions have attracted many researchers in basic science years ago, see e.g. [7] and references therein. The goal has been to approach and understand super-heavy atomic systems [1] with united atomic numbers far beyond existing matter, with $Z_{UA} = Z_1+Z_2 > 100$. Beyond $Z_{UA} = 137$ the normal Dirac equation for a point charge cannot be solved [1]. For $Z_{UA} > 160$ the innermost electron levels even dive into the negative continuum due to tremendous relativistic effects. These super-heavy quasi-atoms or quasimolecules can be approached in relatively slow [24] heavy ion-atom collisions which are slow compared to the orbital velocity of the innermost electrons of concern. In order to probe these tightly-bound inner shell levels, vacancies have to be provided there and their decay by x-ray emission in the separated partners or in the quasi-molecule itself has to be studied. Unfortunately, for very heavy ions it has not been possible (in early 70's) to provide abundant and slow ionic projectiles with incoming inner shell vacancies for testing super-heavy atomic systems. Hence in all previous measurements [7] in this field, inner shell vacancies could only be produced during the close collision itself, i.e. during the collision of interest. Many aspects of super-heavy atomic systems have already been tested by these investigations. However, the great venture to provide initial inner shell vacancies for investigating super-heavy quasimolecules could not be achieved earlier. The aim of this work is exactly to provide a way out of this dilemma.
The dedicated experiments reported here demonstrate

- that abundant highly charged heavy ions, i.e. very heavy ions with incoming K-shell vacancies, can be provided at still useful moderate collision energies,
- that initial inner shell vacancies can survive in a heavy projectile penetrating thin foils of heavy target atoms and can be provided there for super-heavy collisions,
- that tightly bound innermost levels of the superheavy collision molecule can be probed by incoming inner shell projectile vacancies.

Up to H-like heavy U and Bi-ions carrying one K-shell vacancy were produced by stripping after the heavy ion synchrotron SIS at GSI, Darmstadt at an energy of ~69 MeV/u. These charge state selected ion beams with typically 10^6-10^8 ions/s were provided for collision experiments with thin Au foils. An energy of 69 MeV/u is just low enough to be considered as slow compared to the

Au K-shell orbital velocity. Hence during close collisions of the investigated systems, quasimolecules can be formed transiently for inner shells during close collisions. However the charge state of the ions may be reduced quickly towards the mean charge state while passing through matter. As a result during close quasimolecular collisions incoming K-shell vacancies may no longer be available in deeper layers of the target foil. In this respect a less dense gas target would be preferable however it is more than cumbersome to design proper gas or vapor targets of heavy atoms showing appropriate luminosities for the quasimolecular processes. Hence the only realistic way is to try thin foils of heavy target atoms.

The first aim was to probe the survival of an incoming projectile K vacancy of a heavy projectile penetrating the bulk. Several tests were performed giving all comparable results that for the cases considered half of the projectiles still carry their K vacancies up to Au-foil thicknesses of 150±40 $\mu g/cm^2$. It is established by the decrease in intensity of the projectile K x-ray emission with target thickness as well as to some extent by the corresponding but smaller decrease in target K x-ray emission. Furthermore, the shrinking of the ratio for projectile K to target K x-ray emission leads very convincingly to the same result. This result has been confirmed by direct and total charge exchange measurements deduced from charge state distributions behind the target with different thicknesses. The survival thickness can also be observed approximately from the slight reduction in the K centroids of Bi^{q+} and Au with increasing (Au) target thickness. Hence, Au target foils up to 100 – 200 $\mu g/cm^2$ can be used to study superheavy quasimolecules with incoming K-shell vacancies. Apart from this a complete impression of the projectile-ion status (charge state evolution and population distribution) can be obtained from the complex x-ray emission pattern involving outer shells.

With the above positive outcome, a first test on the behavior of the innermost quasimolecular levels with incoming K vacancies could be pursued. Dynamic couplings between the innermost shells (K-K [92] and L-K coupling [93]) were probed for the above mentioned near symmetric and slightly asymmetric super-heavy quasimolecular systems (after the collision). The coupling distances have been deduced from the K x-ray emission of both collision partners. The values found using simple assumptions on the coupling behavior are roughly in accordance with the outcome of quasi-molecular level calculations [99]. Dynamic calculations are necessary for a more detailed comparison and in future more appropriate models have to be applied for the evaluation. It can be observed from the level diagrams (Fig. 6.10 and 6.11), that the innermost couplings investigated by the experiments approach binding energies of around 250 keV which is about twice the binding energy of the innermost K electrons in U. On the whole, all the coupling distances estimated

experimentally including the interaction distance for electron capture fit reasonably well to the corresponding level diagrams and hence the quasimolecular picture is valid for the innermost shells.

7.2 OUTLOOK

With these basic investigations a new path to the investigation of transient super-heavy atomic systems is laid. The next goal would be experiment at lower ion energies of ~10 MeV/u region. The stripping method applied at the present synchrotron (SIS) at GSI would enable only a moderate decrease in energy however coupling the SIS with the storage ring (ESR) would provide still lower energies. High energy ions stripped on ejection from SIS can be re-injected into ESR where they can be decelerated to the required energy. These cooled/decelerated ions can then be slowly extracted and directed towards the (external) target foil.

An interesting experiment would be the U^{92+}-U collision system used to investigate the MO x-rays of the collision system as a function of the impact parameter. This system would be interesting as for both 1s and $2p_{1/2}$ orbitals the central field is ~$1x10^{18}$ V/cm for a nuclear charge of 184 (=92+92). Very thin Uranium targets would be appropriate for this investigation where bare or H-like U-ions decelerated to about 6 MeV/u would be bombarded on solid targets with a slow extraction of 10^7 ions. Large solid angle x-ray detectors along with striped x-ray detectors would provide the information required from the collision. Si(Li) and Ge(i) detectors would be used to cover the entire energy range of K and L x-rays of the collision partners. Position-sensitive particle detectors would be useful in analyzing the charge state of the ejectile-ions after collision.

Internal storage ring experiments would be challenging, demanding specially developed gas targets. Even though they are feasible, investigations of superheavy atomic systems with $Z_{UA} \geq 170$ would be nearly impossible. So the immediate next steps would be to use solid target foils which can permit a glance into systems with $Z_{UA} \geq 170$. Sophisticated x-ray experiments including impact parameter dependences seem feasible. Besides the characteristic K radiation of the collision partners, quasi-molecular radiation from the transient super-heavy atomic systems as well as positron emission can be investigated. However, providing incoming K vacancies will enhance all these cross sections by almost two orders of magnitude. Hence an exciting field in the region of super-heavy atomic systems can be probed uniquely.

BIBLIOGRAPHY

1. J. Reinhardt and W. Greiner: in "Treatise on Heavy-Ion Science", High Energy Atomic Physics, (Vol. 5) ed. D. Allan Bromley (Plenum Press, 1985), p 3.
2. G. Soff and B. Mueller, Z. Phys. A 280 (1977) 243.
3. B. Fricke and G. Soff: At. Data Nucl. Data Tables 19 (1977) 83.
4. J. Reinhardt and W. Greiner: Rep. Prog. Phys. 40 (1977) 219.
5. B. Fricke: in Progress in spectroscopy, Part A, (Plenum Press, 1978), p 183.
6. P.H. Mokler and F. Folkmann: in "Topics in Current Physics", Vol. 15, ed. I.A. Sellin, (Springer Verlag, 1978), p 201.
7. P.H. Mokler and D. Liesen: in "Progress in Atomic Spectroscopy", Part C, ed. H.J. Beyer and Hans Kleinpoppen, (Plenum Publishing Corporation, 1984), p 321 and references therein.
8. P.H. Mokler, D.H.H. Hoffmann, W.A. Schönfeldt, Z. Stachura and A. Warczak, H. Schmidt-Böcking and R. Schuch: Nucl. Instr. and Meth. in Phy. Res. B 10/11 (1985) 58 and P.H. Mokler, D.H.H. Hoffmann, W.A. Schönfeldt, D. Maor, W.E. Meyerhof, Z. Stachura: Nucl. Instr. and Meth. in Phy. Res. B 4 (1984) 34.
9. P.H. Mokler, D.H.H. Hoffmann, W.A. Schönfeldt, D. Maor, Z. Stachura and A. Warczak: J. Phy. B 17 (1984) 4499.
10. D. Liesen, P. Armbruster, H.-H. Behncke, F. Bosch, S. Hagmann, P.H. Mokler, H. Schmidt-Böcking and R. Schuch: in Electronic and atomic Collisions, ed. N. Oda and K. Takayanagi, (North Holland Publishing Co. 1980), p 337.
11. P.H. Mokler, S. Hagmann, P. Armbruster, G. Kraft, H.-J. Stein, K. Rashid and B. Fricke: "Superheavy Quasimolecules" in "Atomic Physics 4", ed. G. zu Putlitz, E.W. Weber and A. Winnacker, (Plenum Publishing Corporation, 1975), p 301.
12. J.S. Greenberg: in "Electronic and Atomic Collisions", ed. N. Oda and K. Takayanagi, (North Holland Publishing Company, 1980), p 351.
13. W. Greiner and W. Scheid: "Heavy-ion atomic physics" in "Heavy ion collisions" Vol. 3, ed. R. Bock (North Holland Publishing Company, 1982), p 301.
14. D. Liesen: in "Comments At. Mol. Phys." Vol. 2, No. 1, (Science Publishers, Inc., 1982), p 39.
15. H. Backe and C. Kozhuharov: in "Progress in Atomic Spectroscopy", Part C, ed. H.J. Beyer and Hans Kleinpoppen, (Plenum Publishing Corporation, 1984), p 459.
16. P.H. Mokler: "Quasimolecular heavy ion-atom collisions", GSI-84-37 (GSI report), Invited lecture to XIX Winter School on Physics, Zakopane, Poland (3-15 April, 1984).
17. J.S. Greenberg and P. Vincent: in "Treatise on Heavy-Ion Science", High Energy Atomic Physics, (Vol. 5) ed. D. Allan Bromley (Plenum Press, 1985), p 3.
18. P.H. Mokler, "Spectroscopy of heavy few electron ions": GSI-86-25 (GSI report), Invited talk at 18 EGAS, Marburg, 8-11 July 1986.
19. A. Warczak, D. Liesen, P.H. Mokler and W.A. Schönfeldt: J. Phy. B 14 (1981) 1315 and P.H. Mokler, D.H.H. Hoffmann, W.A. Schönfeldt, D. Maor, Z. Stachura and A. Warczak: J. Phy. B 17 (1984) 4499.
20. W. Uchai, G. Lapicki, W.T. Miliner, S. Raman, P.V. Rao and C.R. Vane: J. Phys. B 18 (1985) L389.
21. P.H. Mokler: Phys. Rev. Lett. 26 (1971) 811.
22. S. Hagmann, P. Armbruster, G. Kraft, P.H. Mokler and H.-J. Stein: Z. Physik A 288 (1978) 353.
23. J.A. Bearden: Rev. Mod. Phys. 39 (1967) 78.
24. D.H. Madison and E. Merzbacher: *Atomic Inner Shell Processes*, ed. B. Crasemann, (Academic Press, New York 1975) Vol. 1, p 1.

25. U. Fano and W. Lichten: Phys. Rev. Lett. 14 (1965) 627.
26. Yu. Demkov: Sov. Phys. JETP 18, (1964) 138 and J.S. Briggs, J. Macek: J. Phys. B 5 (1972) 579; J.S. Briggs: Reports on Progress in Physics 39 (1976) 217.
27. H.C. Brinkman and H.A. Kramers: Proc. K. Ned. Akad. Wet. 33 (1930) 973.
28. J.D. Garcia: Phys. Rev. A 1 (1970) 280, 1402.
29. J. Bang and J.M. Hansteen: K. Dan. Vidensk. Selsk. Mat-Fys. Medd. 31 (1959) 13.
J.M. Hansteen, O.M. Johnson and L. Kocbach: J. Phys. B 7 (1974) L271.
J.M. Hansteen, O.P. Mosebekk: Nucl. Phys. A 201 (1973) 541.
30. E. Merzbacher and H.W. Lewis: Encyclopedia of Phys. ed. by S. Flugge. (Springer-Verlag, Berlin, 1958) vol. 34 (1958) p 166.
31. W. Brandt and G. Lapicki: Phys. Rev. A 23 (1981) 1717.
32. P. Richard: *Atomic Inner Shell Processes*, ed. B. Crasemann, (Academic Press, New York 1975) Vol. 1, p 74.
33. W. Lichten: Phys. Rev. 164 (1967) 131.
34. F.W. Saris: Physica 52 (1971) 290.
35. F.W. Saris and D. Onderdelinden: Physica 49 (1970) 441.
36. M. Mann, P.H. Mokler, B. Fricke, W-D Sepp, W.A. Schönfeldt and H. Hartung, J. Phys. B 15 (1982) 4199.
37. N. Bohr and K. Lindhard: K. Dan. Vidensk. Selsk. Mat. Fys. Medd. 28 (1954) 1.
38. J. Eichler and T. Stöhlker, Phys. Rep. 439 (1-2) (2007) 1 and references therein.
39. X. Ma, P.H. Mokler, F. Bosch, A. Gumberidze, C. Kozhuharov, D. Liesen, D. Sierpowski, Z. Stachura, Th. Stöhlker, A. Warczak: Phys. Rev. A 68 (2003) 042712.
40. J.R. Oppenheimer: Phys. Rev. 31 (1928) 349.
41. H.C. Brinkman and H.A. Kramers: Proc. Acad. Sci., Amsterdam, Vol. 33 (1930) 973.
42. V.S. Nikolaev: Sov. Phys-JETP 24 (1967) 847.
43. R.M. Drisko: Carnegie Inst. Tech. (1955) (Unpublished).
44. M.H. Mittleman: Phys. Rev. 122 (1961) 499.
45. M. Kleber and M.A. Nagarajan: J. Phys. B 8 (1975) 643.
46. A.M. Halpern and J. Law: Phys. Rev. Lett. 31 (1973) 4.
47. G. Lapicki and F.D. McDaniel: Phys. Rev. A 22 (1980) 1896.
48. D.R. Bates and A. Dalgarno: Proc. Phys. Soc. A 65 (1952) 919.
49. J.D. Jackson and H. Schiff: Phys. Rev. 89 (1953) 359.
50. A.S. Schlachter, J.W. Stearns, W.G. Graham, K.H. Berkner, R.V. Pyle and J.A. Tanis: Phys. Rev. A 27 (1983) 3372; Calculations by Th. Stöhlker (private communication).
51. H. Knudsen, H.K. Haugen, P. Hvelpund: Phys. Rev. A 27 (1983) 3372.
52. J. Eichler: Phys. Rev. A 23 (1981) 498.
53. A. Ichihara, T. Shirai and J. Eichler: Atomic Data and Nuclear Data Tables, 55 (1993) 63 and J. Eichler: Phys. Rev. A 32 (1985)112; Calculations by Th. Stöhlker (private communication).
54. H.D. Betz: Rev. Mod. Phys. 44 (1) (1972) 465.
55. E. Baron: IEEE Transactions on Nuclear Science NS-19 No.2, (1972) 256.
56. V.P. Zaikov, E.A. Kralkina, V.S. Nikolaev, E.I. Sirotinin: Nucl. Instr. and Meth. in Phys. Res. B 33 (1988) 202.
57. V.S. Nikolaev and I.S. Dmitriev: Phys. Lett. 28A (1968) 277.
58. K. Shima, T. Ishihara, T. Miyoshi and T. Mikumo; Phys. Rev. A. 28 4 (1983) 2162 and references therein.
59. C. Scheidenberger, Th. Stöhlker, W.E. Meyerhof, H. Geissel, P.H. Mokler and B. Blank: Nucl. Instr. and Meth. in Phys. Res. B 142 (1998) 441.
60. P.H. Mokler: Phys. Rev. Lett. 26 (1971) 811.
61. J.S. Braich, Punita Verma, H.R. Verma: J. Phys. B 30 (1997) 2359 and Rad. Phys. and Chem. 51, (1998) 411.

62. Punita Verma, Jasbir S. Braich, A. Mandal, T. Nandi and H.R. Verma: Physica Scripta 61 (2000) 335 and references therein.
63. M. Czarnota, D. Banas, J. Braziewicz, J. Semaniak, M. Pajek, M. Jaskóla, A. Korman, D. Trautmann, W. Kretschmer, G. Lapicki, T. Mukoyama: Phys. Rev. A 79 (2009) 032710 and references therein.
64. J.H. Scofield: Atomic Data and Nuclear Data Tables 14 (1974) 121.
65. J.R. Mcdonald, M.D. Brown, S.J. Czuchlewski, L.M. Winters, R. Laubert, I.A. Sellin and J.R. Mowat: Phys. Rev. A 14 (1967) 1997.
66. O. Benka: Nucl. Instr. and Meth. B 4 (1984) 279.
67. GSI heavy-ion accelerator facility: http://www.gsi.de/accelerator.
68. GLOBAL: program to calculated charge states of swift heavy ions in matter; available under http://www-linux.gsi.de/~weick/charge_states; CHARGE: program to calculated charge states of swift heavy ions in matter; available under http://www-aix.gsi.de/~scheid/html charge.html.
69. ATIMA: ATomic Interaction with MAtter; a program to calculate the energy loss, range, energy and angular straggling and stopping power for ion-beams; available under http://www-linux.gsi.de/~weick/atima/.
70. H.W. Schäffer: Ph.D. Thesis; GSI Diss.16, 1999.
71. Labview software: http://www-wnt.gsi.de/LabVIEW.
72. MIRKO: A program for ion optical settings of accelerators and beamlines by B. Franczak; available under http://www-linux.gsi.de/~redelbac/MIRKO/ indexEng.html.
73. E. Berdermann, K. Blasche, P. Moritz, H. Stelzer and B. Voss: Diamond and Related Materials 10 (2001) 1770 and P. Moritz, E. Berdermann, K. Blasche, H. Stelzer and B. Voss: Diamond and Related Materials 10 (2001)1765.
74. http://www-norhdia.gsi.de/talks/Braeuning-Demian_A.pdf and S. Toleikis: Ph.D. Thesis; GSI Diss.11, 2002.
75. J. F. Ziegler, J. P. Biersack, and V. Littmark: "The Stopping and Ranges of Ions in Solids" (Pergamon, New York 1985), Vol I; available under http://www.srim.org.
76. F.P. Hessberger: GSI Report, GSI-11, 1985.
77. W. Adam *et al*.: Nucl. Instr. and Meth. in Phys. Res. A 476 (2002) 686.
78. W. Adam *et al*.: International Conference on Radiation Effects, Florence 2000.
79. E. Berdermann: GSI, private communication.
80. MBS available under: http://www-win.gsi.de/daq/.
81. Go4 available under: http://www-win.gsi.de/go4/.
82. M. Pajek, A.P. Kobzev, R. Sandrik, R.A. Ilkhamov and S.H. Khusmurodov: Nucl. Instr. and Meth. B 42 (1989) 346.
83. M.S. Dias and C. Renner: Nucl. Instr. and Meth. 193 (1982) 91.
84. D.D. Cohen: Nucl. Instr. and Meth. A 267 (1988) 492.
85. R. Mowat: Nucl. Instr. and Meth. 70 (1969) 237 and A. Owens: Nucl. Instr. and Meth (1989) 297.
86. J.H. Hubbell: Int. J. App. Rad. and Isotopes 33 (1982) 1269.
87. E. Berdermann, K. Blasche, P. Moritz, H. Stelzer and B. Voss: Diamond and Related Materials 10 (2001) 1770 and P. Moritz, E. Berdermann, K. Blasche, H. Stelzer and B. Voss: Diamond and Related Materials 10 (2001)1765.
88. S. Toleikis: Ph.D. Thesis. GSI Diss.11, 2002.
89. Marek Polasik and M. Lewandowska-Robak: Phys. Rev. A 70 (2004) 052502 and references therein.
90. M. Lewandowska-Robak and Marek Polasik: Nicholas Copernicus University, Toruń, Poland, private communication.
91. I.P. Grant: Computer Phys. Commun. 94 (1996) 249.

92. W.E. Meyerhof: Phys. Rev. Lett. 31 (1973) 1341.
93. W.E. Meyerhof: Phys. Rev. A 18 (1978) 414.
94. H. Bräuning, P.H. Mokler, D. Liesen, F. Bosch, B. Franzke, A. Krämer, C. Kozhuharov, T. Ludziejewski, X. Ma, F. Nolden, M. Steck, T. Stöhlker, R. W. Dunford, E. P. Kanter, G. Bednarz, A. Warczak, Z. Stachura, L. Tribedi, T. Kambara, D. Dauvergne, R. Kirsch, C. Cohen: Phys. Rev. Lett, 86 (2001) 991.
95. W.E. Meyerhof: Phys. Rev. A 18 (1978) 414.
96. W.E. Meyerhof, R. Anholt, T.K. Saylor: Phys. Rev. A 16 (1978) 169.
97. O. Keski-Rahkonen, M.O. Krause: Atomic Data and Nuclear Data Tables, 14 (1974) 139.
98. P. Kürpick, T. Bastuğ, B. Fricke, W.-D. Sepp, A. Warczak, M. Jäger, J. Ullrich, T. Kandler, M. Schulz, A. Demian, M. Damrau, H. Bräuning, H. Schmidt-Böcking: Phys. Lett. A 207 (1995) 199.
99. J. Anton and B. Fricke, University of Kassel, Kassel, Germany, private communication.
100. W.E. Meyerhof, R. Anholt, T. Saylor, S. Lazarus, A. Little, L. Chase, Phy. Rev. A 14 (1976) 1653.

Acknowledgement

This Ph.D. work which started as an intention to achieve a Doctorate in Physics became slowly a test. A test of human capabilities amidst trying situations and circumstances and I first of all thank The Almighty for having provided me the strength, courage and persistence to sail patiently in turbulent oceans. I also thank my Guru for bestowing on me the correct perspective to view adverse situations and to develop patience and perseverance to complete this task at the same time bringing solace to my soul. How much can I express my eternal gratitude to my parents for their support, it would only be too little.

Had it not been for the unflinching support and supervision of Prof. P.H. Mokler this thesis would never have seen the light of the day. I cannot find appropriate words to express my gratitude for all that he has done to enable me to complete my thesis work and I learnt a lot more from him than just Physics. Such guidance with infinite patience is nothing but a reflection of the almighty extending his helping hand to me.

I wish to thank Prof. M.A. Wahab for providing me the requisite guidance and support due to which this work was financially supported by the Indo-German UGC-DAAD fellowship within the Sandwich Model. I am also grateful to the Atomic Physics Department of GSI for having extended the partial financial support required for completion of this work.

Dr. Angela Bräuning-Demian stood by me like a pillar of strength during the entire course of this work. Her contagious enthusiasm infused energy in me many a times and I fall short of words to express my gratitude for the guidance and help she has extended for this work.

The data analysis would just not have been possible without the help of Dr. C. Kozhuharov to whom I am indebted for teaching me the skills patiently. The discussions with him filled many a times the gap in my understanding of Physics behind this work. I am thankful to Dr. Harald Bräuning for helping me with the electronics and during the data handling; his support during beam times was indispensable.

I wish to thank Prof. B. Fricke and J. Anton for eagerly performing calculations for the level diagrams of the investigated heavy collision systems.

I wish to thank Prof. J.-H. Kluge the former Head, Atomphysik, GSI for providing all the support required for carrying out the experiments and to Prof. T. Stöhlker, the present Head, Atomphysik, GSI for extending financial support when required. I am also thankful to him for helping me with theoretical calculations for charge exchange.

I am thankful to all the members of the Atomphysik group: F. Bosch, S. Hagmann, D. Liesen, A. Gumberidze, D. Banas, S. Chatterjee, U. Spillmann and Z. Stachura of Institute for Nuclear Physics, Cracow for participation in the experiments at Cave-A. Thanks are due to the members of the accelerator group of GSI for supplying the requisite beams for the experiments and especially B. Franczak for the tuning of the beams till the Cave-A experimental area. J. Adamczewski has to be thanked for his eagerness in helping with the Go4 software.

I cannot but express my humble thanks to Hannelore and Gaby for repeatedly bringing a smile back on my face amidst problems and making me feel homely while away from home.

Last but not the least the support of my entire family for this work is something that once again cannot be expressed in words. The support that I got made me feel that the thesis is being made by all of us and not just me. I wish my father was alive to see the fruit of the tree he watered and nurtured with all his wisdom. Thanks to my sweet little daughter who silently put up with my absence during all these years of my involvement with this work and helped me in her cute little ways.

Eidesstattliche Erklärung

Ich erkläre:

“Ich habe die vorgelegte Dissertation selbständig und ohne unerlaubte fremde Hilfe und nur mit den Hilfen angefertigt, die ich in der Dissertation angegeben habe.

Alle Textstellen, die wörtlich oder sinngemäß aus veröffentlichten Schriften entnommen sind, und alle Angaben, die auf mündlichen Auskünften beruhen, sind als solche kenntlich gemacht.

Bei den von mir durchgeführten und in der Dissertation erwähnten Untersuchungen habe ich die Grundsätze guter wissenschaftlicher Praxis, wie sie in der “Satzung der Justus-Liebig-Universität Gießen zur Sicherung guter wissenschaftlicher Praxis” niedergelegt sind, eingehalten”.

Gießen 3.11.2010 Punita Verma